

Mechanical Behaviour of Eco-Efficient Ultra-High Performance Fibre Reinforced Concrete (E-UHPFRC) and Design of E-UHPFRC Screw Piles



A thesis presented for the degree of

Doctor of Philosophy in Civil and Structural Engineering

at The University of Sheffield

By

Muhammad Nura Isa

Sheffield

April 2021

To my parents thank you for the never ending love, support and encouragement
To my wife, thank you for been there with me and supporting me through all the tough times
To my Son, thank you for coming to our life bringing joy to us all
To my siblings thank you for always standing with me through the good and tough times

Abstract

Ultra-High Performance Fibre Reinforced Concrete (UHPFRC) is a novel development in concrete materials that can lead to novel applications due to its excellent strength and durability potential. However, the widespread use of UHPFRC is currently limited due to its high initial cost and high carbon footprint of the cement and steel fibre constituents as well as the lack of recognised design models.

The aim of this research is to develop an Eco-Efficient Ultra-High Performance Fibre Reinforced Concrete (E-UHPFRC) by utilising alternative binders (e.g. GGBS), Recycled Tyre Steel Fibres (RTSF) and Recycled Tyre Steel Cords (RTSC). This is achieved through experimental and numerical studies, as well as the development of analytical models to aid the development of design guidelines. An extensive series of tests is carried out on twelve (12) UHPFRC mixes containing either RTSC or RTSF, or blends of the two in various ratios for total fibre volumes of 2, 3 and 4%. The fresh properties of the designed E-UHPFRC mixes are examined, followed by a comprehensive analysis of the mechanical behaviour of the hardened concrete in: flexure, compression and shear. The results show that 11 of the examined mixes can offer the desired mechanical properties and meet the requirements of workability and strength to be defined as UHPFRC. The performance of the mixes containing RTSC is comparable to what is reported in the literature for mixes containing Manufactured Steel Fibres. Design models are proposed to predict the flexural and shear strengths of E-UHPFRC mixes. The complementary material efficiency study of the mixes shows that use of RTSF and RTSC in UHPFRC provides significant cost and environmental benefits.

The application of the newly developed E-UHPFRC in the manufacturing of screw piles is proposed as a quick and more sustainable means of providing foundations for light weight structures, which given the limitations of ordinary concrete is currently only feasible with costlier steel piles. A detailed design guideline for E-UHPFRC screw piles is provided for two possible geometries.

Acknowledgement

I would like to express my deepest gratitude and appreciation to my Doctoral supervisors, Professor Kypros Pilakoutas and Dr. Maurizio Guadagnini for their great support, guidance, patience and encouragement during the course of this work.

I would also like to show my gratitude to Petroleum Technology Development Fund, Nigeria (PTDF), for providing me with the scholarship to undergo my Doctoral degree under the 2017/2018 Overseas Postgraduate Scholarship Scheme.

My sincere appreciation to the technical staff of the Concrete and Heavy Structures Lab, in particular Kieran Nash, Robin Markwell, Don Jenkins and Shaun Waters, for their great technical support.

I would also like to thank former and current researchers of the Concrete and Earthquake research group for the good time we had together; Harris Angelakopoulos, Abdulaziz Alsaif, Zahran Al-kamyani, Sultan Al-Otaibi, Asif Hussain Shah, Imad El Khouri, Niki Trochoutsou, Hang Hu, Hamed Fergani, Shanker Lah, Panos Papastergiou, Francesca Roscini, Ahmad Mahmoud Kobeiter Abiad and Sumit Chakraborty. Many thanks to the members of Nigerian community who have made my stay in Sheffield a more pleasant one.

Finally, immense thanks and gratitude goes to my family for their tremendous support, love and care they provided during the course of my entire study.

Table of Contents

Abstract	ii
Acknowledgement	iii
Chapter 1: Introduction	1
1.1 Introduction.....	1
1.2 Motivation.....	2
1.3 Research Background	2
1.3.1 Ultra-high Performance Fibre Reinforced Concrete	2
1.3.2 Recycled Tyre Steel Fibres (RTSF) and Recycled Tyre Steel Cords.....	3
1.3.3 Screw Piles.....	4
1.4 Research Aim and Objectives.....	6
1.5 Research Significance.....	7
1.6 Outline of the Thesis.....	7
1.7 References.....	10
Chapter 2: Mechanical Performance of Affordable and Eco-Efficient Ultra-High Performance Concrete (UHPC) Containing Recycled Tyre Steel Fibres.	14
2.1 Introduction.....	16
2.2 Material and Methods	18
2.2.1 E-UHPFRC Mix Design	19
2.2.2 Fibres Characterisation and Processing	19
2.2.3 Pilot Flexural Testing.....	23
2.2.4 Mixing Procedure and Specimen Preparation.....	23
2.2.5 Compressive Strength and Modulus of Elasticity	24
2.2.6 Three-point Bending Test	25
2.3 Material Efficiency	26
2.3.1 Cost	26
2.3.2 Environmental Impact.....	27
2.3.3 Mechanical Efficiency	27
2.3.4 Mix Efficiency	27

2.4	Results and Discussion	28
2.4.1	Effect of RTSC Length and RTSF Refinement on Flexural Behaviour.....	28
2.4.2	Fresh Properties.....	29
2.4.3	Compressive Strength and Modulus of Elasticity	31
2.4.4	Flexural Performance	33
2.4.5	Residual Flexural Strength.....	39
2.4.6	Relationship between Measured Deflection and CMOD	44
2.5	Cost and Environmental Impact Analysis.....	48
2.5.1	Comparison with Ductal UHPFRC mix design	49
2.5.2	Efficiency Comparison	49
2.6	Conclusion	52
2.7	References.....	54
Chapter 3: Determination of Tensile Characteristics and Design of Eco-Efficient UHPC.....		61
3.1	Introduction.....	63
3.2	Experimental Program	65
3.2.1	Materials and Mix Proportions	65
3.2.2	Mixing, Specimen Casting and Curing	67
3.2.3	Compressive Strength and Modulus of Elasticity	67
3.2.4	Three Point Bending Test	68
3.3	Calculation of Fracture Parameters.....	69
3.3.1	Flexural strength	69
3.3.2	Energy Absorption	70
3.3.3	Fracture Energy.....	70
3.4	Tensile Stress Strain Characteristics	71
3.4.1	Model Code 2010 Uniaxial Tensile Model for Strain Hardening FRCs.....	71
3.4.2	FE Inverse Analysis	72
3.5	Experimental Results and Discussion	72
3.5.1	Compressive Strength and Modulus of Elasticity	72
3.5.2	Flexural Behaviour and characteristics	74

3.5.3	Flexural Parameters.....	74
3.5.4	Energy Absorption	76
3.5.5	Fracture Energy.....	78
3.6	Tensile Stress-Strain Behaviour.....	79
3.6.1	FE Inverse Analysis Model.....	79
3.6.2	Assumptions used in Inverse Analysis of E-UHPFRC	82
3.6.3	Determination of Ultimate Tensile Strain	82
3.6.4	Comparison between Experimental and Numerical Load-Deflection Curves	83
3.6.5	Inverse Analysis Tensile Stress Strain Behaviour	87
3.6.6	Evaluation of Stress Strain Relationship of MC10 [39].....	89
3.6.7	Proposed Tensile Stress-Strain Prediction Model.....	89
3.6.8	Accuracy of the Proposed Model in Performance Design Parameters	92
3.7	Conclusions.....	94
3.8	References.....	99
Chapter 4: Shear Behaviour of E-UHPC Containing Recycle Steel Fibres and Design of E-UHPC Screw Piles		105
4.1	Introduction.....	107
4.2	Experimental Program	109
4.2.1	Materials and Mix Proportions	109
4.2.2	Mixing, Specimen Casting and Curing	111
4.2.3	Compressive Strength and Modulus of Elasticity Test	111
4.2.4	Flexural Strength Test.....	112
4.2.5	Shear Test.....	112
4.3	Test Results and Discussions	114
4.3.1	Material properties	114
4.3.2	Shear Stress – Displacement Behaviour	116
4.3.3	Effect of Steel Fibre Type and Volume on Shear Strength.....	120
4.3.4	Correlation with other Mechanical Properties	122
4.3.5	Evaluation of Existing models	123

4.3.6	Proposed Model Based on Fibre Type and Dosage	124
4.3.7	Shear Stress-Strain behaviour	125
4.3.8	Shear Modulus	127
4.4	Design of Screw Piles	129
4.4.1	Proposed E-UHPFRC Screw Pile	130
4.4.2	Installation Torque.....	131
4.4.3	Axial Capacity.....	134
4.4.4	Design Assumptions	138
4.4.5	Design Procedure	138
4.4.6	Design example:.....	140
4.5	Conclusions.....	144
4.6	References.....	146
Chapter 5: Conclusions and Recommendations for Future Work.....		151
5.1	Conclusions.....	152
5.1.1	Mechanical performance of affordable and eco-efficient ultra-high performance fibre reinforced concrete (E-UHPFRC) containing recycled tyre steel fibres (Chapter 2).....	152
5.1.2	Determination of Tensile Characteristics and Design of Eco-Efficient UHPFRC (Chapter 3)	153
5.1.3	Direct shear Behaviour of E-UHPFRC Containing Recycle Steel Fibres and E-UHPFRC Screw Piles (Chapter 4).....	154
5.1.4	Final Remarks	155
5.2	Recommendations for Future Use.....	155
5.2.1	Improvement in Cleaning and Optimising the Length Distribution of RTSF.....	155
5.2.2	Improvement in Evaluating the Market value and Actual Environmental Credentials of Cleaned and Sorted RTSF and of RTSC.....	156
5.2.3	Mix Design Optimisation.....	156
5.2.4	Future Experimental Work.....	157
5.2.5	Life Cycle Cost analysis (LCCA) and Performance Assessment of E-UHPRC structures	158
5.2.6	Validation and Calibration of Design Models	158

5.3	References.....	159
Appendix A:	Data and Experimental Results for Chapter 2.....	162
Appendix B:	Finite Element Inverse Analysis Chapter 3.....	191
Appendix C:	Experimental Results for Chapter 4.....	195
Appendix D:	Torque Resistance derivations for Chapter4.....	210

List of Figures

Figure 1.1: (a) Stockpile of waste tyre [26] (b) RTSF (c) RTSC.....	4
Figure 1.2: Screw pile mode of action [38] (a) in tension (b) in compression.....	5
Figure 1.3: Screw piles for solar farm construction [39, 40]	6
Figure 2.1: (a) Tyre steel cords (b) RTSC (c) Partially sorted RTSF	20
Figure 2.2: Schematic representation of RTSF cleaning process	21
Figure 2.3: Samples from the cleaning process (a) TT (b) BB (c) Short fibres (d) RTSF 3	21
Figure 2.4: RTSF length distribution (a) RTSF 1 (b) RTSF 2 and (c) RTSF 3	22
Figure 2.5: UHPC production (a) Fresh E-UHPFRC mix (b) workability test (c) casting and levelling (d) cast prisms and cylinders.....	24
Figure 2.6: Compressive strength and modulus of elasticity test.....	25
Figure 2.7: Flexural prism test set-up	25
Figure 2.8: Flexural behaviour of E-UHPFRC containing different fibre types and length.....	28
Figure 2.9: Workability of E-UHPFRC mixes.....	30
Figure 2.10: Load/flexural stress – deflection behaviour of E-UHPFRC mixes	33
Figure 2.11: Relationship between ffl and RTSF content.....	35
Figure 2.12: Magnified appearance of some RTSF	36
Figure 2.13: (a) Effect of RTSF content on E_b and (b) Correlation between E_b and E_c	36
Figure 2.14: Flexural behaviour and design CMOD values based on RILEM [57] and Model Code [58]	40
Figure 2.15: Definitions of residual flexural strength of UHPFRC	41
Figure 2.16: Correlation between $fR's$, fibre volume and RTSF content (a) $fR - I$ (b) $fR - II$	43
Figure 2.17: Correlation between ffl and $fR's$	43
Figure 2.18: Relationship between midspan deflection and measured CMOD	44
Figure 2.19: Schematic illustration of post cracking behaviour of prisms under 3-point bending for (a) normal FRC (b) UHPFRC	45
Figure 2.20: Relationship between CMOD, load and hinge length for (a) f 2 (b) f 3 (c) f 4	46
Figure 2.21: Correlation between experimental and model hinge length ratio at Ultimate limit state .	47
Figure 2.22: Comparison between material efficiencies of E-UHPFRC mixes (a) f 2 (b) f 3 (c) f 4 ...	50
Figure 2.23: Comparison between material efficiencies of mix f 2 – CCC and mixes containing FFF51	50
Figure 3.1: (a) Tyre steel cords (b) RTSC (c) RTSF.....	66
Figure 3.2: RTSF length distribution RTSF.....	67
Figure 3.3: Measuring device for axial deformation.....	68
Figure 3.4: Set-up for the three-point bending test	68

Figure 3.5: View of flexural test.....	69
Figure 3.6: Idealised flexural behaviour of E-UHPFRC mixes	69
Figure 3.7: Energy absorption.....	70
Figure 3.8: Idealised uniaxial tensile stress – strain behaviour of UHPFRC.....	71
Figure 3.9: (a) Compressive Strength and (b) Modulus of Elasticity of E-UHPFRC mixes normalised with respect to the plain reference mix	73
Figure 3.10: Load-deflection behaviour of E-UHPFRC mixes [1].....	74
Figure 3. 11: Flexural strength parameters	75
Figure 3.12: Correlation between predicted and experimental flexural strength.....	76
Figure 3.13: Effect of fibre dosage and RTSF content on energy absorption.....	77
Figure 3.14: Histogram with error bars showing effect of RTSF on Fracture Energy	78
Figure 3. 15: Correlation between fracture energy and flexural strength	79
Figure 3.16: (a) Plate response in uniaxial tension (a) plate response using the modified ultimate strain approach.....	81
Figure 3.17: Tensile $\sigma - \varepsilon$ response to determine ε_{tu} using a fracture energy approach	82
Figure 3.18: FE response of f 2 – CCC for different mesh sizes	84
Figure 3.19: Comparison between experimental average load deflection behaviours, FE inverse analysis, MC10 and proposed model	86
Figure 3.20: Tensile stress-cracking strain behaviour of mixes.....	88
Figure 3.21: Correlation between tensile strength parameters and flexural strength.....	89
Figure 3. 22: Uniaxial tensile model of E-UHPFRC	90
Figure 3.23: Stress distribution using predetermined neutral axis depth (a) at crack (b) at peak load capacity and (c) at ultimate capacity.....	93
Figure 3.24: Comparison between moment capacities	93
Figure 4.1: (a) Tyre steel cords (b) RTSC (c) RTSF.....	110
Figure 4.2: Length distribution of RTSF	111
Figure 4.3: Measuring device for axial deformation.....	112
Figure 4.4: (a) Load arrangement (b) shear force diagram	113
Figure 4.5: (a) Test configuration (b) cross section of notched area	114
Figure 4.6: Experimental set-up.....	114
Figure 4.7: Load – Applied displacement relationship of E-UHPFRC mixes	116
Figure 4.8: Shear behaviour of E-UHPFRC mixes: shear stress-crack slip and shear stress-crack width	118
Figure 4.9: Idealised representation of E-UHPFRC shear behaviour	119
Figure 4.10: Effect of fibre volume and RTSF content and prediction model.....	121

Figure 4.11: Correlation between τ_{max} and (a) compressive strength f_c' , and (b) flexural strength f_{fl}	122
Figure 4.12: Correlation between τ_{max} and τ_d	123
Figure 4.13: Correlation between predicted values and experimental values.....	125
Figure 4.14: Shear deformation at notched cross section	125
Figure 4.15: Shear stress –strain behaviour of E-UHPFRC mixes	126
Figure 4.16: Relationship between shear modulus and shear stress for E-UHPFRC mixes	128
Figure 4.17: Relationship between Poisson’s ratio and shear stress of E-UHPFRC mixes	129
Figure 4.18: Proposed E-UHPFRC screw pile models	131
Figure 4.19: Diagrams showing locations where the various torque components act.	132
Figure 4.20: Cylindrical shear approach for determining axial capacity of screw piles	135
Figure 4.21: Variation of breakout factor with $H D t, h$ [45].....	137
Figure 4.22: (a) Relationship between installation depth and installation torque; (b) installation depth and load capacity; (c) load capacity and installation torque.	141
Figure 4.23: Effect of installation depth on (a) individual torque resistances and (b) on torque resistance of individual helices	142
Figure 4.24: Effect of sand type on installation torque	143

List of Tables

Table 2.1: Mix identification and fibre proportions.....	18
Table 2.2: UHPFRC mix design	19
Table 2.3: Statistical analysis of RTSF distribution.....	22
Table 2.4: Fresh and hardened property of E-UHPFRC mixes	29
Table 2.5: Comparison between measured and predicted modulus of elasticity for all mixes (MPa)..	32
Table 2.6: Flexural strength and bending modulus of all mixes	34
Table 2.7: Results of FE modelling	38
Table 2.8: Comparison between unnotched and adjusted E_b	38
Table 2.9: Residual flexural strength	42
Table 2.10: Cost (as at Dec 2019) and environmental impact of constituent materials.....	48
Table 2.11: Cost and GWP's of constituent materials	49
Table 3.1: Mix description and fibre proportions (kg/m ³)	66
Table 3.2: RTSF length distribution and statistical properties.....	67
Table 3.3: Energy absorption of specimens manufactured with different E-UHPFRC mixes.....	77
Table 3.4: Error in Peak Load and Energy absorption.....	87
Table 3.5: Correlation between derived (inverse analysis) and proposed model tensile characteristics	91
Table 3.6: Errors in predicting peak load and energy absorption	92
Table 4.1: Mix description and fibre proportions (kg/m ³)	110
Table 4.2: RTSF length distribution statistical properties	111
Table 4.3: Mechanical properties of the tested concrete mixes	115
Table 4.4: Shear properties of mixes	120
Table 4.5: Ratio of experimental τ_{max} to f_{fl} for the tested mixes.....	123
Table 4.6: Evaluation of existing FRC models	124
Table 4.7: Input design data.....	140
Table 4.8: Pile design parameters Using f 3 – FFF mechanical properties.....	140

List of Symbols and Abbreviations

Abbreviations

2D	Two Dimensional
ASTM	American Society for Testing and Materials
BB	Bottom – Bottom
BS	British Standard
BT	Bottom – Top
CMOD	Crack Mouth Opening Displacement
COV	Coefficient of variation
EN	European Standard
EU	European Union
E – UHPFRC	Eco Efficient – Ultra-High Performance Fibre Reinforced Concrete
FE	Finite Element
FEA	Finite Element Analysis
FHWA	Federal Highway Administration
fib	International Federation for Structural Concrete
FRC	Fibre reinforced concrete
GGBS	Ground Granulated Blast Furnace Slag
GWP	Global warming Potential
LCCA	Life Cycle Cost Analysis
LVDT	Linear variable displacement transducer
MC10	Model Code 2010
MSF	Manufactured Steel Fibres
RCC	Roller Compacted Concrete
RILEM	International Union of Laboratories and Experts in Construction Materials, Systems and Structures
RTSC	Recycled Tyre Steel Cords

RTSF	Recycled Tyre Steel Fibres
SFRC	Steel fibre Reinforced Concrete
SLS	Serviceability Limit State
STDEV	Standard Deviation
TB	Top – Bottom
TT	Top – Top
UHPC	Ultra-High Performance Concrete
UHPFRC	Ultra-High Performance Fibre Reinforced Concrete
ULS	Ultimate Limit State

Symbols

ϕ	Soil angle of friction
ψ	Angle of helix
$\sigma - \varepsilon$	Tensile stress – strain relation
σ_{tc}	Tensile stress at cracking
σ_{tp}	Tensile stress at peak capacity
σ_{tu}	Tensile stress at ultimate deflection
ε_{tc}	Strain at cracking
ε_{tp}	Strain at peak capacity
ε_{tu}	Strain at peak ultimate limit
$\bar{\varepsilon}_{tu}$	Modified ultimate strain
$\gamma_{long.}$	Strain measured in the direction of applied force
$\gamma_{trans.}$	Strain measured perpendicular to applied force
γ	Shear strain
γ'	Effective unit weight of soil
ϵ	Eccentricity
τ	Shear strength

$\tau - \gamma$	Shear stress – strain response
τ_{max}	Maximum shear strength
τ_{cr}	Cracking shear strength
τ_{res}	Residual shear strength
ψ	Dilation angle
K_c	Shape factor
ρ	Fibre dosage
λ	Hinge length
λ	Characteristic length scaling parameter
ξ	Friction coefficient for concrete against steel
μ	Angle of friction between pile surface and soil
η	Krenchel composite efficiency factor for fibre orientation
δ^o	Deflection
δ_c	Deflection at cracking
δ_p	Deflection at ultimate load
δ_u	Deflection at ultimate state
b	Width of specimen
A_c	Area of notched cross section (shear plane)
A_e	Area of rectangular mesh element
A_F	Area of notched cross section for flexural specimens
CO_2	Carbon dioxide
C_{mix}	Cost of mix
C_{mix}'	Cost of the reference Mix
C_i	Cost of material i
C_s	Crack slip
C_w	Crack width
d	Diameter of pile shaft

d_b	Diameter of shaft at lower end of pile
d_b	Diameter of shaft at upper part of pile
d_n	Diameter of shaft at location of helix n
D	Diameter of the helix
D_n	Diameter of the helix n
$D_{b,h}$	Diameter of bottom helix
$D_{t,h}$	Diameter of top helix
D_{n-r}	Diameter of the gyration of the helix n where concentrated forces act upon
E	Mix efficiency
E_b	Bending modulus of elasticity
E_c	Modulus of elasticity
E_C	Economic efficiency
$E_{comp.}$	Composite modulus of elasticity
E_f	Modulus of elasticity of fibres
E_m	Modulus of elasticity of matrix
E_n	Environmental efficiency
E_{pc}	Unloading modulus (at peak tensile capacity)
f_{bo}/f_{bo}	Biaxial to uniaxial compressive strength ratio
f'_c	Compressive strength
f_{fl}	Flexural strength
$f_{fl,c}$	Cracking flexural strength
$f_{fl,u}$	Ultimate flexural strength
f_{LOP}	Flexural strength at limit of proportionality
f_R	Flexural strength of examined mix
f'_R	Flexural strength of reference mix
f_{Ri}	Residual flexural strength at CMOD i
f_{R-I}	Residual flexural strength at $5.5 \cdot \text{CMOD}_{SLS}$

f_{R-II}	Residual flexural strength at $10.5 \cdot \text{CMOD}_{\text{SLS}}$
f_{Fts}	Reference values based on serviceability behaviour
f_{Ftu}	Reference values based on ultimate behaviour
F	Ratio of RTSF to total fibre content
F_q	Breakout factor for cohesionless soils
g_e	Energy absorption during elastic phase
g_h	Energy absorption during hardening phase
g_s	Energy absorption during softening phase
g_F	Total energy absorption
g_t	Energy per unit volume dissipated in tension
G_{exp}	Experimental shear modulus
G_F	Fracture energy
G_T	Volumetric energy dissipated
G_{Theo}	Theoretical shear modulus
h	Height of specimen
h_e	Length of square elements
h_{sp}	Distance between the tip of the notch and top of the specimen
H	Depth of installation (or of bottom helix)
H_n	Depth of helix n
H_t	Length of pile shaft (or depth of top helix)
I	Second moment of area
i	Number of helices
J_b	Polar moment of circular shaft at lower end
J_b	Polar moment of circular shaft at upper end
K_a	Coefficient of active earth pressure
K_f	Coefficient of friction between pile and surrounding soil
K_p	Coefficient of passive earth pressure

K'_p	Modified coefficient of passive earth pressure
l	Span length
l_f	Steel fibre length
l_{ch}	Characteristic length of specimen
l_{ch-FE}	Characteristic length of FE mesh
m_i	Mass of material i
M_E	Mechanical efficiency
M_c	Cracking moment capacity
M_p	Peak moment capacity
M_u	Ultimate moment capacity
N_q	Soil bearing capacity factor
n	Number of constituent materials
p	Helix pitch
P	Load
P_c	Applied compressive load
$P_{cyl.}$	Perimeter of soil cylindrical envelope
P_u	Applied uplift load
Q_c	Design axial load in compression
Q_u	Design axial load in uplift (tension)
r_b	Radius of shaft at lower end of pile
r_t	Radius of shaft at upper part of pile
s_{rm}	Average crack spacing
$t_{o,h}$	Outer thickness of helix
$t_{i,h}$	Inner thickness of helix
T_1	Torque resistance exerted on the pile shaft
T_2	Torque resistance due to passive lateral earth pressure exerted on helix
T_3	Torque resistance acting on helix due to cylindrical column of sand

T_4	Torque resistance due to active earth pressure exerted on the upper surface of helix
T_5	Torque resistance due to passive earth pressure exerted on the lower surface of helix
T_6	Torque resistance acting on helix due to its inclination in the third dimension
T_7	Torque resistance exerted on the outer perimeter of helix
T_8	Moment of resistance due to cutting edge of helix penetrating into the soil
V_f	Volume fraction of fibre
V_m	Volume fraction of matrix
ν	Viscosity parameter
ν	Poisson ratio
w	Crack width of flexural prism
w_h	Helix flange width
w_u	Maximum crack opening accepted in design
y	Distance between neutral axis and tensile side of cross section evaluated in the elastic cracked phase

This page is intentionally left blank

Chapter 1: Introduction

This chapter outlines the motivation and background of this research work, its aim and objectives, research methodology and layout of this thesis.

1.1 Introduction

Recent advances in concrete technology have led to the development of Ultra-High Performance Fibre Reinforced Concrete (UHPFRC). The mechanical properties of UHPFRC include compressive strength greater than 150 MPa and sustained post cracking tensile strength greater than 5 MPa (for fibre reinforced mixes). As compared to conventional and high-performance concretes, UHPFRC has a very dense pore structure, and this reduces fluid ingress and significantly enhances durability [1-3]. The superior mechanical and durability properties of UHPFRC are the result of the adoption of improved concreting techniques and the use of granular materials with optimized gradation, ultra-fine pozzolans, very low water cement ratio, high quality and high dosage of superplasticizer, as well as steel fibres [4]. Although superior to other types of concrete, UHPFRC is still characterised by a relatively low tensile strength. To address this weakness, steel reinforcement is added directly to the mix in the form of steel fibres (Ultra-High Performance Fibre Reinforced Concrete – UHPFRC), or as conventional steel bars. However, steel production contributes to the greenhouse effect, with an average of 1.9 tons of CO₂ per ton of steel produced [5]. This is in addition to the high cement content needed to produce UHPFRC (up to 900kg/m³). Global cement production contributes 4-7% of the worldwide emissions of greenhouse gases. To address the ongoing global challenges of climate change and sustainability, there is a need to reduce the use of steel and cement produced from virgin raw materials by encouraging the use of suitable waste or recycled substitutes.

Despite the promising mechanical and durability performance, the widespread application of UHPFRC is limited due to its high initial costs, concerns regarding sustainability [6], as well as lack of design standards and guidelines [7]. UHPFRC can cost up to 10 times more than ordinary concrete [7], and this discourages its use by contractors and end users, who can easily overlook the potential lower life cycle costs. The lack of existing design standards and procedures for UHPFRC is due to limited research

and understanding of the mechanical and physical properties of the material. As a result, the few contractors and engineers that want to take advantage of its potentials have to rely on a design by testing approach rather than on a rational design methodology. Thus, there is a need to establish models for the material properties and develop design guidelines for using UHPFRC in structural applications, as well as provide suitable construction technologies and solutions for this material.

1.2 Motivation

The hypothesis of this work is that specially designed UHPFRC can be developed to meet strength requirements, yet ensuring good sustainability credentials. An in-depth understanding of the mechanical behaviour of this material can then be leveraged to develop improved design models. However, to achieve this and make UHPFRC a competitive construction material, there is a need to improve both its cost and environmental credentials using a sustainable mix design with reduced cement content and recycled steel fibres (RTSF and RTSC), without compromising workability and mechanical properties. Civil engineering structures are usually built on foundations. In weak soils, especially in marshy soils and marine environments, piles are often the only foundation solution. As driving piles requires heavy equipment and can cause undesirable vibrations, steel screw piles are often used. However, steel screw piles can corrode, especially in marine environments. For many decades, the development of concrete screw piles has been attempted, and many design patents exist [8-12]. However, ordinary concrete cannot resist the high shear/torsional stresses that develop during installation and large amounts of steel reinforcement are needed, leading to large sections that are impracticable to drive. Furthermore, unless additional costly measures are adopted, steel reinforcement corrosion would still be an issue. The superior strength and durability properties of UHPFRC make it a suitable candidate for the development of concrete screw piles.

1.3 Research Background

1.3.1 Ultra-high Performance Fibre Reinforced Concrete

Over the last two decades, various studies have been carried out on the mechanical properties of UHPFRC. Hakeem [4] studied the compressive strength and flexural behaviour of UHPFRC, while other studies examined their performance in tension [13], shear [14], biaxial loading [15], as well as

under blast [16] and high temperature loading [17]. Many other studies have been conducted on the performance of UHPFRC under various loading conditions, and the results have shown its superior performance compared to normal strength and high strength concrete. However, further studies in UHPFRC material characterisation are needed, in particular regarding shear/torsional performance, in order to aid the development of comprehensive design guidelines.

High initial cost and sustainability problems are among the factors limiting the widespread use of UHPFRC due to its high cement content and high cost of steel fibres. UHPFRC containing 1.5% by volume of steel fibres costs approximately \$950/m³ against \$150-200 for conventional concrete [18]. The environmental impact of these two constituent materials (cement and steel) is known to be significant, with about 0.9 tons of CO₂ emitted for every ton of cement produced [19] and 1.9 tons of CO₂ per ton of steel produced [5]. Nonetheless, life cycle cost analysis (LCCA) has shown that UHPFRCC structures can be more competitive than conventional concrete structures [20]. According to [21], approximately 56% reduction in materials costs can be achieved by utilizing UHPFRC rather than conventional concrete, because the high strength of UHPFRC allows the design of more slender structures, thereby reducing the overall volume of construction materials [22].

1.3.2 Recycled Tyre Steel Fibres (RTSF) and Recycled Tyre Steel Cords

Approximately 1.5 billion tyres are produced worldwide [23], and a large percentage of this number is disposed annually (Fig 1.1a). Over the past two decades, waste tyre disposal has become a key concern for environmental bodies and the society at large. In 2006, the European Union (EU) banned disposal of tyres and their by-products into landfills. Similarly, in the United States, 42 states have restricted depositing of end of life tyres in landfills [24]. In 2008, The European directive 2008/98/EC [25] set up a disposal plan to encourage management and recycling of waste tyre products (rubber granules, steel fibres and polymer fibres) for novel applications.

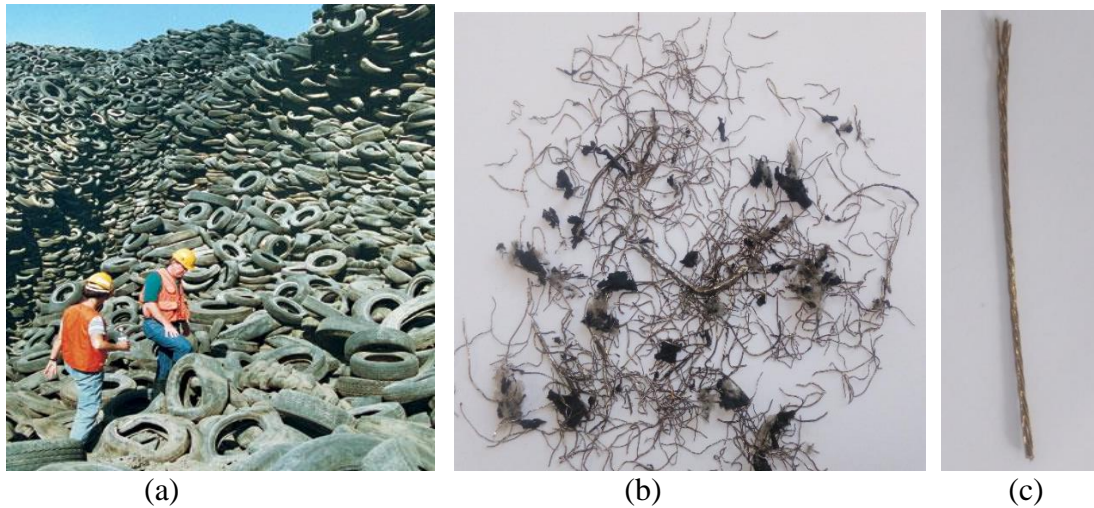


Figure 1.1: (a) Stockpile of waste tyre [26] (b) RTSF (c) RTSC

The construction industry strives to contribute to environmental sustainability by minimizing the consumption of natural resources and increasing the use of waste materials. Over the past 8 years, research work at the University of Sheffield on the reuse of RTSF (Figure 1.1b) has demonstrated its use for various concrete applications and patents have been awarded for the use of RTSF in concrete (e.g. EP 1 466 060 B1). Work includes studies on: shrinkage [27-29], roller compacted concrete (RCC) [30,31] and slabs on grade [32-33]. The results from these studies have demonstrated the viability of RTSF as a substitute for manufactured steel fibres. A spin-out company is already providing RTSF for slabs on grade applications. This study aims to utilise these fibres so as to design sustainable UHPFRC mixes.

RTSC obtained from end of reels' offcuts or extracted from un-vulcanised rubber belts from tyre manufacturing plants has the potential, if processed to desired lengths, to be used as a substitute for manufactured steel fibres in UHPFRC. The use of RTSC in concrete mixes has been demonstrated by [34,35]. RTSC (Fig 1.1c) is obtained in cleaned form (free from impurities) as a series of twisted filaments (0.5 – 3m long) and does not need much processing, apart from untwisting and cutting to the desired length.

1.3.3 Screw Piles

Screw or helical piles were first introduced as a deep foundation option in the early 1800's, [36]. They differ from traditional piles in that they consist of helices, which are fixed to the shaft at specific spacing, and are installed by screwing them into the ground [37]. Early uses of helical piles consisted of offshore

anchorage in very soft marine soils, most commonly required in the construction of lighthouse foundations. Screw piles are capable of resisting both tensile and compressive loads (Figure 1.2), and their strength is developed by the combined contribution of the helix bearing capacity and shaft resistance. However, their performance depends on the soil properties, pile geometry, soil-pile interaction and type of loading [38].

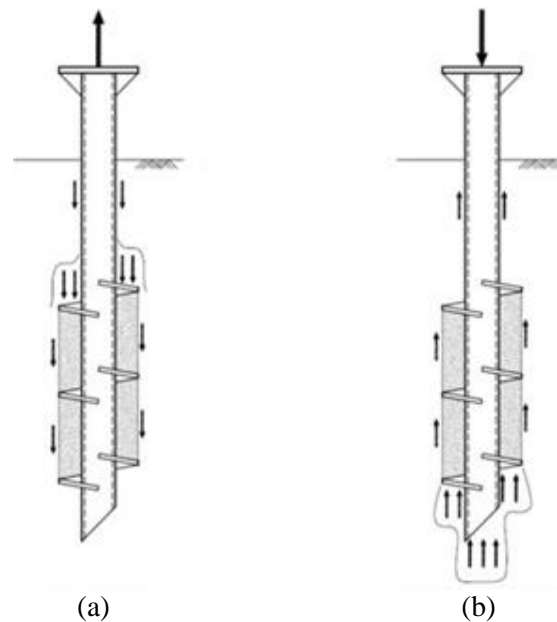


Figure 1.2: Screw pile mode of action [38] (a) in tension (b) in compression

With the advent of modern installation equipment and improved practical knowledge and engineering design, screw piles applications developed substantially. Presently, helical piles are utilized to resist a wide range of actions, including uplift, bearing, and/or lateral loading, and are employed in structures ranging from bridges, buildings, machine foundations to pipeline supports and more recently foundations for solar panel frames (Figure 1.3). The advantages of screw piles include: rapid installation, immediate load carrying capability, minimal site disturbance, installation in shallow groundwater and resistance to wide load applications.



Figure 1 3: Screw piles for solar farm construction [39, 40]

However, screw piles have some limitations as they cannot be installed on hard soil strata. Furthermore, despite the corrosion vulnerability of steel, especially in marine environments, at the moment only steel screw piles are used in practice, due to the weakness of conventional concrete in shear (as high shear stresses are developed during installation). Hence, to develop concrete screw piles, a concrete with high shear strength needs to be developed.

Although designs and patents for precast reinforced concrete screw piles existed as far back as 1911 [8-12], the use of concrete screw piles has not been successful in practice mainly because conventional concrete is inadequate to resist the high shear stresses that develop during the installation phase. To resist such high shear stresses, a large amount of steel reinforcement is required leading to large sections that are practically impossible to drive. These weaknesses and drawbacks can be overcome using UHPFRC. The shear strength of UHPFRC is the key strength parameter needed to resist the shear stresses that develop from the torsional load applied during installation. Hence there is a need to study and understand the shear behaviour of UHPFRC and identify the critical parameters for the design of UHPFRC screw piles.

1.4 Research Aim and Objectives

The aim of this research is to investigate the feasibility of developing an Eco-Efficient Ultra-High Performance Fibre Reinforced Concrete (E-UHPFRC) by utilising recycled steel fibres (RTSC and sorted RTSF) in screw pile applications.

To achieve this aim, the following objectives have been defined.

- Obj.1:** Optimise RTSF fibre length distribution through cleaning and sorting of fibres for optimum mechanical performance of UHPFRC.
- Obj. 2:** Evaluate the fresh and mechanical properties of E-UHPFRC, and check their compliance with the requirements necessary to be classified as UHPFRC.
- Obj. 3:** Evaluate the tensile strength characteristics of E-UHPFRC through Finite Element (FE) inverse analyses of flexural tests and develop a constitutive model to predict the tensile response of E-UHPFRC for design purposes.
- Obj. 4:** Study the shear behaviour of E-UHPFRC experimentally and analytically.
- Obj. 5:** Develop predictive models for the critical mechanical properties of E-UHPFRC.
- Obj. 6:** Carryout physical modelling of E-UHPFRC screw pile in cohesionless soil and develop design guidelines.

1.5 Research Significance

The successful completion of this study will lead to a better understanding of the mechanical behaviour and performance of E-UHPFRC. The proposed predictive and design models will provide valuable information to designers and standardization committees. The use of waste and recycled materials (GGBS and RTSF) will contribute to increasing the sustainability and decreasing the initial cost of UHPFRC, thus addressing the major factors hindering its widespread acceptance in construction. E-UHPFRC screw piles can offer a suitable alternative to expensive and corrosion vulnerable steel screw piles, especially in marine and coastal environments. E-UHPFRC screw piles can be suitably used as foundations for electric poles and telecommunication masts, solar panel frames, fence foundations and other applications.

1.6 Outline of the Thesis

The thesis consists of five chapters in a mixed format. It comprises 3 chapters based on research papers (Chapters 2, 3 and 4) published or submitted to peer reviewed journals, and two conventional chapters that provide the Introduction (Chapter 1) and summarise the overall Conclusions of this study and provide relevant Recommendations (Chapter 5). The methodologies and concepts for each component of the work is presented under the relevant chapters/papers.

Chapter 2: Titled “*Mechanical performance of affordable and eco-efficient ultra-high performance concrete (UHPC) containing recycled tyre steel fibres*” is based on Isa et al. [41] published in “*Construction and Building Materials*” and addresses Objectives 1, 2 and part of Objective 5. This chapter presents the results of a preliminary investigation using three-point bending tests on 40×40×120mm prisms and examines the effect of fibre length and RTSF cleanliness on mechanical performance. The results show that rubber and other impurities, as well as fibres with less than 9 mm length, significantly reduce the strength of E-UHPFRC mixes. Based on these results, twelve E-UHPRCC mixes containing either RTSC, cleaned and sorted RTSF or blends of the two in various ratios are studied for total fibre volumes of 2, 3 and 4%. The fresh properties of the mixes are assessed in terms of workability and density, while the mechanical performance is assessed in terms of compressive strength and modulus of elasticity, which are obtained from tests on 100×200mm cylinders, and overall flexural behaviour, which was examined through three-point bending tests on 75×75×225mm prisms. Five specimens were tested for each of the designed E-UHPFRC mixes. The efficiency of the studied mixes is evaluated in terms of cost credentials, environmental impact and mechanical performance.

Chapter 3: Titled “*Determination of Tensile Characteristics and Design of Eco-Efficient UHPC*” is based on Isa et al. [42] published in “*Structures*”. This chapter addresses Objectives 3 and 5. The experimental flexural behaviour of notched prisms subjected to three-point bending tests is used in conjunction with Finite Element (FE) inverse analysis to characterise the uniaxial tensile properties of E-UHPFRC. A mesh independent solution for the post crack tensile properties is developed based on a fracture energy approach using a characteristic length scaling procedure as a function of finite element size. Prediction models for the constitutive tensile stress strain ($\sigma-\varepsilon$) laws of E-UHPFRC are proposed based on simple strength and mix parameters. These proposed models are used to develop specific design guidelines in line with current fib Model Code design provisions.

Chapter 4: Titled “*Shear Behaviour of E-UHPFRC Containing Recycle Steel Fibres and E-UHPFRC Screw Piles*” is based on Isa et al. [43] which has been submitted to “*Construction and Building Materials*”. The chapter investigates the shear behaviour of beam specimens manufactured using twelve different E-UHPFRC mixes and tested under an asymmetric four-point loading configuration. A shear

strength prediction model based on flexural properties and fibre dosages is proposed for design purposes. Due to its excellent shear performance, the use of the developed E-UHPFRC in screw piles is proposed as a suitable application. E-UHPFRC can offer numerous advantages, including rapid installation, immediate load carrying capability, minimal site disturbance, resistance to wide load applications, and will solve the problem of corrosion vulnerability of steel screw piles. The behaviour and response of E-UHPFRC screw piles is modelled analytically based on existing models developed for steel anchors and screw piles. Finally, design guidelines for E-UHPFRC screw piles in cohesionless soils are proposed.

Chapter 5: This chapter presents the conclusions derived from this research work and offers recommendations for future work.

1.7 References

1. Graybeal, B. 2009. UHPC Making Strides. Public Roads, 72, 17-21, Federal Highway Administration, McLean, VA.
2. Shi C., Wu Z., Xiao J., Wang D., Huang Z. & Fang Z. 2015. A review on ultra-high performance concrete: Part I. Raw materials and mixture design. *Construction and Building Materials*, 101, 741-751.
3. Wang, D., Shi, C., Wu, Z., Xiao, J., Huang, Z., & Fang, Z. (2015). A review on ultra-high performance concrete: Part II. Hydration, microstructure and properties. *Construction and Building Materials*, 96, 368–377.
4. Hakeem, I.Y.A. 2011. Characterization of an ultra-high performance concrete. MSc, King Fahd University of Petroleum & Minerals.
5. Kundak M., Lazic L., crnko J. (2009). Co2 emissions in the steel industry. *Metalurgija -Sisak then Zagreb*, 48, 193-197.
6. Zhong, R., Wille, K. & Viegas, R. 2018 Material efficiency in the design of UHPC paste from a life cycle point of view. *Construction and Building Materials*, 160, 505–513.
7. Juan Ángel López Martínez (2007). Characterisation of the tensile behaviour of UHPFRC by means of four-point bending tests, PhD, Universitat Politècnica De València.
8. G. C., Vernon-Inkpen, "Concrete pile." U.S. Patent 996,688, issued July 4, 1911.
9. Cummings, Robert A. "Corrugated concrete pile." U.S. Patent 1,041,035, issued October 15, 1912.
10. Vernon-Inkpen, George Charles. "Concrete screw-pile for foundations and similar purposes." U.S. Patent 1,070,862, issued August 19, 1913.
11. G., Grimaud. "Reinforced-concrete stake." U.S. Patent 1,563,024, issued November 24, 1925.
12. Gillen Jr, William F. "Precast concrete threaded pilings." U.S. Patent 4,239,419, issued December 16, 1980.
13. Leutbecher, T., 2008. Rissbildung & Zugtragverhalten von mit Fasern und Stabstahl bewehrtem Ultrahochfesten Beton (UHPC)” Dissertation, Schriftenreihe Baustoffe und Massvbau, Heft 9, Kassel university press GmbH, Kassel.

14. Fehling E. & Thiemickie J. 2011. Shear bearing behaviour of ultra-high performance concrete (UHPC). Concrete engineering for excellence and efficiency, fib Symposium Prague, 2, 975-978.
15. Fehling E., Leutbecher T., Roder F. K., & Sturwald S. 2008. Structural behaviour of UHPC under biaxial loading. Second International Symposium on Ultra-High Performance Concrete, 10, 569-576.
16. Ellis B. D., Di Paolo, B. P., McDowell, D. L. & Zhou, M. 2014. Experimental investigation and multiscale modelling of ultra-high-performance concrete panels subject to blast loading. International Journal of Impact Engineering, 69, 95-103.
17. Lee, N. K., Koh, K. T., Park, S. H. & Ryu G. S. 2018. Microstructural investigation of calcium aluminate cement-based ultra-high performance concrete (UHPC) exposed to high temperatures. Cement and Concrete Research, 102, 109-118.
18. Graybeal B. 2013. Development of Non-Proprietary Ultra-High Performance Concrete for Use in the Highway Bridge Sector. Federal Highway Administration (FHWA) report, Development of Non-Proprietary Ultra-High Performance Concrete for Use in the Highway Bridge Sector. FHWA Publication No.: FHWA-HRT-13-100.
19. Natesan M., Steve S., & Kenneth H., 2003. The Cement Industry and Global Climate Change: Current and Potential Future Cement Industry CO₂ Emissions, Greenhouse Gas Control Technologies - 6th International Conference, Pergamon, 2003, 995-1000.
20. Dong Y. (2018). Performance assessment and design of ultra-high performance concrete (UHPC) structures incorporating life-cycle cost and environmental impacts Construction and Building Materials, 167 , pp. 414-425.
21. Racky, P. 2004. Cost-effectiveness and sustainability of UHPC. In Proceedings of the International Symposium on Ultra High Performance Concrete, Kassel, Germany, 797–805.
22. Hajek, P., & Fiala, C. 2008. Environmentally optimized floor slabs using UHPC-contribution to sustainable building. In Proceedings of the 2nd International Symposium on Ultra-High Performance Concrete, Kassel, Germany, 879–886.

23. ETRA, The European Tyre Recycling Association, 2016, Available at: <http://www.etra-eu.org> [Last accessed: 02/01/2018].
24. Neocleous, K., Angelakopoulos, H., Pilakoutas, K. & Guadagnini, M. 2011. Fibre-reinforced roller-compacted concrete transport pavements. *Proceedings of the ICE-Transport*, 164, 97-109.
25. Council of European Union 2008. Council Directive 2008/98/EC of 26th April on the landfill of waste.
26. <https://bioenergyinternational.com/biochemicals-materials/basf-signs-waste-tyre-pyrolysis-oil-off-take-agreements-with-new-energy>
27. Jafarifar, N., 2012. Shrinkage Behaviour of Steel Fibre Reinforced Concrete Pavements. PhD, University of Sheffield.
28. Younis, K. H. 2014. Restrained Shrinkage Behaviour of Concrete with Recycle Materials. PhD, University of Sheffield.
29. Al-Kamyani, Z. S. 2018. Controlling crack widths in RC structures using hybrid fibres. PhD, University of Sheffield.
30. Angelakopoulos, H., Papastergiou, P. & Pilakoutas, K. 2015. Fibrous roller-compacted concrete with recycled materials – feasibility study. *Magazine of Concrete Research*, 67, 801-811.
31. Graeff, A. 2011. Long Term Performance of Recycled Steel Fibre Reinforced Concrete for Pavement Applications. PhD, University of Sheffield.
32. Tlemat, H. 2004. Steel fibres from waste tyres to concrete: testing, modelling and design. University of Sheffield.
33. Hu, H., Papastergiou, P., Angelakopoulos, H., Guadagnini, M. & Pilakoutas, K. 2018. Mechanical properties of SFRC using blended manufactured and recycled tyre steel fibres. *Construction and Building Materials*, 187, 553-564.
34. Hu, H., Papastergiou, P., Angelakopoulos, H., Guadagnini, M., & Pilakoutas, K. (2018). Mechanical properties of SFRC using blended Recycled Tyre Steel Cords (RTSC) and Recycled Tyre Steel Fibres (RTSF). *Construction and Building Materials*, 187, 553–564.

35. Al-Musawi, H., Figueiredo, F. P., Bernal, S. A., Guadagnini, M., & Pilakoutas, K. (2019). Performance of rapid hardening recycled clean steel fibre materials. *Construction and Building Materials*, 195, 483–496.
36. Perko, H. A. 2009. *Helical Piles: A Practical Guide to Design and Installation*. New Jersey: John Wiley & Sons.
37. Arup Geotechnics, 2005. *Design of screw piles: Assessment of pile design methodology*. Arup & Partners Ltd, London.
38. Mohajerani, A., Bosnjak, D. & Bromwich, D. (2016). Analysis and design methods of screw piles: A review. *Soils and Foundations*, 56, 115-128.
39. <https://www.revisionenergy.com/blogs/revision-energy-now-offering-ground-screw-installation/>
40. <https://www.ebsgeo.com/who-we-are/blog/details/~41-Uses-of-Helical-Piles-Micropiles>
41. Isa, M. N., Pilakoutas, K., Guadagnini, M., & Angelakopoulos, H. (2020). Mechanical performance of affordable and eco-efficient ultra-high performance concrete (UHPC) containing recycled tyre steel fibres. *Construction and Building Materials*, 255, 119-272.
42. Isa, M. N., Pilakoutas & K., Guadagnini (2021). Determination of Tensile Characteristics and Design of Eco-Efficient UHPC. *Structures*, 32, 2174-2194.
43. Isa, M. N., Pilakoutas & K., Guadagnini (2021). Shear Behaviour of E-UHPFRC Containing Recycle Steel Fibres and E-UHPFRC Screw Piles – *Submitted to Construction and Building Materials*.

Chapter 2: Mechanical Performance of Affordable and Eco-Efficient Ultra-High Performance Concrete (UHPC) Containing Recycled Tyre Steel Fibres.

M.N. Isa, K. Pilakoutas, M. Guadagnini, H. Angelakopoulos, Mechanical performance of affordable and eco-efficient ultra-high performance concrete (UHPC) containing recycled tyre steel fibres, Construction and Building Materials 255 (2020) 119-272.

Author Contribution Statement

M.N. Isa: Conceptualisation, Methodology, Investigation, Formal analysis, Writing - original draft. **Kypros Pilakoutas:** Supervision, Writing - review & editing. **Maurizio Guadagnini:** Supervision, Writing - review & editing. **Harris Angelakopoulos:** Formal analysis of fibre distribution.

ABSTRACT

This study aims to develop an affordable eco-efficient ultra-high performance fibre reinforced concrete (UHPFRC) using normal mortar, recycled tyre steel cords (RTSC) and recycled tyre steel fibre (RTSF). Twelve UHPFRC mixes containing either RTSC, RTSF or blends of the two in various ratios are studied for total fibre volumes of 2, 3 and 4%. The effect of short fibres and cleanliness of RTSF on flexural strength of UHPFRC is examined, and it is shown that rubber and other impurities, as well as fibres with less than 9mm length, significantly reduce the strength of the UHPFRC mix. This confirms that cleaning and reducing the amount of short fibres is necessary for improved performance. Although mixes containing RTSF only do not exhibit the same flexural performance of mixes containing RTSC or manufactured fibres, similar strength can be achieved by using hybrids (RTSC and RTSF) or a higher dosage of RTSF. The main strength parameters used in serviceability and ultimate limit state design are experimentally derived and prediction models are proposed. A material efficiency study of the mixes shows that use of RTSF in UHPFRC provides significant cost and environmental benefit. Such affordable and robust UHPFRC mixes can help develop new and more sustainable applications for the construction industry.

Keywords: Ultra-High Performance Fibre Reinforced Concrete, Recycle Tyre Steel Cords, Recycled Tyre Steel Fibres, Fibre Characterisation, Flexural Test, Residual Flexural Strength, Deflection, Crack Mouth Opening Displacement, Mix Efficiency.

2.1 Introduction

Developments in concrete technology in the past two decades have led to the development of Ultra-High Performance Fibre Reinforced Concrete (UHPFRC) [1], which has compressive strength greater than 150 MPa and a sustained post cracking tensile strength greater than 7 MPa [1,2]. UHPFRC has a very dense pore structure that reduces liquid ingress, and significantly enhances durability as compared to conventional and high-performance concretes [1,3–5]. These improved mechanical and durability properties are achieved through the use of high strength cementitious materials, optimized gradation of high strength granular materials, very low water-cement ratio, high quality and high dosage of superplasticizer as well as the use of fibres (with steel and carbon fibres being the most commonly used [1,6]). Despite the superb performance characteristics of UHPFRC, its widespread application is limited due to high initial cost, concerns regarding sustainability [7] and lack of standardization. The lack of standard design guidelines means that contractors and practicing engineers wanting to take advantage of the superior properties of UHPFRC must rely on the more onerous design by testing procedures, rather than rational design rules [8].

The high initial cost and sustainability problems are due to the use of high cement content and high cost steel fibres. UHPFRC containing 1.5% by volume steel fibres costs approximately \$950/m³ against \$150-200/m³ for conventional concretes [9]. The environmental impact of the two main constituent materials (cement and steel fibres) is also high, with about 0.9 tons of CO₂ emitted for every ton of cement produced [10] and 1.9 tons of CO₂ per ton of steel produced [11]. Nonetheless, life cycle cost analysis (LCCA) has shown that UHPC structures can be stronger, more durable and cheaper than conventional concrete structures [12]. According to [13], approximately 56% reduction in material costs can be achieved by utilizing UHPC rather than conventional concrete, as the high strength of UHPC allows the design of slender structures, thereby reducing the overall volume of construction materials [14]. To address the sustainability issue of UHPFRC, the cement content could be reduced by using alternative cheaper and greener pozzolanic materials like Ground Granulated Blast Furnace Slag (GGBS) [15–17] as well as alternative steel fibres. Steel cord obtained from end of reels or unvulcanised rubber belt offcuts from tyre manufacturing plants, otherwise known as Recycled Tyre Steel

Cords (RTSC) [18] has the potential, if processed to desired lengths, to be used as a substitute to manufactured steel fibres in UHPFRC. Moreover, steel fibres extracted from end of life tyres (RTSF) and processed to high specifications may also provide a better substitute to manufactured steel fibres in terms of economic and environmentally sustainability.

Approximately 1.5 billion tyres are produced worldwide [19], and a large percentage of these number is disposed of annually. Over the past two decades, waste tyre disposal has become a key societal concern and as a result, in 2006, the European Union (EU) banned the disposal of tyres and their by-products into landfills. Similarly, in the United States, 42 states have restricted depositing end of life tyres in landfills [20]. In 2008, the European directive 2008/98/EC [18] set up a disposal plan to encourage management and recycling of waste tyre products (rubber granules, steel fibre and polymer fibres) for novel applications. The viability of using Recycle Tyre Steel Fibre (RTSF) and RTSC was demonstrated by researchers at the University of Sheffield [22–25] as a substitute for manufactured steel fibres (MSF) in conventional concrete. However, conventional UHPFRC relies on the use of high quality fibres with optimal geometry and the use of recycled fibres from tyres, which have a non-uniform length distribution (the very short fibres are likely to reduce post cracking strength, while the very long ones might affect workability and fresh properties) and can include rubber impurities, has never been examined. This study will assess the viability of using RTSF and RTSC in UHPFRC and will examine some of the technological issues that need to be addressed to obtain reliable mixes.

While RTSC do not need much processing apart from cutting to the desired lengths, extracting fibres from used tyres requires a series of operations. The most commonly used tyre recycling technique involves mechanical shredding and granulation, which produces secondary products including unsorted RTSF, polymer (textile) fibres and rubber granules for use in several other applications. Partially sorted RTSFs used in conventional concrete is contaminated with rubber (which can be up to 20% by weight [24]), and comprises of fibres of irregular shapes, length and diameter. These will have a degrading effect on the strength and durability of UHPFRC. To obtain cleaned RTSF that can suitably be used in UHPFRC, further processing (cleaning and sorting) is required to minimize the rubber content as well as the amount of fibres of unsuitable length and diameter.

To facilitate the widespread use of UHPFRC, there is a need to reduce the environmental and cost credentials of UHPFRC by using alternative cementitious materials, readily/locally available sands and steel fibres without loss of mechanical characteristics. Moreover, the main parameters used in serviceability and ultimate limit state design will be examined and prediction models proposed to promote the development of design codes and guidelines.

This study assesses the mechanical performance of E-UHPFRC containing normal mortar and recycled steel fibres, cured at room temperature. The fresh properties, compressive strength and flexural characteristics of 12 UHPC mixes containing RTSC, RTSF, and blends of the two are examined in this study.

2.2 Material and Methods

Twelve mixes containing fibres and one plain mix used as control were prepared as shown in Table 2.1.

The mixes were designed with fibre dosages of 2, 3 and 4% by volume. For each fibre dosage, 4 mixes were produced using ratios of RTSF to total fibre content equal to: 0, 1/3, 2/3 and 100%.

The mix design and the characterisation of the recycled fibres are discussed in Sections 2.2.1 and 2.2.2, respectively.

Table 2.1: Mix identification and fibre proportions

Mixes	RTSC kg/m ³	RTSF kg/m ³
Plain	0.0	0.0
f 2 - CCC	157.0	0.0
f 2 – CCF	104.7	52.3
f 2 – CFF	52.3	104.7
f 2 – FFF	0.0	157.0
f 3 – CCC	235.5	0.0
f 3 – CCF	157.0	78.5
f 3 – CFF	78.5	157.0
f 3 – FFF	0.0	235.5
f 4 – CCC	314.0	0.0

Mixes	RTSC	RTSF
	kg/m ³	kg/m ³
f 4 – CCF	209.3	104.7
f 4 – CFF	104.7	209.3
f 4 – FFF	0.0	314.0

The following nomenclature was used to identify mixes;

1st item is a letter f stands for mix with fibre

2nd item is a number designated as either “2, 3 or 4” which stands for total fibre volume

3rd item a three letter stands for proportion of fibre type where C stands for RTSC and F stands for RTSF e.g.

f 2 – CCF = mix containing 2% fibre volume and 1/3 RTSF and

f 4 – FFF = mix containing 4% fibre volume and 100% RTSF

2.2.1 E-UHPFRC Mix Design

The constituent materials used for the mix design include: locally available silica sand having a maximum particle sizes less than 500 μ m, dry densified silica fume having approximate particle mean size of 0.15 μ m and density of 500 – 700 kg/m³; polycarboxylate superplasticizer (Sika ViscoCrete 30HE); 52.5N type I cement and GGBS having approximate density of 2400-3000 kg/m³. The mix (Table 2.2) is based on a low cement content mix developed by [15] and also used by [26–29].

Table 2.2: UHPFRC mix design

Material	Mix	
	Quantity (kg/m ³)	Per unit weight of cement
Cement	657	1
GGBS	418	0.64
Silica Fume	119	0.18
Silica Sand	1051	1.6
Superplasticizer	59	0.09
Water	185	0.28

2.2.2 Fibres Characterisation and Processing

The RTSC and RSTF used in this study were obtained from TWINCON Ltd. Partially sorted RTSF contain fibres of various lengths ranging from 1-45mm as well as rubber impurities (Figure 2.1c). The fibres have a nominal diameter of 0.22mm and a nominal direct tensile strength of 2,500MPa [30].

RTSC (Figure 2.1a and b) comprise of brass coated straight fibres having a diameter of 0.2mm and a tensile strength of 2500MPa.

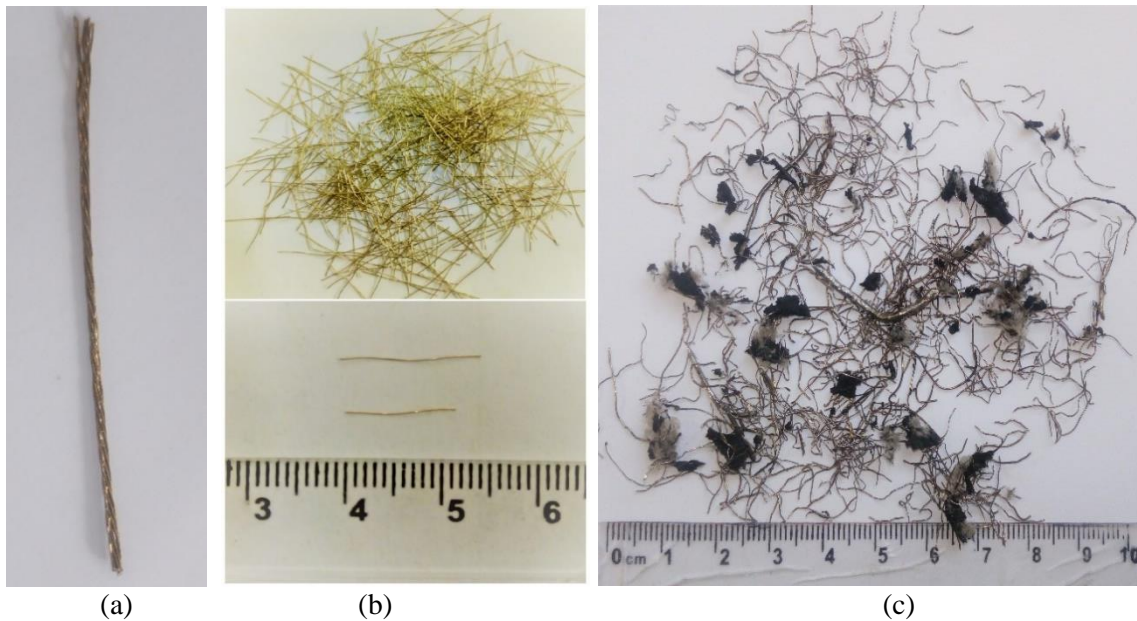


Figure 2.1: (a) Tyre steel cords (b) RTSC (c) Partially sorted RTSF

Based on the performance of the mix during pilot testing (Sec. 2.2.3 and 2.4.1), RTSF 1 was subjected to a refinement process which aimed to clean and improve length distribution as shown in Figure 2.2. The cleaning process removes rubber particles and impurities, and reduces the amount of shorter fibre lengths, which are known to contribute less to the flexural strength of UHPC. The process, which involves the use of sieves and a sieve shaker, is carried out in 3 stages: Stages 1 and 2 aim to clean the partially sorted RTSF using 1mm size screen to remove very long and very short fibres, rubber particles and dust, while stage 3 aims to further reduce the amount of short fibres by sieving using a 600 μ m screen. At each stage, the fibres retained on sieve (T) and those that passed through (B) were collected separately and samples of these are shown in Figure 2.3. To obtain the length distribution of RTSF, a system of advance photogrammetric pattern recognition based on digital optical correlation is used [30,31]. The system uses a high-speed camera to capture images of fibres dispersed on a screen

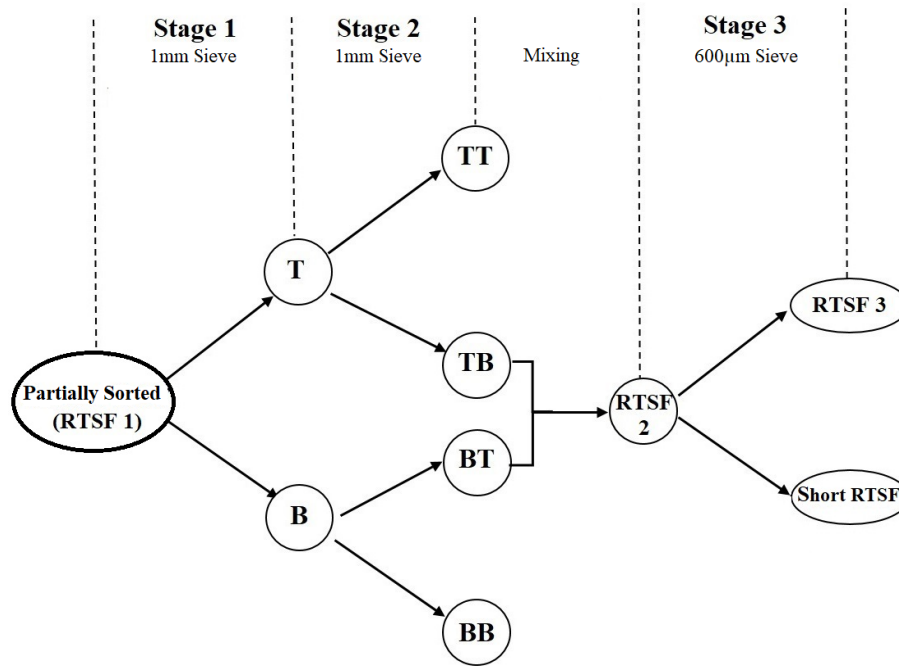


Figure 2.2: Schematic representation of RTSF cleaning process

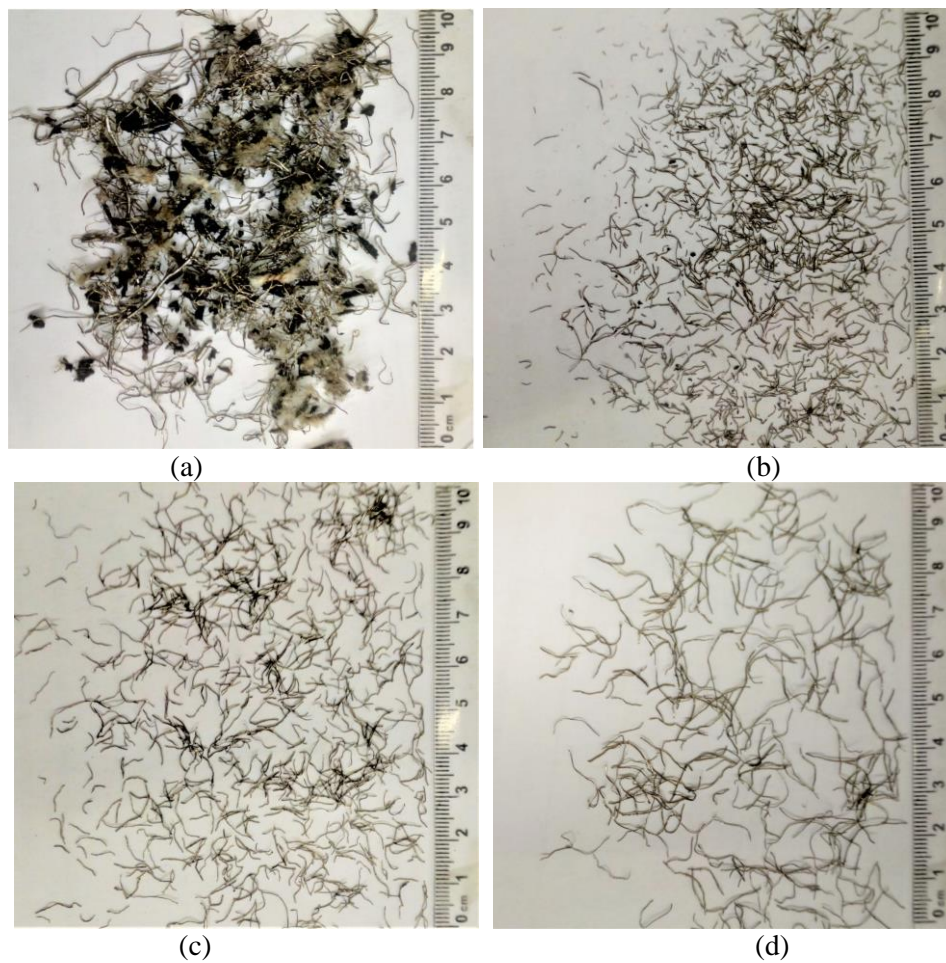


Figure 2.3: Samples from the cleaning process (a) TT (b) BB (c) Short fibres (d) RTSF 3

The RTSF fibre distribution and statistical analysis are given in Figure 2.4 and Table 2.3, respectively.

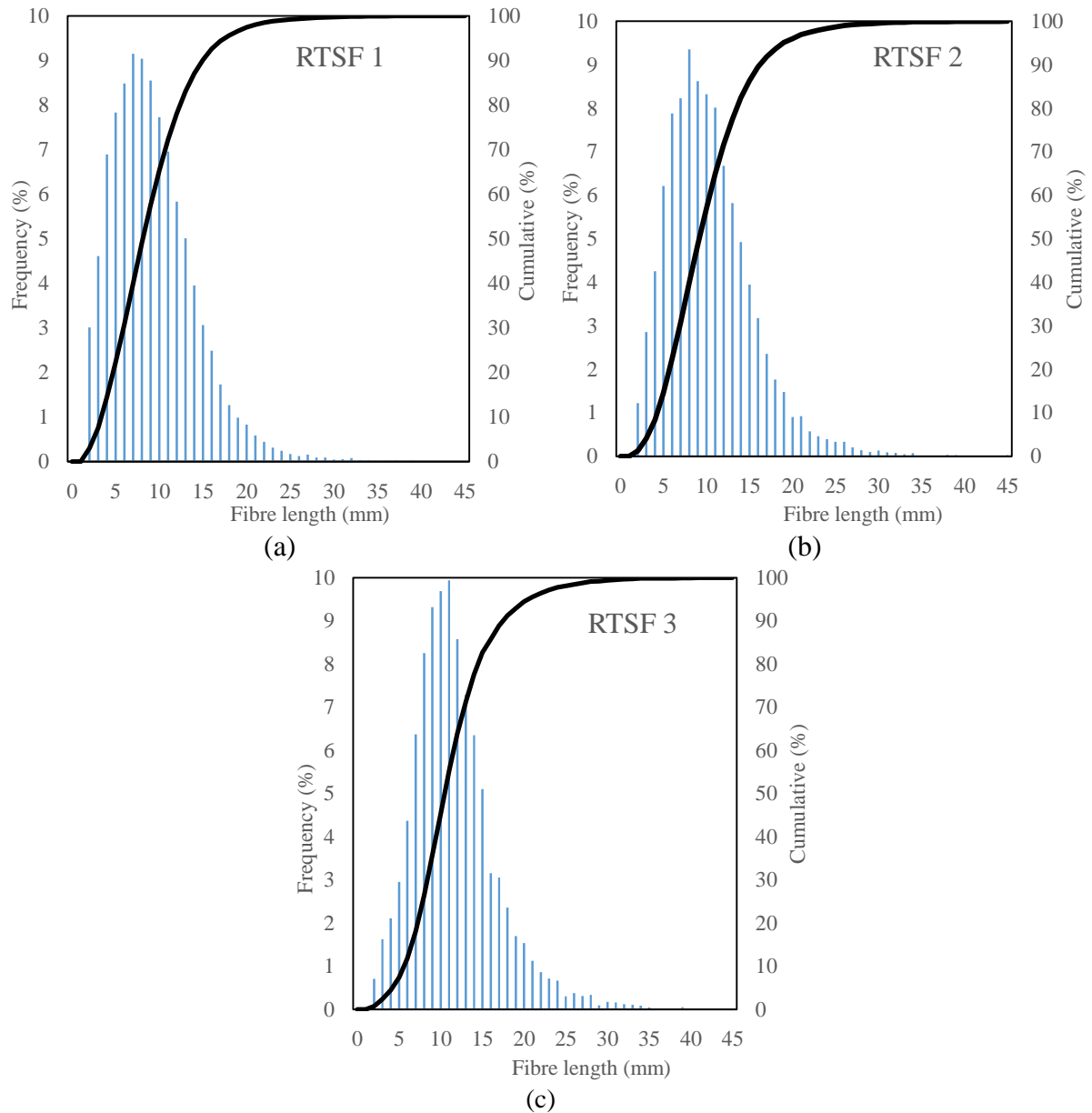


Figure 2.4: RTSF length distribution (a) RTSF 1 (b) RTSF 2 and (c) RTSF 3

Table 2.3: Statistical analysis of RTSF distribution

Property	RTSF 1	RTSF 2	RTSF 3
Fibre length			
< 9mm	57.6%	48.6%	35.7%
9 – 15mm	32.4%	37.7%	47%
>15mm	9.9%	13.7%	17.3%
Mean	9.3	10.4	11.6
STDEV	4.8	5.0	5.1
Variance	23.3	25.5	25.8
Kurtosis	2.8	2.9	2.5
Skewness	1.2	1.3	1.1

2.2.3 Pilot Flexural Testing

To examine the suitability of RTSC and partially sorted RTSF in UHPFRC, pilot flexural strength tests were conducted on a 40×40×160mm prisms made with mixes containing 3% of fibres. The parameters for the pilot study were; the length of RTSC (6, 9, 12 and 15mm) and cleanliness and distribution of RTSF (Sec 2.1.1). Mixes containing RTSF with 3 different level of cleanliness (RTSF 1 – 3) and distribution were examined. The control mix for this batch contained the partially sorted RTSF (RTSF 1) as obtained from the suppliers.

2.2.4 Mixing Procedure and Specimen Preparation

Cement, silica fume, GGBS and silica sand were dry-mixed in a pan mixer for 5 minutes. Clean water and superplasticizer were mixed together and half of the mix was added to the dry-mixed materials. The materials were mixed further until the mixture changed to granules. At this point, the remaining half of the mixing water was added and the mixing continued for a further 5mins until the mix achieved a homogenous self-flowing state. Steel fibres were then added slowly while mixing for 2mins. The mortar was then further mixed for another 2mins to ensure that all fibres were well dispersed.

Immediately after mixing was completed, workability (flow table) (Figure 2.5b) and fresh density tests were conducted in accordance to ASTM C1437-15 [32] and BS EN 12350-6 [33], respectively. The prepared E-UHPFRC mix was then cast into 3 plastic cylindrical moulds (100 × 200mm) and 5 steel prismatic moulds (75 × 75 × 225mm) in accordance to EN 12390-2 [34]. Although E-UHPFRC is a form of self-compacting mortar, each specimen was cast in two layers, with each layer consolidated on a vibrating table for 10 seconds per layer (Figure 2.5c). After casting, the specimens were covered with plastic sheets to prevent moisture loss (Figure 2.5d). The specimens were de-moulded after 24hrs and placed inside a curing tank at a water temperature of 20±2 °C for 28 days.



Figure 2.5: UHPC production (a) Fresh E-UHPFRC mix (b) workability test (c) casting and levelling (d) cast prisms and cylinders

2.2.5 Compressive Strength and Modulus of Elasticity

Compressive strength and modulus of elasticity of the mixes were obtained from 100×200 mm cylinders using a servo hydraulic testing machine. Prior to testing, the cylinders were prepared by grinding the top (rough) face and their exact dimensions measured. A special measuring device consisting of two metal rings equipped with laser displacement sensors was used for measuring axial deformation (Figure 2.6). The specimen were tested under uniaxial compressive loading in accordance to BS EN 12390-3: 2009 [35].



Figure 2.6: Compressive strength and modulus of elasticity test.

2.2.6 Three-point Bending Test

The flexural behaviour of E-UHPFRC prisms was assessed through three-point bending tests (Figure 2.7), using an electromagnetic universal testing machine with a capacity of 300kN. A day prior to the testing date, a notch (2.5mm wide and 12.5mm deep) was sawn at the bottom mid-span of each prism. A specially designed aluminium yoke holding two central LVDT's (one on each face) was assembled on the specimen to measure central deflections. A clip gauge was used to measure the crack mouth opening displacement (CMOD) at the notch. The tests were conducted in accordance to EN 14651: 2005 [36] with CMOD control at a constant rate of 0.05mm/min for CMOD from 0 to 0.1mm and 0.2mm/min after 0.1mm.

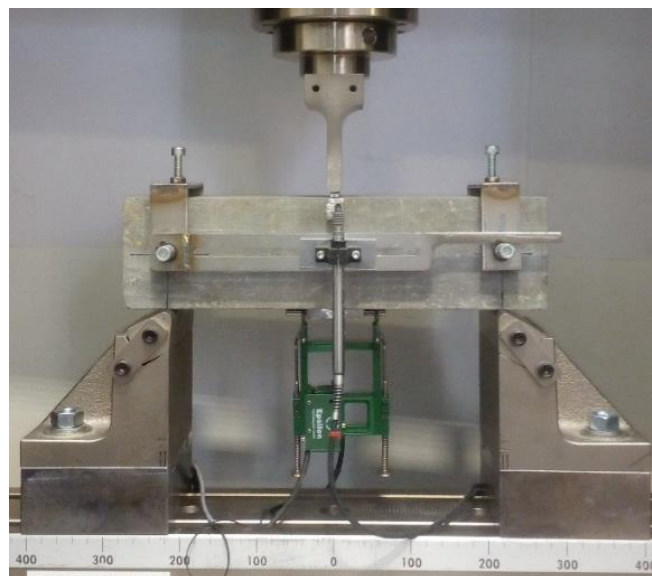


Figure 2.7: Flexural prism test set-up

2.3 Material Efficiency

A material efficiency analysis was conducted to ascertain the efficiency of the mixes and the effect of RTSC and RTSF on the efficiency. The efficiency (E) is computed based on cost, environmental and mechanical credentials for each mix.

In determining the environmental impact of the constituent materials, GGBS and Silica fume are treated as waste products and their environmental impact is based on the Global Warming Potential (GWP) attributed to the energy consumed during the industrial processes needed to make them suitable for direct application in concrete (i.e. grinding, classifying etc.). Likewise, the environmental impact of RTSF is determined using the energy used in processing of the steel extracted from waste tyre into clean and sorted RTSF. RTSC is basically produced from leftover steel cords such as the end of reels that cannot be used to manufacture tyre. Thus RTSC after cutting has the same mechanical and properties and appearance as MSF. Hence, in this study, RTSC is treated as MSF, and the cost and GWP of MSF applies to it.

2.3.1 Cost

The cost of each mix is calculated as the sum of cost of the amount of each constituent material required to produce a unit volume of UHPC as shown in Eq. (2 – 1) below;

$$C_{mix} = \sum_i^n C_i \cdot m_i \quad (2 - 1)$$

Where C_i is the cost of material i , m_i is the mass of material i and n is the number of constituent materials.

Economic Efficiency (E_C) of the mixes can then be computed using Eq. (2 – 2);

$$E_C = \frac{C_{mix}'}{C_{mix}} \quad (2 - 2)$$

Where C_{mix}' is the cost of the reference mix (CCC).

2.3.2 Environmental Impact

The environmental impact is computed in terms of GWP. It is calculated as the sum of the product of the GWPs per unit mass of each constituent materials and the corresponding mass used to produce 1m^3 of E-UHPFRC, as shown in Eq. (2 – 3)

$$GWP_{mix} = \sum_i^n GWP_i \cdot m_i \quad (2 - 3)$$

Where GWP_i is the global warming potential of material i , m_i is the mass of material i , and n is the number of constituent materials.

Environmental Efficiency (E_n) of the mixes can also be computed using Eq. (2 – 4);

$$E_n = \frac{GWP'}{GWP} \quad (2 - 4)$$

Where GWP' is the for the reference mix (CCC).

2.3.3 Mechanical Efficiency

The mechanical efficiency (M_E) is typically calculated in terms of compressive strength and workability [9]. However, with regards to the objectives of this study, M_E is adjusted to be dependent on flexural strength and workability as shown in Eq. (2 – 5).

$$M_E = 0.7 \left(\frac{f_R}{f'_R} \right) + 0.3 \left(\frac{W}{W'} \right) \quad (2 - 5)$$

Where f_R and f'_R are the flexural strength of the mix examined and the reference mix, respectively. W and W' are the workabilities of examined and reference mixes respectively. The factors 0.7 and 0.3 were chosen to give strength a higher weight over workability [9].

2.3.4 Mix Efficiency

The mix efficiency or total efficiency (E) is used to describe the overall efficiency of the mix based on the contribution of all other material indices. It is calculated as the product of mechanical, economic and environmental efficiencies as shown in Eq. (2 – 6) below.

$$E = M_E \times E_C \times E_n \quad (2 - 6)$$

2.4 Results and Discussion

2.4.1 Effect of RTSC Length and RTSF Refinement on Flexural Behaviour

Figure 2.8 shows the average flexural stress versus deflection curve of E-UHPFRC prisms containing RTSC of different lengths and RTSF obtained from the refinement process (described in section 2.2.2). Three samples were tested for each mix. The results show that length of RTSC fibre affects both the peak strength and post-peak stiffness of E-UHPFRC. Mixes containing short RTSC (RTSC-6 and RTSC-9) show lower performance compared to mixes containing long fibres (RTSC-12 and RTSC-15). This can be attributed to the poor anchorage of fibres with low aspect ratio (in this case l/d less than 45) resulting in premature fibre slip. This is consistent with findings available in the literature on the effect of manufactured steel fibre length on the flexural strength of UHPFRC (e.g. [37]). As there is no further strength enhancement from 12 to 15mm, for this type of fibre, the optimum fibre length is expected to be found between these two limits. It should be noted that the flexural capacity of RTSC-12 and RTSC-15 is 3.8 times higher than that of the plain mix.

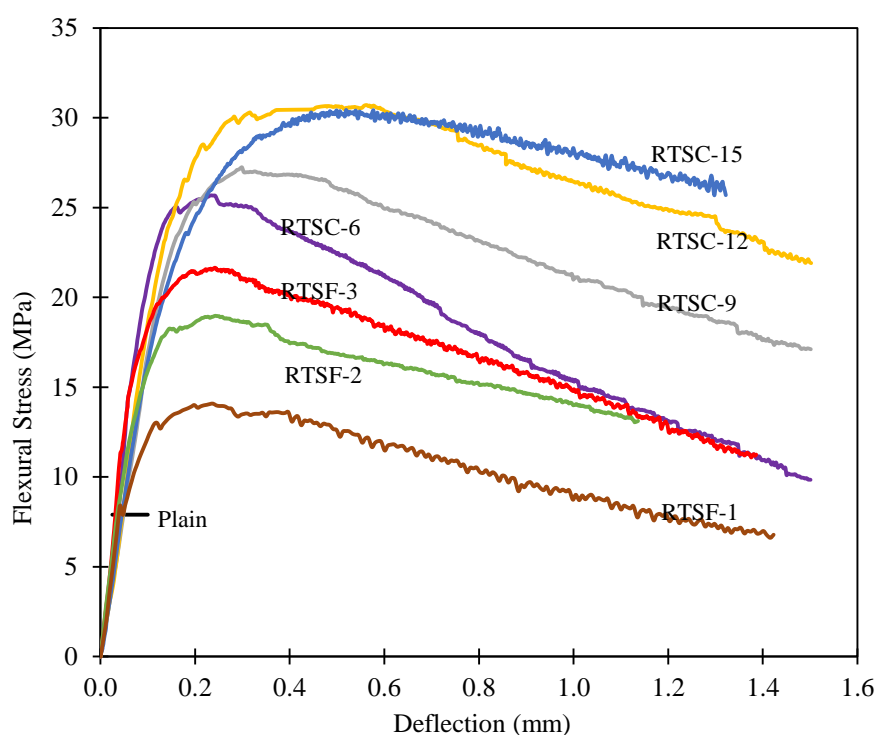


Figure 2.8: Flexural behaviour of E-UHPFRC containing different fibre types and length

The flexural capacity of all RTSF mixes is lower than that of the RTSC mixes, with RTSF-1 exhibiting the lowest flexural capacity. This is because RTSF-1 contains rubber impurities and a high content (57.1%) of fibres with low aspect ratio (< 9 mm in length) which makes it unsuitable for direct use into

UHPFRC. After the first cleaning (Figure 2.4b), RTSF 2 contains considerably less impurities and 48.6% of fibres less than 9mm. The amount of short fibres is further reduced at the end of final refinement process and the final product RTSF 3 (see Figure 2.3(d) and 2.4(c)) contains only 35.7% of fibres less than 9mm.

As a result, the mixes containing the refined RTSFs show superior flexural performance compared to mix RTSF-1, with an increase in the flexural strength of 34 and 54% for RTSF 2 and RTSF 3, respectively. The flexural capacity of RTSF-2 and RTSF-3 were 2.4 and 2.7 times the strength of the plain mix, respectively. Based on this pilot test study, all subsequent RTSF mixes were designed using RTSF 3.

2.4.2 Fresh Properties

Table 2.4 summarizes the fresh properties of the mixes examined in this study (Table 2.1) in terms of workability and fresh density.

Table 2.4: Fresh and hardened property of E-UHPFRC mixes

Mix ID	Flow Diameter (mm)	Fresh Density (kg/m ³)
Plain	> 255	2464
f 2 - CCC	> 255	2596
f 2 – CCF	243	2590
f 2 – CFF	238	2592
f 2 – FFF	222	2587
f 3 – CCC	228	2691
f 3 – CCF	217	2687
f 3 – CFF	211	2688
f 3 – FFF	205	2682
f 4 – CCC	201	2769
f 4 – CCF	198	2751
f 4 – CFF	186	2757
f 4 – FFF	179	2747

All mixes show adequate flow, greater than 200mm, meeting the UHPFRC workability requirement generally recommended in the literature [38], the only exceptions are; mixes f4 – CCF, f4 – CFF and f4 – FFF that show slightly lower flow, but still meet the flow requirement recommended by the US Department of Transportation report (FHWA–HRT–18 -036) [39], i.e. > 178mm (7 inches). Figure 2.9 shows that for the same total fibre volume, mixes containing CCC result in higher workability than mixes containing FFF. As expected, the flow further decreases with increasing fibre content, due to increased friction between the fibres and the paste. Mixes containing CCC up to 4% by volume showed no sign of balling, as opposed to f4 – CCF and f4 – FFF for which the fibres started to ball as the friction between the fibres and paste built up.

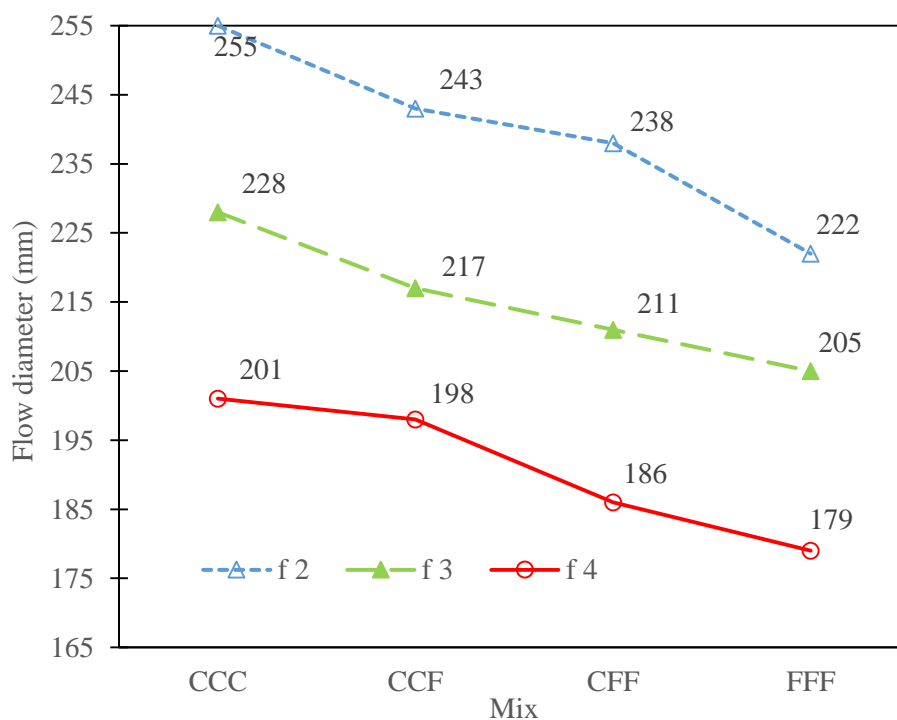


Figure 2.9: Workability of E-UHPFRC mixes

The fresh density test results show that for the same total fibre dosage, mixes containing FFF have slightly lower density < 1% than mixes containing CCC. This may be due to higher air content and tiny rubber particles that are still attached to the surface of some of the RTSF fibres.

2.4.3 Compressive Strength and Modulus of Elasticity

The results of the compressive strength tests (Table 2.5) show that all mixes achieved a compressive strength greater than 150MPa, and as such can be defined as UHPCs. Mixes containing CCC have higher compressive strength compared to mixes containing FFF. The lower strength in mixes containing FFF can be attributed to possible entrapped air in the mixes due to the nature of the RTSF fibres [30,40–43] and small rubber particles inclusions. For the fibre dosages of 2 – 4% by volume tested, the fibre volume does not appear to affect much the compressive strength, similar to the findings that are reported for MSF in UHPFRC [44,45]. However, the reductions in strength of FFF compared to CCC of 8.7, 7.5 and 3.6% for 2, 3 and 4%, respectively, show that the loss in strength decreases as the total fibre volume increases.

The modulus of elasticity (E_c) was determined using the gradient of the compressive stress-strain curve measured between 20-70% of the peak strength and was found to range between 49 – 54 GPa for all mixes. It was found that E_c increases slightly (1 – 8%) with fibre volume (Table 2.4), and is higher for mixes containing CCC. For the same fibre dosage, the addition of RTSF results in a small reduction in E_c possibly due to the presence of fibres containing rubber remnants. However, no clear trend can be established in the decrease in E_c with increasing RTSF content. Comparison between the measured E_c and prediction models based on the rule of composites or as a function of f_c' are shown in Table 2.5.

Table 2.5: Comparison between measured and predicted modulus of elasticity for all mixes (MPa)

Mix ID	f'_c (MPa)	E_c (GPa)	Prediction models			
			$E_{comp.}$	[46]	[47]	[48]
				$9500(f'_c)^{1/3}$	$4150(f'_c)^{1/2}$	$4069(f'_c)^{1/2}$
Plain	158	49.6	49.6	51.1	52.3	51.2
f 2 – CCC	173	51.4	50.7	52.9	54.6	53.5
f 2 – CCF	171	51.5	50.7	52.8	54.4	53.3
f 2 – CFF	159	50.7	50.7	51.5	52.4	51.4
f 2 – FFF	158	50.5	50.7	51.4	52.2	51.2
f 3 – CCC	173	52.5	51.3	53.0	54.7	53.7
f 3 – CCF	169	52.1	51.3	52.5	54.0	52.9
f 3 – CFF	167	51.8	51.3	52.3	53.7	52.6
f 3 – FFF	160	51.0	51.3	51.7	52.6	51.6
f 4 – CCC	172	53.6	51.9	52.8	54.4	53.4
f 4 – CCF	169	53.2	51.9	52.6	54.0	53.0
f 4 – CFF	170	53.4	51.9	52.7	54.2	53.2
f 4 – FFF	165	52.6	51.9	52.2	53.5	52.4

The values of E_c found for the tested mixes are in close agreement with prediction models reported by [46–48]. The small differences between the experimental and predicted values can be attributed to the difference in constituent materials and curing regimes, as most UHPFRCs reported in literature used higher cement content, high strength sands (e.g. quartz) and high temperature curing regimes. For further validation of the measured values, the theoretical modulus of elasticity based on the rule of mixture for composites ($E_{comp.}$) is calculated using Eq. (2 – 7).

$$E_{comp.} = E_m V_m + \eta E_f V_f \quad (2 - 7)$$

Where, E_m and E_f are the modulus of elasticity of matrix (plain mix) and fibres ($E_f = 200GPa$), respectively, and V_m and V_f are the volume fraction of matrix and fibre respectively ($V_m = 1 - \eta V_f$), $\eta = 0.375$ (Krenchel composite efficiency factor for fibre orientation [49]).

The composite modulus is slightly lower than the measured modulus, this may be due to a low reading of the plain mix or an additional synergetic mechanism by which the fibres enhance the axial modulus by preventing the lateral expansion of the mix.

2.4.4 Flexural Performance

The load-deflection and flexural stress behaviour for all examined E-UHPFRC mixes are presented in Figure 2.10(a-c). As expected, all mixes after cracking exhibit an initial strain hardening behaviour due to the high volume of fibre used.

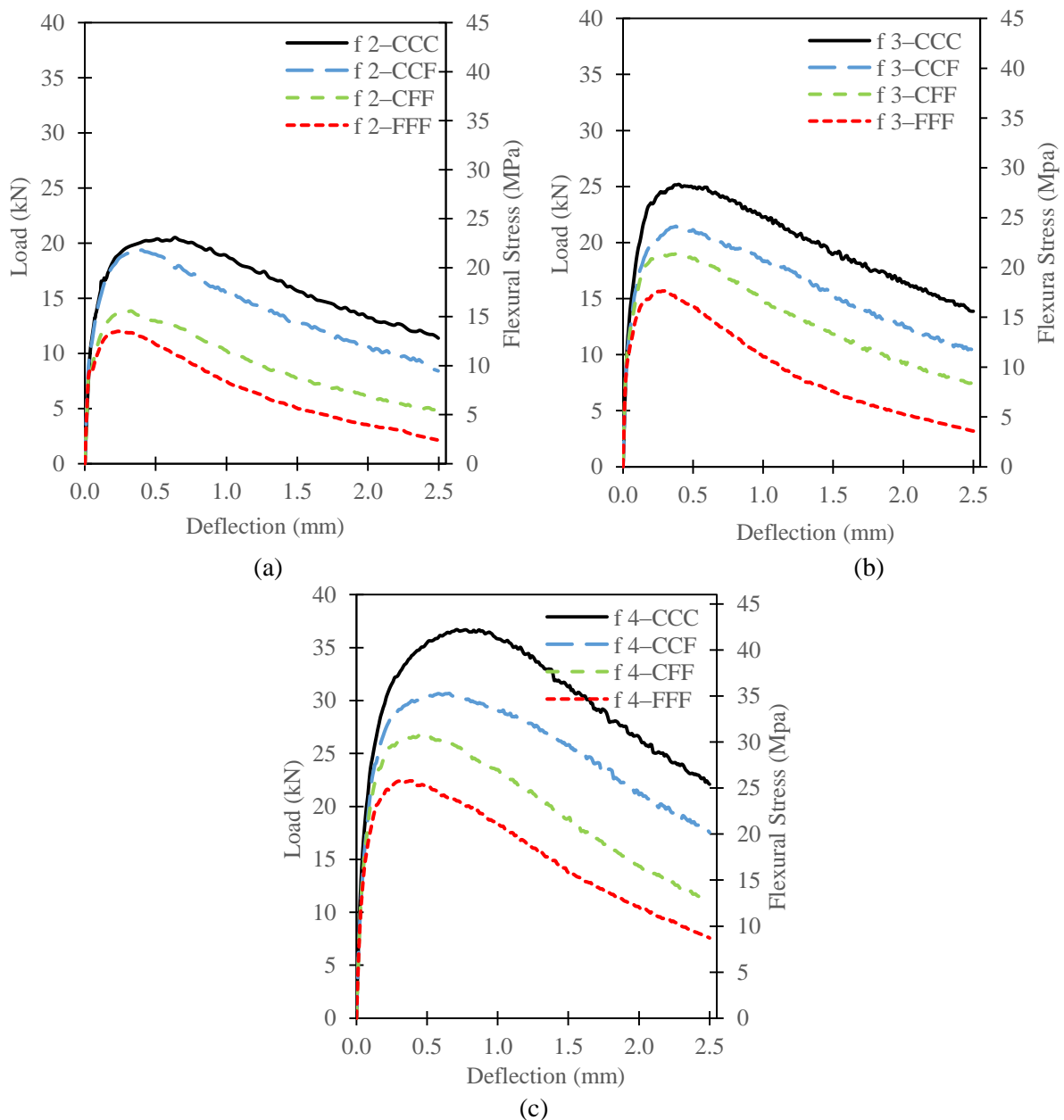


Figure 2.10: Load/flexural stress – deflection behaviour of E-UHPFRC mixes

The values of flexural strength (f_{fl}) and bending modulus of elasticity (E_b) were determined from the experimental load – deflection curves and are shown in Table 2.6, along with their coefficient of variation (COV). It should be noted that BS EN 14651: 2005 [36], based on which the flexural tests were carried out, determines f_{fl} as the strength at limit of proportionality (f_{LOP}), calculated from Eq. (2 – 8) using the highest load value recorded at a CMOD value of 0.05mm (0.025mm CMOD for the prisms size in this study). The strength values based on this approach (see f_{LOP} in Table 2.6) however, are not suitable to describe strain hardening materials like UHPFRC, as the highest load value measured within the recommended CMOD range represents only between 36 – 69% of the ultimate load capacity, thus providing a significant underestimation of the flexural strength of UHPFRC. To address this drawback, f_{fl} was determined the approach proposed by BS EN 12390–5 [50] which relies on the maximum load obtained from the load-deflection curve, of the UHPFRC mixes from Eq. (2 – 8).

$$f_{fl} = \frac{3Pl}{2bh_{sp}^2} \quad (2 - 8)$$

Where P is the load (N), h_{sp} (mm) is the distance between the tip of the notch and top of the specimen, b (mm) is the width of specimen and l (mm) is the span length.

The bending modulus of elasticity E_b was determined using Eq. (2 – 9), which relates load-deflection stiffness to E_b as shown below;

$$E_b = \frac{Pl^3}{48 I \delta} \quad (2 - 9)$$

Where $\frac{P}{\delta}$ (kN/m^3) is the slope of the load-deflection curve measured from 30-90% of the ultimate load of the plain mix, l (mm) is the span length, and I (mm^4) is the second moment of area of the full section.

Table 2.6: Flexural strength and bending modulus of all mixes

Mix ID	f_{LOP} , MPa (COV)	f_{fl} , MPa (COV)	Bending Modulus E_b GPa (COV)
Plain	–	6.6 (5%)	45.8 (3%)
f 2 – CCC	11.7 (9%)	23.8 (6%)	47.1 (3%)
f 2 – CCF	10.8 (14%)	22.4 (13%)	46.8 (4%)
f 2 – CFF	9.9 (7%)	16.0 (8%)	47.0 (4%)
f 2 – FFF	9.7 (5%)	14.0 (7%)	46.5 (6%)

f 3 – CCC	14.9 (7%)	30.0 (5%)	49.0 (3%)
f 3 – CCF	12.7(6%)	24.9 (8%)	48.8 (4%)
f 3 – CFF	11.8 (4%)	22.3 (6%)	47.4 (4%)
f 3 – FFF	11.2 (12%)	18.2 (12%)	47.3 (6%)
f 4 – CCC	15.5 (4%)	42.9 (7%)	50.0 (4%)
f 4 – CCF	14.7 (13%)	35.5 (8%)	49.4 (4%)
f 4 – CFF	14.1 (3%)	31.2 (11%)	49.0 (5%)
f 4 – FFF	13.2 (10%)	26.0 (6%)	49.2 (5%)

For the same fibre volume, mixes containing CCC show the highest f_{fl} (24 – 43 MPa) while mixes containing FFF show the least f_{fl} (14 – 26 MPa). The f_{fl} of mixes containing CCC are similar to the strength of mixes containing manufactured steel fibres (MSF) reported in the literature [2,51–53] for specimens that have been cured at room temperature. This confirms that RTSC can successfully be used to substitute MSF with no loss in strength. The effect of fibre volume and RTSF content on f_{fl} is shown in Figure 2.11

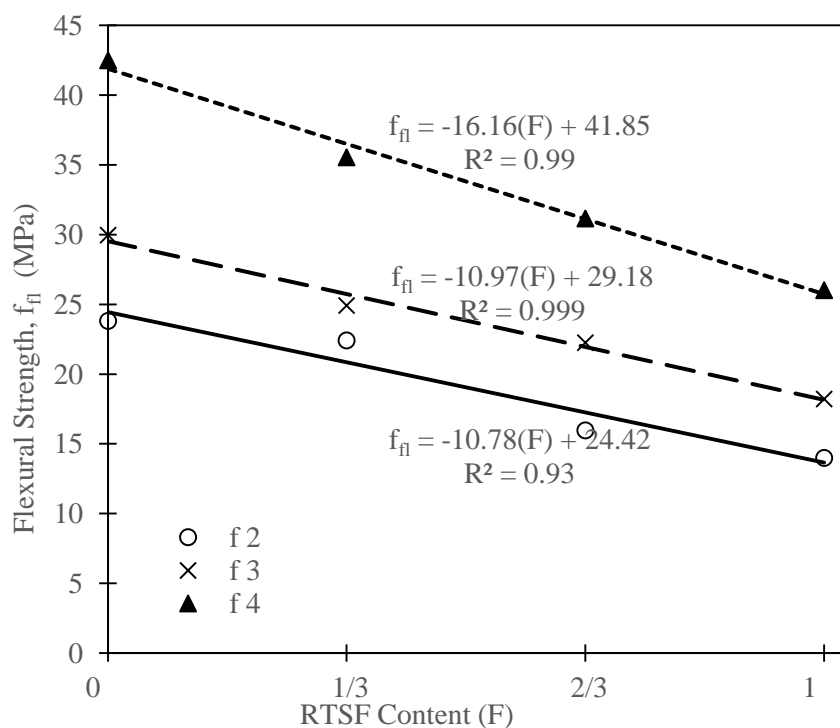


Figure 2.11: Relationship between f_{fl} and RTSF content

The flexural strength increases as the total fibre volume increases, while for the same fibre volume f_{fl} decreases with an increase in RTSF content. The decrease in f_{fl} due to the addition of RTSF can be attributed to the amount of short fibres (35.7%) with low aspect ratio (<45) that do not anchor sufficiently. Additionally, remnants of rubber particles attached to the surfaces of some RTSF fibre as shown in Figure 2.12 may also decrease the bond strength between the fibres and the paste, thus contributing to the reduction in f_{fl} . Comparing the loss in strength of hybrid mixes to that of their corresponding CCC mix, f 2 – CCF shows the best performance at 94% the f_{fl} of CCC indicating the best synergic effect between RTSC and RTSF at this ratio and fibre volume.

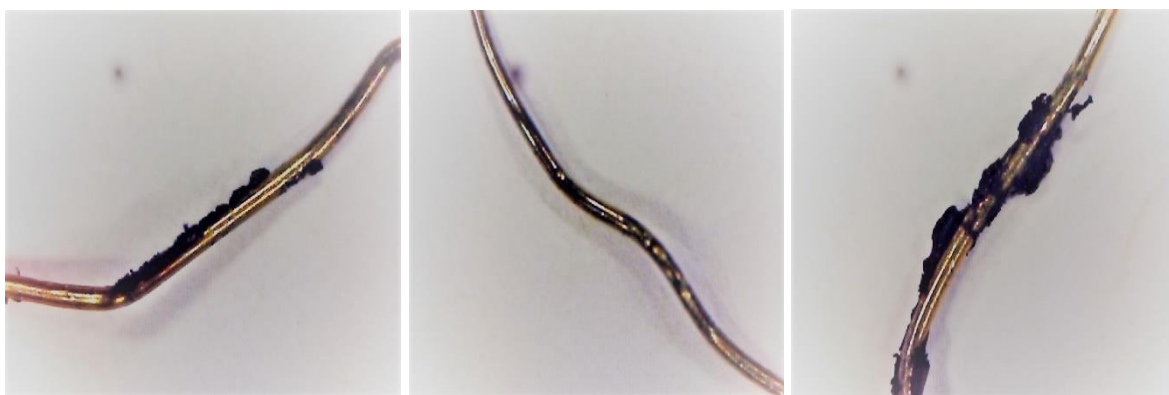


Figure 2.12: Magnified appearance of some RTSF

The effect of fibre volume and RTSF content on E_b and correlation between measured E_b and E_c are shown in Figure 2.13 a and b, respectively.

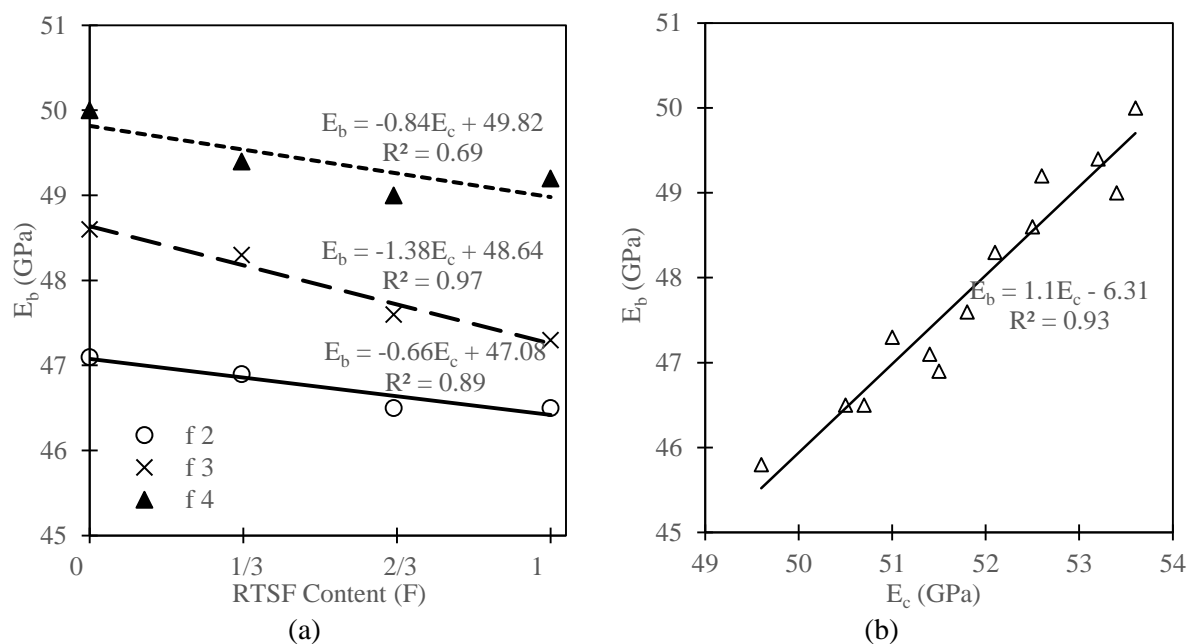


Figure 2.13: (a) Effect of RTSF content on E_b and (b) Correlation between E_b and E_c

All fibre reinforced mixes have E_b greater than that of the plain mix. As expected, E_b increases with increasing fibre volume, while, for the same fibre volume, mixes containing CCC show higher E_b , compared to mixes containing RTSF. However, the reduction in E_b , due to addition of RTSF is less than 3% for all fibre dosages.

Strong correlation was found between E_b and E_c with an R^2 value of 93% (Figure 2.13b). The result shows that E_b for all mixes are less than E_c by 6 – 9%. Studies on E_b of UHPFRC are rarely reported in the literature, and most studies on UHPC modulus of elasticity are based on the compression test (E_c) [8,54,55], which is based on the uniaxial deformation of the entire body of the specimen and as such is expected to yield a more reliable stiffness value, than E_b which is obtained indirectly and is more sensitive to the accuracy of the measurements. However, measuring deformations from bending tests can be less demanding compared to compression test in terms of machine capacity (more than 1200kN is needed to test 100×200mm UHPC cylinders) and instrumentation required.

The lower values of E_b compared to E_c can also be related to the effect of the notch on the prism specimens, as the formula used to calculate E_b (Eq. (2 – 9)) is based on the second moment of area (I) of the full section. To investigate the effect of the notch, a finite element (FE) study was carried out using the FE analysis package Abaqus. Two models, one each for notched and unnotched prisms were developed using a deformable 2D planar shell-like element 285mm long and 75mm deep (with plane stress thickness of 75mm). The models were assembled in a three-point bending arrangement having a span of 225mm and meshed using a 4-noded bilinear plane stress quadrilateral element (CPS4I) with a finite element size of 5mm (2.5mm for the notched section). The modulus of elasticity obtained from the compression test (E_c) for the selected specimens and a Poisson ratio of 0.18 [55] was used to model material behaviour. The load was applied using displacement control rather than CMOD control (used in experiment). The interaction between prism, loading plate and support is modelled using a friction coefficient (ξ) of 0.3 ($\xi \approx 0.271$ for concrete against steel [56]). The δ_{FE} at midspan of the prism is obtained by subtracting deformation at the support from the recorded midspan displacement (since δ_{exp} also does not include deformation at supports). The results of FEA at the pre-cracking load of 6kN for the four specimens are shown in Table 2.7.

Table 2.7: Results of FE modelling

Specimen	E_c (GPa)	Deflection at 6kN		Bending Modulus (GPa)	
		$\delta_{FE-notch}$	δ_{FE}	$E_{FE-notch}$	E_{FE}
Plain	49.6	0.0117	0.0102	46.2	52.9
f 2 – FFF	50.5	0.0116	0.0101	46.6	53.5
f 3 – CFF	51.8	0.0113	0.0098	47.8	55.1
f 4 – CCC	53.6	0.0107	0.0093	50.5	58.1

It can be seen that the notched prisms have on average 15% more midspan deflection than the unnotched prisms. Hence ignoring the notch can lead to significant errors up to 15%. To account for the notch effect and possible load spreading and support friction effect, a factor $k = 1.1$ is introduced to adjust the expression for E_b that will give a more accurate prediction of modulus of elasticity of UHPFRC as shown in Eq. (2 – 10) below.

$$E_b = k \frac{Pl^3}{48 I \delta} \quad (2 - 10)$$

It should be noted that the effect of notch will vary with notch-depth to full-depth ratio of the prisms. However, the correction provided in this study will also apply to the standard notched specimens described by BS EN 14651[36] as they have similar notch to full depth ratio.

Comparison between E_c and the adjusted E_b (Eq. (2 – 10)) are shown in Table 2.8. The results show that Eq. (2 – 10) can effectively account for the presence of the notch and provide a good estimate of the Young's modulus, as evidenced by the average value of the normalised modulus close to unity and the low standard deviation.

Table 2.8: Comparison between unnotched and adjusted E_b

Mix ID	E_c (MPa)	Eq. (2 – 10) (MPa)	Normalised Modulus $\left(\frac{E_b}{E_c}\right)$
Plain	49.6	50.0	1.01
f 2 – CCC	51.4	51.4	1.00
f 2 – CCF	51.5	51.2	0.99
f 2 – CFF	50.7	50.7	1.00

Mix ID	E_c (MPa)	Eq. (2 – 10) (MPa)	Normalised Modulus $\left(\frac{E_b}{E_c}\right)$
f 2 – FFF	50.5	50.7	1.00
f 3 – CCC	52.5	53.0	1.01
f 3 – CCF	52.1	52.7	1.01
f 3 – CFF	51.8	51.9	1.00
f 3 – FFF	51.0	51.6	1.01
f 4 – CCC	53.6	54.6	1.02
f 4 – CCF	53.2	53.9	1.01
f 4 – CFF	53.4	53.5	1.00
f 4 – FFF	52.6	53.7	1.02
Average			1.01
Standard Deviation			0.01

2.4.5 Residual Flexural Strength

Existing design codes classify SFRCs according to their residual flexural strengths (f_R - values) obtained at specific CMOD values, which characterise the material behaviour at the serviceability and ultimate limit states. While RILEM [57] measure f_R -values at CMODs of 0.5 and 3.5mm (f_{R1} and f_{R4} respectively), Model Code 2010 [58] measures at 0.5 and 2.5mm (f_{R1} and f_{R3} respectively). However, these CMOD values apply to standard prisms of dimensions 150×150×500mm. As the specimen size and notch dimensions used in the current study, is scaled down by 50%, the CMOD values are also determined at scaled-down CMOD of 50%. For example, the f_{R1} will be measured at CMOD of 0.25mm. Figure 2.14 shows the relationship between flexural stress and CMOD for the mixes, and the locations where f_R -values are obtained.

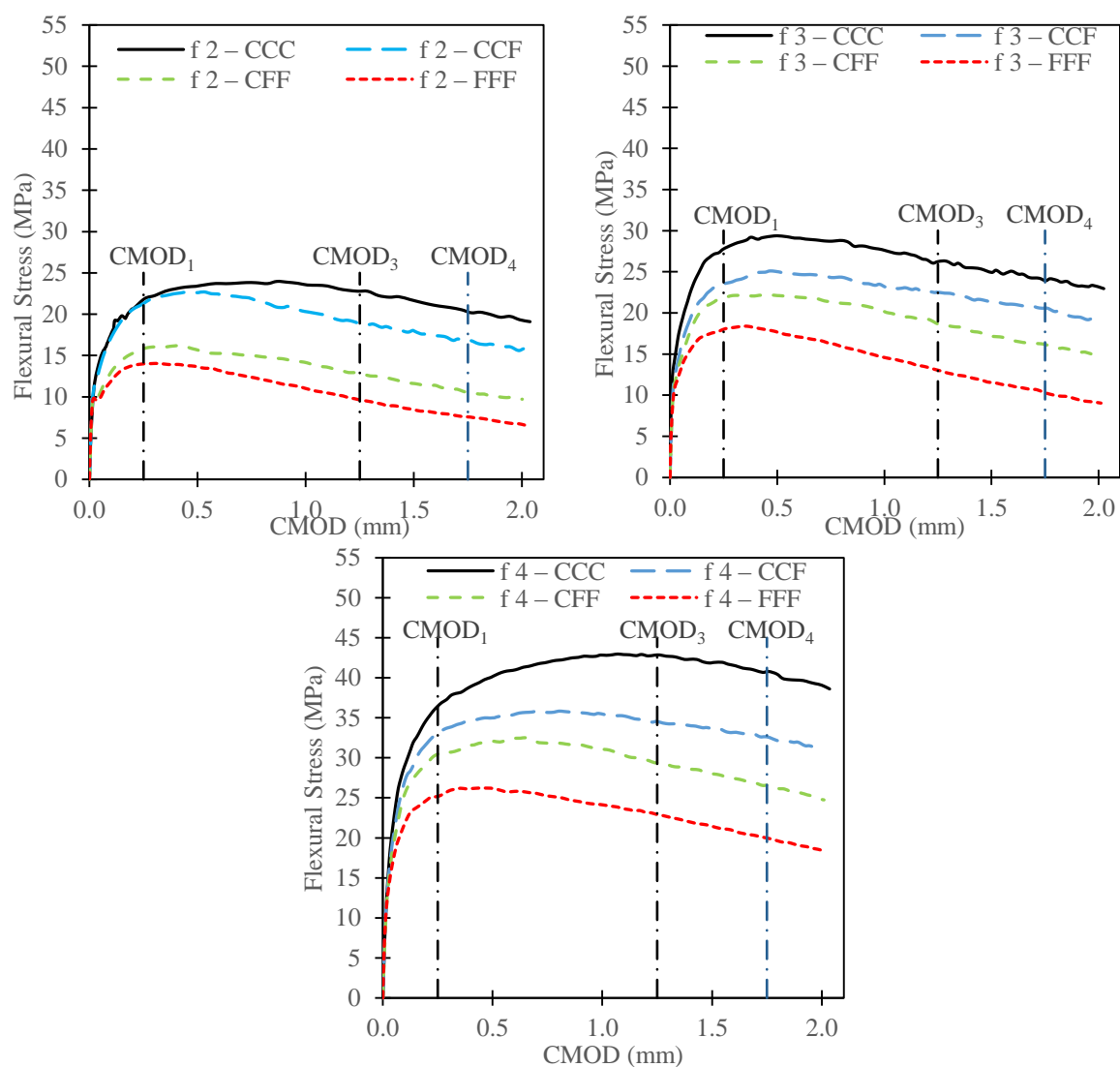


Figure 2.14: Flexural behaviour and design CMOD values based on RILEM [57] and Model Code [58]

It was found that $CMOD_1$ at which f_{R1} is measured is attained before the flexural strength f_{fl} is reached for all mixes. Hence for UHPFRC, f_{R1} cannot be considered as a residual strength. For cracked normal SFRC it is assumed that the tensile strength contribution of the remaining un-cracked section is negligible, however, this is not the case in UHPFRC because at the initial cracking stage, there is high resistance to crack propagation (due to high fibre dosage and bond strength) and thus at low CMOD values the un-cracked section may be large enough and contribute significantly to the overall tensile stress of the UHPFRC prisms. Similarly, the residual strength designated for ultimate limit design i.e. f_{R3} in Model Code [58] and f_{R4} in RILEM [[57]] will not be suitable for ultimate limit design of UHPC. This is due to the fact that UHPFRC possesses adequate flexural capacity even beyond these values ($CMOD_4$). Residual strengths f_{R3} and f_{R4} show flexural capacity between 72-99% and 55-98% of f_{fl}

respectively, depending on the mix type (highest for CCC and lowest for FFF mixes). Based on this observation, it is recommended that residual strength of UHPFRC at ultimate limit state should not be measured at a fixed CMOD value as designated by the codes, but rather should be selected based on the function of the structure and the steel fibre type to be used.

The proposed approach for determining the design parameters at ULS (f_R -values) for UHPFRC utilises the toughness determination for FRC by ASTM C 1018 [59], but CMOD values are preferred over deflection values. The approach involves identifying the serviceability CMOD ($CMOD_{SLS}$) and then determining the f_R -values parameters at multiples of the $CMOD_{SLS}$ as shown in Figure 2.15.

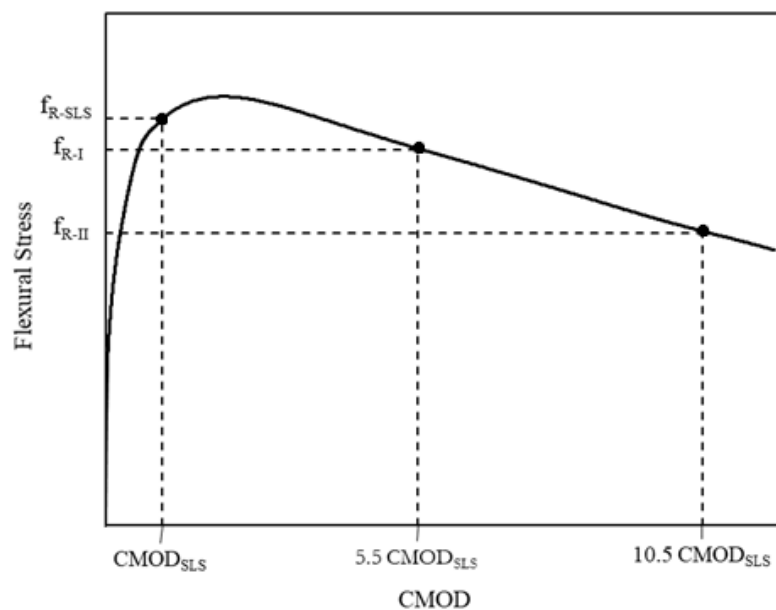


Figure 2.15: Definitions of residual flexural strength of UHPFRC

The $CMOD_{SLS}$ value of 0.25mm (corresponding to 0.5mm recommended by RILEM [57] and Model Code [58]) is used, representing the yielding of the material. Table 2.9 shows the proposed f_R -values values for all E-UHPFRC mixes and their COV.

Table 2.9: Residual flexural strength

Mix ID	f_{fl} (MPa)	f_{R-I} (MPa) (COV)	f_{R-II} (MPa) (COV)
Plain	6.6 (5%)	-	-
f 2 – CCC	23.8 (6%)	21.8 (7%)	16.2 (7%)
f 2 – CCF	22.4 (13%)	17.4 (15%)	12.9 (12%)
f 2 – CFF	16.0 (8%)	12.1 (10%)	8.0 (12%)
f 2 – FFF	14.0 (7%)	8.8 (15%)	5.0 (19%)
f 3 – CCC	30.0 (5%)	25.6 (10%)	20.1 (16%)
f 3 – CCF	24.9 (8%)	21.6(14%)	15.9 (17%)
f 3 – CFF	22.3 (6%)	17.9 (15%)	11.8 (24%)
f 3 – FFF	18.2 (12%)	12.1 (25%)	6.9 (33%)
f 4 – CCC	42.9 (7%)	41.6 (8%)	33.7 (10%)
f 4 – CCF	35.5 (8%)	33.6 (8%)	27.1 (10%)
f 4 – CFF	31.2 (11%)	27.3 (13%)	19.8 (13%)
f 4 – FFF	26.0 (6%)	21.8 (13%)	14.6 (17%)

For all mixes, f_R -values are lower than f_{fl} . The COV for all the mixes were found to be between 5 – 33% (Table 2.9) which is within the range of values <40% reported in the literature [30,60–62] for FRCs. For the same total fibre volume, mixes containing CCC have lower COV (6 – 16%) compared to mixes containing FFF (5 – 25%). The variation in COV for mixes containing RTSF can be attributed to the higher variability of RTSF fibres in terms of length and surface conditions. Also, f_{R-I} was found to have lower COV (7 – 25%) compared to f_{R3} (7 – 33%). This may be due to fact that the f_{R1} variability is dominated by the matrix, while the f_{R3} variabilities is dominated by the number of fibres crossing the main cracks and their bond characteristics. The relationship between f_{Ri} values for each mix with their corresponding RTSF content for the same fibre dosage is as shown in Figure 2.16.

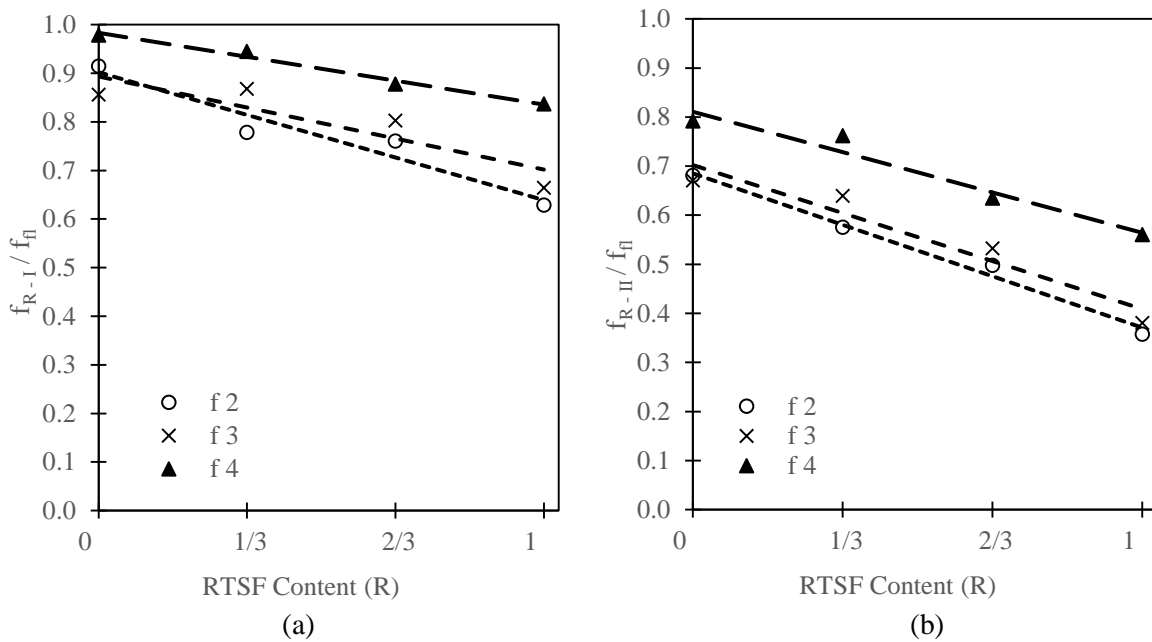


Figure 2.16: Correlation between f_{RIS} , fibre volume and RTSF content (a) f_{R-I} (b) f_{R-II}

It can be seen that both f_{R-I} and f_{R-II} decrease with increasing RTSF content. Mixes containing 4% fibres decrease at the lowest rate, while mixes containing 2% fibres decrease at the highest rate indicating faster loss of post cracking stiffness. This shows that RTSF offers better performance in mixes containing higher fibre dosage. Correlation between f_{RIS} and f_{fl} is very strong with R^2 values above 0.94 as shown in Figure 2.17.

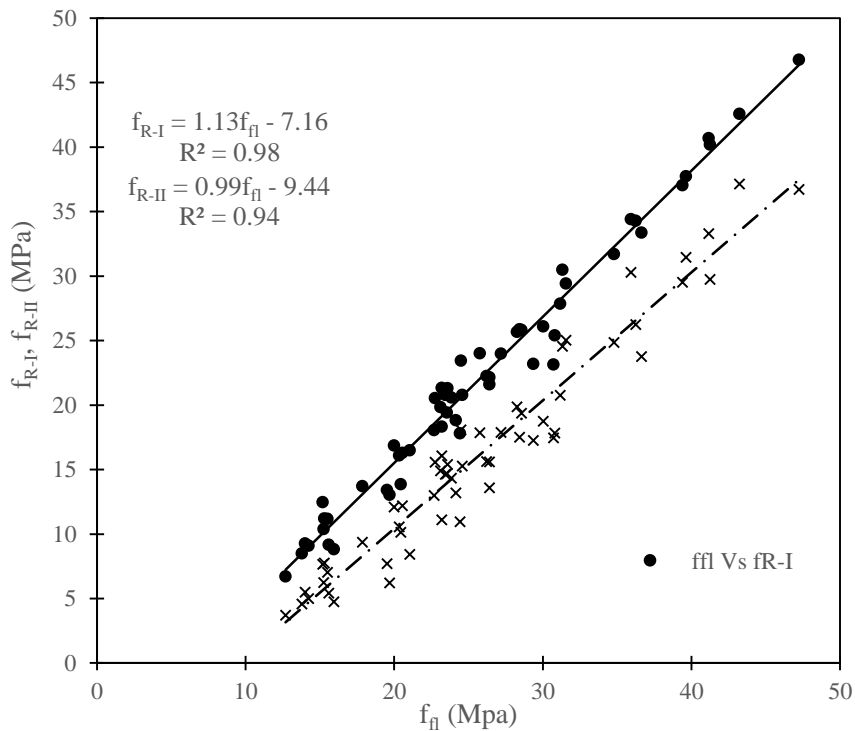


Figure 2.17: Correlation between f_{fl} and f_{RIS}

Utilising the correlation models given in Figures 2.11 and 2.17 a complete prediction of f_{fl} and $f_{Ri}'s$ of E-UHPFRC mixes containing various RTSF/total fibre volume ratio can be obtained, using f_{fl} of mix containing only RTSC (or MSF) as input. The proposed models can be used to estimate the design parameters ($f_{Ri}'s$) required for the design of structural members in bending at serviceability and ultimate limit state without the need to conduct expensive and time consuming material testing.

2.4.6 Relationship between Measured Deflection and CMOD

Only a few studies on the relationship between $\delta - CMOD$ for UHPFRCs are available in the literature (e.g. [64]). BS EN 14651: 2005 [36], based on which the flexural strength test was conducted, adopts the constant linear $\delta - CMOD$ relationship given in Eq. (2 – 11).

$$\delta = 0.85CMOD + 0.04 \quad (2 - 11)$$

Theoretically, the $\delta - CMOD$ in the post cracked phase can be computed based on rigid body kinematics as proposed by RILEM TC 162 [63]. For the prism size used in this study, the relationship is as shown in Eq. (2 – 12) below;

$$\delta = 0.75CMOD \quad (2 - 12)$$

A comparison between the $\delta - CMOD$ relationships of f 2 and f 4 specimens against the prediction models proposed by BS EN 14651 [36] and RILEM TC 162 [63] is shown in Figure 2.18.

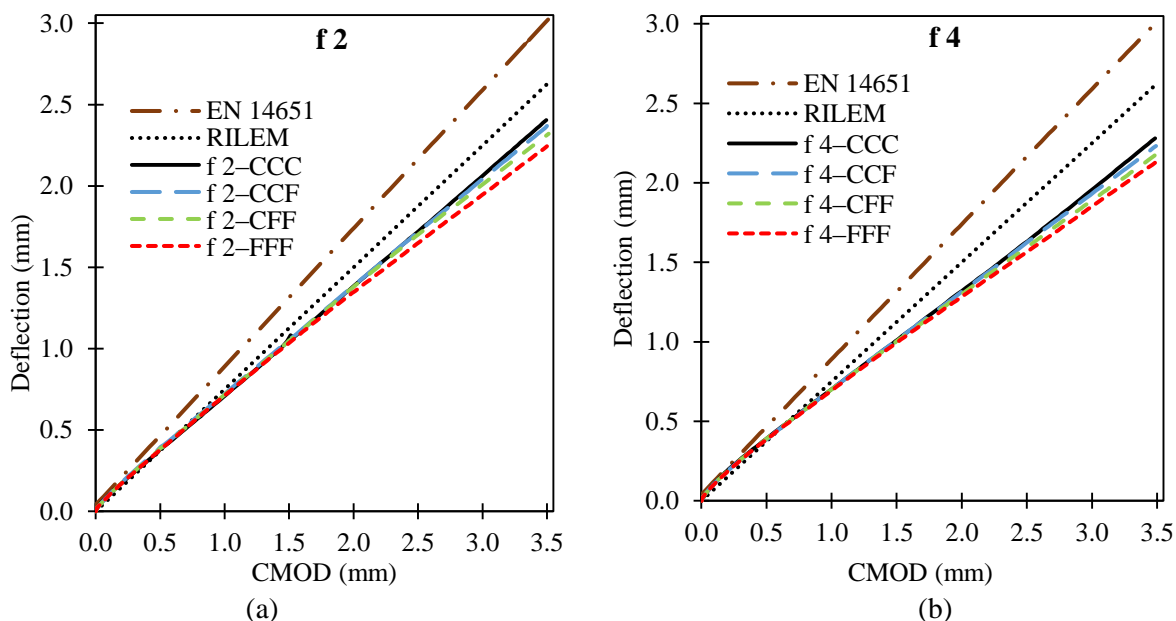


Figure 2.18: Relationship between midspan deflection and measured CMOD

It can be seen that the tested specimens show lower post cracking $\delta - CMOD$ gradient compared to the proposed models, and exhibit some degree of nonlinearity. Thus, the use of a linear $\delta - CMOD$ relationship as employed by the current models does not apply to UHPFRC. This is in agreement with findings by [64,65] for high strength SFRC. The reason for the nonlinear behaviour can be attributed to the high strain hardening capacity of UHPFRC, which leads to the development of multiple small cracks alongside the major crack leading to the formation of a hinge region located at the centre of the prism (Figure 2.19b), rather than a zero length hinge as assumed by RILEM TC 162 [63] (Figure 2.19a).

Understanding the development of the plastic hinge zone is important for flexural members as it affects both their load carrying capacity and deformation. Information regarding length of plastic hinge is useful when designing for ductility, especially in the design of members to resist extreme events such as earthquake [66]. To investigate the development of the hinge and its behaviour, a new $\delta - CMOD$ model is developed based on rigid body kinematics taking into account the formation of a hinge at midspan as shown in Figure 2.19b and Eq. (2 – 13).

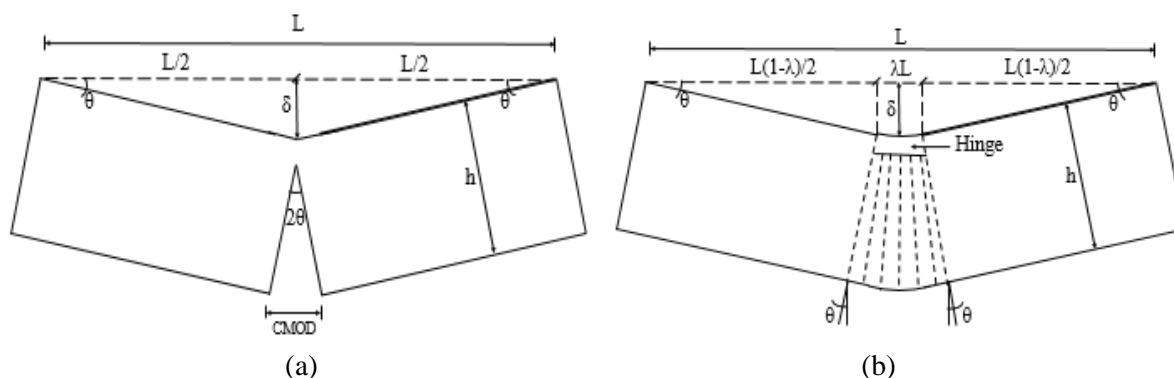


Figure 2.19: Schematic illustration of post cracking behaviour of prisms under 3-point bending for (a) normal FRC (b) UHPFRC

$$\frac{\delta}{CMOD} = \frac{L(1 - \lambda)}{4h} \quad (2 - 13)$$

An inverse analysis method was used to obtain the values of hinge length ratio (λ) from the experimental behaviour $\delta - CMOD$ results. The relationship between λ and hinge length (λL) with CMOD, or applied load were examined and a comparative analysis shown in Figure 2.20.

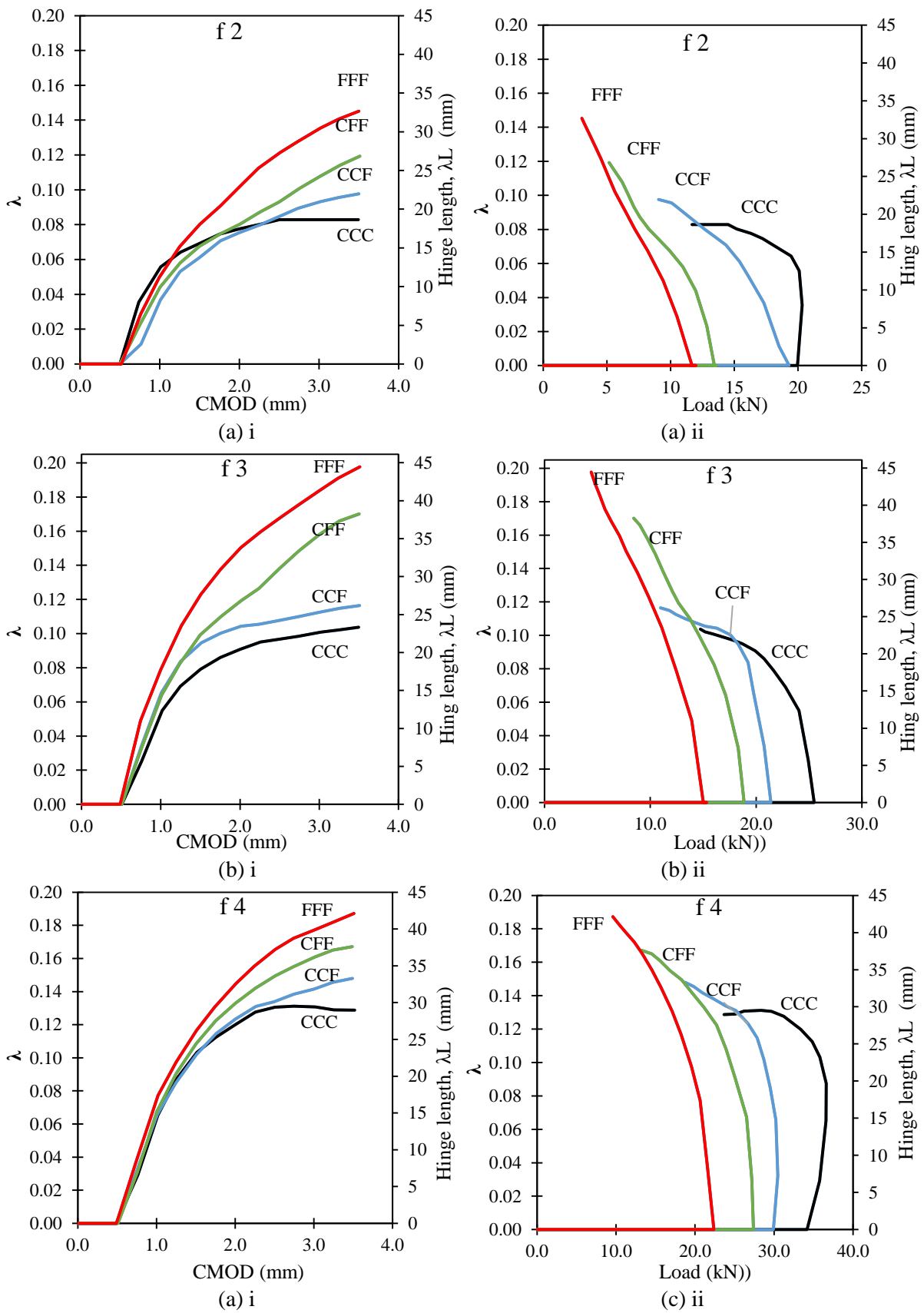


Figure 2.20: Relationship between CMOD, load and hinge length for (a) f 2 (b) f 3 (c) f 4

A nonlinear relationship between λ and CMOD can be seen for all mixes. For values of CMOD smaller than $CMOD_{SLS}$, the values of λ can be considered to be zero. At high CMOD values, λ increase with

increasing fibre dosage for all mix. For example, at $CMOD_{II}$ (2.625mm), λ of CCF mixes equals to 9, 11 and 14% for 2, 3 and 4% fibre dosages, respectively. Similarly, it was found that λ increases with increasing RTSF content, with mixes containing FFF showing the highest λ , which is equal to 8, 11 and 11% at $CMOD_I$ (1.375mm) and 12, 16 and 16% at $CMOD_{II}$ for 2, 3 and 4% fibre dosages, respectively. Mixes containing CCC show the smallest values of λ equal to 6, 8 and 10% at $CMOD_I$ and 9, 10 and 13% at $CMOD_{II}$ for 2, 3 and 4% fibre dosages, respectively. A model for predicting the value of λ at $CMOD_I$ and $CMOD_{II}$ is shown in Eq. (2 – 14) below.

$$\lambda = \rho k(1 + 0.5F) \quad (2 - 14)$$

Where ρ is the fibre volume dosage, F is the RTSF to total fibre volume ratio and k is a constant. $k = 2.24$ at $CMOD_I$, and $k = 3.37$ at $CMOD_{II}$.

A correlation between experimental and predicted values (λ_{model} and $\lambda_{exp.}$, respectively) is shown in Figure 2.21. The model predicting λ at $CMOD_I$ offers slightly higher accuracy (having an average $\lambda_{model}/\lambda_{exp.}$ of 1.0022 and a COV of 11%) than at $CMOD_{II}$ (which has an average $\lambda_{model}/\lambda_{exp.}$ of 1.0013 and a COV of 13%).

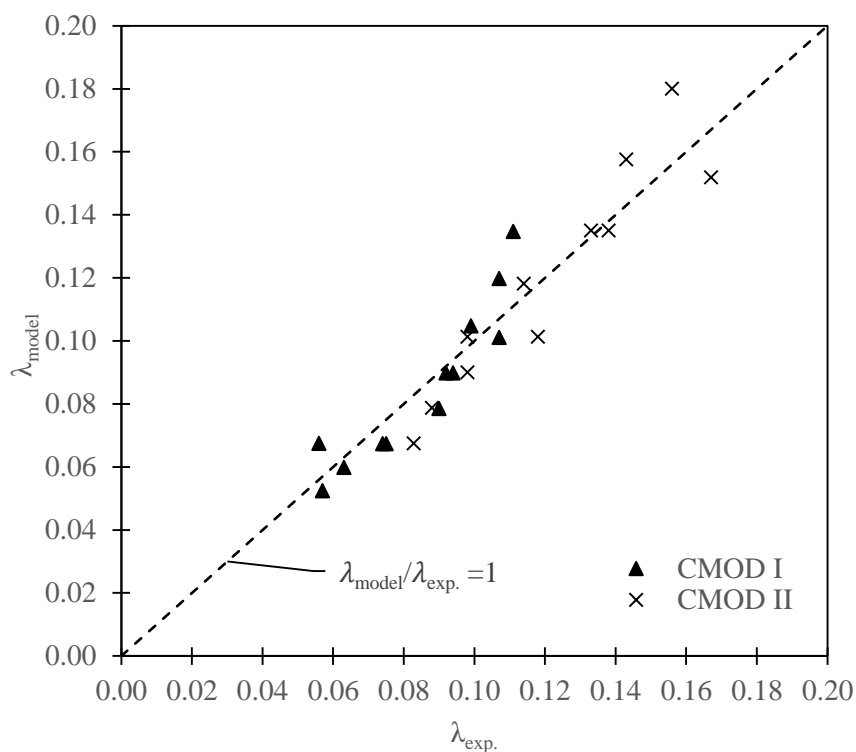


Figure 2.21: Correlation between experimental and model hinge length ratio at Ultimate limit state

A more reliable equation to determine the δ – CMOD relationship of UHPFRC (Eq. (2 – 13)) would lead to better estimates of crack widths, and in turn to better predictions of load carrying capacity and durability of structures at ULS. Similarly, the proposed models in Eq. (2 – 14) will aid designers to estimate the length of hinge regions in UHPFRC members with greater accuracy, thus leading to more refined plastic design models of rigid connections (e.g. in earthquake engineering design).

2.5 Cost and Environmental Impact Analysis

In this section, a comparative study on the efficiency of the examined E-UHPFRC mixes is presented. Table 2.10 gives the cost and environmental impact in terms of GWP of the constituent materials used in this study. The prices relate to supplied quantities of 1 tonne (e.g. 1000L for water and 833L for superplasticizer/accelerators).

Table 2.10: Cost (as at Dec 2019) and environmental impact of constituent materials

Constituent Material	Cost (£/ton)	Environmental footprint	
		GWP (kg CO ₂ /kg)	Source
Cement	170	0.782	[67]
GGBS	50	1.88×10^{-2}	[68]
Silica Fume	600	3.1×10^{-4}	[69]
Natural Sand	180	2.4×10^{-3}	[69]
Ground Quartz	700	2.34×10^{-2}	[70]
Water	1.5	1.5×10^{-4}	[69]
Superplasticizer	3000	0.944	[71]
Accelerators	Same as SP	Same as SP	
RTSC/MSF	3000	2.68	[69]
RTSF	860	0.083	TWINCON Data

2.5.1 Comparison with Ductal UHPFRC mix design

Table 2.11 shows a mix design comparison between the studied E-UHPFRC mixes and commercial UHPFRC mix Ductal (mix proportion reported by [8,55]) containing no fibres, based on the prices of constituent materials as presented in Table 2.10.

Table 2.11: Cost and GWP's of constituent materials

Material	Studied Mix	Ductal
	Quantity (kg/m ³)	Quantity (kg/m ³)
Cement	657	712
Silica Fume	119	231
GGBS	418	-
Natural Sand	1051	1020
Ground Quartz	-	211
Water	185	109
Superplasticizer	59	30
Accelerators	-	30
Cost (£/m³)	570	773
GWP (kg CO₂ /m³)	579	621

It was shown that the studied mix costs 26% less than the Ductal mix. This is attributed to the fact the studied mix I contains high GGBS content as supplementary material which is cheap compared to ground quartz contained in Ductal. Also, the GWP of the studied was found to be 7% lower than the Ductal design, which is as a result of its lower cement content.

2.5.2 Efficiency Comparison

Figure 2.22 shows a comparison in terms of mechanical (M_E), economic (E_C), environmental (E_N) and total efficiency (E) between mixes of the same fibre volume.

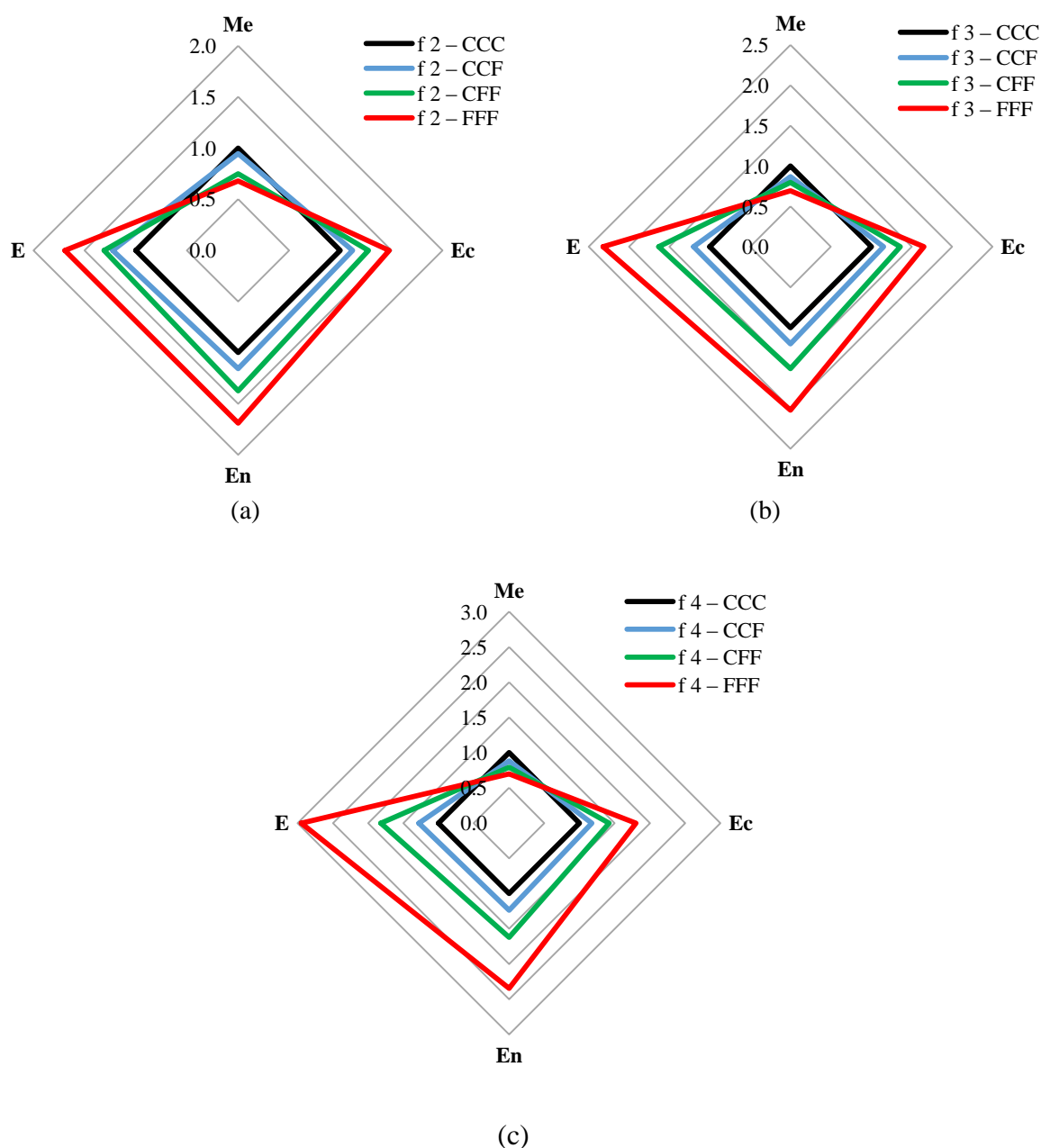


Figure 2.22: Comparison between material efficiencies of E-UHPFRC mixes (a) f 2 (b) f 3 (c) f 4

The mechanical efficiency is in line with the results of workability and flexural strength, with mixes containing CCC (100% MSF) showing the highest M_E . For the same fibre volume, M_E decreases as the RTSF content increases, with mixes containing FFF being 32, 30, and 30% less efficient for fibre volumes of 2, 3 and 4%, respectively. This can be attributed to the fact that RTSF offers relatively lower workability and flexural strength. In terms of economy, E_c increases with increasing RTSF content with mixes containing FFF having 48, 65, and 80% more efficiency than mixes containing CCC for fibre volume of 2, 3 and 4%, respectively. The higher E_c of mixes containing RTSF can be attributed to the

lower cost of RTSF (3.5 times cheaper than CCC/MSF). Similarly, mixes containing FFF show significantly higher E_N than mixes containing CCC, having 69, 102 and 135% more environmental efficiency for fibre volume of 2, 3 and 4%, respectively. This is due to the fact that RTSF is obtained from waste product and the energy consumed during its processing is much lower than the energy consumed in manufacturing MSF. In terms of total efficiency E , it was found that E increases as RTSF content increases. For mixes containing FFF only, the efficiency increases as the fibre volume increases i.e. 69, 132 and 195% more efficiency for 2, 3 and 4% fibre volume respectively compared to their corresponding CCC mixes.

The reduction in M_E of mixes containing RTSF compared to CCC for the same fibre volume can be resolved by using hybrid mixes or a higher dosage of RTSF. For example, a similar or higher M_E than f 2 CCC can be achieved by using f 4 FFF (i.e. 4% RTSF) or hybrid mix (e.g. f 3 CFF) as shown in Figure 2.23.

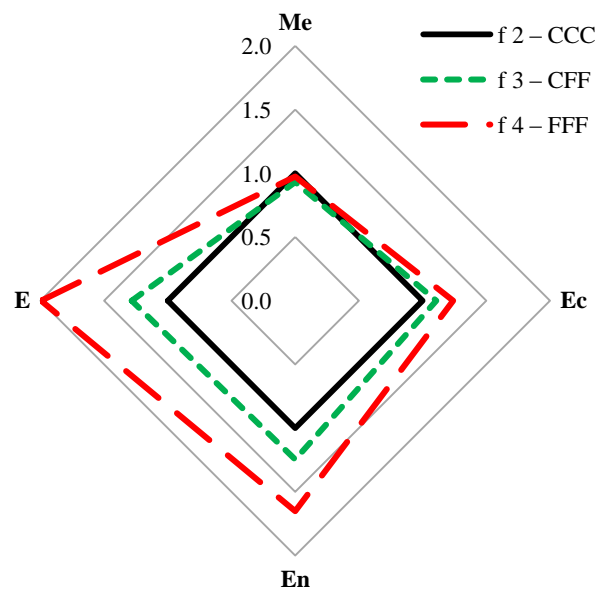


Figure 2.23: Comparison between material efficiencies of mix f 2 – CCC and mixes containing FFF. The analysis shows that the total efficiency of f 4 – FFF is 100% greater than that of f 2 – CCC, while f 2 – CFF is 28% more efficient, with both mixes being more economically viable and environmentally friendly.

2.6 Conclusion

The study investigates the mechanical properties of E-UHPFRC mixes containing two types of recycled fibres (RTSC and RTSF) used individually and in hybrids solutions. Fresh properties, compressive strength and 3-point bending test are used to assess the performance of the designed mixes. The material efficiencies of the mixes are also determined in terms of their mechanical, cost and environmental credentials. Based on the experimental findings, the following conclusions can be drawn:

- For similar fibre dosages and curing regimes to those reported in the literature, mixes containing RTSC offer comparable performance to that of mixes containing manufactured steel fibres (MSF). This can be related to the fact that RTSC share similar properties with MSF in terms of cleanliness, geometry and mechanical strength.
- The performance of mixes containing RTSC is affected by fibre length. Owing to the better anchorage provided by longer fibres, mixes containing RTSC with length of 12 and 15mm show superior strength (11 and 19% more than mixes containing 9 and 6mm long RTSC, respectively) and post cracking stiffness.
- Sustainable UHPFRC mixes can be effectively developed with RTSF fibres, provided the fibres are clean, with little or no impurities. Very short fibres, however, can fail to develop high strength due to insufficient anchorage length, while longer fibres affect workability making the mix susceptible to balling. Improved flexural performance can be achieved when 50% or more of the fibres have lengths within the range of 9-15mm. By cleaning and reducing the percentage of fibres shorter than 9mm from 57.1% to 35.7%, a 48% increase in flexural capacity was achieved.
- For the same fibre dosage, the use of RTSF reduces the workability of mixes (10-13% decrease in flow diameter depending on fibre dosage) and slightly reduces fresh density, compressive strength and modulus of elasticity compared to RTSC.
- For the same fibre dosage, mixes containing RTSF (FFF) have about 40% lower flexural strength than mixes containing RTSC (CCC). To achieve similar strength values, a hybrid or higher dosage of RTSF need to be used.

- The use of new design parameters (f_R -values) is proposed for the design of UHPFRC flexural members at serviceability and ultimate limit states, and analytical predictive models are proposed for these parameters.
- The $\delta - \text{CMOD}$ model proposed by BS EN 14651 [36] and RILEM TC 162 – TDF [63] are not suitable for strain hardening materials like E-UHPFRC. A new model is proposed to predict the hinge length based on fibre types and dosage.
- The use of RTSF in E-UHPFRC offers significant cost and environmental benefits compared to RTSC/MSF. Mixes containing RTSF (FFF) are 48 – 80% more cost efficient than mixes containing RTSC/MSF (CCC), and 69 – 135% more environmentally efficient (depending on fibre dosage). While the use of RTSF only can result in lower mechanical efficiency, the total efficiency of mixes containing RTSF (FFF) is always higher and varies from 69 – 195%, depending on fibre dosage.

Acknowledgement

The first author will like to thank the Petroleum Technology Development Fund (PTDF), Nigeria, for sponsoring his PhD studies. The authors would also like to thank TWINCON Ltd and SIKA Group for supply of materials and related information.

2.7 References

- [1] C. Shi, Z. Wu, J. Xiao, D. Wang, Z. Huang, Z. Fang, A review on ultra-high performance concrete: Part I. Raw materials and mixture design, *Constr. Build. Mater.* 101 (2015) 741–751.
- [2] S. Abbas, A.M. Soliman, M.L. Nehdi, exploring mechanical and durability properties of ultra-high performance concrete incorporating various steel fibre lengths and dosages, *Constr. Build. Mater.* 75 (2015) 429–441.
- [3] A. Alsalman, C.N. Dang, W. Micah Hale, Development of ultra-high performance concrete with locally available materials, *Constr. Build. Mater.* 133 (2017) 135–145.
- [4] B.A. Graybeal, UHPC making strides, *Public Roads.* 72 (2009) 17–21.
- [5] D. Wang, C. Shi, Z. Wu, J. Xiao, Z. Huang, Z. Fang, A review on ultra-high performance concrete: Part II. Hydration, microstructure and properties, *Constr. Build. Mater.* 96 (2015) 368–377.
- [6] I.Y. Hakeem, Characterisation of ultra-high performance concrete, King Fahd University of Petroleum and Minerals, Saudi Arabia, 2011.
- [7] R. Zhong, K. Wille, R. Viegas, Material efficiency in the design of UHPC paste from a life cycle point of view, *Constr. Build. Mater.* 160 (2018) 505–513.
- [8] Federal Highway Administration, Ultra-High Performance Concrete: A State-of-the-Art Report for the Bridge Community, Mclean, VA, 2013.
- [9] B.A. Graybeal, Development of Non-Proprietary Ultra-High Performance Concrete for Use in the Highway Bridge Sector, Mclean, VA, 2013.
- [10] N. Mahasenan, S. Smith, K. Humphreys, The Cement Industry and Global Climate Change Current and Potential Future Cement Industry CO₂ Emissions, in: *Green Gas Control Technol. - 6th Int. Conf.*, Pergamon, 2003: pp. 995–1000.
- [11] M. Kundak, CO₂ Capture in the Steel Industry, 48 (2009) 193–197.
- [12] Y. Dong, Performance assessment and design of ultra-high performance concrete (UHPC) structures incorporating life-cycle cost and environmental impacts, *Constr. Build. Mater.* 167 (2018) 414–425.
- [13] Peter Racky, Cost-effectiveness and sustainability of UHPC, in: *International Symposium on Ultra High Performance Concrete*, Kassel, Germany 2004: pp. 797–805.

- [14] Petr Hájek, Ctislav Fiala, environmentally optimized floor slabs using UHPC-contribution to sustainable building, in: Proceedings of 2nd International Symposium on. Ultra High Performance Concrete, Kassel Germany, 2008: pp. 879–886.
- [15] Le T. Ultra high performance fibre reinforced concrete paving flags. Liverpool, UK: University of Liverpool; 2008.
- [16] H. Yazici, M.Y. Yardimci, H. Yiğiter, S. Aydin, S. Türkel, Mechanical properties of reactive powder concrete containing high volumes of ground granulated blast furnace slag, *Cem. Concr. Compos.* 32 (2010) 639–648.
- [17] C. Wang, C. Yang, F. Liu, C. Wan, X. Pu, Preparation of Ultra-High Performance Concrete with common technology and materials, *Cem. Concr. Compos.* 34 (2012) 538–544.
- [18] H. Hu, P. Papastergiou, H. Angelakopoulos, M. Guadagnini, K. Pilakoutas, Mechanical properties of SFRC using blended Recycled Tyre Steel Cords (RTSC) and Recycled Tyre Steel Fibres (RTSF), *Constr. Build. Mater.* 187 (2018) 553–564.
- [19] ETRA, The European Tyre Recycling Association, (2016). <https://www.etra-eu.org/>.
- [20] K. Neocleous, H. Angelakopoulos, K. Pilakoutas, M. Guadagnini, Fibre-reinforced roller compacted concrete transport pavements, *Proc. Inst. Civ. Eng. Transp.* 164 (2011) 97–109.
- [21] E.U. Council of, Waste Framework Directive. Council Directive 2008/98/EC, 2008. <https://ec.europa.eu/environment/waste/framework/>.
- [22] H. Tlemat, Steel fibres from waste tyres to concrete: testing, modelling and design, PhD, The University of Sheffield, 2004.
- [23] Ângela Gaio Graeff, Long Term Performance of Recycled Steel Fibre Reinforced Concrete for Pavement Applications, PhD, The University of Sheffield, 2011.
- [24] Hang Hu, Mechanical Properties of Blended Steel Fibre Reinforced Concrete Using Manufactured and Recycled Fibres from Tyres, PhD, The University of Sheffield, 2018.
- [25] H. Al-Musawi, F.P. Figueiredo, S.A. Bernal, M. Guadagnini, K. Pilakoutas, Performance of rapid hardening recycled clean steel fibre materials, *Constr. Build. Mater.* 195 (2019) 483–496.

- [26] A.M.T. Hassan, S.W. Jones, G.H. Mahmud, Experimental test methods to determine the uniaxial tensile and compressive behaviour of Ultra High Performance Fibre Reinforced Concrete(UHPFRC), *Constr. Build. Mater.* 37 (2012) 874–882.
- [27] A.P. Lampropoulos, S.A. Paschalis, O.T. Tsioulou, S.E. Dritsos, strengthening of reinforced concrete beams using ultra high performance fibre reinforced concrete (UHPFRC), *Eng. Struct.* (2016).
- [28] O. Tsioulou, A. Lampropoulos, S. Paschalis, Combined Non-Destructive Testing (NDT) method for the evaluation of the mechanical characteristics of Ultra High Performance Fibre Reinforced Concrete (UHPFRC), *Constr. Build. Mater.* 131 (2017) 66–77.
- [29] S. Paschalis, A. Lampropoulos, Fibre content and curing time effect on the tensile characteristics of ultra-high performance fibre reinforced concrete, *Struct. Concr.* 18 (2017) 577–588.
- [30] H. Hu, P. Papastergiou, H. Angelakopoulos, M. Guadagnini, K. Pilakoutas, Mechanical properties of SFRC using blended manufactured and recycled tyre steel fibres, *Constr. Build. Mater.* 163 (2018) 376–389.
- [31] A. Alsaif, L. Koutas, S.A. Bernal, M. Guadagnini, K. Pilakoutas, Mechanical performance of steel fibre reinforced rubberised concrete for flexible concrete pavements, *Constr. Build. Mater.* 172 (2018) 533–543.
- [32] ASTM, Test method for slump of hydraulic cement concrete ASTM 1437, *Am. Soc. Test. Mater.* (2005) 12–15.
- [33] BSI, EN 12350-6: Testing fresh concrete Part 6: Density, BSI 389 Chiswick High Road, London, W4 4AL, UK. (2009).
- [34] BSI, EN 12390-2: Testing hardened concrete, Part 2: Making and curing specimens for strength tests, BSI 389 Chiswick High Road, London W4 4AL, UK. (2009).
- [35] BSI, EN 12390-3: Testing hardened concrete, Part3: Compressive strength of test specimens, BSI 389 Chiswick High Road, London W4 4AL, UK. (2009).
- [36] BS EN 14651, Test method for metallic fibred concrete — Measuring the flexural tensile strength (limit of proportionality (LOP), residual), *Br. Stand. Inst.* 3 (2005) 1–17.

- [37] A. Le Hoang, E. Fehling, Influence of steel fibre content and aspect ratio on the uniaxial tensile and compressive behavior of ultra-high performance concrete, *Constr. Build. Mater.* 153 (2017) 790–806.
- [38] K. Wille, A.E. Naaman, G.J. Parra-Montesinos, Ultra-high performance Concrete with compressive strength exceeding 150 MPa (22 ksi): A simpler way, *ACI Mater. J.* 108 (2011) 46–54.
- [39] Federal Highway Administration, Properties and Behavior of UHPC-Class Materials, FHWA-HRT-18-036, Mclean, VA, 2018.
- [40] H. Angelakopoulos, P. Papastergiou, K. Pilakoutas, Fibrous roller-compacted concrete with recycled materials - Feasibility study, *Mag. Concr. Res.* 67 (2015) 801–811.
- [41] A. Baricevic, D. Bjegovic, M. Skazlic, Hybrid fibre-reinforced concrete with unsorted recycled-tire steel fibres, *J. Mater. Civ. Eng.* 29 (2017).
- [42] M. Mastali, A. Dalvand, A.R. Sattarifard, M. Illikainen, Development of eco-efficient and cost-effective reinforced self-consolidation concretes with hybrid industrial/recycled steel fibres, *Constr. Build. Mater.* 166 (2018) 214–226.
- [43] D. Bjegovic, A. Baricevic, S. Lakusic, D. Damjanovic, I. Duvnjak, Positive interaction of industrial and recycled steel fibres in fibre reinforced concrete, *J. Civ. Eng. Manag.* 19 (2013).
- [44] M. Reda, N. Shrive, J. Gillott, Microstructural investigation of innovative UHPC, *Cem. Concr. Res.* 29 (1999) 323–329.
- [45] M. Schmidt, E. Fehling, R. Bornemann, K. Bunje, T. Teichmann, Ultra-high performance concrete: Perspective for the precast concrete industry, *Betonw. UND Fert.* 69 (2003) 16–29.
- [46] SETRA (Service d'études techniques des routes et autoroutes), AFGC (Association Française de Génie Civil), Ultra High Performance Fibre – Reinforced Concretes- Interim Recommendations,” (Bétons Fibrés à Ultra- Hautes Performacnes – Recommandations Provisoires), France, 2002.
- [47] S. Sritharan, V.H. Perry, B.J. Bristow, Characterizing an ultra-high performance material for bridge applications under extreme loads., in: 3rd Int. Symp. High Perform. Concr. PCI, Orlando, Florida, 2003.

- [48] A.B. Graybeal, Compression Response of a Rapid-Strengthening Ultra-High Performance Concrete Formulation, FHWA-HRT-12-064, Fed. Highw. Adm. (2012).
- [49] H. Krenchel, Fibre reinforcement; theoretical and practical investigations of the elasticity and strength of fibre-reinforced materials, 1964.
- [50] British Standards Institution, Testing hardened concrete - Part 5: Flexural strength of test specimens, BS EN 12390-5 2009.
- [51] M. Shafieifar, M. Farzad, A. Azizinamini, Experimental and numerical study on mechanical properties of Ultra High Performance Concrete (UHPC), *Constr. Build. Mater.* 156 (2017) 402–411.
- [52] H.S. El-Din, H. Mohamed, M.A.E.-H. Khater, S. Ahmed, Effect of Steel Fibers on Behavior of Ultra High Performance Concrete, in: *First Int. Interact. Symp. UHPC*, Des Moines, Iowa, 2016: pp. 1–10.
- [53] S. Abbas, M.L. Nehdi, M.A. Saleem, Ultra-High Performance Concrete: Mechanical Performance, Durability, Sustainability and Implementation Challenges, *Int. J. Concr. Struct. Mater.* 10 (2016) 271–295.
- [54] A. Alsalman, C.N. Dang, G.S. Prinz, W.M. Hale, Evaluation of modulus of elasticity of ultra-high performance concrete, *Constr. Build. Mater.* 153 (2017) 918–928.
- [55] Federal Highway Administration, Material Property Characterization of Ultra-High Performance Concrete, FHWA-HRT-06-103, Washington, DC, 2006.
- [56] W. Zhao, B. Zhu, Theoretical model for the bond–slip relationship between ribbed steel bars and confined concrete, *Struct. Concr.* 19 (2018) 548–558.
- [57] RILEM TC 162-TDF: Test and Design methods for steel fibre reinforced concrete, *Mater. Struct.* 36 (2003) 560–567.
- [58] The International Federation for Structural Concrete (fib), Model Code 2010, *Fib Model Code for Concrete Structures 2010*.
- [59] American Society for Testing and Materials, Standard Test Method for Flexural Toughness and First-Crack Strength of Fiber-Reinforced Concrete (C 1018-97), 04 (1998) 1–8.

- [60] S. Oikonomou-Mpegetis, Behaviour and Design of Steel Fibre Reinforced Concrete Slabs, PhD Thesis, Imperial College London, UK, 2012.
- [61] Z. Zamanzadeh, L. Lourenço, J. Barros, Recycled Steel Fibre Reinforced Concrete failing in bending and in shear, *Constr. Build. Mater.* 85 (2015) 195–207.
- [62] B.I.G. Barr, M.K. Lee, E.J. De Place Hansen, D. Dupont, E. Erdem, S. Schaerlaekens, B. Schnütgen, H. Stang, L. Vandewalle, Round-robin analysis of the RILEM TC 162-TDF beam-bending test: Part 1 - Test method evaluation, *Mater. Struct. Constr.* 36 (2003) 609–620.
- [63] B.I.G. Barr, M.K. Lee, E.J. De Place Hansen, D. Dupont, E. Erdem, S. Schaerlaekens, B. Schnütgen, H. Stang, L. Vandewalle, Round-robin analysis of the RILEM TC 162-TDF beam-bending test: Part 2 - Approximation of δ from the CMOD response, *Mater. Struct. Constr.* 36 (2003) 621–630.
- [64] S. Zhao, D. Lange, W. Sun, Deflection-crack mouth opening displacement relationship for concrete beams with and without fibres, *Mag. Concr. Res.* 67 (2015) 532–540.
- [65] R.K. Navalurkar, C.T.T. Hsu, S.K. Kim, M. Wecharatana, True fracture energy of concrete, *ACI Mater. J.* 96 (1999) 213–225.
- [66] Zhao, X., Wu, Y. F., Leung, A. Y., & Lam, H. F. (2011). Plastic hinge length in reinforced concrete flexural members. *Procedia Engineering*, 14, 1266–1274.
- [67] C. Chen, G. Habert, Y. Bouzidi, A. Jullien, Environmental impact of cement production: detail of the different processes and cement plant variability evaluation, *J. Clean. Prod.* 18 (2010) 478–485.
- [68] C. Chen, G. Habert, Y. Bouzidi, A. Jullien, A. Ventura, LCA allocation procedure used as an incitative method for waste recycling: An application to mineral additions in concrete, *Resour. Conserv. Recycl.* 54 (2010) 1231–1240.
- [69] G. Habert, E. Denarié, A. Šajna, P. Rossi, Lowering the global warming impact of bridge rehabilitations by using Ultra High Performance Fibre Reinforced Concretes, *Cem. Concr. Compos.* 38 (2013) 1–11.

- [70] H.S. Müller, M. Haist, M. Vogel, Assessment of the sustainability potential of concrete and concrete structures considering their environmental impact, performance and lifetime, *Constr. Build. Mater.* 67 (2014) 321–337.
- [71] P. Schießl, T. Stengel, Nachhaltige Kreislaufführung mineralischer Baustoffe." Abteilung Baustoffe, Forschungsbericht der Technischen Universität München, München, 2006.

Chapter 3: Determination of Tensile Characteristics and Design of Eco-Efficient UHPC

M.N. Isa, K. Pilakoutas, M. Guadagnini, H. Angelakopoulos, Determination of Tensile Characteristics and Design of Eco-Efficient UHPC, Structures 32 (2021) 2174-2194.

Author Contribution Statement

M.N. Isa: Conceptualisation, Methodology, Investigation, Formal analysis, Writing - original draft. **Kypros Pilakoutas:** Supervision, Writing - review & editing. **Maurizio Guadagnini:** Supervision, Writing - review & editing.

ABSTRACT

Eco-efficient Ultra-High Performance Fibre Reinforced Concrete (E-UHPFRC) containing Recycled Steel Fibres has been recently developed to reduce the cost and environmental impact of UHPRC in the construction industry. Nevertheless, currently there are no design guidelines for high-performance fibre reinforced materials with hardening post-crack tensile characteristics, such as UHPFRC. The determination of the post-crack tensile characteristics of UHPFRC is also a major challenge experimentally and numerically. In this paper, the notched three-point bending test is used in conjunction with Finite Element (FE) inverse analysis to characterise the tensile properties of E-UHPFRC. To address issues of spurious mesh dependency in smeared crack FE models, the post crack tensile properties are determined using a fracture energy approach. A mesh independent solution is developed by using a characteristic length scaling procedure as a function of finite element size. Based on that, a simple and precise model for predicting the constitutive tensile stress strain ($\sigma - \varepsilon$) law of UHPFRC using simple strength and mix parameters (compressive strength, flexural strength, fracture energy, fibre dosage and recycle steel fibre content) is developed. This model is then used to derive E-UHPFRC specific design guidelines in line with current *fib* Model Code design provisions.

Keywords: Ultra-High Performance Fibre Reinforced Concrete, Recycle Tyre Steel Cords, Recycled Tyre Steel Fibres, Energy absorption, Fracture Energy, Uniaxial Tensile Stress-Strain, Finite Element Inverse Analysis, Model Code 2010.

3.1 Introduction

Owing to its high compressive and flexural strengths, as well as its dense microstructure, Ultra-high Performance Fibre Reinforced Concrete (UHPFRC) can facilitate the development of more durable [1-5] and efficient structural elements with reduced sectional areas and weight [6], such as thin shell and grid structures. However, as a high strength concrete, UHPFRC is more brittle than conventional concrete and fibre reinforcement is generally added to improve its post-crack tensile strength and ductility. Although steel fibres are the most widely used type of fibre reinforcement, various other non-metallic fibres have shown great potential for UHPFRC, including: polymer [7], polyester [8], aramid [9], polypropylene [10-13], basalt [14,15], carbon and glass fibres [16].

Despite its enormous potential, the widespread use of UHPFRC is currently limited by a lack of design guidelines, as well as the high initial cost and high carbon footprint of cement and steel fibres. Recent advancements in the field have led to the development of Eco-efficient Ultra-High Performance Concrete (E-UHPFRC) [1], which uses low-cost and sustainable constituent materials to enhance the environmental credentials of UHPFRC and increase its demand as a primary construction material. E-UHPFRC uses conventional sand, Ground Granulated Blast Furnace Slag (GGBS) to reduce the cement content, and Recycled Tyre Steel Fibres (RTSF) and Recycled Tyre Steel Cords (RTSC) in lieu of conventional Manufactured Steel Fibres (MSF). Both RTSC and RTSF can offer a significant reduction in cost and environmental footprint compared to MSF and other synthetic fibres (the most expensive constituent of UHPFRC) [17]. RTSC are similar to some MSF (made of cords) in geometry and surface conditions as they are obtained directly from ends of reels (used for rubber belt manufacture) or are extracted from unvulcanised rubber belt offcuts from tyre manufacturing [18] and cut to the desired length. RTSF, on the other hand, are extracted from end of life tyres or reinforced vulcanised rubber that are mechanically processed and sorted to obtain a suitable steel fibre (filament) length distribution. As such, RTSF consist of individual fibre filaments of varying length, diameter, curliness, and surface condition, with some filaments having remnant rubber particles attached to their surface. To date, only limited studies have been carried out on the mechanical properties of E-UHPFRC [1] and a more in-depth mechanical characterisation of its performance is required to develop much needed design guidance and support its uptake in practice.

The lack of standard design guidelines means that practical applications of UHPFRCs in general must rely on a costly design by testing approach rather than the implementation of a rational design process [2]. Hence, more research is needed to address this fundamental issue and characterise the mechanical behaviour of UHPFRC. Fracture properties such as flexural strength, energy absorption capacity and fracture energy are important parameters for characterising and numerically modelling the post-cracking response of fibre reinforced concretes (FRC), which is required for design purposes [19]. Numerical modelling has become an indispensable tool in structural engineering as it helps to gain a deeper understanding of material performance and can save time and resources when developing design guidelines and optimising structural elements. In finite element (FE) analysis concrete is commonly modelled using the smeared crack approach, which requires the stress – strain ($\sigma - \varepsilon$) relationship to be known. According to this approach, materials are modelled as a continuum and cracks are assumed to be smeared over a fracture zone, which is typically represented by the width of a finite element. As a result, in strain softening materials the smeared crack approach is mesh sensitive [20-22]. The fracture energy of the material can be used to adjust the softening modulus of the ($\sigma - \varepsilon$) relationship so that the correct fracture energy is dissipated irrespective of element size, thus removing mesh dependency. As the fracture properties of UHPFRC are influenced by fibre characteristics, such as aspect ratio, surface condition and fibre shape as well as volume fraction [23-25], the fracture properties of E-UHPFRC containing different fibre types and distribution need to be determined experimentally.

The experimental determination of the tensile properties of UHPFRC, however, is also a major challenge as there is currently no agreement on the type of test setup and specimen geometry that is best suited for determining its uniaxial tensile behaviour. Direct tensile tests, which are supposed to provide directly the tensile behaviour, are adopted by some researchers [26-31]. However, the reliability of data obtained from direct tensile tests on concrete composites is low, because their accuracy relies on the ability to eliminate any off axis bending by accurate alignment of the central axis of the specimen with the axis of thrust of the machine. In addition, specimen geometry imperfections and the non-uniform composition of cement composites result in variable stiffness and strength along and across the specimen, and with additional stress concentrations at boundaries, it means that bending in these specimens is practically inevitable [32-37]. Furthermore, conversion of measured stress–crack width ($\sigma - w$) into stress–strain ($\sigma - \varepsilon$), which is used

in most design guidelines, is also challenging. These complexities have led many researchers to adopt bending tests, which are easier to conduct and yield less variable results, in conjunction with inverse analysis to determine the tensile characteristics [32,33,38]. However, a standardised bending test is not yet universally accepted and the merits of different test set-ups are still being debated [32,33], with different researchers using either three- or four-point bending tests on notched or unnotched prisms.

Among the available design codes, only Model Code 2010 (MC10) [39] proposes a uniaxial tensile stress–strain ($\sigma - \varepsilon$) constitutive model for strain hardening FRCs. The model is based on a bilinear post-crack $\sigma - \varepsilon$ relationship derived from load and CMOD values from a three-point bending test on notched prisms [40]. As this model is proposed for strain hardening FRCs in general and not UHPFRC specifically, the suitability of this model for determining the tensile stress–strain ($\sigma - \varepsilon$) of UHPFRC needs to be ascertained.

The objective of this paper is to investigate the fracture properties of E-UHPFRC containing RTSC and RTSF and utilise fracture parameters to develop design oriented stress–strain ($\sigma - \varepsilon$) models through the implementation of mesh independent inverse FE analyses. The paper summarises the parametric experimental work and discusses the methodology used to derive the basic mechanical properties of the examined E-UHPFRC mixes based on data obtained from three-point bending tests. A design oriented model that can fully describe the constitutive tensile stress–strain ($\sigma - \varepsilon$) law of E-UHPFRC based on simple strength and mix parameters is then presented. Finally, the suitability of the proposed model to capture the behaviour of UHPFRC is evaluated and its performance is compared to that of the MC10 model.

3.2 Experimental Program

3.2.1 Materials and Mix Proportions

A total of 12 fibre reinforced E-UHPFRC mixes were tested for this parametric study along with one plain reference mix (full details can be found in [1]). Fibre dosages of 2, 3 and 4% by volume were used in the different mixes, corresponding to 157, 235.5 and 314 kg/m³, respectively. For each fibre dosage, four fibre ratios of RTSF to total fibre content were prepared: 0, 1/3, 2/3 and 1. A nomenclature based on fibre dosage and fibre type content (RTSC = C and RTSF = F) is adopted to identify the mixes, e.g. f 2 – CCF, where the first item f 2 stands for total fibre dosage of 2% and CCF indicates the use of 2/3 RTSC and 1/3 RTSF,

similarly f 4 – FFF indicates a mix containing 4% total fibre volume and 100% RTSF. The exact fibre amounts for each mix are shown in Table 3.1.

Table 3.1: Mix description and fibre proportions (kg/m³)

Mix ID/Fibre type content	Plain	f2 – CCC	f2 – CCF	f2 – CFF	f2 – FFF	f3 – CCC	f3 – CCF	f3 – CFF	f3 – FFF	f4 – CCC	f4 – CCF	f4 – CFF	f4 – FFF
RTSC	0	157	104.7	52.3	0	235.5	157	78.5	0	314	209.3	104.7	0
RTSF	0	0	52.3	104.7	157	0	78.5	157	235.5	0	104.7	209.3	314

The constituent materials per cubic meter were: 657 kg of 52.5N type I OPC, 119 kg of microsilica with approximate particles size of 0.15 μ m, 418 kg of GGBS with approximate particle size of 15 μ m, 59 kg of polycarboxylate superplasticizer and 1051 kg of natural silica sand (HST 95) with particle size less than 500 μ m. The RTSC used in this study have a nominal diameter of 0.22 mm and a direct tensile strength of approximately 2,500 MPa [1,18]. A combination of 12 and 15 mm long RTSC was used (Figure 3.1) in a 50:50 ratio as these fibre lengths were shown to result in optimum performance for UHPFRC [1]. RTSF free from impurities were obtained by cleaning and sorting factory supplied RTSF and comprised fibres of lengths ranging from 3 to 30 mm, with an average length of 11.6 mm. The distribution and statistical properties of the RTSF are shown in Figure 3.2 and Table 3.2.

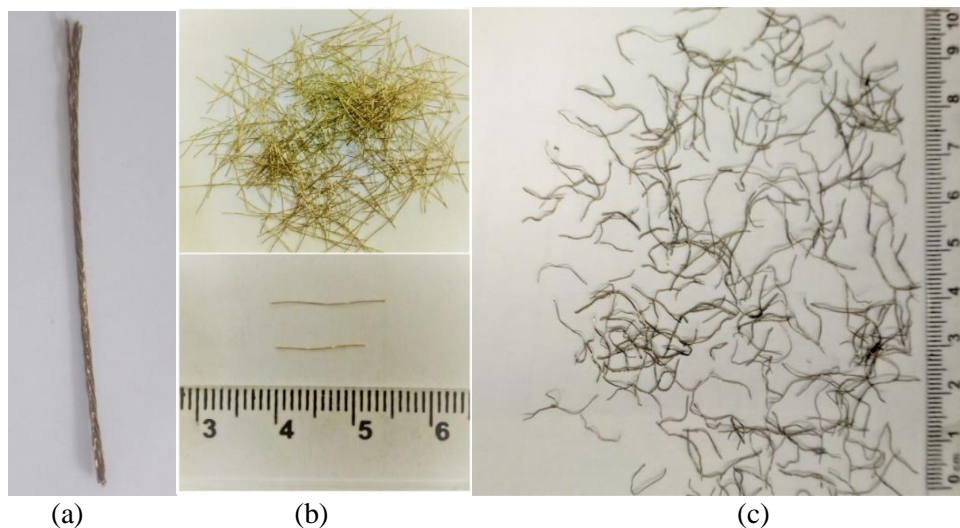


Figure 3.1: (a) Tyre steel cords (b) RTSC (c) RTSF

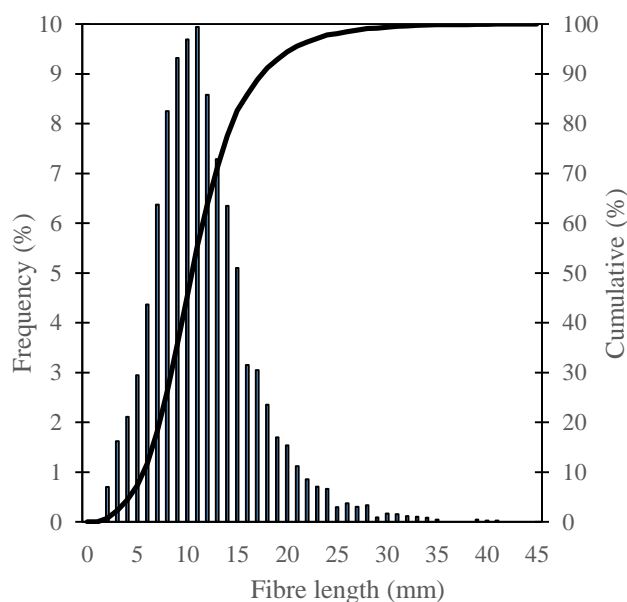


Figure 3.2: RTSF length distribution RTSF

Table 3.2: RTSF length distribution and statistical properties

Property	< 9 mm	9 – 15 mm	>15 mm	Mean (mm)	STDEV (mm)	Variance	Kurtosis	Skewness
	35.7%	47%	17.3%	11.6	5.1	25.8	2.5	1.1

3.2.2 Mixing, Specimen Casting and Curing

Specimen preparation and curing were carried out in accordance with BS EN 12390-2:2009 [41]. The constituent materials were mixed in a pan type concrete mixer until the mix attained a self-flowing state (approximately 12 – 15 minutes). Steel fibres were then added slowly and mixing continued for two additional minutes to ensure that the fibres were well dispersed. Three 100×200 mm cylinders and five 75×75×285 mm prisms were cast for each mix. Immediately after casting, the specimens were covered with polythene sheets to prevent moisture loss. The specimens were de-moulded after 24hrs and placed inside a curing tank at a water temperature of $20\pm 2^{\circ}\text{C}$ for an additional 27 days.

3.2.3 Compressive Strength and Modulus of Elasticity

The compressive strength and modulus of elasticity of the mixes were obtained in accordance with BS EN 12390-3: 2009 [42] and BS EN 12390-13: 2013 [43], respectively, from tests on 100 × 200 mm cylinders in a servo hydraulic universal testing machine. The axial deformation was measured using a device

consisting of two metal rings, fixed to the cylinders by spring loaded pins at a gauge length of 100 mm and equipped with three equally spaced laser displacement sensors (Figure 3.3).



Figure 3.3: Measuring device for axial deformation

3.2.4 Three Point Bending Test

The flexural behaviour of the examined mixes was determined by conducting three-point bending tests on $75 \times 75 \times 285$ mm prisms, in accordance with EN 14651: 2005 [40]. A specially designed aluminium yoke equipped with two Linear Variable Differential Transducers (LVDT), one on each side of the specimen, was used to measure relative midspan deflections. A clip gauge was installed across the notch to measure the crack mouth opening displacement (CMOD) (see Figure 3.4 and 3.5). The tests were carried out in an electromagnetic universal testing machine with a capacity of 300kN and using a CMOD control rate of 0.05 mm/min for CMOD from 0 to 0.1 mm, and 0.2 mm/min thereafter.

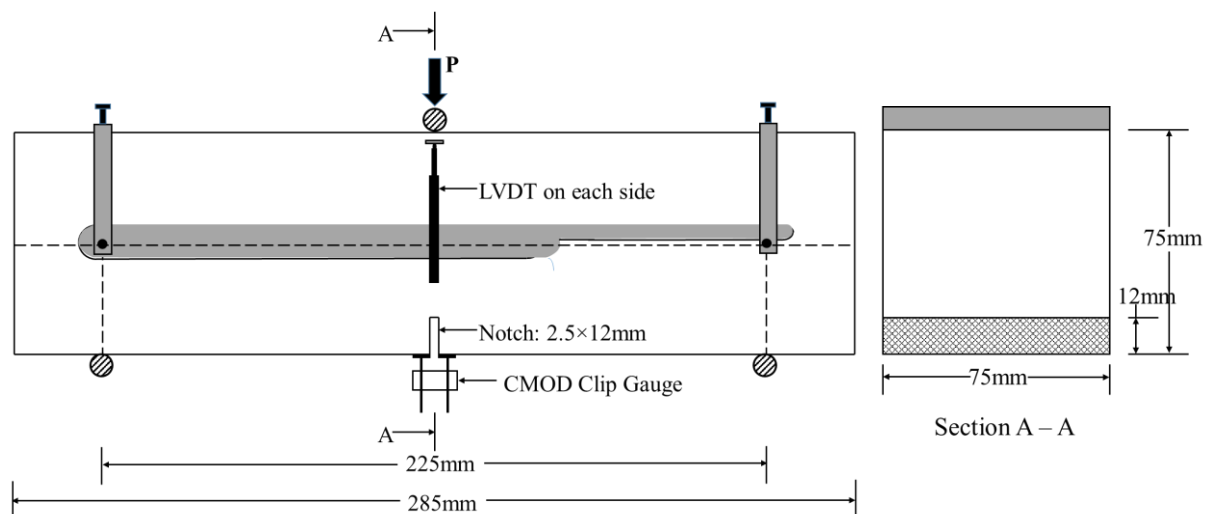


Figure 3.4: Set-up for the three-point bending test

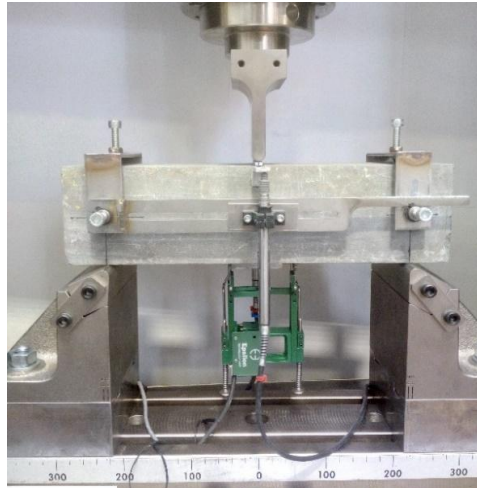


Figure 3.5: View of flexural test

3.3 Calculation of Fracture Parameters

3.3.1 Flexural strength

The parameters that define flexural behaviour at various levels of the fracture process are shown in Figure 3.6.

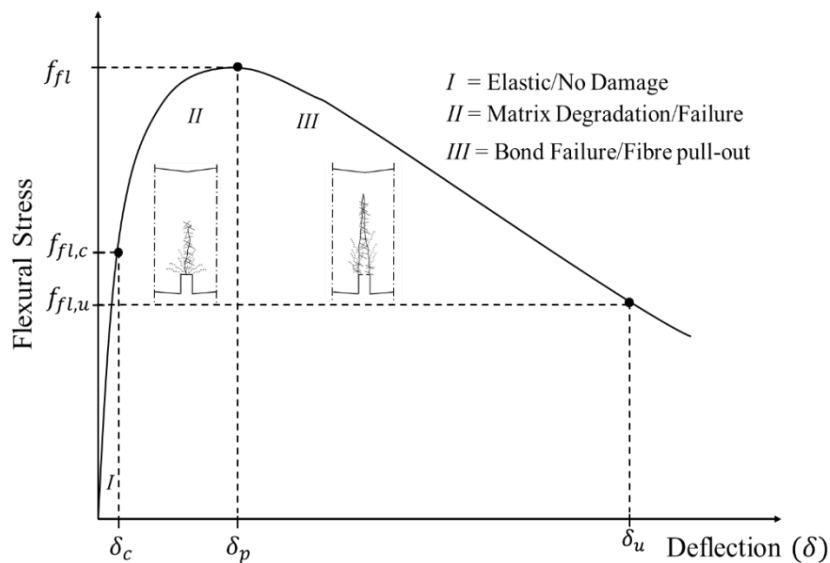


Figure 3.6: Idealised flexural behaviour of E-UHPFRC mixes

The strength parameters $f_{fl,i}$ for a three-point bending configuration is calculated using Eq. (3 – 1).

$$f_{fl,i} = \frac{3P_i l}{2bh_{sp}^2} \quad (3 - 1)$$

Where; P_i = applied load (N), l = span length (mm), b = width of the specimen (mm), $h_{sp} = h - a_o$, h is the depth of the unnotched cross section and a_o is the depth of the notch, and i is the fracture level.

The cracking flexural strength ($f_{fl,c}$) is calculated using the load (P_c) causing a deflection or CMOD of 0.016 mm. This corresponds approximately to the deflection or CMOD of the plain mix at cracking. f_{fl} is calculated in accordance with BS EN 12390-5 [44], using the peak load (P_p). As there are no standard provisions for selecting ultimate deflection values, in this study the “ultimate” flexural strength ($f_{fl,u}$) is determined using the load P_u corresponding to an ultimate deflection δ_u of 2.5 mm.

3.3.2 Energy Absorption

The energy absorption representing the external work done by the applied load (Eq. (3 – 2)) is calculated using the area under the load – deflection ($P - \delta$) curve. For strain hardening materials like E-UHPFRC, this consists of three components (Figure 3.7): (i) recoverable elastic energy (g_e) - up to δ_c ; (ii) energy absorption during deflection–hardening (g_h) - from δ_c to δ_p ; and energy absorption during deflection–softening (g_s) - from δ_p to δ_u .

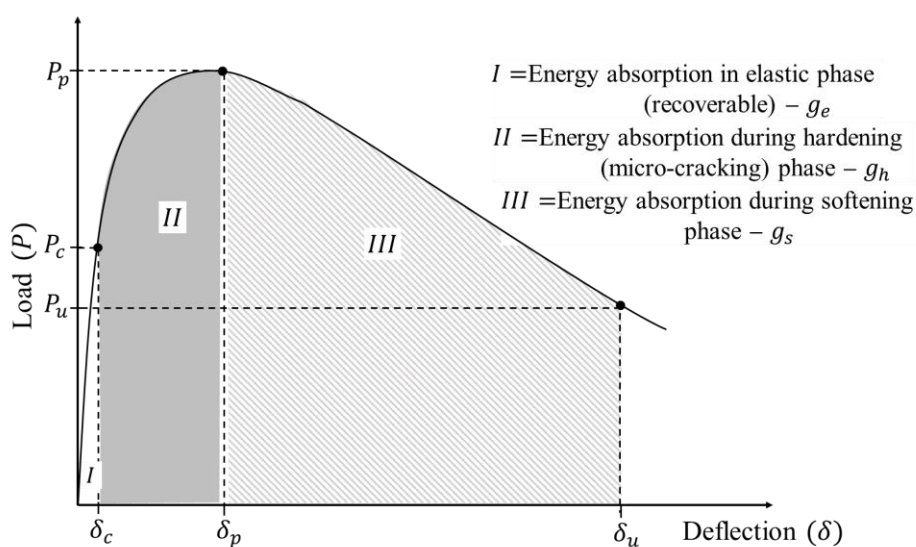


Figure 3.7: Energy absorption

$$g_i = \int_0^{\delta_i} P(\delta) d\delta \quad (2)$$

3.3.3 Fracture Energy

Fracture energy (G_F) is defined as the amount of energy per unit area required to open a crack. The method developed by Hillerborg [45] and adopted by RILEM TC 50-FMC [46] expresses fracture energy as the area under the $P - \delta$ curve of the notched prism divided by the area of the notched cross section (A_F), as shown in Eq. (3 – 3).

$$G_F = \frac{\int_{\delta_c}^{\delta_u} P(\delta) d\delta}{A_F} = \frac{g_h + g_s}{bh_{sp}} \quad (3-3)$$

3.4 Tensile Stress Strain Characteristics

A linearized uniaxial tensile stress – strain curve versus crack width of UHPFRC is shown in Figure 3.8 [33,47]. The behaviour is divided into three phases: (I) a linear elastic $\sigma - \varepsilon$ response up to cracking; (II) an inelastic strain hardening phase characterised by micro-cracking; and (III) a crack opening softening phase.

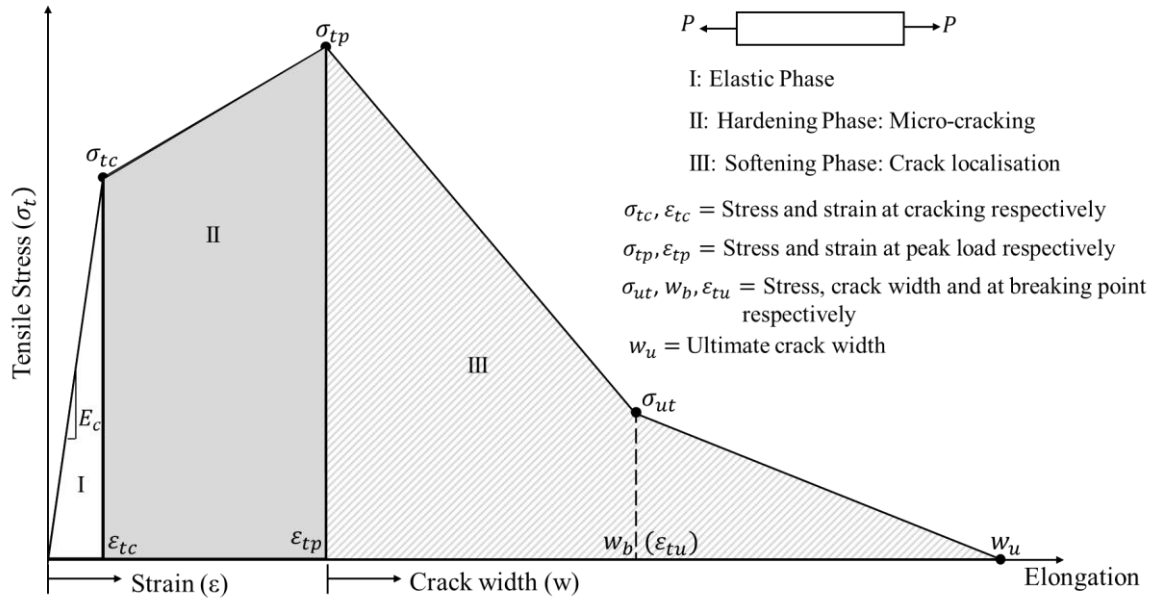


Figure 3.8: Idealised uniaxial tensile stress – strain behaviour of UHPFRC

The softening phase is typically represented by a bilinear $\sigma - \varepsilon$ relationship with a change in slope at a crack width of w_b often referred to as the breaking point.

3.4.1 Model Code 2010 Uniaxial Tensile Model for Strain Hardening FRCs

Model Code 2010 (MC10) [39] proposes the use of a uniaxial tensile constitutive model for strain hardening FRC based on *load – CMOD* data obtained from three point bending tests of notched prisms and uses a “suitable” characteristic length (l_{ch}) to convert CMOD to strain. For simplicity, the model characterises the tensile behaviour using the bilinear post-crack curve shown in Figure 3.8. The model parameters are determined using Eq. (3-4) – (3-7).

$$\sigma_{tc} = 0.9f_{Fts} = 0.405f_{R1}, \quad \varepsilon_{tc} = \frac{\sigma_{tc}}{E} \quad (3-4)$$

$$\sigma_{tp} = f_{Fts} = 0.45f_{R1}, \quad \varepsilon_{tp} = \frac{CMOD_1}{l_{ch}} \quad (3-5)$$

$$\sigma_{tu} = f_{Ftu} = f_{Fts} - \frac{w_u}{CMOD_3} (f_{Fts} - 0.5f_{R3} + 0.2f_{R1}) \geq 0, \quad (3-6)$$

$$\varepsilon_{tu} = \frac{w_u}{l_{ch}} = \min\{2\%, 2.5/l_{cs}\}$$

$$l_{ch} = \min\{s_{rm}, y\} \quad (3-7)$$

Where:

f_{Fts}, f_{Ftu} = Reference values based on serviceability and ultimate behaviour respectively.

f_{R1}, f_{R3} = Residual flexural strengths corresponding to $CMOD_1$ and $CMOD_3$ respectively.

$CMOD_1, CMOD_3$ = Crack mouth opening displacement corresponding to 0.5 and 2.5 mm respectively.

w_u = Maximum crack opening accepted in design.

s_{rm} = Average crack spacing.

y = Distance between neutral axis (N.A.) and tensile side of cross section evaluated in the elastic cracked phase.

The model parameters (f_{R1} and f_{R3}) are measured at $CMOD_1$ and $CMOD_3$ values of 0.5 and 2.5 mm, respectively, for standard prisms of dimensions 150×150×500 mm. As the specimen size and notch dimensions used in the current study are scaled down by 50%, the same scale factor was applied to define the $CMOD$ values used in this analysis.

3.4.2 FE Inverse Analysis

FE inverse analyses were carried out using the FE analysis software ABAQUS to determine the uniaxial $\sigma - \varepsilon$ behaviour of the studied mixes from flexural tests. The Concrete Damage Plasticity model (CDP) [21] developed by [20] adopts the smeared cracking approach. It was used to model the nonlinear behaviour of UHPFRC as it allows the definition of the strain-hardening and softening behaviour of cracked concrete in as many stages as needed. This model has been used successfully to model the behaviour of UHPFRC in various studies [48-52]. This method is suitable for the analysis of flexure dominated slab and beam elements. The inverse analysis procedure involves changing the tensile stress-strain characteristics incrementally, until a stress-strain relationship is found that predicts the experimental load deflection behaviour within certain limits of accuracy.

3.5 Experimental Results and Discussion

3.5.1 Compressive Strength and Modulus of Elasticity

The compressive strength (f'_c) and modulus (E_c) of elasticity of the tested mixes, normalised to the respective values of the plain reference mix, are shown in Figure 3.9.

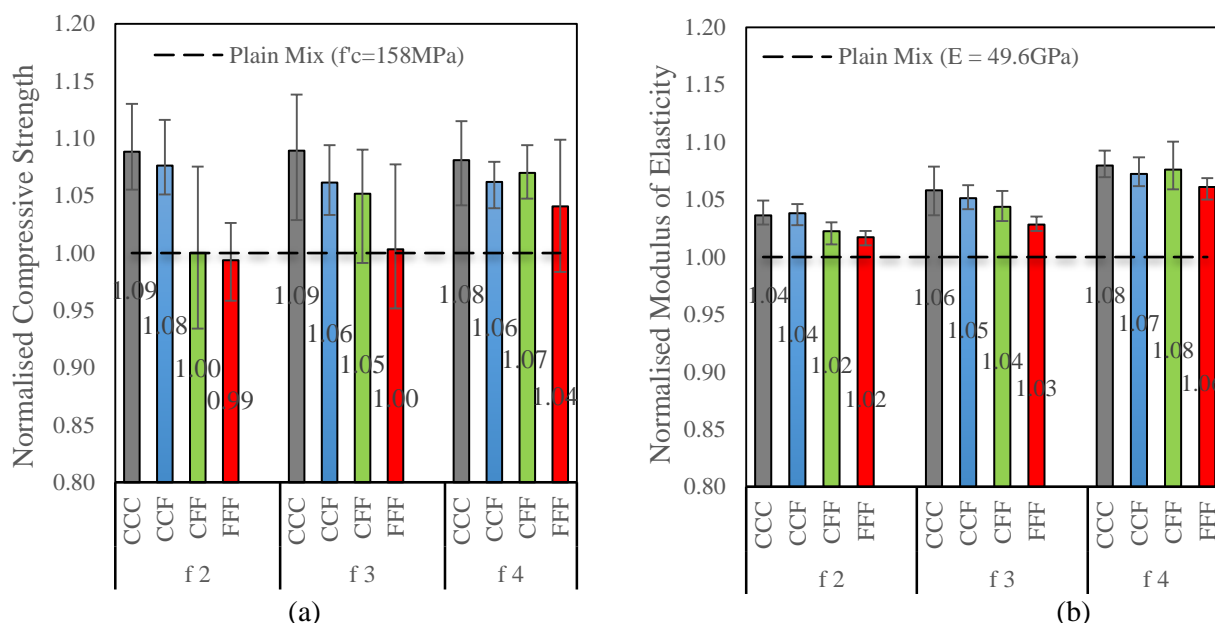


Figure 3.9: (a) Compressive Strength and (b) Modulus of Elasticity of E-UHPFRC mixes normalised with respect to the plain reference mix

The plain mix achieved an average compressive strength of 158 MPa, thus satisfying the strength requirement of UHPC. Overall, an increase in strength was observed for all fibre reinforced mixes with the only exception of f 2 – FFF, which developed an average strength 1% lower than that of the reference mix. Mixes containing RTSC (CCC) show the highest relative increase in average strength, about 10%, while mixes containing RTSF show a maximum average increase of only 4%. The lower strength of mixes containing RTSF can be attributed to the non-uniform characteristics of RTSF, the presence of entrapped air along the surface of the fibres, as well as the presence of remnant rubber particles attached to some fibres [1,53,54]. Compared to the negligible variation in the plain mix strength (COV of 1%), the strength of the FRC mixes was affected by a relatively high variability. Mixes containing higher RTSF content show the highest variation.

The modulus of elasticity E_c was found to increase slightly with an increase in fibre dosage, as anticipated by the rule of mixtures. Mixes containing RTSC show the highest increase in E_c (8% in f 4 – CCC). For the same fibre dosage, there is a small reduction in E_c (less than 3%) for RTSF mixes compared to RTSC mixes. The prediction model proposed by [55] and given in Eq. (3 – 8) can predict the modulus of elasticity of the studied mixes with high accuracy having an average prediction/actual ratio of 0.99 and a standard deviation of 0.01.

$$E_c = 4069 (f'_c)^{1/2} \quad (\text{MPa}) \quad (3-8)$$

3.5.2 Flexural Behaviour and characteristics

The load – deflection behaviour of the E-UHPFRC specimens is shown in Figure 3.10.

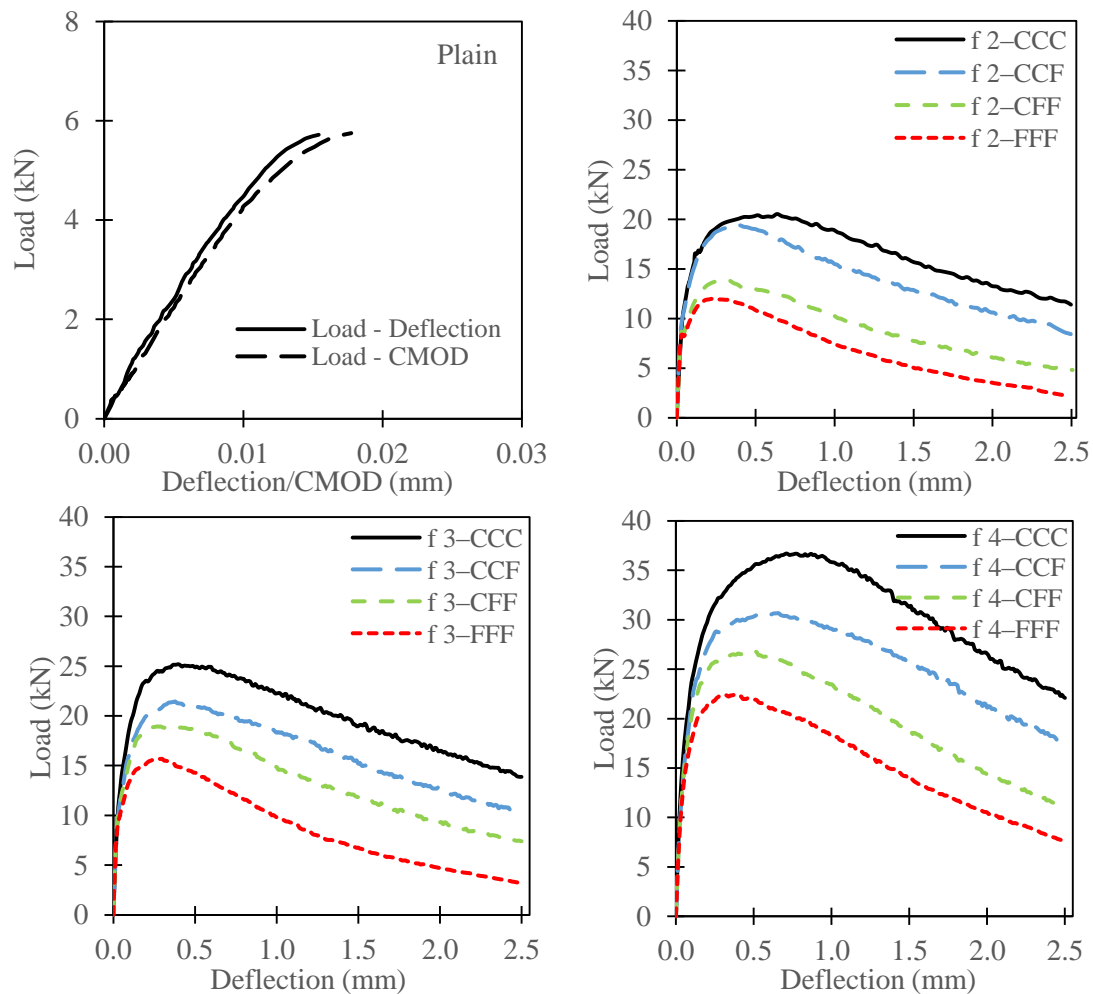


Figure 3.10: Load-deflection behaviour of E-UHPFRC mixes [1]

3.5.3 Flexural Parameters

The values of the flexural strength parameters that characterise the behaviour of the mixes at serviceability ($f_{fl,c}$) and ultimate limit state (f_{fl} and $f_{fl,u}$) are presented in Figure 3.11 . It can be observed that these strength parameters increase with increasing total fibre dosage. The values of all strength parameters ($f_{fl,c}$, f_{fl} and $f_{fl,u}$) for the fibre reinforced mixes are generally higher than the f_{fl} of the plain mix, with the exception of $f_{fl,c}$ and $f_{fl,u}$ of f 2 – CFF, f 2 – FFF and f 3 – FFF. For the same fibre dosage, the strength parameters decrease with an increase in RTSF content.

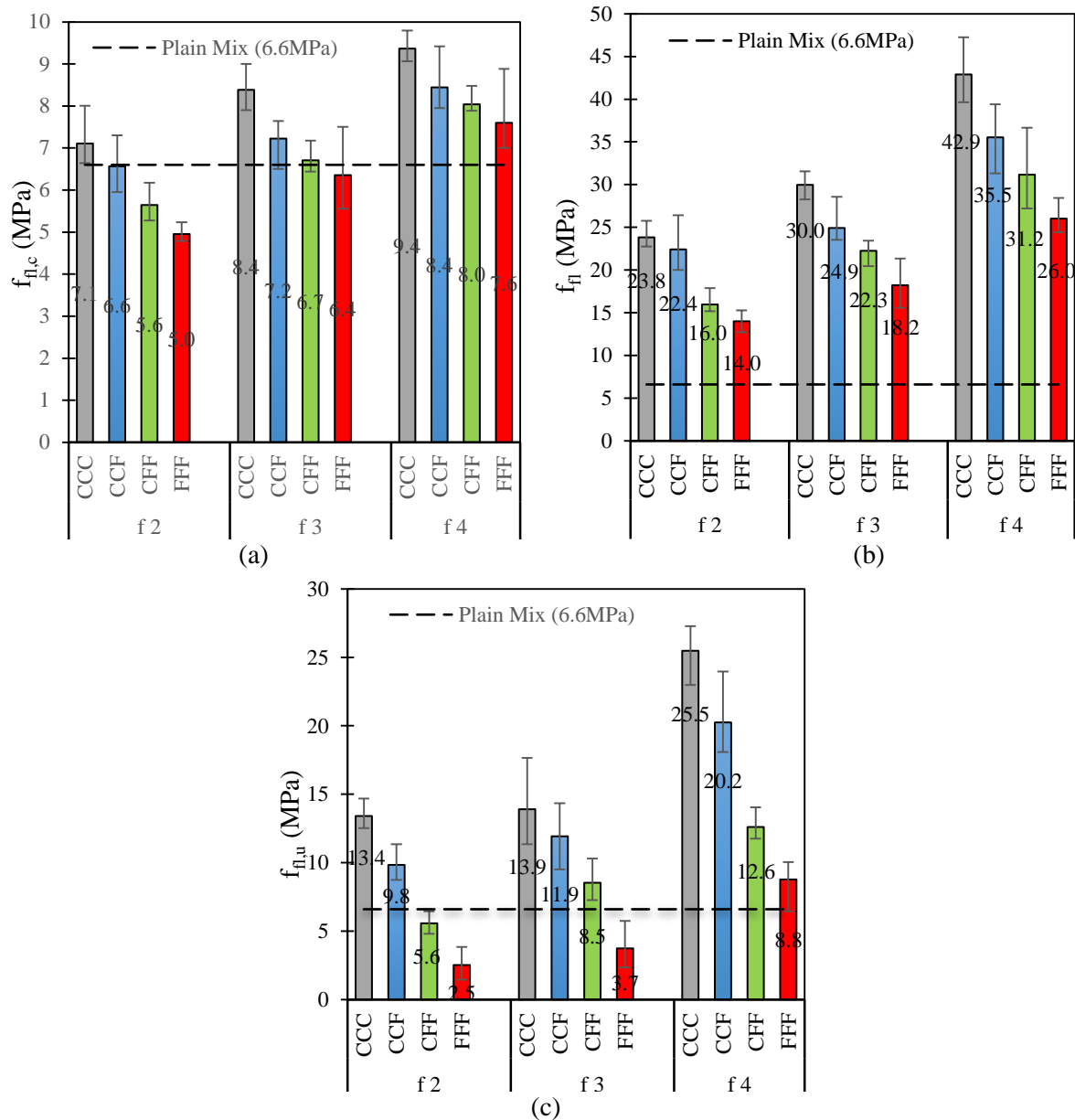


Figure 3. 11: Flexural strength parameters

The lower strength of the RTSF mixes can be attributed to the relatively high amount of short fibres (35.7% with length less than 9 mm) and residual rubber particles. Short fibres do not anchor well across cracks and as such tend to pull out at lower stress levels leading to an overall reduction in strength [1]. Likewise, residual rubber particles reduce the bond stiffness along the fibre – matrix interface, thus causing an overall reduction in fibre contribution to strength. However, desirable high strength capacities can still be achieved using higher RTSF dosages or hybrid mixes. The variation in flexural strength between specimens of the same mix is like that observed in terms of compressive strength. From the three strength parameters, the

lowest variation is observed in $f_{fl,c}$ (COV 3 – 12%) while the highest variation is observed in $f_{fl,u}$ (COV 7 – 33%). The variation in f_{fl} was also low (COV 5 – 12%).

An equation derived by fitting the experimental data is presented in Eq. (3 – 9) to predict the flexural strength (f_{fl}) of the studied E-UHPFRC mixes as a function of fibre dosage (ρ) and ratio of RTSF to total fibre content (F).

$$f_{fl} = 1100\rho \left(1 - \frac{F}{2.3}\right) \quad (3 - 9)$$

As shown in Figure 3.12, the proposed equation provides a strong correlation between predicted strength ($f_{fl-model}$) and experimental strength (f_{fl}) values, with an average of their ratios ($f_{fl-model}/f_{fl-Exp.}$) close to unity (1.01) and a low standard deviation (0.11).

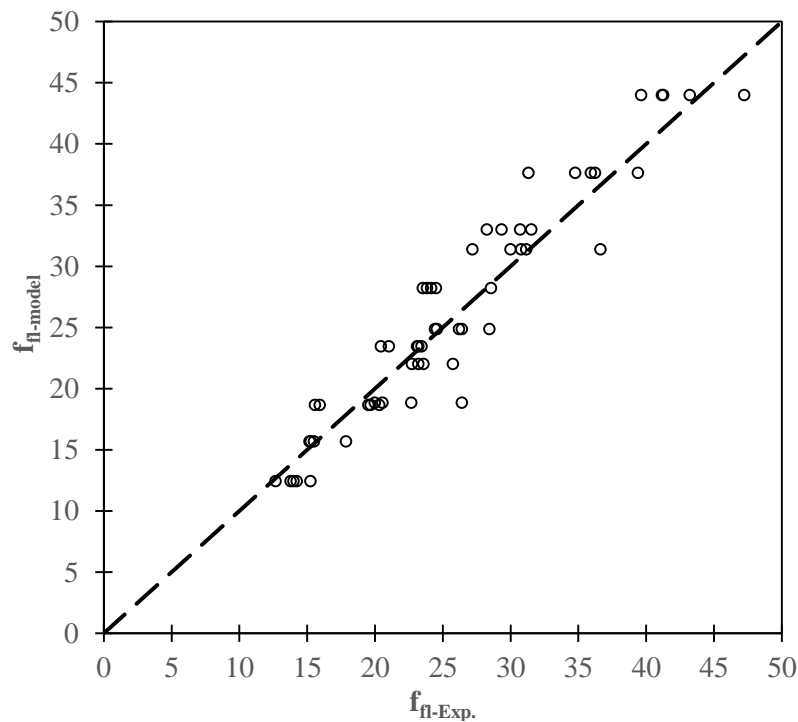


Figure 3.12: Correlation between predicted and experimental flexural strength

3.5.4 Energy Absorption

The energy absorption for all the examined mixes is evaluated based on Eq. (3 – 3) and the results are presented in Table 3.3. It can be seen that the addition of steel fibres increases the energy absorption of E-UHPFRC.

Table 3.3: Energy absorption of specimens manufactured with different E-UHPFRC mixes

Mix/ Energy (N.mm×10 ³)	Plain	f 2 – CCC	f 2 – CCF	f 2 – CFF	f 2 – FFF	f 3 – CCC	f 3 – CCF	f 3 – CFF	f 3 – FFF	f 4 – CCC	f 4 – CCF	f 4 – CFF	f 4 – FFF
g_e	0.1	0.4	0.4	0.3	0.2	0.4	0.3	0.3	0.2	0.3	0.3	0.3	0.3
g_h	–	11.6	9.6	3.9	2.4	12.1	9.7	6.1	3.6	24.2	16.8	11.1	6.7
g_s	–	28.8	25.6	18.8	14.0	38.8	33.3	25.7	17.9	51.2	47.9	38.8	31.2
g_F	0.1	40.8	35.6	23.0	16.6	50.3	41.3	33.1	22.2	75.7	64.5	50.7	38.2

The energy absorbed in the elastic phase (g_e) is mainly controlled by the cracking strength of the paste rather than the fibre content. Nonetheless, a small increase in the values of g_e is still observed due to the addition of fibres (Table 3.3). The energy absorbed during the hardening (g_h) and softening phases (g_s) increases considerably with increasing fibre dosage. The total energy absorption (g_F) for all fibre reinforced mixes is in the range of (16.6 – 75.7) × 10³ N.mm (highest in CCC mixes and lowest in FFF mixes), which is 166 – 757 times higher than that of the plain mix. The effect of RTSF content on g_F of E-UHPFRC mixes is shown in Figure 3.13.

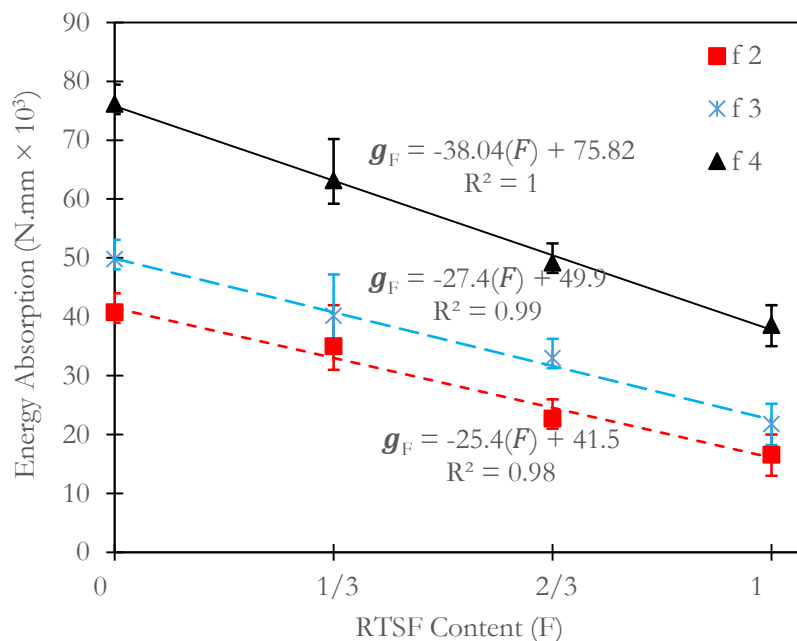


Figure 3.13: Effect of fibre dosage and RTSF content on energy absorption

For the same fibre dosage, the energy absorption decreases with an increase in RTSF content (Figure 3.13). For fibre dosages equal to 2, 3 and 4%, mixes containing only RTSF (FFF) have 59, 55 and 50% lower g_F than mixes containing only RTSC (CCC), respectively. This can again be attributed directly to the fact that the short fibres present in RTSF pull out at lower loads leading to an overall lower post-cracking energy absorption capacity.

3.5.5 Fracture Energy

The fracture energy (G_F) for all fibre reinforced mixes is shown in Figure 3.14. The G_F values for the fibre reinforced mixes range between 3.54 – 16.26 N/mm. Similar to most other properties, the G_F increases with an increase in fibre dosage and, for the same fibre dosage, decreases with an increase in RTSF content.

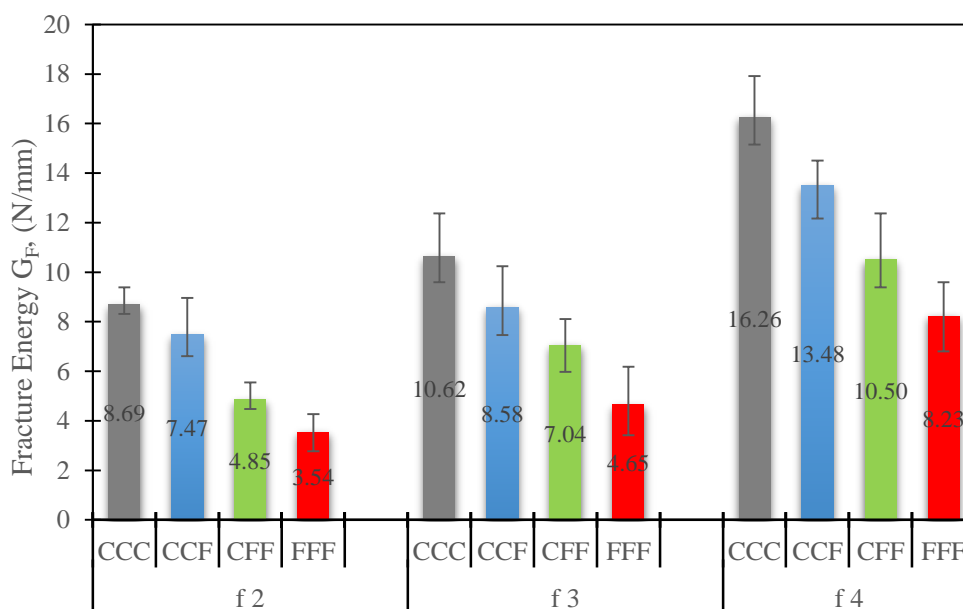


Figure 3.14: Histogram with error bars showing effect of RTSF on Fracture Energy

For the same fibre dosage, mixes containing FFF are characterised by values of G_F corresponding to 41 – 51% that of CCC mix. However, the RTSF relative efficiency is higher at higher fibre dosages. When fibre dosage is increased from 2 to 3% and 3 to 4%, G_F increases by 14 – 45% and 80 – 132%, respectively. Mixes containing f 3 and f 4 show the highest variation in G_F between specimens with the same ratio of RTSF to total fibre content (COV of 10 – 23% and 8 – 21% respectively). The high degree of correlation between f_{fl} and G_F for the mixes examined in this study is shown in Figure 3.15 and a simple regression model can be used to predict the fracture energy of E-UHPFRC mixes based on their f_{fl} .

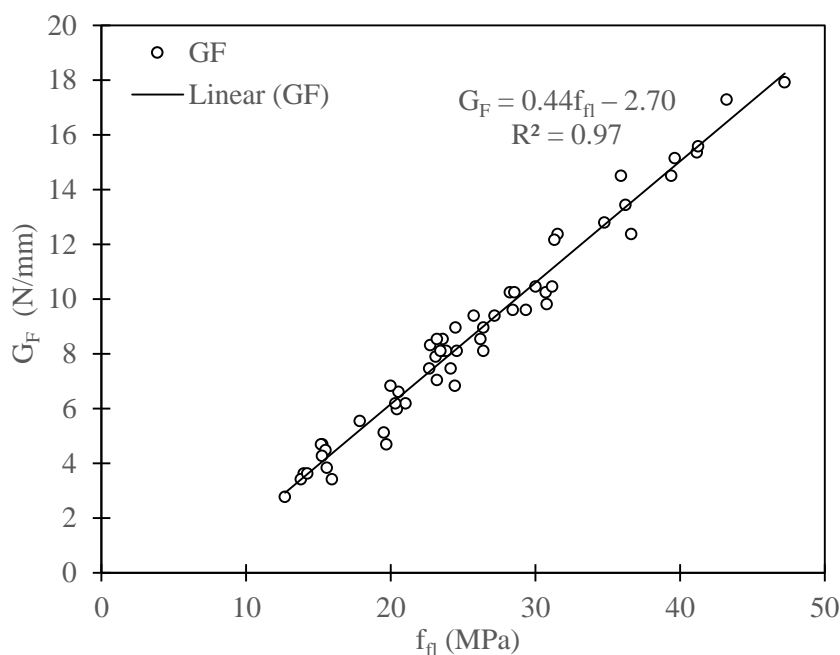


Figure 3. 15: Correlation between fracture energy and flexural strength

3.6 Tensile Stress-Strain Behaviour

3.6.1 FE Inverse Analysis Model

The numerical analysis was carried out using deformable two-dimensional planar shell elements, meshed using an 8-noded bilinear plane stress quadrilateral element (CPS8) having nine (3×3) integration points. The input parameters for the CDP model include the inelastic $\sigma - \epsilon$ relationship in uniaxial compression as well as the multi axial and flow parameters: dilation angle (ψ), eccentricity (ϵ), shape parameter (K_c), viscosity parameter (ν) and the biaxial to uniaxial compressive strength ratio (f_{bo}/f_{co}). The default values of the multi axial and flow parameters were used ($\psi = 45^\circ$, $\epsilon = 0.1$, $K_c = 2/3$, and $f_{bo}/f_{co} = 1.16$) as recommended in [21], while a low viscosity parameter, $\nu = 2 \times 10^{-6}$, was used to avoid convergence problems.

While the tensile response of strain hardening FRCs in general consists of a trilinear post-cracking tensile behaviour (see Figure 3.8 for UHPFRC), the tensile response provided by MC10 for design of FRCs considers only a bilinear post-cracking behaviour. Similarly, in this study, a simplified bilinear post-cracking tensile response is adopted, as the third branch of the curve (beyond the breaking point; see Figure 3.8) can only develop at levels of deformation that are too high to be relevant for practical design applications. According to [33], the stress at the breaking point of UHPFRC can be taken to be

approximately one-third of the peak stress, while MC10 [39] for FRCs approximates this to one-fifth of the peak stress. In this study, the ultimate tensile stress (σ_{tu}) is assumed to be between one-third and one-half of the peak stress. Compression failure is not expected to dominate the behaviour due to the high compressive strength of the mixes, thus a linear elastic $\sigma - \varepsilon$ response is used in compression with a strength equal to the compressive strength f'_c [27,56].

A preliminary study on the behaviour of a square plate (100×100 mm) subjected to uniaxial tension was carried out using five different mesh sizes (100, 50, 25, 12.5 and 5 mm) to investigate mesh sensitivity. The results from the plate test (Figure 3.16a) show that the elastic and hardening phases are not affected by the mesh size. However, the softening phase is highly mesh dependent and the dissipated energy decreases with decreasing mesh size. This can be solved by adjusting the softening modulus of the tensile $\sigma - \varepsilon$ behaviour such that the desired amount of energy is absorbed irrespective of element size. This can be achieved by adopting a characteristic length scaling parameter λ equal to the ratio of the specimen characteristic length to that of the FE element, as given in Eq. (3 – 10).

$$\lambda = \frac{l_{ch}}{l_{ch-FE}} \quad (3 - 10)$$

Where, l_{ch} = Characteristic length of specimen

l_{ch-FE} = Characteristic length of FE mesh; $l_{ch-FE} = h_e$ or $\sqrt{A_e}$

h_e = Length of square elements

A_e = Area of rectangular element

Thus, the modified ultimate strain ε_u for a given element size is given by Eq. (3 – 11):

$$\bar{\varepsilon}_{tu} = \lambda \varepsilon_u \quad (3 - 11)$$

Figure 3.16 (b) shows the comparison between input $\sigma - \varepsilon$ curves and output data for various mesh sizes after implementing the adjustments based on Eq. (3 – 10) and (3 – 11). It can be seen that a mesh independent solution can be achieved by modifying the energy dissipated during the softening stage using the characteristic length scaling parameter λ .

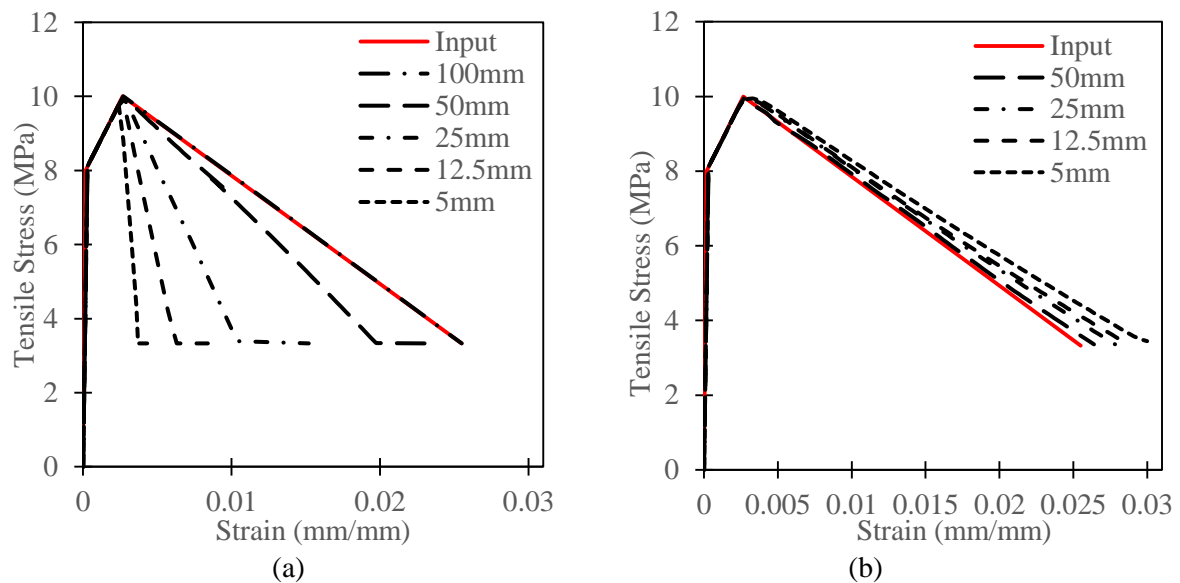


Figure 3.16: (a) Plate response in uniaxial tension (a) plate response using the modified ultimate strain approach

Mesh dependency was also observed on the energy absorption of UHPFRC flexural prisms and a similar approach to that implemented above can be used to develop a mesh independent solution. Such approach has also been used and validated by [57]. However, most of the existing methods to calculate l_{ch} from bending tests [58-63] are unsuitable, as they give unreasonably high values ($l_{ch} >$ span of prism specimens) when applied to UHPFRC. Furthermore, the approach proposed in [62], although commonly used to determine l_{ch} , cannot be applied to mortars like UHPFRC as it relies on the maximum size of the coarse aggregates.

MC10 [39] provides a simplified approach for calculating l_{ch} and recommends the use of $l_{ch} = h_{sp}$ (depth of notched cross section) for elements without traditional reinforcement, and $l_{ch} = y$ (distance between the neutral axis and the tensile side of the prism) for elements with traditional reinforcement. However, due to their strain hardening behaviour, UHPFRC elements behave more like steel reinforced members (depending on fibre dosage) rather than ordinary FRCs. Studies by [30] and [19] have adopted values of $y = 0.75h_{sp}$ and $0.9h_{sp}$ respectively, while the Swiss Standard SIA 2052: 2014-12 [64] proposes a value of $y = 0.82h_{sp}$. Based on the current literature, this study adopts a value of characteristic length within the range $0.75h_{sp} \leq l_{ch} \leq h_{sp}$.

3.6.2 Assumptions used in Inverse Analysis of E-UHPFRC

The following assumptions are made when conducting the inverse analysis:

1. A main crack dominates the fracture zone.
2. The elastic energy is negligible and the total energy absorption can be taken equal to the externally applied energy.
3. The uniaxial tensile softening part can be represented by a single linear branch up to an ultimate tensile strain (not exceeding the breaking point of the bilinear softening curve, see Figure 3.8).
4. The ultimate tensile strain of 2 – 3% can be considered appropriate for the structural design of E-UHPFRC elements at ultimate limit state and to prevent excessive crack width openings.
5. The characteristic length of E-UHPFRC specimens lies within the range $0.75h_{sp} \leq l_{ch} \leq h_{sp}$.

3.6.3 Determination of Ultimate Tensile Strain

As mesh size affects mainly the post peak (softening) behaviour, reliable estimates of the cracking and peak tensile properties (σ_{tc} , ε_{tc} , σ_{tp} and ε_{tp} in Figure 3.17) can be obtained (through inverse analysis) by fitting the FE pre-peak $P - \delta$ behaviour with the experimental response, irrespective of mesh size. However, the ultimate strain is highly dependent on mesh size and a fracture energy approach needs to be implemented to obtain a reliable estimate, as outlined in the following.

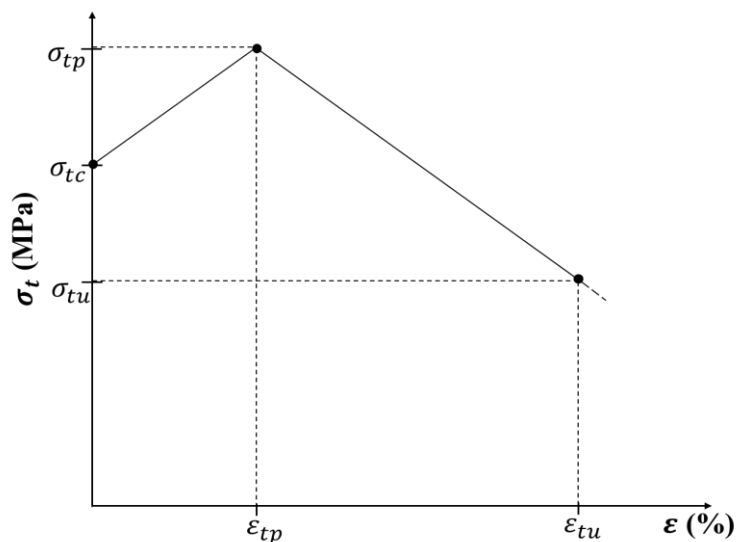


Figure 3.17: Tensile $\sigma - \varepsilon$ response to determine ε_{tu} using a fracture energy approach

- **Energy per Unit Volume Dissipated in Tension (g_t):**

The energy per unit volume dissipated in tension is given by the area under the tensile $\sigma - \varepsilon$ curve shown in Figure 3.17 and can be calculated by using Eq. (3 – 12).

$$g_t = (\sigma_{tp} \times \varepsilon_{tu}) - \frac{1}{2} (\sigma_{tp} - \sigma_{tu})(\varepsilon_{tu} - \varepsilon_{tp}) - \frac{1}{2} (\sigma_{tp} - \sigma_{tc}) \times \varepsilon_{tp} \quad (N/mm^2) \quad (3 - 12)$$

- **Volumetric Energy dissipated (G_T):**

The energy dissipated per unit volume (G_T) is given by Eq. (3 – 13).

$$\begin{aligned} G_T &= g_t \times l_{ch} \times b \times h_{sp} \quad (N \text{ mm}) \\ G_T &= g_t \times l_{ch} \times A_F \quad (N \text{ mm}) \end{aligned} \quad (3 - 13)$$

- **Equivalent Energy Dissipation:**

The energy g_F representing the total work done by the external load in flexure is equivalent to the energy dissipated per unit volume in direct tension Eq. (3 – 14):

$$\begin{aligned} g_F &= G_T \quad (N \text{ mm}) \\ g_F &= g_t \times l_{ch} \times A_F \quad (N \text{ mm}) \\ G_F &= g_t \times l_{ch} \quad (N/mm) \\ g_t &= G_F / l_{ch} \end{aligned} \quad (3 - 14)$$

The ultimate tensile strain ε_{tu} can be obtained by substituting $\sigma_{tu} = \sigma_{tp}/k$ and equating Eq. (3 – 12) to Eq. (3 – 14)

$$\varepsilon_{tu} = \frac{2G_F + l_{ch}\varepsilon_{tp} \left(\frac{\sigma_{tp}}{k} - \sigma_{tc} \right)}{l_{ch}\sigma_{tp} \left(\frac{1+k}{k} \right)} \quad (3 - 15)$$

Where k can vary from 2.5 – 3 (highest for CCC mixes)

For a given finite element size, the adjusted ultimate strain ($\bar{\varepsilon}_{tu}$) needed to dissipate the correct amount of energy can be obtained by multiplying ε_{tu} by the characteristic length scaling parameter (λ) of the selected mesh based on Eq. (3 – 9) and (3 – 10). The step by step procedure for the inverse analysis is given in Appendix A, while an example is shown in Table A1.

3.6.4 Comparison between Experimental and Numerical Load-Deflection Curves

The load-deflection response of specimens made with mix f 2 – CCC is examined using three different mesh sizes after implementing the ultimate strain scaling. As shown in Figure 3.18, all models reach the

same peak load and energy absorption irrespective of mesh size. All subsequent numerical analyses (Figure 3.19) are carried out using the 14×12.6 mm mesh element.

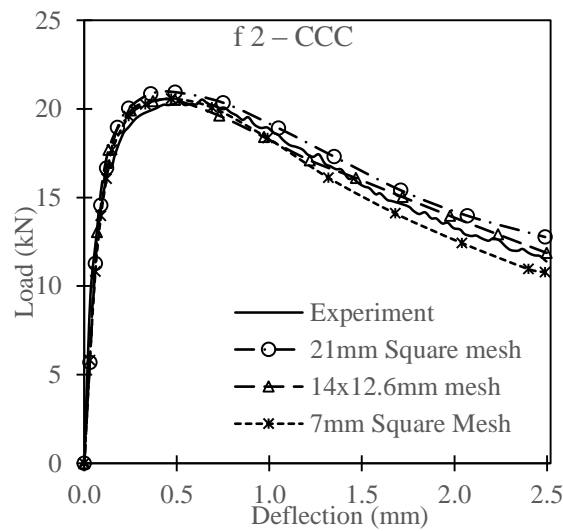
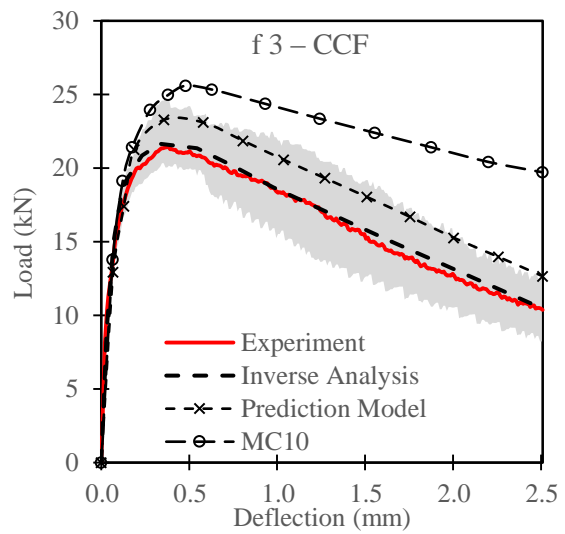
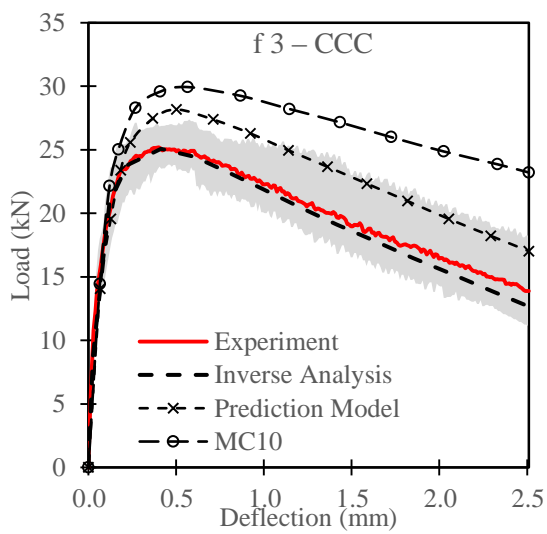
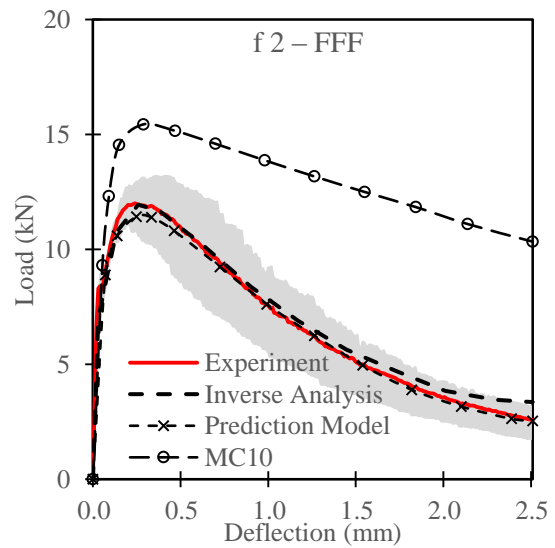
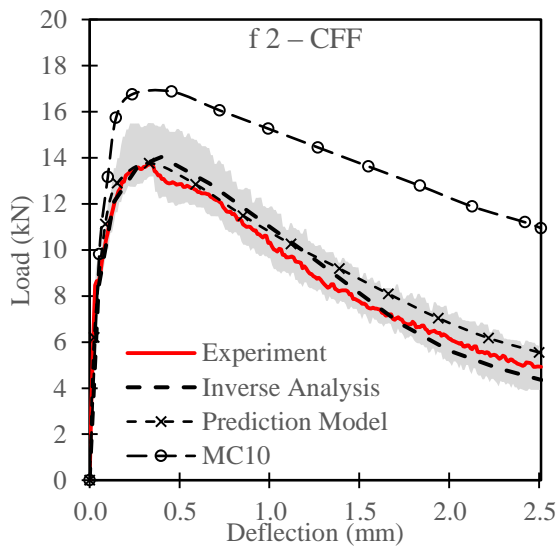
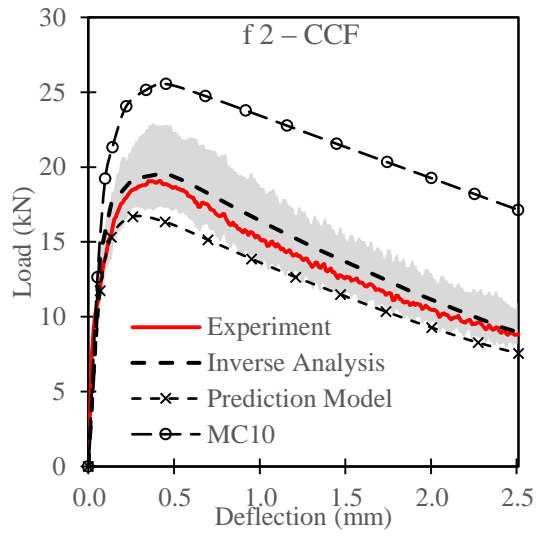
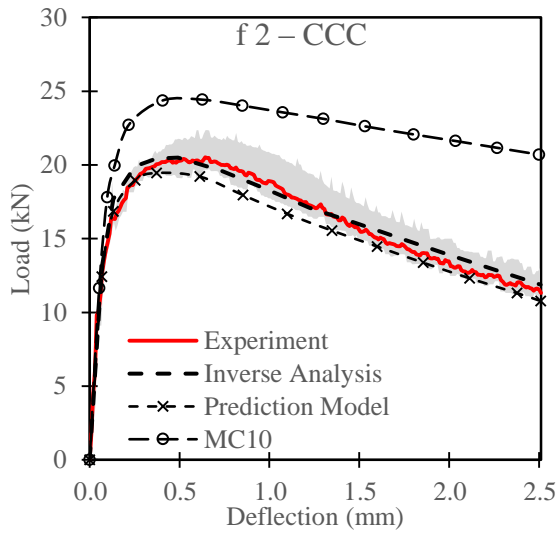


Figure 3.18: FE response of f 2 – CCC for different mesh sizes

Figure 3.19 compares the average experimental load-deflection curves for all the E-UHPFRC mixes with those obtained from the FE inverse analysis, MC10 [39] and the proposed prediction model. A detailed discussion on the MC10 approach and the proposed prediction model is provided in subsequent sections (Sec. 3.4.1 and 3.6.6 for MC10 and Sec. 3.6.7 for prediction model). The prediction model work on similar approach to MC10 [39] (See Sec. 3.4.1) i.e. using a trilinear uniaxial tensile relationship. However, the model uses f_{fl} and E_c to calculate tensile strength parameters rather than residual strength values (f_R) used by MC10 [39]. It also avoided the use of CMOD values (which is specimen size dependant) to calculate strain, as such can be applied to flexural prism of various sizes.



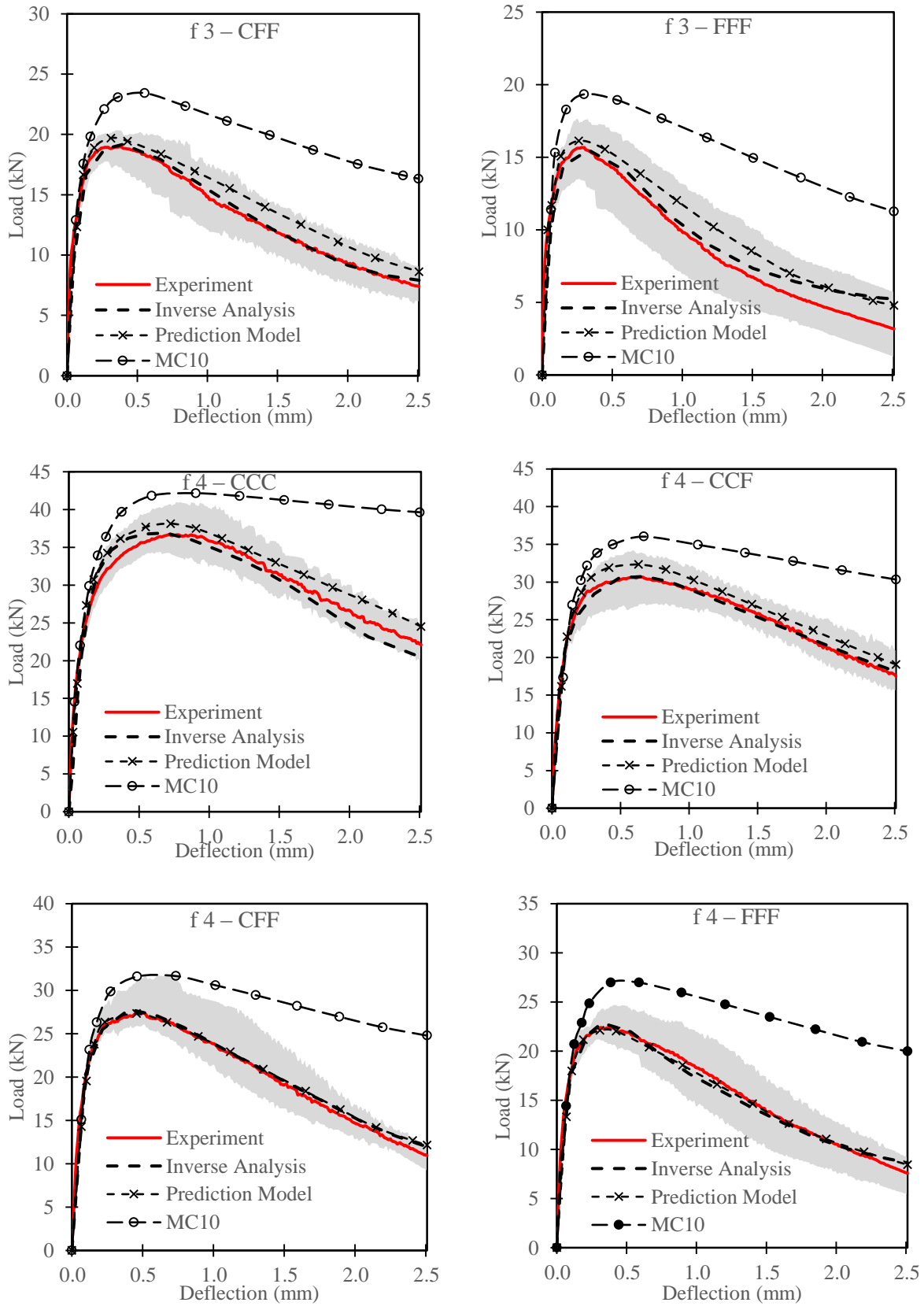


Figure 3.19: Comparison between experimental average load deflection behaviours, FE inverse analysis, MC10 and proposed model

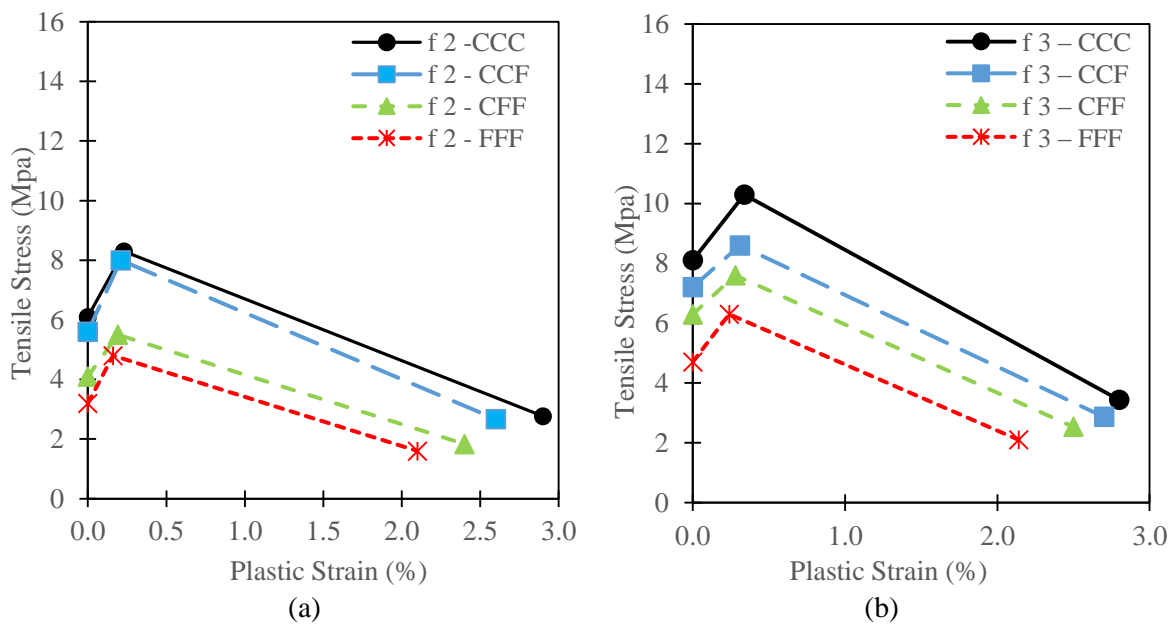
For easier comparison, Table 3.4 shows the percentage error in peak load and energy absorption between the values determined using the FE analyses and the experimental data. The low percentage errors (ranging -1.5 – 1.3% in peak load and -3.5 – 7.3% in energy absorption) provide clear evidence that experimental and FE derived load deflection are in good agreement and the derived tensile properties are equivalent to the tensile properties of the mixes.

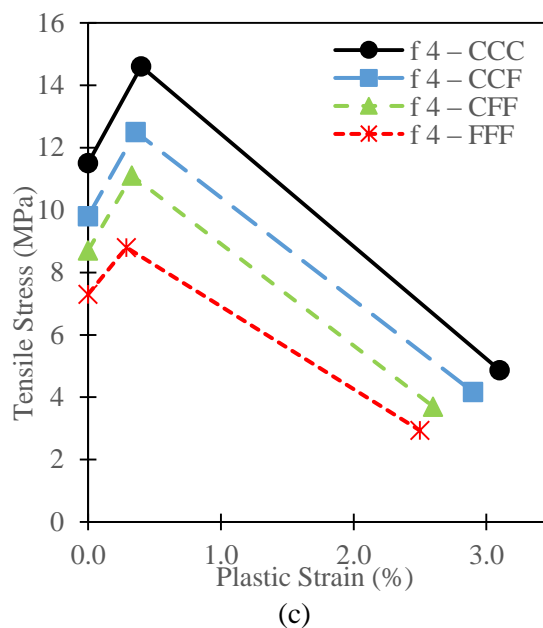
Table 3.4: Error in Peak Load and Energy absorption

Error	Plain	f2 – CCC	f2 – CCF	f2 – CFF	f2 – FFF	f3 – CCC	f3 – CCF	f3 – CFF	f3 – FFF	f4 – CCC	f4 – CCF	f4 – CFF	f4 – FFF
P_p (%)	0	-0.1	1.2	1.3	-0.5	-1.5	1.0	-1.1	-1.1	0.6	0.4	0.4	2.0
g_F (%)	0	-0.1	4.9	0.5	4.1	-3.5	2.1	0.2	7.3	1.4	-0.6	0.1	-0.8

3.6.5 Inverse Analysis Tensile Stress Strain Behaviour

Figure 3.20 shows the uniaxial tensile stress vs plastic strain of all E-UHPFRC mixes examined in this study.





(c)
Figure 3.20: Tensile stress-cracking strain behaviour of mixes

The results show that the tensile strength increases with an increase in fibre dosage and, for the same fibre dosage, it decreases with increasing RTSF content. All mixes except f 2 – FFF attained a post-cracking tensile strength greater than 5 MPa, thus meeting the requirements for UHPC in accordance with the US Department of Transportation FHWA report [2]. This signifies that a minimum RTSF dosage of 3% must be used in the manufacture of E-UHPFRC. However, 2% fibre dosage of hybrid mixes of RTSF with RTSC or MSF can still meet the desired tensile strength requirement e.g. f 2 – CCF. Mixes containing RTSC (CCC) show values of σ_{tc} and σ_{tp} that are comparable to those obtained with MSF [27,30,31,65].

As shown in Figure 3.21, a strong correlation was found to exist between σ_{tc} or σ_{tp} and f_{fl} , and this information can be used to simplify the derivation of serviceability limit state equations.

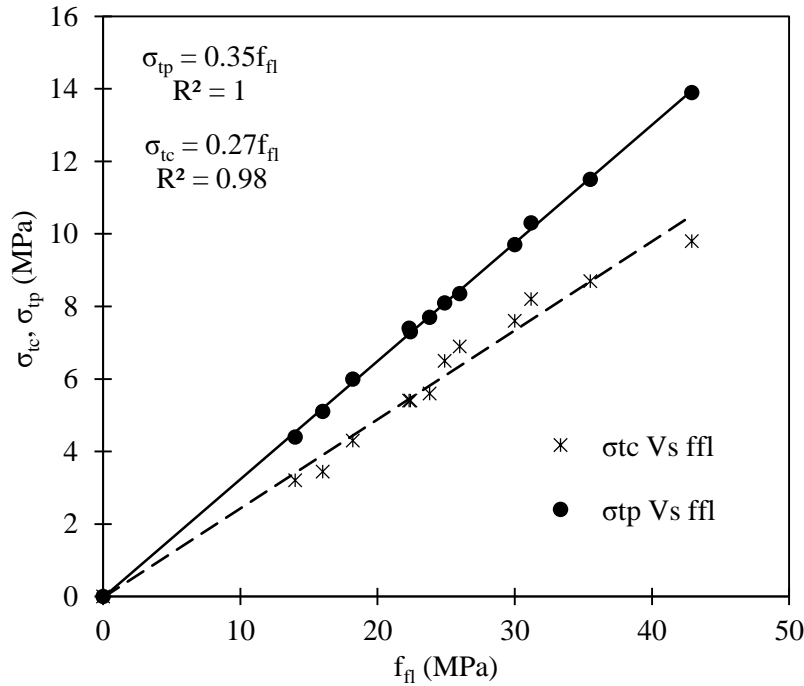


Figure 3.21: Correlation between tensile strength parameters and flexural strength

3.6.6 Evaluation of Stress Strain Relationship of MC10 [39]

The MC10 [39] guidelines outlined in Section 3.4.1 were used to derive the input tensile $\sigma - \epsilon$ characteristics for the FE analysis. A characteristic length of $l_{ch} = h_{sp}$ was used in strain calculations as recommended for FRC sections without traditional steel reinforcement and subjected to bending [35]. The results are shown in Figure 3.19, while errors are summarised in Table 3.6. From the analysis of the results it can be seen that the MC10 [39] approach overestimates the tensile strength of UHPC in terms of σ_{tc} and σ_{tp} by 45 – 82% and 16 – 41%, respectively. Furthermore, MC10 [39] shows a maximum overestimation of 43 and 116% in peak load and energy absorption, respectively. As a result, the current model used in MC10 [39] is found to be unconservative for the design of UHPFRCs.

3.6.7 Proposed Tensile Stress-Strain Prediction Model

To address the lack of a suitable simplified tensile model for fibre reinforced, a new predictive model that utilises easy to determine mechanical properties (f'_c and f_{fl}) and fibre content is proposed in Eqs. (3 – 15) – (3 – 18). The idealised response for the proposed model is shown in Fig 3.22.

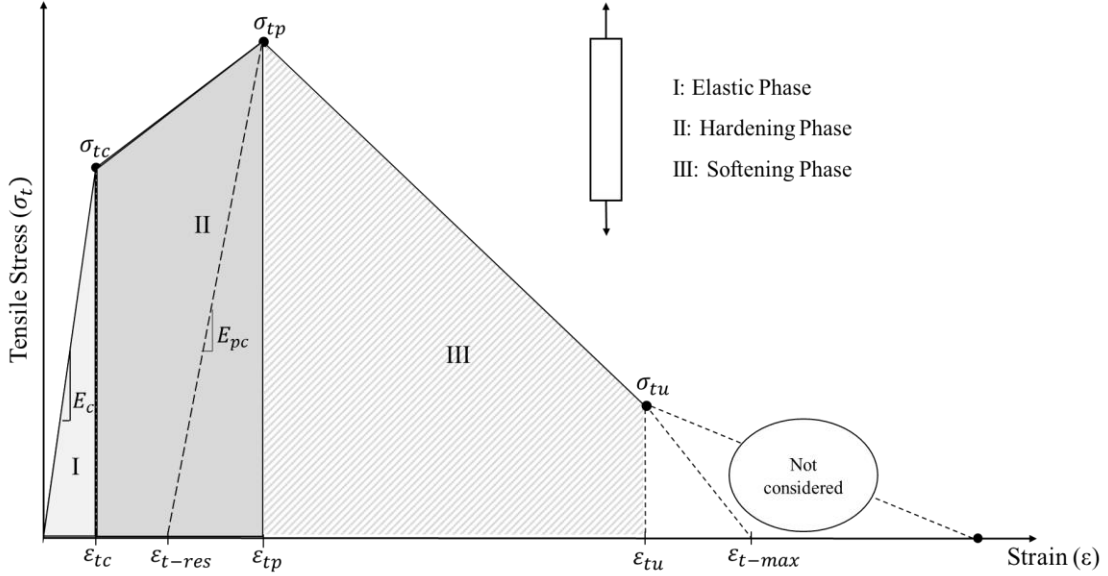


Figure 3. 22: Uniaxial tensile model of E-UHPFRC

$$f_{fl} = 1100\rho \left(1 - \frac{F}{2.3}\right) \quad (3 - 15)$$

$$\sigma_{tc} = 0.27f_{fl}, \quad \varepsilon_{tc} = \frac{\sigma_{tc}}{E_c} \quad (3 - 16)$$

$$\sigma_{tp} = 0.35f_{fl}, \quad \varepsilon_{tp} = \left(\frac{\sigma_{tp}}{E_{pc}}\right), \quad E_{pc} = 6\% E_c, \quad E_c = 4069 (f'_c)^{1/2} \quad (3 - 17)$$

$$\sigma_{tu} = \frac{\sigma_{tp}}{k}; \quad \varepsilon_{tu} = \frac{2G_F + l_{ch}\varepsilon_{tp} \left(\frac{\sigma_{tp}}{k} - \sigma_{tc}\right)}{l_{ch}\sigma_{tp} \left(\frac{1+k}{k}\right)} \quad (3 - 18)$$

Alternatively, the ultimate strain can be obtained from the following simplified equation (Eq. (3 - 19))

$$\varepsilon_{tu} = (\varepsilon_{t-max} - \varepsilon_{tp}) \left(1 - \frac{\sigma_{tu}}{\sigma_{tp}}\right) + \varepsilon_{tp}; \quad \varepsilon_{t-max} = (4.2(1 + 1.5\rho) - F)\% \quad (3 - 20)$$

Where: k is a constant between 2.5 – 3, ρ = fibre dosage by volume, F = ratio of RTSF to total fibre content.

A comparison between the predictions of the numerical analysis and the proposed model is presented in Table 3.5 as a ratio of the two predictions. The overall average and standard deviation are also reported.

Table 3.5: Correlation between derived (inverse analysis) and proposed model tensile characteristics

Mix ID	$f_{fl}/f_{fl-model}$	$\sigma_{tc}/\sigma_{tc-model}$	$\sigma_{tp}/\sigma_{tp-model}$	$\sigma_{tu}/\sigma_{tu-model}$	$\varepsilon_{tp}/\varepsilon_{tp-model}$	$\varepsilon_{tu}/\varepsilon_{tu-model}$
f 2 – CCC	1.08	1.03	1.08	1.08	0.97	0.98
f 2 – CCF	1.19	1.10	1.22	1.22	1.04	0.96
f 2 – CFF	1.02	0.97	1.01	1.01	1.10	0.96
f 2 – FFF	1.13	0.95	1.10	1.10	1.16	0.93
f 3 – CCC	0.91	0.91	0.89	0.89	0.97	0.92
f 3 – CCF	0.88	0.95	0.87	0.87	1.02	0.97
f 3 – CFF	0.95	1.00	0.93	0.93	1.11	0.98
f 3 – FFF	0.98	0.93	0.97	0.97	1.17	0.92
f 4 – CCC	0.98	0.97	0.95	0.95	0.88	1.00
f 4 – CCF	0.94	0.96	0.95	0.95	0.92	1.01
f 4 – CFF	1.00	1.03	1.01	1.01	1.01	0.99
f 4 – FFF	1.05	1.09	1.01	1.01	1.10	1.05
Average	1.01	0.99	1.00	1.00	1.04	0.97
S.D.	0.09	0.06	0.10	0.10	0.09	0.04

The correlation shows excellent agreement between the predicted and measured parameters, with average ratios close to unity (between 0.97 – 1.04) and a very low standard deviation (0.04 – 0.1). This indicates that the proposed model can adequately predict the tensile response of UHPFRC mixes.

Figure 3.19 shows comparisons between experimental, proposed design model and MC10 [39] derived load–deflection behaviours for each tested E-UHPFRC mix. It can be seen that the proposed model captures the tensile behaviour of the studied mixes reasonably well.

Table 3.6 shows the percentage error in peak load and energy absorption values predicted by the proposed model and MC10 [39]. The proposed model shows a maximum underestimation of -13.2 and -12.4% and a maximum overestimation of 9.6 and 15.7% in peak load and energy absorption, respectively. MC10 always overestimates the performance of all mixes and predicts values of peak load and energy absorption with

errors up to 30 and 90%, respectively. Hence, the proposed model provides a rather accurate prediction of the uniaxial tensile behaviour of fibre reinforced mixes and can serve as a useful design tool for the design of E-UHPFRC structures.

Table 3.6: Errors in predicting peak load and energy absorption

Mix ID/Model	f 2 – CCC	f 2 – CCF	f 2 – CFF	f 2 – FFF	f 3 – CCC	f 3 – CCF	f 3 – CFF	f 3 – FFF	f 4 – CCC	f 4 – CCF	f 4 – CFF	f 4 – FFF
Error in Peak Load (%)												
P. Model	-4.9	-13.2	-0.6	-4.9	9.6	8.9	3.8	2.9	4.0	5.3	-1.4	-1.4
MC10	19.3	31.8	23.2	28.5	17.5	19.4	24.3	23.4	15.2	17.6	15.6	21.5
Error in Energy absorption (%)												
P. Model	-6.3	-12.4	5.2	-2.4	14.1	13.5	8.2	15.7	5.4	4.6	0.2	0.4
MC10	35.9	53.8	53.9	93.0	32.1	37.8	48.9	76.2	29.7	28.0	38.1	52.7

3.6.8 Accuracy of the Proposed Model in Performance Design Parameters

In most design guidelines (e.g. MC10), the flexural characteristics of concrete are normally used directly to predict moment capacities at different performance stages using a simple section analysis approach. The approach adopts predetermined neutral axis depths (x) and assumes that the concrete remains elastic in compression (see Appendix B for more details). From the analysis, it was found that the value of x does not vary significantly for the mixes examined (less than ± 1 mm). Hence, a constant neutral axis depth was determined by taking the average of the neutral axis depths at a given stage for all mixes, as shown in Figure 3.23.

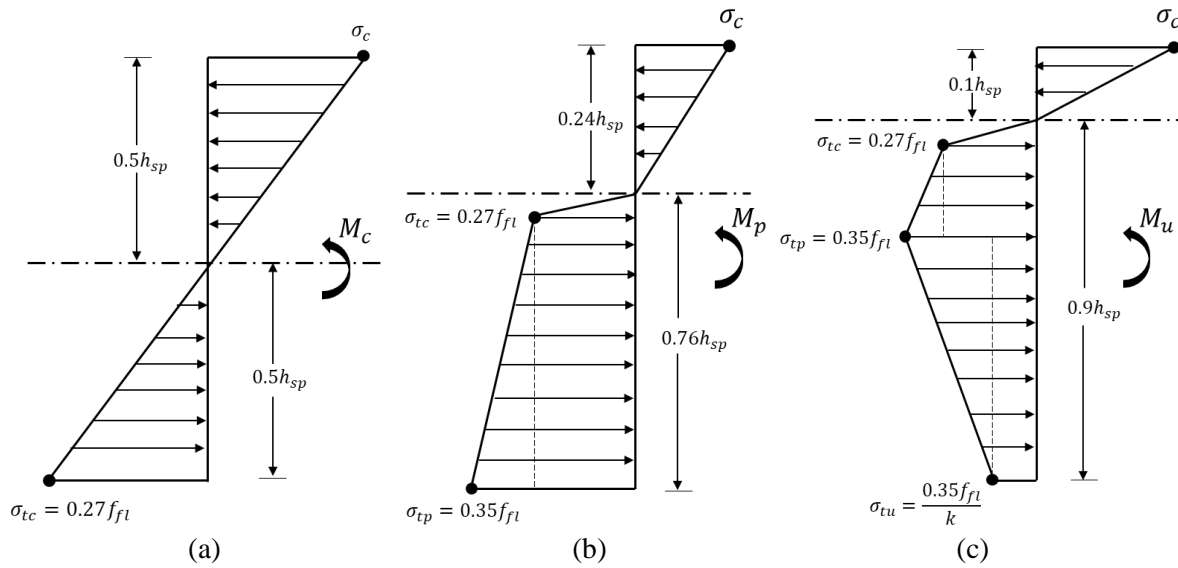


Figure 3.23: Stress distribution using predetermined neutral axis depth (a) at crack (b) at peak load capacity and (c) at ultimate capacity

The moment capacities determined using the stress levels shown in Figure 3.23 for all the fibre reinforced mixes were calculated and are compared with the numerical (inverse analysis) and experimental moment capacities in Figure 3.24. Values below the diagonal indicate underestimation of the moment capacity.

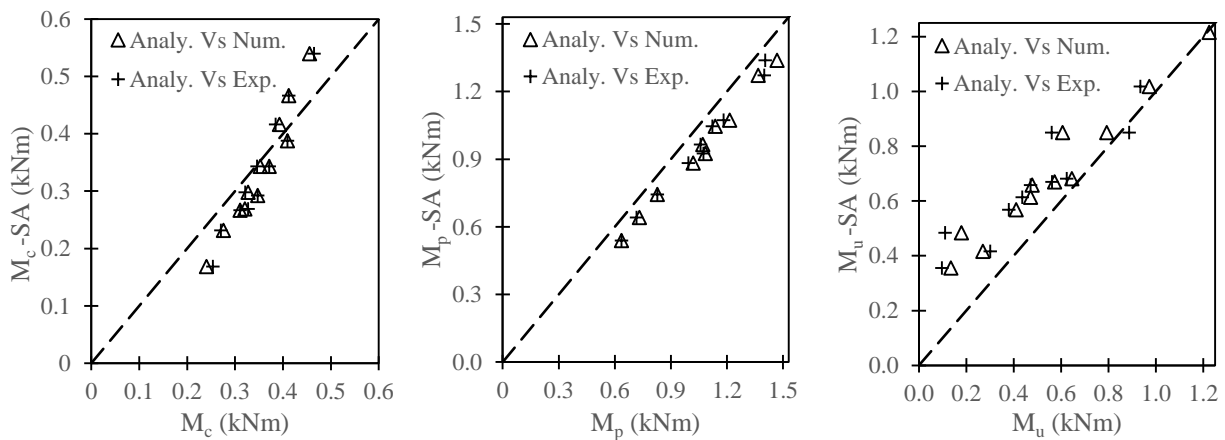


Figure 3.24: Comparison between moment capacities

The results show that predicted cracking moment (M_c) and peak moment (M_p) capacities correlate well, with correlation factors of 12% for M_c and 3% for M_p , while relatively overestimated values are obtained for the ultimate moment capacity (M_u) of some specimens. Nonetheless, it can be concluded that this approach leads to safe and accurate results and can be used for design purposes.

3.7 Conclusions

This paper presents an experimental study on mechanical properties of E-UHPFRC and an approach for determining the tensile $\sigma - \varepsilon$ characteristics of E-UHPFRC by using three-point bending test results and FE inverse analysis. Experimental results show that compared to RTSC only mixes, the inclusion of RTSF causes a slight reduction in compressive strength and modulus of elasticity, and a higher reduction in flexural strength, energy absorption and fracture energy. Nevertheless, similar mechanical properties to RTSC mixes can be achieved by using higher RTSF dosages or hybrid RTSC-RTSF mixes.

Inverse analysis is shown to be an effective tool to estimate the tensile characteristics of E-UHPFRC. The mesh dependency of crack models encountered when modelling the softening part of E-UHPFRC is solved by adopting an adaptive fracture energy approach. The approach uses fracture energy, characteristic length and mesh size as input parameters. The determined tensile properties of RTSC mixes are similar, and in some cases higher than those reported in literature for mixes containing MSF cured under the same conditions.

The MC10 [39] model for strain hardening materials is shown to largely overestimate both the tensile strength and energy absorption of E-UHPFRCs by up to 31 and 76% respectively. A model for predicting the constitutive tensile $\sigma - \varepsilon$ law of E-UHPFRC based on simple mix parameters (compressive strength, flexural strength, fracture energy, fibre dosage and RTSF content) is developed. The proposed model predicts well the flexural capacities of E-UHPFRC at all performance levels and it is well suited for design.

Acknowledgement

The first author would like to thank the Petroleum Technology Development Fund (PTDF), Nigeria, for sponsoring his PhD studies. The authors would also like to thank TWINCON Ltd and SIKA Group for supplying the materials. This project was supported by the Royal Academy of Engineering under the Research Chairs and Senior Research Fellowships scheme”.

Appendix A

A1: Procedure for Inverse Analysis

A step by step procedure for conducting the inverse analysis is given below:

1. Assume σ_{tc} , σ_{tp} , ε_{tp} and calculate $\varepsilon_{tc} = \frac{\sigma_{tc}}{E}$
2. Conduct FE modelling and compare pre-peak $P - \delta$ behaviour with experimental behaviour.
3. Repeat step (1) – (2) until FE pre peak $P - \delta$ approximately matches with experiment.
4. Assume k , Calculate the ultimate tensile stress $\sigma_{tu} = \frac{\sigma_{tp}}{k}$
5. Assume a suitable characteristic length $0.75h_{sp} < l_{cs} < h_{sp}$ ($0.85h_{sp}$ most used in this study).
6. Calculate the ultimate strain ε_{tu} , from the relation; $\varepsilon_{tu} = \frac{2G_F + l_{ch}\varepsilon_{tp}\left(\frac{\sigma_{tp}}{k} - \sigma_{tc}\right)}{l_{ch}\sigma_{tp}\left(\frac{1+k}{k}\right)}$.
7. Calculate the characteristic length scaling factor: $\lambda = \frac{l_{ch}}{\sqrt{A_e}}$
8. Calculate adjusted ultimate strain for the selected mesh size: $\bar{\varepsilon}_{tu} = \lambda \varepsilon_{tu}$
9. Carry out FE analysis and compare $P - \delta$ with experimental up to deflection of 2.5 mm. If the difference between FE $P - \delta$ behaviour and experimental is more than 5%. Re-adjust parameters in step (1) and Repeat step (2) – (10)
10. Check that the ultimate strain in the element at bottom of the notch section is approximately equal to $\lambda \varepsilon_{tu}$. If the difference is greater than 20% change repeat step (5) – (12).

A2: Inverse Analysis solved example

A detailed case study for determining the uniaxial tensile behaviour of some of f 2 – CCC, f 3 – FFF and f 4 – CCC as shown in Table A1.

Table A1: Inverse analysis case study

ID	Material Input			Step (1) – (3)				Step (4) and (5)			(6)	(7)	(8)	(10)
	E_c (GPa)	G_F (N/mm)	A_e (mm ²)	σ_{tc} (MPa)	$\varepsilon_{tc} = \frac{\sigma_{tc}}{E}$ (mm/mm)	σ_{tp} (MPa)	ε_{tp} (mm/mm)	k	$\sigma_{tu} = \frac{\sigma_{tp}}{3}$ (MPa)	l_{ch} (mm)	ε_{tu} (mm/mm)	$\lambda = \frac{l_{ch}}{\sqrt{A_e}}$	$\bar{\varepsilon}_{tu}$	$\bar{\varepsilon}_{tu-FE}$
f 2 – CCC	51.4	8.7	21×21	6.1	0.0001	8.2	0.0023	3	2.7	54	0.0290	2.6	0.0754	0.0841
f 3 – FFF	51.8	4.7	14×12.6	4.7	0.0001	6.3	0.0024	2.8	2.2	50	0.0216	3.8	0.0822	0.0938
f 4 – CCC	53.6	16.3	7×7	11.5	0.0002	14.6	0.0041	3	4.9	54	0.0301	7.7	0.2322	0.2461

Appendix B

B1: Details of section Analysis

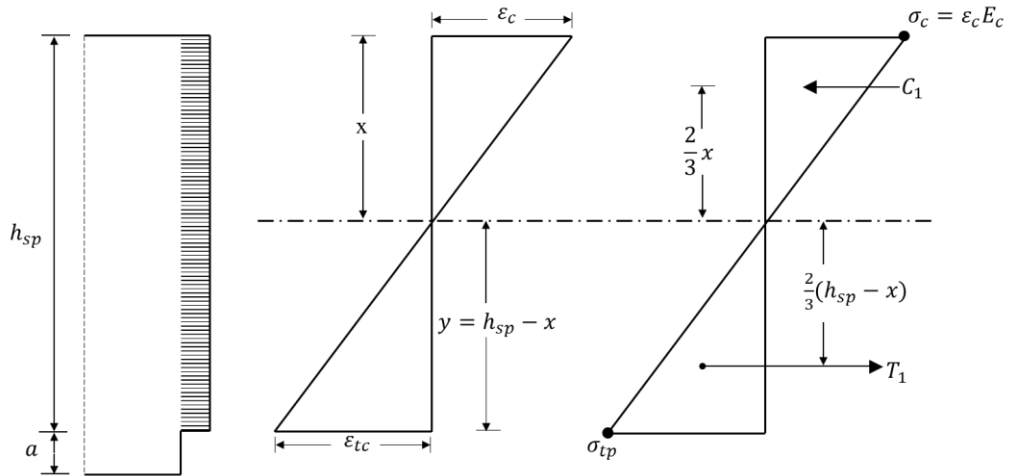


Figure B1: Stage I: At cracking

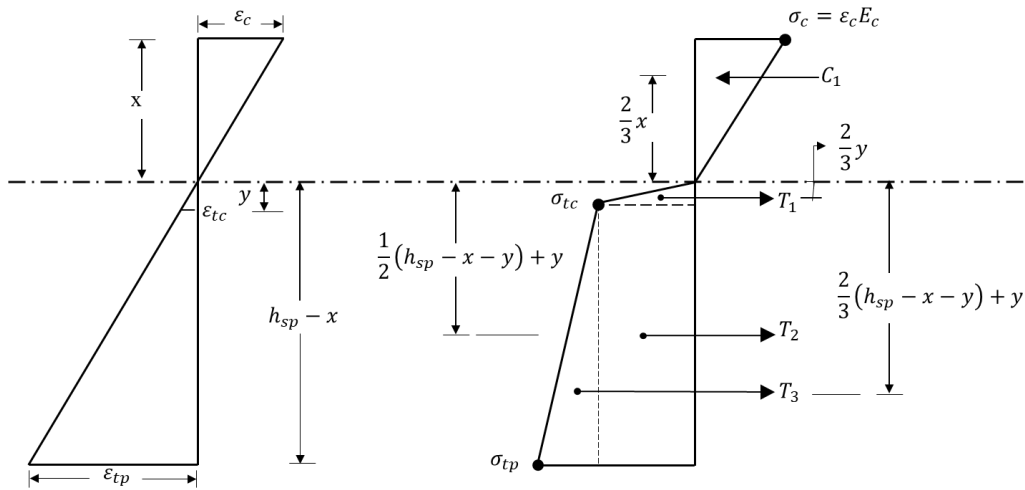


Figure B2: At peak capacity

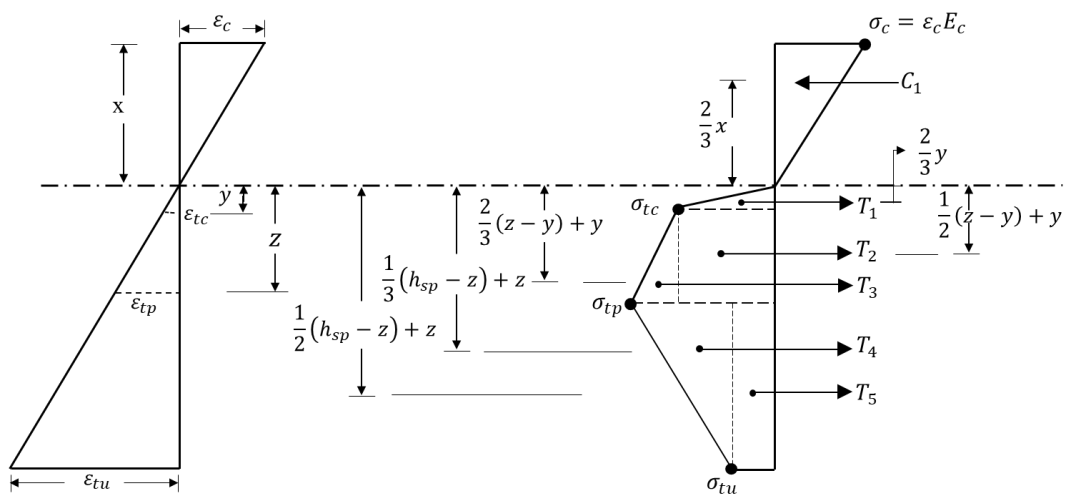


Figure B3: At ultimate capacity

Table B1: Determining neutral axis depth and moment capacity of UHPC mixes

Stage	Step 1: Determine compressive strain and stress point locations	Step 2: Determine x from force equilibrium	Establish average x (optional)	Step 3: Bending Moment
I	$0 < \varepsilon_t \leq \varepsilon_{tc}$: $\varepsilon_c = \frac{\varepsilon_{tc}x}{h_{sp} - x}$	$C_1 = T_1$		$M_c = T_1 a_1$
II	$\varepsilon_{tc} < \varepsilon_t \leq \varepsilon_{tp}$: $\varepsilon_c = \frac{\varepsilon_{tp}x}{h_{sp} - x}$, $y = \frac{\varepsilon_{tc}x}{\varepsilon_c}$	$C_1 = T_1 + T_2 + T_3$		$M_p = T_1 b_1 + T_2 b_2 + T_3 b_3$
III	$\varepsilon_{tp} < \varepsilon_t \leq \varepsilon_{tu}$: $\varepsilon_c = \frac{\varepsilon_{tu}x}{h_{sp} - x}$, $y = \frac{\varepsilon_{tc}x}{\varepsilon_c}$, $z = \frac{\varepsilon_{tp}x}{\varepsilon_c}$	$C_1 = T_1 + T_2 + T_3 + T_4 + T_5$		$M_u = T_1 c_1 + T_2 c_2 + T_3 c_3 + T_4 c_4 + T_5 c_5$

For easier formulation, the lever arms for the internal forces are represented as:

$$a_1 = y$$

$$b_1 = \frac{2}{3}y + \frac{2}{3}x; \quad b_2 = \frac{h-x-y}{2} + y + \frac{2x}{3}; \quad b_3 = \frac{2(h-x-y)}{3} + y + \frac{2x}{3};$$

$$c_1 = \frac{2}{3}y + \frac{2}{3}x; \quad c_2 = \frac{z-y}{2} + y + \frac{2x}{3}; \quad c_3 = \frac{2(z-y)}{3} + y + \frac{2x}{3}; \quad c_4 = \frac{h-z}{3} + z + \frac{2x}{3}; \quad c_5 = \frac{h-z}{2} + z + \frac{2x}{3}$$

3.8 References

- 1 M.N. Isa, K. Pilakoutas, M. Guadagnini, H. Angelakopoulos, Mechanical performance of affordable and eco-efficient ultra-high performance concrete (UHPC) containing recycled tyre steel fibres, *Constr. Build. Mater.* 255 (2020) 119272.
- 2 Federal Highway Administration, *Ultra-High Performance Concrete: A State-of-the-Art Report for the Bridge Community*, Mclean, VA, 2013.
- 3 C. Shi, Z. Wu, J. Xiao, D. Wang, Z. Huang, Z. Fang, A review on ultra-high performance concrete: Part I. Raw materials and mixture design, *Constr. Build. Mater.* 101 (2015) 741–751.
- 4 D. Wang, C. Shi, Z. Wu, J. Xiao, Z. Huang, Z. Fang, A review on ultra-high performance concrete: Part II. Hydration, microstructure and properties, *Constr. Build. Mater.* 96 (2015) 368–377.
- 5 Z. B. Haber, I. De la Varga, B.A. Graybeal, Nakashoji, B., & El-Helou, R. *Properties and behavior of UHPC-class materials* (No. FHWA-HRT-18-036). United States. Federal Highway Administration. Office of Infrastructure Research and Development 2018.
- 6 C. Wu, J. Li, Y. Su, Development, testing, and numerical simulation of ultra-high performance concrete at material level, *Dev. Ultra-High Perform. Concr. Against Blasts.* (2018) 23–93.
- 7 D. J. Kim, A. E. Naaman, S. El-Tawil, Comparative flexural behavior of four fibre reinforced cementitious composites, *Cem. Concr. Compos.* 30 (2008) 917–928.
- 8 A. Sivakumar, M. Santhanam, Mechanical properties of high strength concrete reinforced with metallic and non-metallic fibres. *Cement Concrete Comp* 29 (2007) 603–8.
- 9 Y. Uchida & T. Takeyama, T. Dei, Ultra high strength fibre reinforced concrete using aramid fibre *Fracture Mechanics of Concrete and Concrete Structures – High Performance, Fibre Reinforced Concrete, Special Loadings and Structural Applications-* B. H. Oh, et al. (eds) 1492-1497.
- 10 F. Bencardino, L. Rizutti, G. Spadea, R.N. Swamy, Experimental evaluation of reinforced concrete fracture properties. *Compos Part B-Eng.* 41 (2010):17–24.
- 11 P. Smarzewski. Effect of Curing Period on Properties of Steel and Polypropylene Fibre Reinforced Ultra-High Performance Concrete. *IOP Conf Ser Mater Sci. Eng.* 245 (2017):1–7.

- 12 P. Smarzewski, Study of toughness and macro/micro-crack development of fibre-reinforced ultra-high performance concrete after exposure to elevated temperature, *Materials (Basel)*. 12 (2019).
- 13 M. Hsie, C. Tu, P.S. Song. Mechanical properties of polypropylene hybrid fibre reinforced concrete. *Mat Sci Eng A-Struct.* 494 (2008) :153–7.
- 14 P. Smarzewski, Flexural toughness evaluation of basalt fibre reinforced HPC beams with and without initial notch, *Compos. Struct.* 235 (2020) 111769.
- 15 N. Kabay. Abrasion resistance and fracture energy of concretes with basalt fibre. *Constr. Build Mater* 50 (2014) 95–101.
- 16 J.M.L Reis, A.J.M Ferreira. Assessment of fracture properties of epoxy polymer concrete reinforced with short carbon and glass fibres. *Constr. Build Mater.* 18 (2004) 18:523–8.
- 17 K. Neocleous, H. Angelakopoulos, K. Pilakoutas, M. Guadagnini, Fibre-reinforced roller compacted concrete transport pavements, *Proc. Inst. Civ. Eng. Transp.* 164 (2011) 97–109.
- 18 H. Hu, P. Papastergiou, H. Angelakopoulos, M. Guadagnini, K. Pilakoutas, Mechanical properties of SFRC using blended Recycled Tyre Steel Cords (RTSC) and Recycled Tyre Steel Fibres (RTSF), *Constr. Build. Mater.* 187 (2018) 553–564.
- 19 M. O. Kim, A. Bordelon, Determination of total fracture energy for fibre-reinforced concrete. American Concrete Institute, ACI Special Publication 2015. 55-69.
- 20 J. Lubliner, J. Oliver, S. Oller, E. Onate, A plastic-damage model for concrete, *Int. J. Solids Struct.* 25 (3) (1989) 299–326.
- 21 Abaqus, Abaqus User Manual (Version 6.14), 2014.
- 22 D.J. Burnett, H.L. Schreyer, A mesh objective method for modelling crack propagation using the smeared crack approach, *Int. J. Numer. Methods Eng.* 117 (2019) 574–603.
- 23 R. Yu, P. Spiesz, H.J.H. Brouwers, Development of Ultra-High Performance Fibre Reinforced Concrete (UHPRFC): towards an efficient utilization of binders and fibres, *Constr. Build. Mater.* 79 (2015) 273–282.
- 24 A. Le Hoang, E. Fehling, Influence of steel fibre content and aspect ratio on the uniaxial tensile and compressive behavior of ultra-high performance concrete, *Constr. Build. Mater.* 153 (2017) 790–806.

- 25 T. Stengel, Effect of Surface Roughness on the Steel Fibre Bonding in Ultra High Performance Concrete (UHPC), in: *Nanotechnol. Constr.* 3, 2009.
- 26 B.A. Graybeal, F. Baby, Development of direct tension test method for ultra-high-performance fibre-reinforced concrete, *ACI Mater. J.* 110 (2013) 177–186. doi:10.14359/51685532.
- 27 A.M.T. Hassan, S.W. Jones, G.H. Mahmud, Experimental test methods to determine the uniaxial tensile and compressive behaviour of Ultra High Performance Fibre Reinforced Concrete(UHPFRC), *Constr. Build. Mater.* 37 (2012) 874–882.
- 28 S.H. Park, D.J. Kim, G.S. Ryu, K.T. Koh, Tensile behavior of ultra-high performance hybrid fibre reinforced concrete, *Cem. Concr. Compos.* 34 (2012) 172–184.
- 29 D.J. Kim, S. El-Tawil, A.E. Naaman, Rate-dependent tensile behavior of high performance fibre reinforced cementitious composites, *Mater. Struct. Constr.* 42 (2009) 399–414.
- 30 V. Savino, L. Lanzoni, A.M. Tarantino, M. Viviani, Tensile constitutive behavior of high and ultra-high performance fibre-reinforced-concretes, *Constr. Build. Mater.* 186 (2018) 525–536.
- 31 Y. Kusumawardaningsih, E. Fehling, M. Ismail, A.A.M. Aboubakr, Tensile strength behavior of UHPC and UHPFRC, *Procedia Eng.* 125 (2015) 1081–1086.
- 32 S. Qian, & V.C. Li. Simplified inverse method for determining the tensile strain capacity of strain hardening cementitious composites. *Journal of Advanced Concrete Technology*, 5(2) (2007) 235–246.
- 33 J. Á. López, P. Serna, J. Navarro-Gregori, H. Coll, H. A simplified five-point inverse analysis method to determine the tensile properties of UHPFRC from unnotched four-point bending tests. *Composites Part B: Engineering*, 91 (2016) 189–204.
- 34 L. Ostergaard, R. Walter, & J. F. Olesen, (2005). Method for determination of tensile properties of engineered cementitious composites (ECC). *Proceedings of ConMat'05*.
- 35 H. Tlemat, K. Pilakoutas, K. Neocleous, Modelling of SFRC using inverse finite element analysis, *Mater. Struct. Constr.* 39 (2006) 221–233.
- 36 Z. Wang, H. Hu, I. Hajirasouliha, M. Guadagnini, K. Pilakoutas, Tensile stress-strain characteristics of rubberised concrete from flexural tests, *Constr. Build. Mater.* 236 (2020) 117591.
- 37 T. Kanakubo, Tensile characteristics evaluation method for ductile fibre-reinforced cementitious composites. *Journal of Advanced Concrete Technology*, 4 (2006), 3–17.

- 38 S.C. Lee, H.B. Kim, C. Joh, Inverse analysis of UHPFRC beams with a notch to evaluate tensile behavior, *Adv. Mater. Sci. Eng.* 2017 (2017).
- 39 The International Federation for Structural Concrete (fib). Model Code 2010. *Fib Model Code for Concrete Structures* 2010.
- 40 BS EN 14651, Test method for metallic fibred concrete — Measuring the flexural tensile strength (limit of proportionality (LOP), residual), *Br. Stand. Inst.* 3 (2005) 1–17.
- 41 BS EN 12390-2:2009: Testing hardened concrete. Making and curing specimens for strength tests, BSI 389 Chiswick High Road, London W4 4AL, UK. (2009).
- 42 BSI, EN 12390-3: Testing hardened concrete, Part 3: Compressive strength of test specimens, BSI 389 Chiswick High Road, London W4 4AL, UK. (2013).
- 43 BSI, EN 12390-13: Testing hardened concrete, Part 3: Determination of secant modulus of elasticity in compression, BSI 389 Chiswick High Road, London W4 4AL, UK. (2013).
- 44 BS EN 12390-5 2009: Testing hardened concrete - Part 5: Flexural strength of test specimens. BSI 389 Chiswick High Road, London W4 4AL, UK. (2013)
- 45 A. Hillerborg. The theoretical basis of a method to determine the fracture energy G_f of concrete. *Mater Struct.* 18 (1985) 291–6.
- 46 RILEM TC 50-FMC. Determination of the fracture energy of mortar and concrete by means of three-point bend tests on notched beams. *Mater Struct*;18 (1985) 285–90.
- 47 K. Wille, S. El-Tawil, A.E. Naaman, Properties of strain hardening ultra-high performance fibre reinforced concrete (UHP-FRC) under direct tensile loading, *Cem. Concr. Compos.* 48 (2014) 53–66.
- 48 M.A. Al-Osta, M.N. Isa, M.H. Baluch, M.K. Rahman, Flexural behavior of reinforced concrete beams strengthened with ultra-high performance fibre reinforced concrete, *Constr. Build. Mater.* 134 (2017) 279–296.
- 49 H. Othman, H. Marzouk, Applicability of damage plasticity constitutive model for ultra-high performance fibre-reinforced concrete under impact loads, *Int. J. Impact Eng.* 114 (2018) 20–31.

- 50 M. Shafieifar, M. Farzad, A. Azizinamini, Experimental and numerical study on mechanical properties of Ultra High Performance Concrete (UHPC), *Constr. Build. Mater.* 156 (2017) 402–411.
- 51 M. Farzad, M. Shafieifar, A. Azizinamini, Experimental and numerical study on bond strength between conventional concrete and Ultra High-Performance Concrete (UHPC), *Eng. Struct.* 186 (2019) 297–305.
- 52 L. Chen, B.A. Graybeal, Modeling structural performance of ultrahigh performance concrete I-girders, *J. Bridg. Eng.* 17 (2012) 754–764.
- 53 H. Angelakopoulos, P. Papastergiou, K. Pilakoutas, Fibrous roller-compacted concrete with recycled materials - Feasibility study, *Mag. Concr. Res.* 67 (2015) 801–811.
- 54 A. Baricevic, D. Bjegovic, M. Skazlic, Hybrid fibre-reinforced concrete with unsorted recycled-tire steel fibres, *J. Mater. Civ. Eng.* 29 (2017).
- 55 A.B. Graybeal, Compression Response of a Rapid-Strengthening Ultra-High Performance Concrete Formulation, FHWA-HRT-12-064, Fed. Highw. Adm. (2012).
- 56 S. Abbas, A.M. Soliman, M.L. Nehdi. Exploring mechanical and durability properties of ultra-high performance concrete incorporating various steel fibre lengths and dosages, *Constr. Build. Mater.* 75 (2015) 429–441.
- 57 Z. Wang, H. Hu, I. Hajirasouliha, M. Guadagnini, K. Pilakoutas, Tensile stress-strain characteristics of rubberised concrete from flexural tests, *Constr. Build. Mater.* 236 (2020) 117591.
- 58 G.R. Irwin. (1958). "Fracture." *Encyclopaedia of physics*. Vol VI, Springer, Berlin Germany.
- 59 Hillerborg A. Theoretical basis of method to determine fracture energy G_F of concrete. *Mater. Struct.* 1985; 18:291.
- 60 M.T. Kazemi, H. Golsorkhtabar, M.H.A. Beygi, M. Gholamitabar, Fracture properties of steel fibre reinforced high strength concrete using work of fracture and size effect methods, *Constr. Build. Mater.* 142 (2017) 482–489.
- 61 M. Gesoglu, E. Güneyisi, G.F. Muhyaddin, D.S. Asaad, Strain hardening ultra-high performance fibre reinforced cementitious composites: Effect of fibre type and concentration, *Compos. Part B Eng.* 103 (2016) 74–83.

- 62 Z. P. Bazant, and B. H. Oh, Crack band theory for fracture of concrete. *Mater. Struct.*, RILEM, Paris, France, 16, (1983) 155-177.
- 63 Z.P. Bažant, G. Pijaudier-Cabo Measurement of Characteristic Length of Nonlocal Continuum, *Journal of Engineering Mechanics* 115 (1989) 755-767.
- 64 SIA 2052: 2014-12. (n.d.). Béton Fibré Ultra-Performant (BFUP): Matériaus, dimensionnement et exécution. Draft.
- 65 S. Paschalis, A. Lampropoulos, Fibre content and curing time effect on the tensile characteristics of ultra-high performance fibre reinforced concrete, *Struct. Concr.* 18 (2017) 577–588.

Chapter 4: Shear Behaviour of E-UHPC Containing Recycle Steel Fibres and Design of E-UHPC Screw Piles

M.N. Isa, K. Pilakoutas, M. Guadagnini, Shear Behaviour of E-UHPFRC Containing Recycle Steel Fibres and Design E-UHPFRC Screw Piles, Construction and Building Materials – Accepted for publication

Author Contribution Statement

M.N. Isa: Conceptualisation, Methodology, Investigation, Formal analysis, Writing - original draft.

Kypros Pilakoutas: Supervision, Writing - review & editing. **Maurizio Guadagnini:** Supervision, Writing - review & editing.

ABSTRACT

The shear behaviour of Eco-Efficient Ultra-High Performance Concrete (E-UHPFRC) has not been investigated until now and this limits the potential applications for this material that uses low-cost and sustainable constituent materials including Recycled Tyre Steel Fibres (RTSF) and Recycled Tyre Steel Cords (RTSC). The potentially high shear resistance of E-UHPFRC could enable its use in more complex applications such as screw piles, something not easily achievable with conventional concrete. This study presents experimental and numerical work to address this research gap. It provides a detailed account of the experimental testing of 13 E-UHPFRC mixes containing various dosages of recycle steel fibres. Prismatic specimens are tested under an asymmetric four-point loading configuration and their deformation response is used to investigate the shear performance of the studied mixes. The shear stress – strain behaviour as well as shear modulus is determined. The results show that mixes containing RTSC can develop a high shear strength at the level of their flexural strength and comparable to that obtained from mixes with manufactured steel fibres. While mixes containing RTSF overall have lower shear strengths, high shear strengths can be achieved by using higher dosages of RTSF or using hybrid mixes of RTSF and RTSC. Shear strength prediction models based on flexural properties and fibres dosage are proposed for design purposes. An E-UHPFRC screw pile design model is developed for screw pile use in foundations of light and medium weight structures. Theoretical and physical modelling of the E-UHPFRC screw pile model is carried out and a design guideline is proposed. E-UHPFRC screw piles

can offer various practical advantages, including rapid installation, immediate load carrying capability, minimal site disturbance, resistance to wide load applications, i.e. compression and tensile loads, and will solve the corrosion vulnerability of steel screw piles.

Keywords: Shear Strength, Eco-Efficient Ultra-High Performance Concrete, Recycle Tyre Steel Cords, Recycled Tyre Steel Fibres, Screw Piles, Installation Torque

4.1 Introduction

Owing to its high strength and exceptional durability, Ultra-High Performance Fibre Reinforced Concrete (UHPRFC) has significant structural potential and its use can lead to the development of new and sustainable applications in the construction industry [1-4]. One such application is a more durable alternative to steel screw piles, especially for marshy or corrosive ground conditions, which are currently the only possible solution as the shear/torsional resistance of conventional concrete is relatively low.

Currently, the use of UHPRFC in the construction industry is limited due to lack of adequate understanding of the material behaviour and availability of design guidelines, as well as the high initial cost and high carbon footprint of cement and steel fibres [5,6]. Recent advancements in the field, however, have led to the development of Eco-Efficient Ultra-High Performance Concrete (E-UHPRFC) [5], which uses low-cost and sustainable constituent materials to enhance the environmental credentials of UHPRFC and increase its demand as a primary construction material. E-UHPRFC uses conventional sand, Ground Granulated Blast Furnace Slag (GGBS) to reduce the cement content, as well as Recycled Tyre Steel Fibres (RTSF) and Recycled Tyre Steel Cords (RTSC) in lieu of conventional Manufactured Steel Fibres (MSF) (the costliest constituent of UHPRFC). The authors have demonstrated that E-UHPRFC provides significant sustainability benefits, while offering similar mechanical properties (flexural and tensile behaviour) to existing UHPRFCs, and have developed design guidelines for flexural E-UHPRFC members [5]. To extend the range of uses of this material, however, it is important to assess the shear/torsional behaviour and performance of E-UHPRFC.

The development of high shear stresses arising from both shear and torsional actions can lead to brittle and catastrophic failures in concrete elements [8]. In the design of conventional reinforced concrete and Fibre Reinforced Concrete (FRC) elements, shear is resisted by providing reinforcement in the form of stirrups. However, in slender elements or sections subjected to high shear stresses, reinforcement congestion is a major concern, as it is practically impossible to accurately install the reinforcing steel and also achieve adequate compaction of concrete around the reinforcement. E-UHPRFC, being a self-flowing concrete with high tensile strength, has the capacity to eliminate or reduce the amount of steel reinforcement needed in such structural elements or sections.

The shear behaviour of UHPFRC, however, has not been widely explored and this may be partly due to the lack of a universally accepted testing method [9-12] and the difficulties in developing “pure shear” at the desired cross section with minimal or no influence from other actions (e.g. bending) [11]. Several test set-up configurations have been proposed by various researchers, including: four-point asymmetric test with V-shaped indentations [10], four-point asymmetric test with two opposite notches [11-13], double shear test [14,15], push-off compression test [16], axisymmetric punch through shear test [17] etc. The choice of loading arrangement depends on practicality and ease of preparation. In this research, the four-point asymmetric test (a modification of the Iosipescu setup [18]) with two opposite notches that creates a constant shear force and nearly zero bending stress in the fracture plane is adopted. The few studies on shear behaviour of UHPFRC identify the effect of some key parameters, but more in-depth investigations are needed to develop a better understanding of this response. Wu et. al [19] investigated the influence of micro steel fibre volume and stirrup reinforcement ratio on the shear transfer behaviour of UHPFRC from push-off tests and found that shear strength and shear slip increase with an increase in fibre volume, while crack width decreases. Ngo et. al [20], investigated the shear behaviour of UHPFRC prisms with fixed ends and loaded with two point loads along the span with varying span-to-depth ratio and found that shear resistance of UHPFRC also depends on the span-to-depth ratio (lower span-to-depth ratio yields higher strength).

All structures need foundations, and as population growth drives fast infrastructure development, exposure to less suitable soil conditions increases rapidly. In weak soils, especially in marshy soils and marine environments, piles are often the only foundation solution. As driving piles requires heavy equipment and can cause undesirable vibrations, screw or helical piles are often used. Screw piles differ from traditional piles in that they consist of helices, which are fixed/welded to the shaft at specific spacings, and a pointy toe to allow for easier installation into the ground [21]. Early uses of screw piles include anchorages in very soft marine soils, foundations for lightweight structures and transmission towers. Screw piles are capable of resisting both tensile and compressive loads and their anchorage is developed by the combined contribution of the helix bearing capacity and shaft shear resistance. With the development of modern installation equipment and improved practical knowledge and engineering design, screw pile applications are on the increase. Presently, screw piles are utilized for a wide range

of uplift, bearing, and/or lateral loading situations, where they are employed to support structures ranging from overhead bridges, buildings, machine and wind turbine tower foundations and more recently foundations for solar panel frames. The advantages of screw piles include: rapid installation, immediate load carrying capability, minimal site disturbance, installation in shallow groundwater and resistance to wide load applications [21].

Despite the high vulnerability of steel to corrosion, especially in marine environments and grounds with high chloride content, steel screw piles are currently the only practical solution, due to the low shear strength of conventional concrete. Although designs and patents of precast reinforced concrete screw piles existed as far back as 1911 [22-26], the use of concrete screw piles has not been successful in practice mainly because conventional concrete is inadequate in resisting the high shear stresses that develop during screw pile installation. To resist such high shear stresses, large amounts of steel reinforcement are needed leading to large sections that are uneconomical and practically impossible to drive. Although UHPFRC can overcome these weaknesses and drawbacks, the lack of design guidelines, along with the high cost and poor sustainability credentials of existing UHPFRCs, makes its application in screw piles challenging. However, recent advances in UHPFRC, and the development of E-UHPFRC that can offer the desired mechanical properties at a reduced cost, means that the development of concrete screw piles might be possible. Hence, there is a need to understand the shear performance of E-UHPFRC and establish the parameters needed for design of shear/torsional structural elements such as screw piles.

This paper examines the shear behaviour of E-UHPFRC and proposes predictive design models based on easily obtainable material properties. The potential of using E-UHPFRC for the development of more sustainable and durable screw piles is explored, and a design methodology is presented.

4.2 Experimental Program

4.2.1 Materials and Mix Proportions

For this parametric study, 12 fibre reinforced E-UHPFRC mixes were tested along with one plain reference mix. Fibre dosages of 2, 3 and 4% by volume were used in these mixes, corresponding to 157, 235.5 and 314 kg/m³, respectively. For each fibre dosage, four fibre ratios of RTSF to total fibre content were prepared: 0, 1/3, 2/3 and 1. A nomenclature based on fibre dosage and fibre type content (RTSC

= C and RTSF = F) is adopted to identify the mixes. For example, in f 2 – CCF, the first part f 2 represents the total fibre dosage of 2% and CCF shows the use of 2/3 RTSC and 1/3 RTSF, similarly f 4 – FFF indicates a mix containing 4% total fibre volume and 100% RTSF. The fibre amounts used in each mix are shown in Table 4.1.

Table 4.1: Mix description and fibre proportions (kg/m³)

Mix ID/Fibre type content	Plain	f 2 – CCC	f 2 – CCF	f 2 – CFF	f 2 – FFF	f 3 – CCC	f 3 – CCF	f 3 – CFF	f 3 – FFF	f 4 – CCC	f 4 – CCF	f 4 – CFF	f 4 – FFF
RTSC	0	157	104.7	52.3	0	235.5	157	78.5	0	314	209.3	104.7	0
RTSF	0	0	52.3	104.7	157	0	78.5	157	235.5	0	104.7	209.3	314

The constituent materials per cubic meter were: 657 kg of 52.5N type I OPC, 119 kg of microsilica with approximate particles size of 0.15 μ m, 418 kg of GGBS with approximate particle size of 15 μ m, 59 kg of polycarboxylate superplasticizer and 1051 kg of natural silica sand (HST 95) with particle size less than 500 μ m. The RTSC fibres used in this study have a nominal diameter of 0.22 mm and a direct tensile strength of approximately 2,500 MPa [5,27]. A combination of 12 and 15 mm long RTSC was used (Figure 4.1) in a 50:50 ratio as these fibre lengths were found to result in optimum performance for UHPFRC [5]. RTSF free from impurities were obtained by cleaning and sorting factory supplied RTSF. The cleaned fibres had lengths ranging from 3 to 30 mm, with an average length of 11.6 mm. The distribution and statistical properties of the RTSF are shown in Figure 4.2 and Table 4.2.

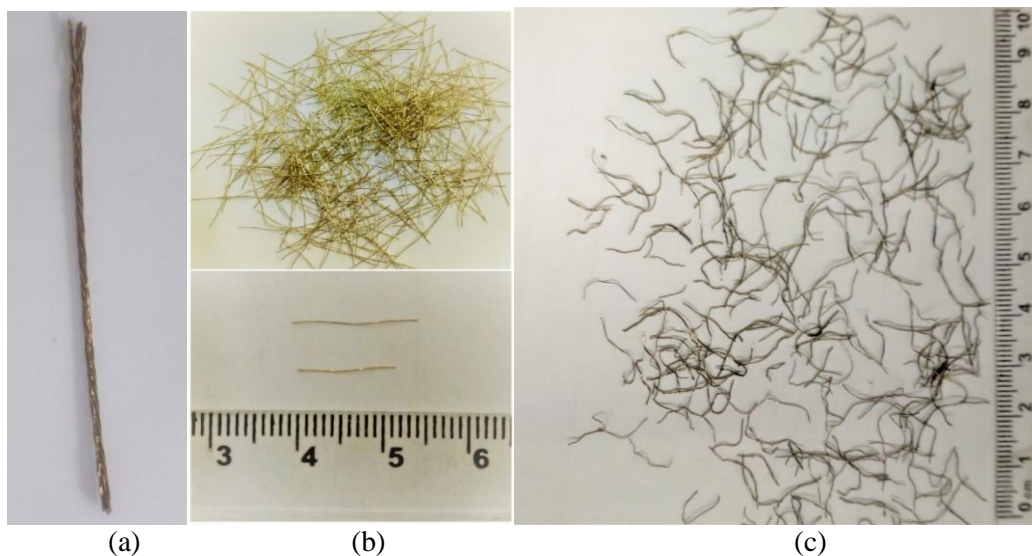


Figure 4.1: (a) Tyre steel cords (b) RTSC (c) RTSF

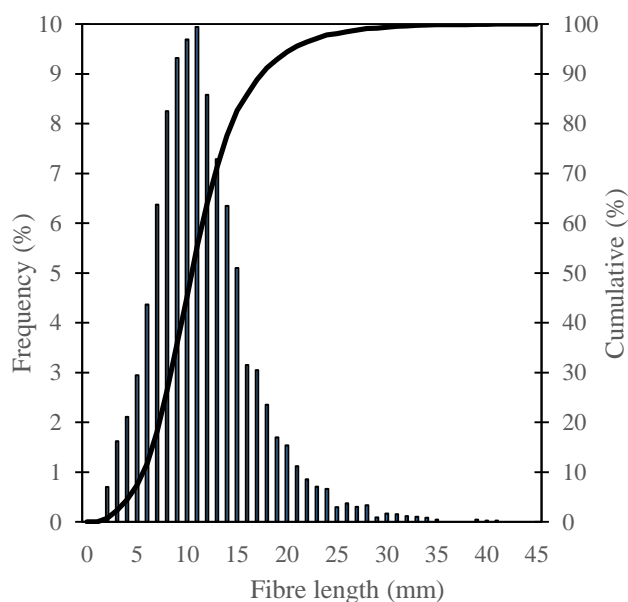


Figure 4.2: Length distribution of RTSF

Table 4.2: RTSF length distribution statistical properties

Property	< 9 mm	9 – 15 mm	>15 mm	Mean (mm)	STDEV (mm)	Variance	Kurtosis	Skewness
	35.7%	47%	17.3%	11.6	5.1	25.8	2.5	1.1

4.2.2 Mixing, Specimen Casting and Curing

Specimen preparation and curing were carried out in accordance with BS EN 12390-2:2009 [41]. The constituent materials were mixed in a pan type concrete mixer until the mix attained a self-flowing state (approximately 12 – 15 minutes). Steel fibres were then added slowly, and mixing continued for two additional minutes to ensure that the fibres were well dispersed. Three 100×200 mm cylinders and five 75×75×285 mm prisms were cast for each mix. Immediately after casting, the specimens were covered with polythene sheets to prevent moisture loss. The specimens were de-moulded after 24hrs and placed inside a curing tank at a water temperature of 20±2°C for an additional 27 days.

4.2.3 Compressive Strength and Modulus of Elasticity Test

The compressive strength and modulus of elasticity of the mixes were obtained in accordance with BS EN 12390-3: 2009 [42] and BS EN 12390-13: 2013 [43], respectively, from tests on 100 × 200 mm cylinders in a servo hydraulic universal testing machine. The axial deformation was measured using a

device consisting of two metal rings, fixed to the cylinders using spring loaded pins at a gauge length of 100 mm and equipped with three equally spaced laser displacement sensors (Figure 4.3).



Figure 4.3: Measuring device for axial deformation

4.2.4 Flexural Strength Test

The flexural behaviour of E-UHPFRC mixes was obtained by conducting three-point bending tests on $75 \times 75 \times 285$ mm prisms, in accordance to EN 14651: 2005 [40]. A specially designed aluminium yoke equipped with two Linear Variable Differential Transducers (LVDT), one on each side of the specimen, was used to measure relative midspan deflections. A clip gauge was installed across the notch to measure the crack mouth opening displacement (CMOD). The tests were carried out in an electromagnetic universal testing machine with a capacity of 300kN and using a CMOD control rate of 0.05mm/min for CMOD from 0 to 0.1mm and 0.2mm/min thereafter.

4.2.5 Shear Test

The loading configuration for the asymmetric four-point test employed in this study is shown in Figure 4.4(a). This test can be performed in a single axis universal testing machine, or even a cube crusher. A beam specimen is loaded with two compression forces and is simply supported over two points which are anti-symmetrical to the loading points (Figure 4.4(a)). A constant maximum shear action and zero or minimal bending moment develops at the fracture plane (Figure 4.4(b)).

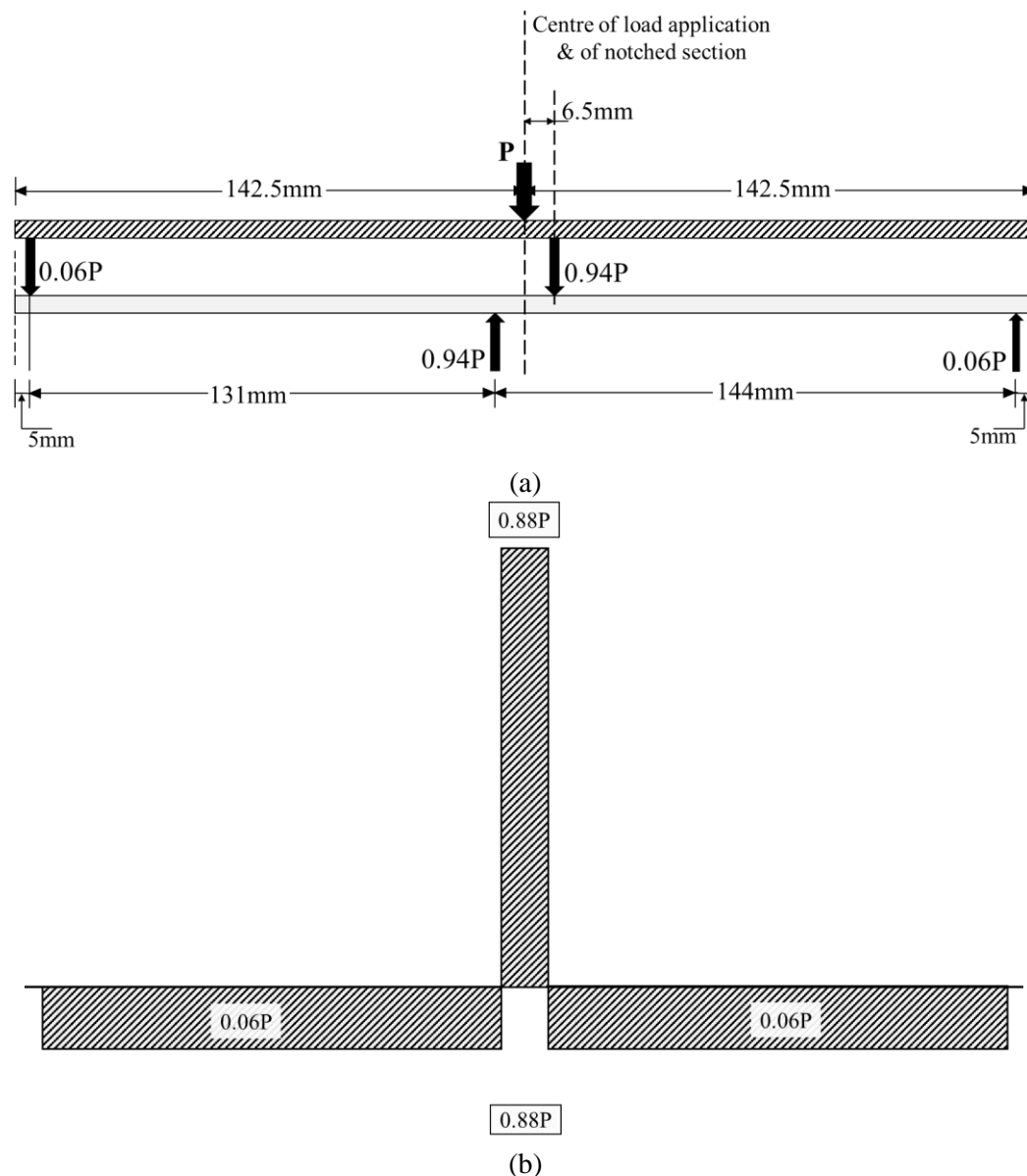


Figure 4.4: (a) Load arrangement (b) shear force diagram

To ensure specimen shear failure at the desired section and avoid compression failures below the loading plates, 3mm wide and 10mm deep notches were sawn around the fracture cross section (Figure 5b). The testing configurations and instrumentation are as shown in Figure 4.5 and 4.6. Two Linear Variable Differential Transducer (LVDTs) for measuring crack slip and crack width were fixed on each face of the specimen (Fig 4.5a).

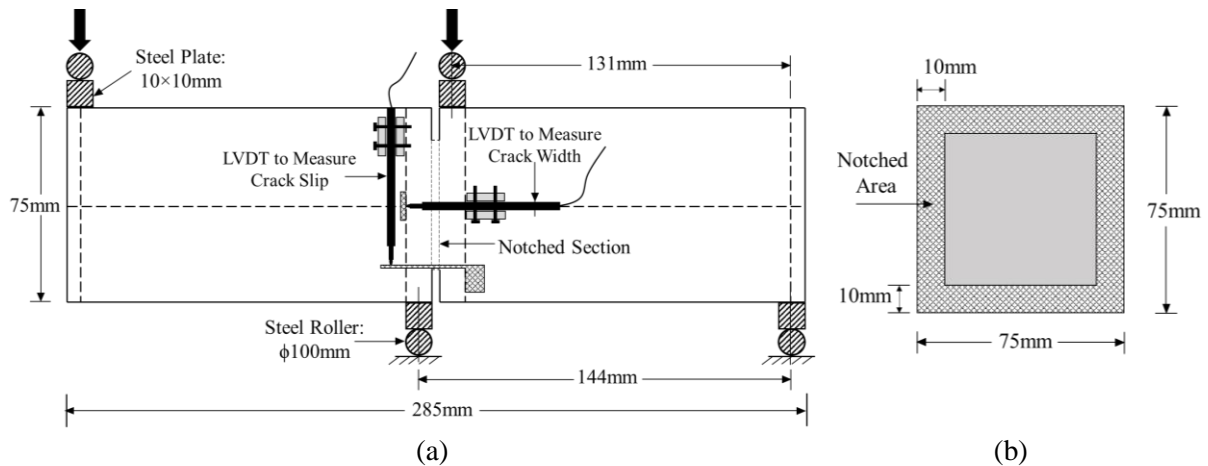


Figure 4.5: (a) Test configuration (b) cross section of notched area

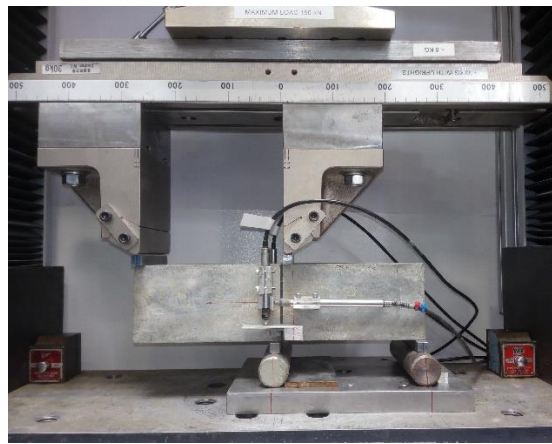


Figure 4.6: Experimental set-up

The direct shear strength of each specimen can be calculated using Eq. (4 – 1) below;

$$\tau = \frac{0.88P}{A_c} \quad (4 - 1)$$

Where τ is the shear strength in MPa, $0.88P$ is the applied shear force in N and A_c is the cross sectional area of shear plane (notched cross section). The displacement measured in the direction of the shear force, and parallel to the shear plane, is referred to as “crack slip(C_s)”, while the displacement measured across (normal) the shear plane is referred to as the “crack width (C_w)”.

4.3 Test Results and Discussions

4.3.1 Material properties

The compressive strength, modulus of elasticity, flexural and tensile strength of the tested concrete mixes are shown in Table 4.3.

Table 4.3: Mechanical properties of the tested concrete mixes

Mix ID	f'_c (MPa)	E_c (GPa)	f_{fl} (MPa)
Plain	158	49.6	6.6
f 2 – CCC	173	51.4	23.8
f 2 – CCF	171	51.5	22.4
f 2 – CFF	159	50.7	16.0
f 2 – FFF	158	50.5	14.0
f 3 – CCC	173	52.5	30.0
f 3 – CCF	169	52.1	24.9
f 3 – CFF	167	51.8	22.3
f 3 – FFF	160	51.0	18.2
f 4 – CCC	172	53.6	42.9
f 4 – CCF	169	53.2	35.5
f 4 – CFF	170	53.4	31.2
f 4 – FFF	165	52.6	26.0

All of the tested concrete mixes exhibit a compressive strength (f'_c) greater than 150MPa, and as such can be defined as UHPCs. Fibre reinforced mixes have slightly higher f'_c and E_c compared to the plain mix, with fibre dosage playing a marginal role. Mixes containing RTSC (CCC) show higher compressive strength and modulus of elasticity compared to mixes containing RTSF (FFF). This can be attributed to the non-uniform characteristics of RTSF filaments, as well as entrapped air on the surface of RTSF fibres due to their irregular shapes and remnant rubber particles attached to their surface.

The flexural strength (f_{fl}) increases as the total fibre volume increases, while for the same fibre volume f_{fl} decreases with an increase in RTSF content. Mixes containing CCC show similar, and in some cases higher, f_{fl} compared to mixes containing MSF reported in the literature [32-35], for UHPFRC

specimens cured at room temperature. The lower f_{fl} exhibited by FFF mixes can be attributed to the amount of short fibres (35.7%) with low aspect ratio (<45) that do not anchor sufficiently.

4.3.2 Shear Stress – Displacement Behaviour

Figure 4.7 shows the average load versus applied displacement curves from three specimens for each of the studied mixes.

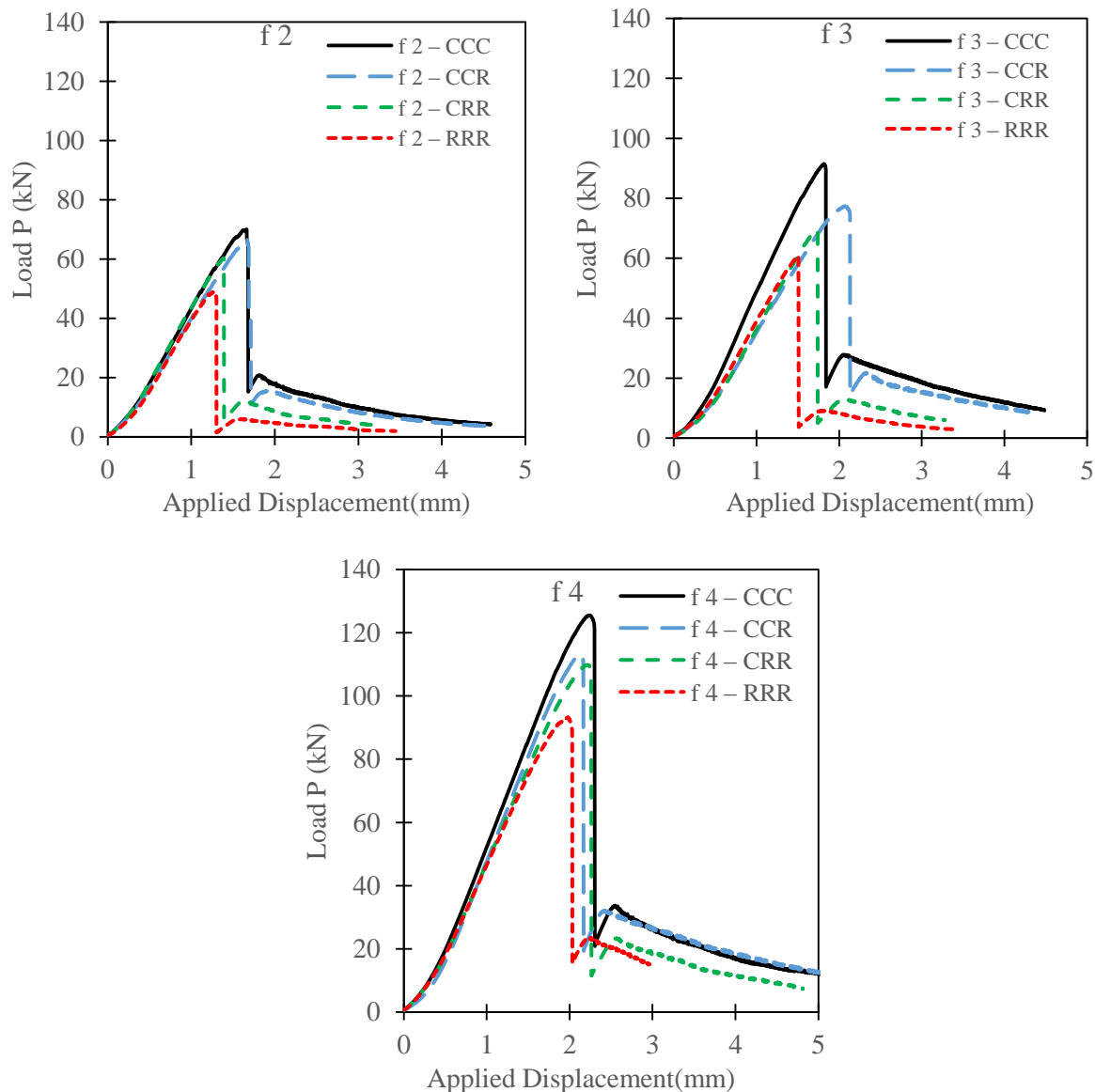
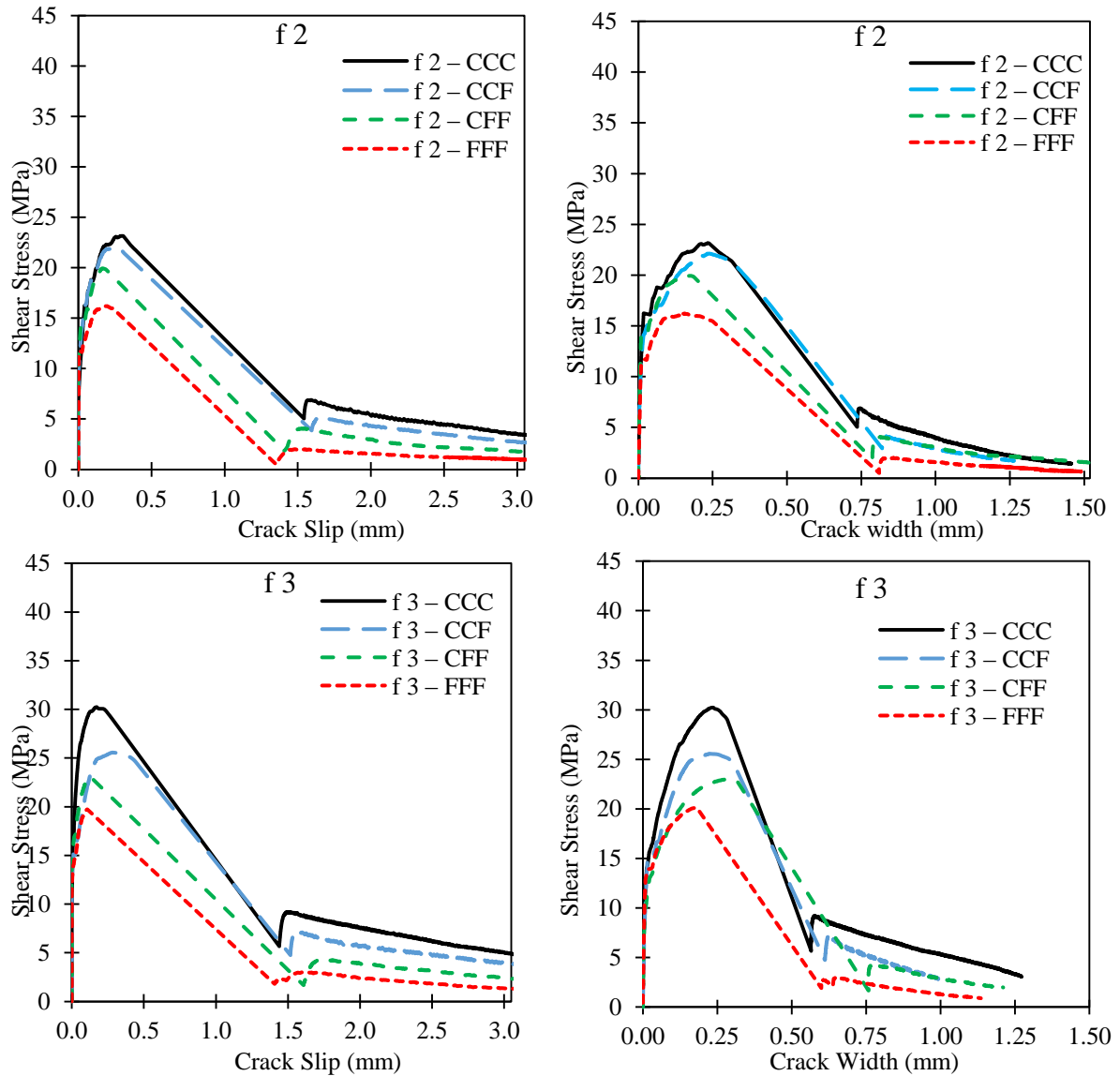


Figure 4.7: Load – Applied displacement relationship of E-UHPFRC mixes

The results show an almost linear increase in load with applied displacement up to peak load. After that, a sudden and rapid loss in load capacity takes place (with no increase in displacement). This is followed by a slight recovery in load capacity (due to contribution of fibres that have not been completely pulled out during the sudden drop phase) followed by a gradual loss in capacity as deflection increases. The

displacement at which the sudden drop in load occurs increases with increasing fibre dosage, and for the same fibre dosage, it decreases with increasing RTSF content.

Figure 4.8 shows the average shear stress versus shear slip and shear stress versus crack width displacement curves from three specimens for each of the studied mixes.



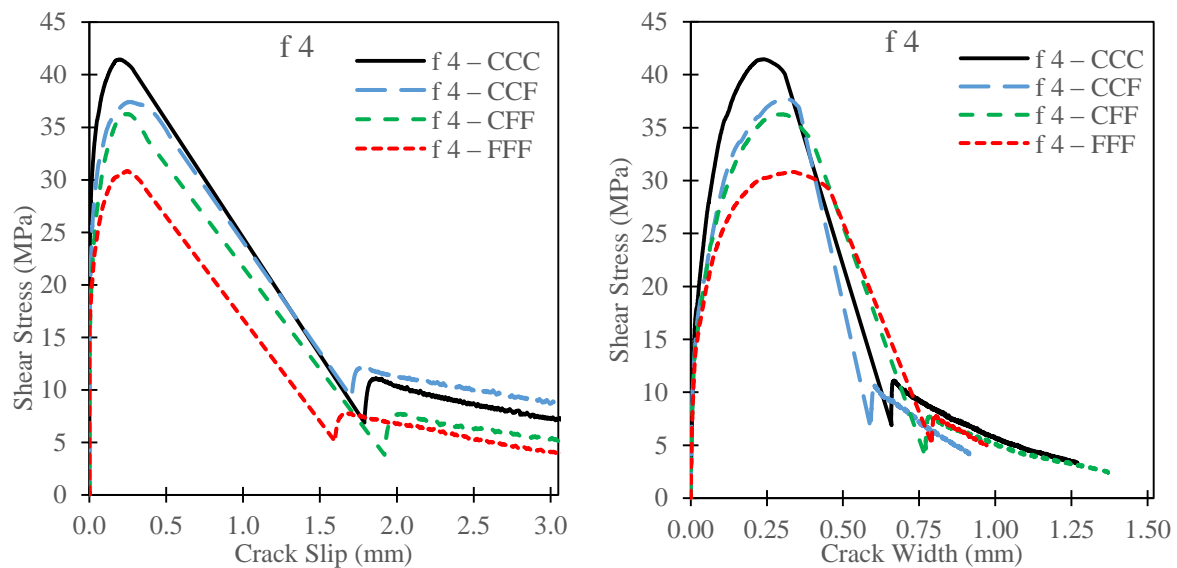


Figure 4.8: Shear behaviour of E-UHPFRC mixes: shear stress-crack slip and shear stress-crack width

The results show that both shear stress – crack slip ($\tau - C_s$) and shear stress – crack width ($\tau - C_w$) relationships are of similar type, but the crack width curve softens faster after initial cracking. All fibre reinforced mixes show significantly higher maximum shear strength (τ_{max}) compared to the plain mix (up to 2 – 5 times, with the highest for CCC mixes and higher fibre dosage). The stress – displacement relationships are linear up to the cracking stress (τ_{cr}). After cracking, the fibres are activated and the response shows a considerable strain hardening behaviour. Some softening behaviour is shown after the peak load with increasing fibre content. However, despite the high fibre dosage in some of the mixes, all specimens suffer a sudden and catastrophic loss in strength. This indicates that fibres may not be able to completely replace conventional steel reinforcement in critical sections subjected to direct shear, especially under extreme displacement demand, but can increase the load capacity and significantly reduce the amount of steel reinforcement needed. The typical behaviour of E-UHPFRC under direct shear is illustrated in Figure 4.9. At peak stress specimens reach higher C_s than C_w .

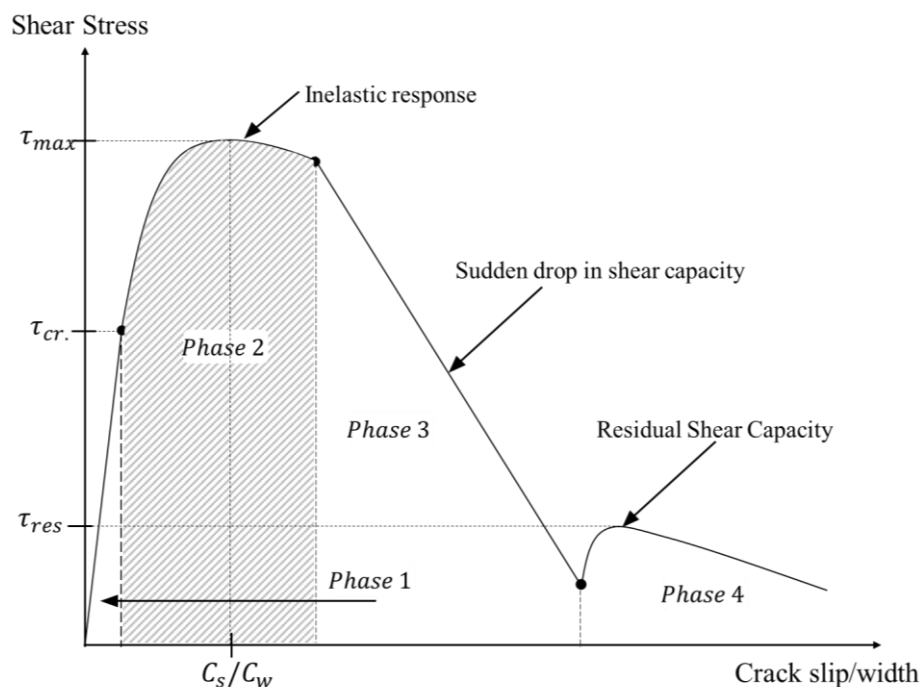


Figure 4.9: Idealised representation of E-UHPFRC shear behaviour

The shear behaviour can be described in four phases. Phase 1 represents the elastic response before crack development in the shear plane, when the fibre and concrete work in composite fashion. The shear strength at this phase τ_{cr} is similar for all mixes and can be taken as the shear strength of the plain mix. The energy absorption up to this stage is completely recoverable and displacements are very small, in the region of 0.001 – 0.005mm. Phase 2 is characterised by the development of micro cracks along the fracture zone and a prominent decrease in stiffness and increase in displacement. This phase spans the stage from cracking up to the moment before the sudden load drop and the majority of fibres spanning the shear plane are thought to be fully anchored. Towards the end of this phase, the paste/matrix in the proximity of the shear failure plane appears to be degrading and the fibres across the shear plane are thought to start to pull out. The energy absorption in this phase depends largely on the matrix-fibre bond strength and the volume of fibres across the shear plane. Phase 3 is characterised by the rapid and sudden loss in shear strength and a significant increase in displacement. This is attributed to the complete breakdown of the matrix along the shear plane and pull out of fibres across the shear fracture zone. Finally, Phase 4 is characterised by a slight recovery in shear capacity, possibly due to relaxation of the loading arrangement. For design purposes only Phase 1 and 2 need to be considered.

4.3.3 Effect of Steel Fibre Type and Volume on Shear Strength

Table 4.4 shows the average values of peak (τ_{max}) and residual shear strength (τ_{res}) for all the tested mixes (COV shown in brackets), along with the corresponding average displacements at peak strength.

Table 4.4: Shear properties of mixes

Mix ID	τ_{max} MPa (COV)	τ_{res} MPa (COV)	C_s at τ_{max}	C_w at τ_{max}
Plain	8.8 (2%)	–	–	–
f 2 – CCC	23.0 (4%)	4.9 (21%)	0.30	0.23
f 2 – CCF	22.1 (4%)	5 (25%)	0.25	0.25
f 2 – CFF	19.9 (4%)	4.1 (12%)	0.17	0.18
f 2 – FFF	16.2 (6%)	2.5 (32%)	0.19	0.16
f 3 – CCC	30.4 (5%)	8.7 (6%)	0.17	0.24
f 3 – CCF	25.7 (4%)	7.6 (13%)	0.28	0.23
f 3 – CFF	23.0 (7%)	5 (17%)	0.13	0.29
f 3 – FFF	19.7 (4%)	2.9 (14%)	0.11	0.17
f 4 – CCC	41.5 (2%)	10.5 (6%)	0.20	0.24
f 4 – CCF	37.8 (9%)	10 (6%)	0.27	0.30
f 4 – CFF	36.2 (4%)	9 (10%)	0.24	0.29
f 4 – FFF	30.8 (7%)	7.2 (18%)	0.25	0.33

Mixes containing CCC show higher τ_{max} and τ_{res} compared to mixes containing FFF. The residual strength τ_{res} for all mixes ranges between 15 – 29% of their respective τ_{max} (highest in CCC mixes and lowest in FFF mixes). The COV in τ_{max} between specimens of the same mix is very low (2 – 9%), while the COV in τ_{res} is relatively high (between 12 – 32% highest in FFF mixes), as the latter relies more heavily on the number of fibres still effectively anchored across the shear failure plane. In most cases, mixes with higher content of RTSC (CCC and CCF in particular) show higher crack slip compared to mixes containing higher RTSF content (CFF and FFF). However, there is no clear trend on the effect of fibre type and fibre dosage on crack width. The maximum shear strength, τ_{max} , for

mixes containing CCC are higher than τ_{max} reported by [19] for UHPFRC containing MSF obtained from push off tests. Despite having a lower fibre dosage and a lower cement content (657kg/m^3 vs 750kg/m^3), mix f 2 – CCC tested in this study exhibits a higher τ_{max} (23.0 MPa) than that of a mix containing 2.5% MSF fibres (20.14MPa [19]).

Figure 4.10 shows a correlation between fibre dosage and RTSF content on the maximum shear strength (τ_{max}) of E-UHPFRC mixes.

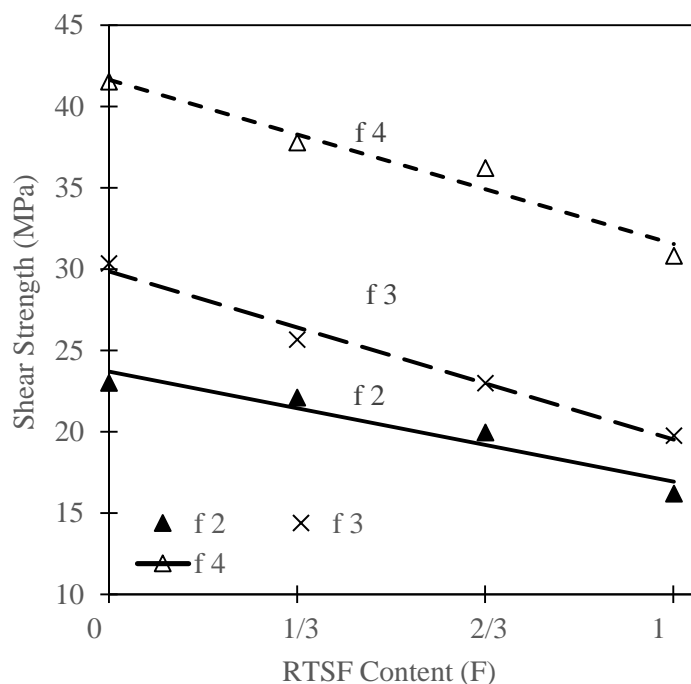


Figure 4.10: Effect of fibre volume and RTSF content and prediction model.

The results clearly show that τ_{max} increases with an increase in fibre dosage. For the same total amount of fibre (RTSF to RTSC ratio) a 22 – 32% increase in τ_{max} is recorded when fibre dosage increases from 2 to 3%. However, for a fibre dosage increase from 3 to 4% a 36 – 56% increase in τ_{max} is obtained. This non-linear increase indicates that a higher fibre content may also benefit from a higher anchorage efficiency than lower fibre dosages. The results also show that for the same fibre dosage, τ_{max} decreases as RTSF content increases and FFF mixes show 30, 35 and 26% lower τ_{max} than their corresponding CCC mixes for 2, 3 and 4% fibre dosage respectively. The reduced strength observed in RTSF mixes can be attributed to the high amount of short fibres that do not anchor as effectively across cracks. Nonetheless, FFF mixes with similar τ_{max} to CCC mixes can be achieved by using higher dosage of FFF, or hybrid mixes containing RTSC and RTSF.

4.3.4 Correlation with other Mechanical Properties

The correlation between τ_{max} and a) compressive strength (f'_c) and b) flexural strength (f_{fl}) is shown in Figure 4.11. This information provides a measure of how strong a relationship is between τ_{max} and other mechanical properties and can be used to develop predictive models to determine τ_{max} from material properties that are more easily determined.

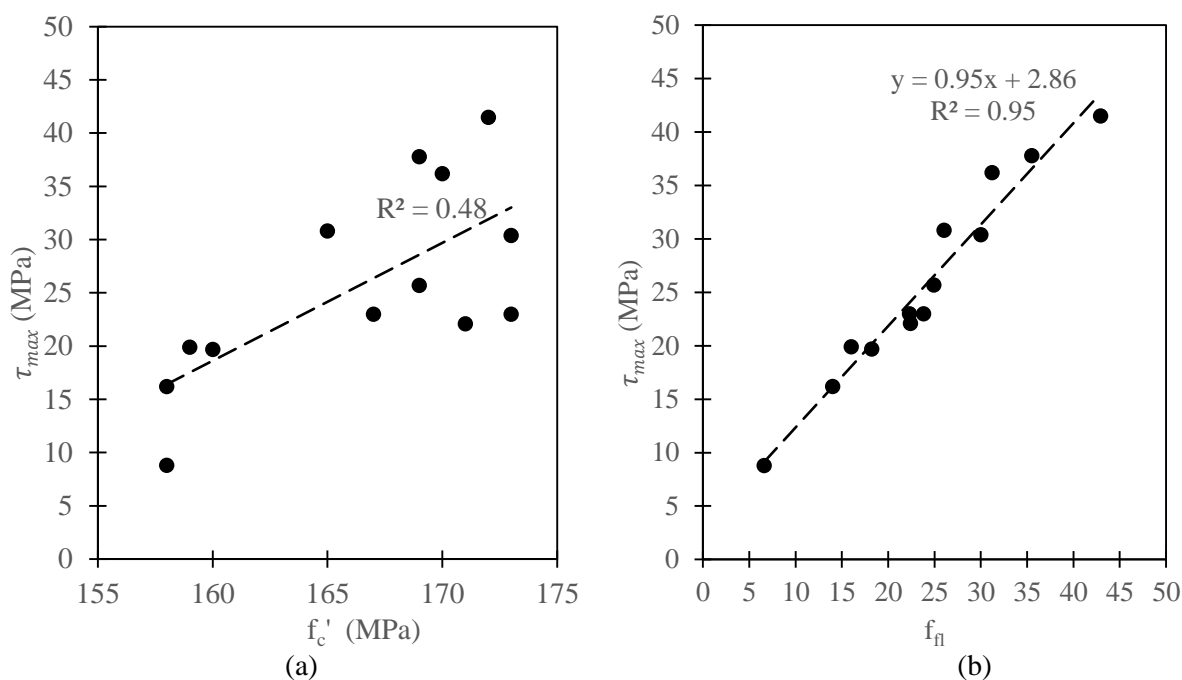


Figure 4.11: Correlation between τ_{max} and (a) compressive strength f'_c , and (b) flexural strength f_{fl}

The results show that τ_{max} does not correlate strongly with f'_c (R-squared value of 0.48). This can be due to the fact that even at very high shear stress the minimum principal stress (compressive stress component in the principal direction) is much lower than the f'_c of UHPFRC. As the material fails in tension, a strong correlation between the two peak strengths (τ_{max} and f'_c) is unlikely. On the other hand, a strong correlation is obtained between τ_{max} and f_{fl} (R-squared value of 0.95). This is due to the fact that failure of UHPFRC specimens in direct shear is controlled by the maximum principal stress (tensile stress component in principal direction), i.e. the material fails when the maximum principal stress exceeds its tensile strength (and direct tensile stress is directly proportional to f_{fl}). Eq. (4 – 2) provides a simple model for predicting the maximum shear stress for design purposes τ_d of E-UHPFRC based on f_{fl} .

$$\tau_d = 1.1f_{fl} \quad (4 - 2)$$

The factor 1.1 in Eq. (4 – 2) was determined on the basis of a regression analysis as shown in Table 4.5 and Figure 4.12.

Table 4.5: Ratio of experimental τ_{max} to f_{fl} for the tested mixes

ID	Plain	f 2 – CCC	f 2 – CCF	f 2 – CFF	f 2 – FFF	f 3 – CCC	f 3 – CCF	f 3 – CFF	f 3 – FFF	f 4 – CCC	f 4 – CCF	f 4 – CFF	f 4 – FFF	Average	S.D
$\left(\frac{\tau_{max}}{f_{fl}}\right)$	1.3	1.0	1.0	1.2	1.2	1.0	1.0	1.0	1.1	1.0	1.1	1.2	1.2	1.1	0.11

Figure 4.12 shows correlation between τ_{max} and τ_d .

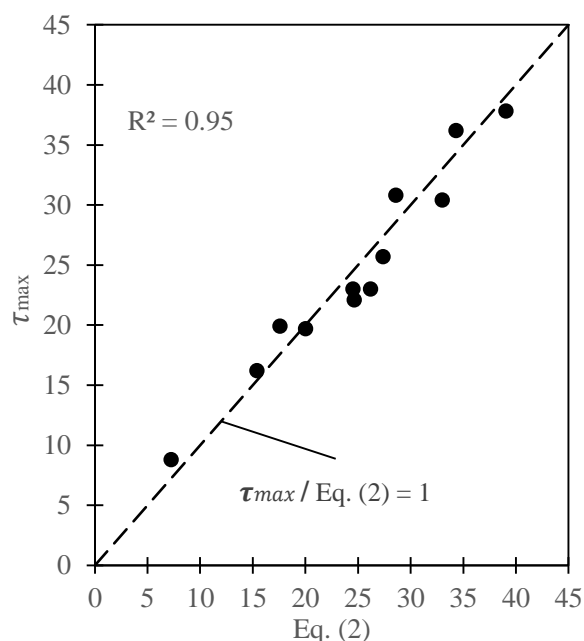


Figure 4.12: Correlation between τ_{max} and τ_d

The strong correlation between the experimentally determined values of τ_{max} and τ_d (Figure 4.12 - $R^2=0.95$), indicates that this model can accurately predict the shear strength of the studied mixes and can be used for design purposes.

4.3.5 Evaluation of Existing models

Presently, most of the existing models for predicting τ_{max} were generated from shear strength test data of FRC (containing MSF). The suitability of such models in predicting τ_{max} for E-UHPFRC is evaluated in Table 4.6 using models proposed by [37-39]. The evaluation only considers CCC mixes,

since the models are developed for mixes containing MSF, and RTSC have more in common with MSF in terms of uniformity in geometry, shape and cleanliness, which is not the case with RTSF.

Table 4.6: Evaluation of existing FRC models

ID	τ_{max} MPa	Khanlou et. al [37]		Mirsayah & Banthia [38]		Boulekbache et. al [39]	
		$\tau_{max-pred.}$	<i>Error</i>	$\tau_{max-pred.}$	<i>Error</i>	$\tau_{max-pred.}$	<i>Error</i>
f 2 – CCC	23.0	17.3	-24%	17.3	-24%	56.4	+145%
f 3 – CCC	30.4	20.6	-32%	21.5	-29%	62.4	+105%
f 4 – CCC	41.5	23.8	-43%	25.7	-38%	68.2	+64%

$$^{[37]} \tau_{max} = 0.75\sqrt{f'_c} + 400\rho^{0.9}$$

$$^{[38]} \tau_{max} = \tau_0 + 423\rho$$

$$^{[39]} \tau_{max} = 0.72f'_c{}^{0.8} + 8\rho(l_f/d_f)$$

τ_0 = Shear strength of plain mix

ρ = fibre volume dosages (i.e. $\rho = 2, 3$ and 4% for f 2, f 3 and f 4 mixes respectively)

l_f =fibre length and d_f = fibre diameter

The results show that the predictions models proposed by [37] and [38] underestimate τ_{max} of E-UHPFRC (24 – 43% and 24 – 38% respectively) while the model proposed by [39] show significant overestimation (64 – 145%). It should be pointed out that none of the models uses the tensile or flexural strength as a means of determining shear strength.

4.3.6 Proposed Model Based on Fibre Type and Dosage

For E-UHPFRC mixes containing different fibre types, such as the hybrid mixes of RTSC and RTSF in this study, prediction models based on concepts proposed by [37-39] cannot apply. Two simple models for predicting the τ_d of the studied E-UHPFRC mixes is proposed, in terms plain mix strength, fibre dosage and RTSF to total fibre ratio as shown in Eq. (4 – 3), using the flexural strength of the plain mix, respectively Correlation between experimental and predicted values are shown in Figure 4.13.

$$\tau_d = 1.1f_{fl-plain} + 786\rho \left(1 - \frac{F}{2.9}\right) \quad (4 - 3)$$

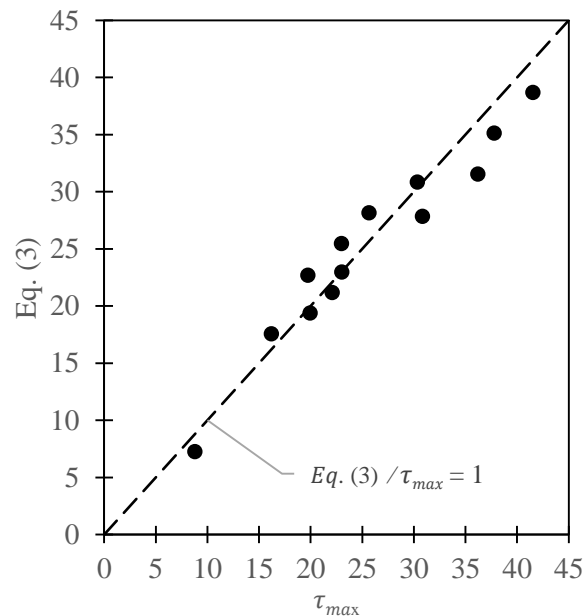


Figure 4.13: Correlation between predicted values and experimental values

The results show reasonable agreement between the predicted and experimental values with R^2 of 0.93 for both correlations in (Figure 4.13)

4.3.7 Shear Stress-Strain behaviour

The shear stress – strain ($\tau - \gamma$) behaviour of E-UHPFRC mixes is determined from the experimental shear deformations of the notched cross sections as shown in Figure 4.14. The shear strain (γ) values are calculated for Phase 1 (elastic) and Phase 2 (micro cracking) only.

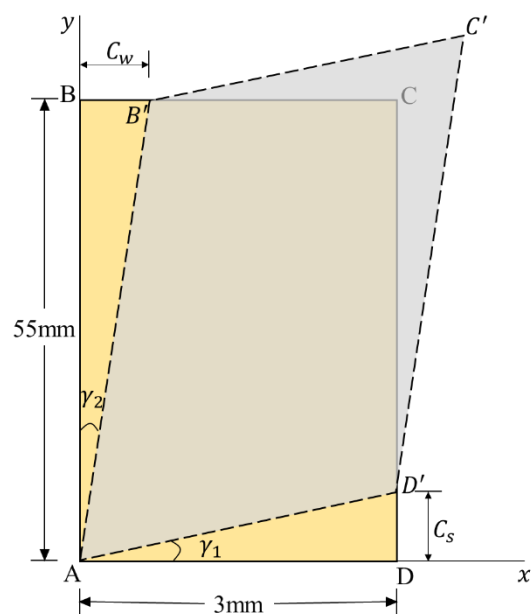


Figure 4.14: Shear deformation at notched cross section

The shear strain along the shear plane is calculated as the sum of change in angles with respect to the vertical and horizontal axes due to the horizontal and vertical deformations as shown in Eq. (4 – 4) to (4 – 5)

$$\tan \gamma_1 = \frac{C_s}{3mm} \quad \text{and} \quad \tan \gamma_2 = \frac{C_w}{55mm} \quad (4 - 4)$$

For small γ , $\tan \gamma = \gamma$. Therefore $\gamma_1 = \frac{C_s}{3mm}$ and $\gamma_2 = \frac{C_w}{55mm}$ and

$$\gamma = \gamma_1 + \gamma_2 \quad (4 - 5)$$

The $\tau - \gamma$ response of all tested fibre reinforced mixes is shown in Figure 4.15.

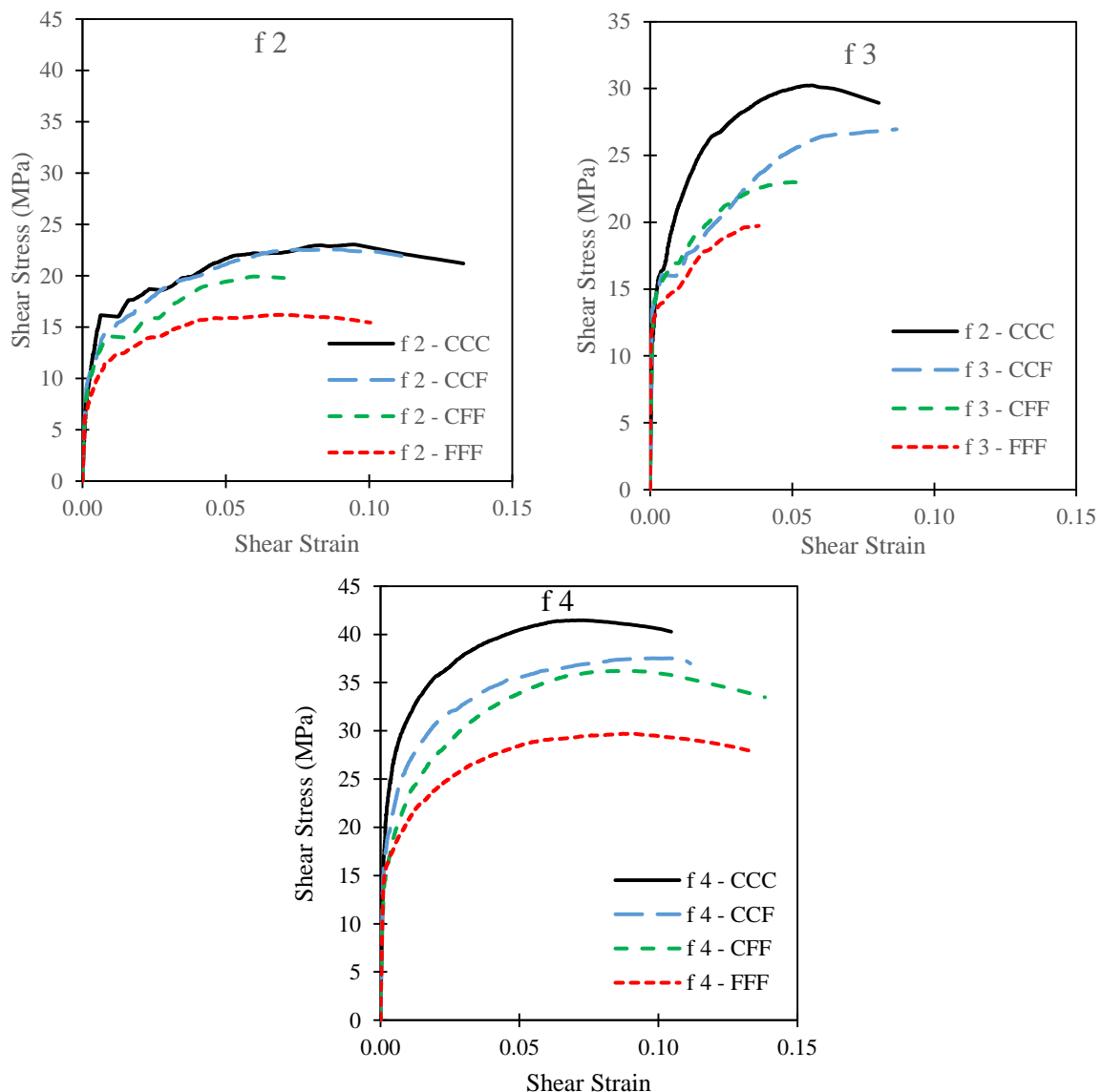


Figure 4.15: Shear stress –strain behaviour of E-UHPFRC mixes

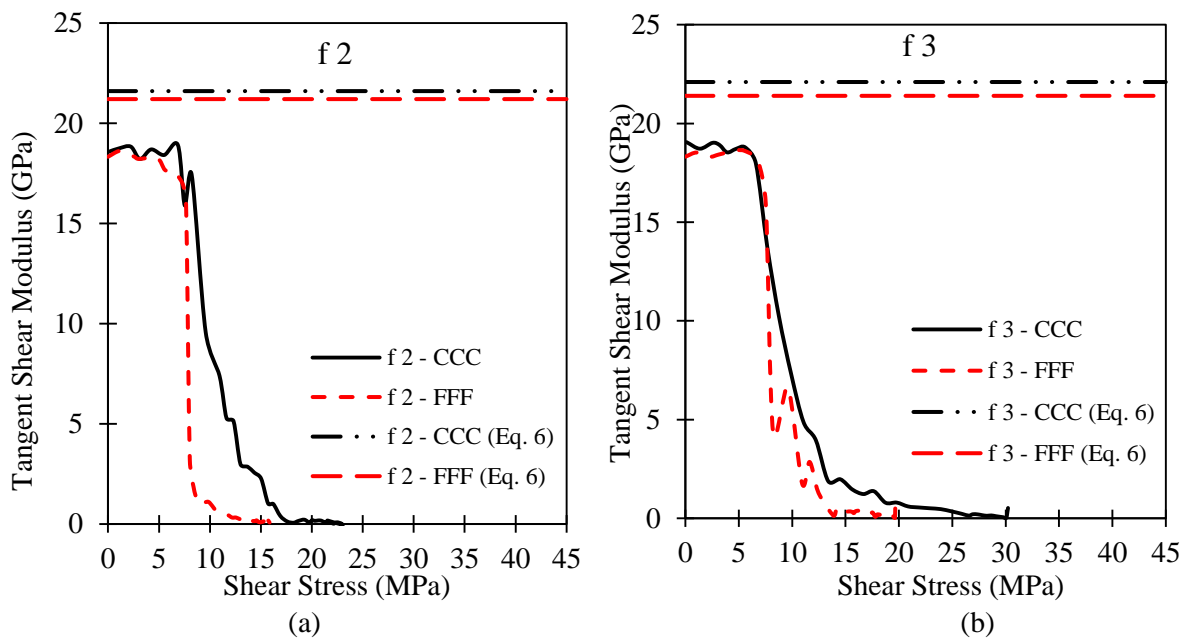
The results shown an initial linear response up to a shear stress of about 10 MPa (slightly higher than τ_{max} of the plain mix) and a shear strain (γ) of about 0.0005 for all mixes followed by a nonlinear

(hardening) response. Mixes containing f 2, f 3 and f 4 show a maximum γ of 0.13, 0.08 and 0.14 and a minimum γ of 0.07, 0.04 and 0.10, respectively. However, the effect of RTSF to total fibre dosage on γ cannot be clearly identified.

4.3.8 Shear Modulus

Figure 4.16 shows the relationship between shear modulus (obtained as tangent of the stress-strain response) and the shear stress for CCC and FFF mixes. A comparison is also made with the elastic or theoretical shear modulus, G_{Theo} (also shown in Figure 4.16) calculated based on Eq. (4 –6) using the Modulus of Elasticity (E_c) shown in Table 4.3 and a Poisson's ratio (ν) of 0.19 (in line with the values of Poisson's ratio suggested in FHWA 2006 [40] for UHPFRC, which are in the range of 0.184 - 0.199).

$$G_{Theo} = \frac{E_c}{2(1 + \nu)} \quad (4 - 6)$$



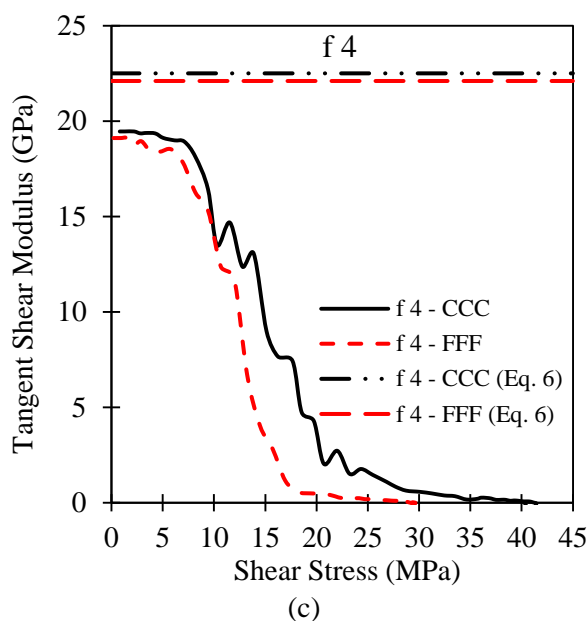


Figure 4.16: Relationship between shear modulus and shear stress for E-UHPFRC mixes

The results show that for CCC mixes the experimental shear modulus G_{exp} using the Poisson's ratio of 0.19 in the elastic phase is approximately 13, 15 and 15% lower than the theoretical shear modulus (G_{Theo}) for f 2, f 3 and f 4 mixes respectively. While for FFF mixes G_{exp} is 13, 13 and 16% lower than G_{Theo} . This may indicate that the Poisson's ratio for these mixes is slightly higher than 0.19

For the same fibre volume, CCC mixes were found to have slightly higher G_{exp} compared to FFF mixes. A significant drop in shear modulus is observed after cracking of the specimen and this usually happens between 7 – 9 MPa, which is the shear strength of the plain mix specimens.

The post cracking G_{exp} was found to increase with an increase in fibre dosage, with f 4 mixes showing the highest post cracking G_{exp} and f 2 mixes showing the least G_{exp} . Likewise, for the same fibre dosage FFF mixes show lower post cracking G_{exp} compared to its corresponding CCC mix. This can be attributed to the lower anchorage capacity of FFF, as explained earlier.

The difference between the elastic G_{exp} and G_{Theo} can be related to the effect of the test setup, which can result in varying values of Poisson's ratio. The value of the Poisson's ratio (ν) used in Eq. (4 – 12) was obtained from compression tests by [40] based on ASTM C469 [41]. However, results from this study did not give a clear value for the Poisson's ratio of the E-UHPFRC mixes. An example is given

in Figure 4.17, which shows the relationship between Poisson's ratio (calculated using Eq. (4 – 7)) and shear stress/strain for f 4 mixes.

$$\text{Poisson's Ratio } (\nu) = \frac{\text{Strain measured perpendicular to applied force}}{\text{Strain measured in the direction of applied force}} = \frac{\gamma_{trans.}}{\gamma_{long.}} \quad (4 - 7)$$

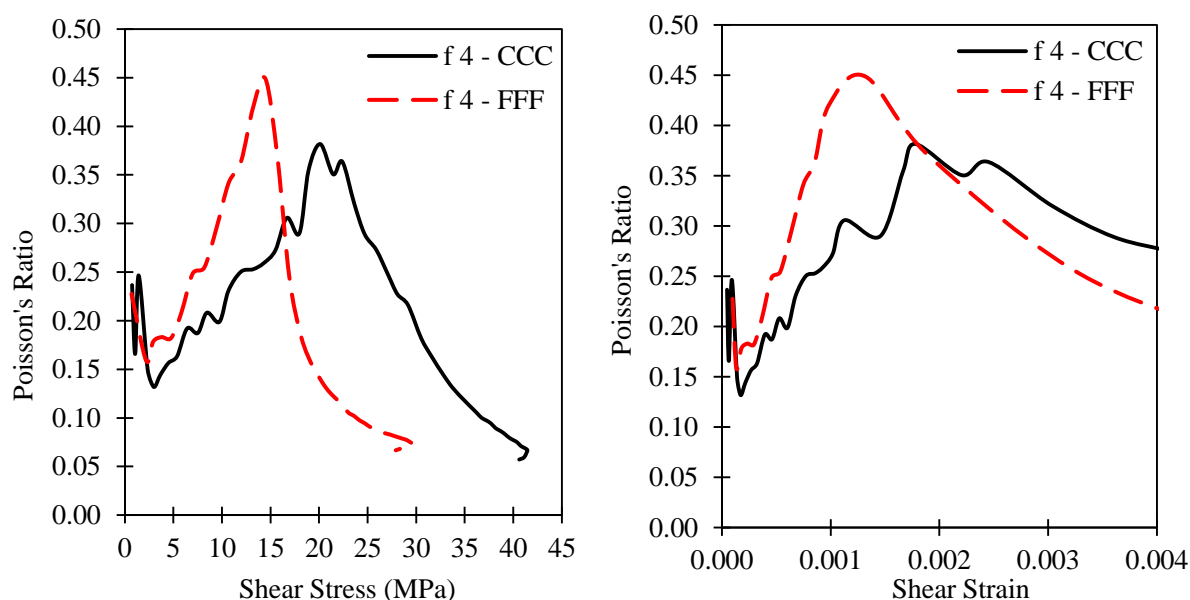


Figure 4.17: Relationship between Poisson's ratio and shear stress of E-UHPFRC mixes

It can be seen that the Poisson's ratio in the elastic phase (shear stress up to 9 MPa and strain up to 0.0005) varies significantly, but typically lies within a range of 0.13 – 0.25 (average of 0.18) for CCC and 0.16 – 0.26 (average of 0.21) for FFF mixes. Due to this variation in Poisson's ratio it can be stated that the four-point asymmetrical shear test is not exactly suitable for determining the actual Poisson's ratio of UHPFRCs. The increase in Poisson's ratio with shear stress strain observed after cracking can be attributed to the influence of steel fibres and the test arrangement, which allows the $\epsilon_{trans.}$ to increase at a higher rate than the $\epsilon_{long.}$ up to a strain of 0.001 – 0.002, after which it slows down and allows the Poisson's ratio to approach zero.

4.4 Design of Screw Piles

The design of screw piles is based on identifying the material strength and geometrical properties needed to resist the torsional stresses on the shaft arising during installation and the bending stresses along the helix due to axial loading. The determination of the installation torque needed to install a screw pile is a crucial part of the design. Underestimating the torque requirement or overestimating the torsional strength of the pile can result in incomplete pile installation, failure of the pile under torsion,

or inability to reach the desired depth, which will reduce the pile load carrying capacity. For installation of screw piles in cohesionless soils, the most comprehensive models are based on the approach developed by Ghaly and Hanna [42], who detailed a methodology for predicting the installation torques of screw anchors and screw piles. This approach has been experimentally validated for steel anchors and steel screw piles by [42-44].

The cylindrical shear method developed by [45] for estimating the axial load capacity of steel screw piles in cohesionless soils is used in this study. Various experimental and numerical studies on the capacity of screw piles [46-53] have validated the suitability of the cylindrical shear models in predicting the axial capacity of steel anchors and screw piles. These models can be extended to E-UHPFRC screw piles, provided that the correct geometrical and material parameters are used.

4.4.1 Proposed E-UHPFRC Screw Pile

Figure 4.18 shows the proposed E-UHPFRC screw pile models. These models were designed based on the “Precast Concrete Threaded Pilings” designed and patented by [26]. Two model geometries are considered: a “Partially Threaded Pile (PTP)” (Figure 4.18 (a)) and a Fully Threaded Pile (FTP) (Figure 4.18 (b)). The choice of geometry depends on the nature of loading to be resisted, as PTP can resist both compressive and uplift load, whilst FTP can effectively resist only compressive loads.

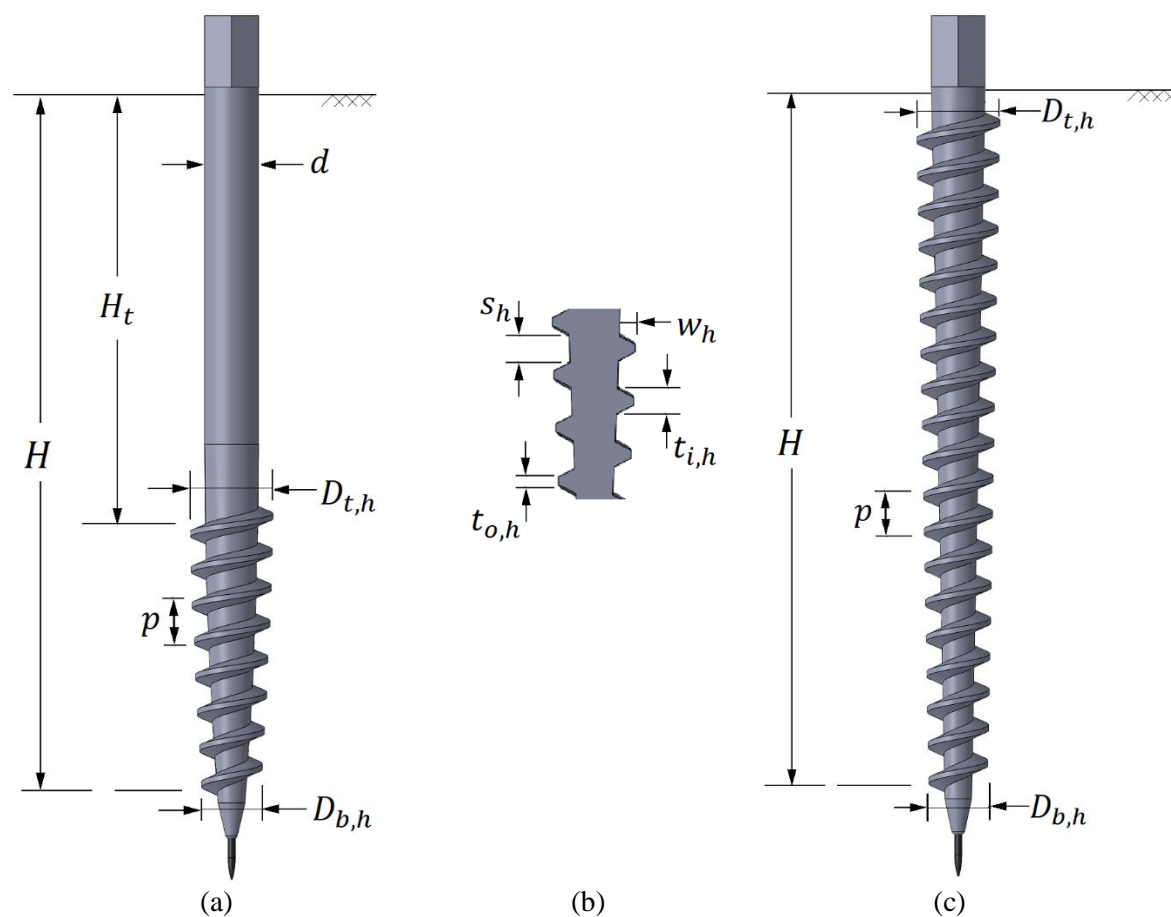


Figure 4.18: Proposed E-UHPFRC screw pile models

4.4.2 Installation Torque.

In theory the applied torque during installation of screw piles into cohesionless soils is resisted by the frictional and bearing stresses acting along the pile shaft and helices. These resistances are influenced to different degrees by the following design parameters: effective unit weight of soil (γ'), soil angle of friction (ϕ), diameter of pile shaft (d), diameter of the helix (D), pitch (p) and angle of helix (ψ), general configuration of the screw, angle of friction between pile surface and soil (μ), and shape of cutting edge.

To reduce driving resistance and achieve the desired verticality, a pilot hole is normally made into the exact position where the pile is to be installed. Similarly, to avoid punching through the soil during installation, a vertical displacement equal to the pitch of the helix is applied for every revolution of the screw pile. Equations (14) – (22) summarize the different resisting moment components during the installation of a threaded screw pile. Figure 4.19 shows a diagrammatical representation of the torque

resistances and where they act. Details of torque derivations and forces acting against rotation or offering resistance to the installation of a screw pile can be found in the work of [42-46].

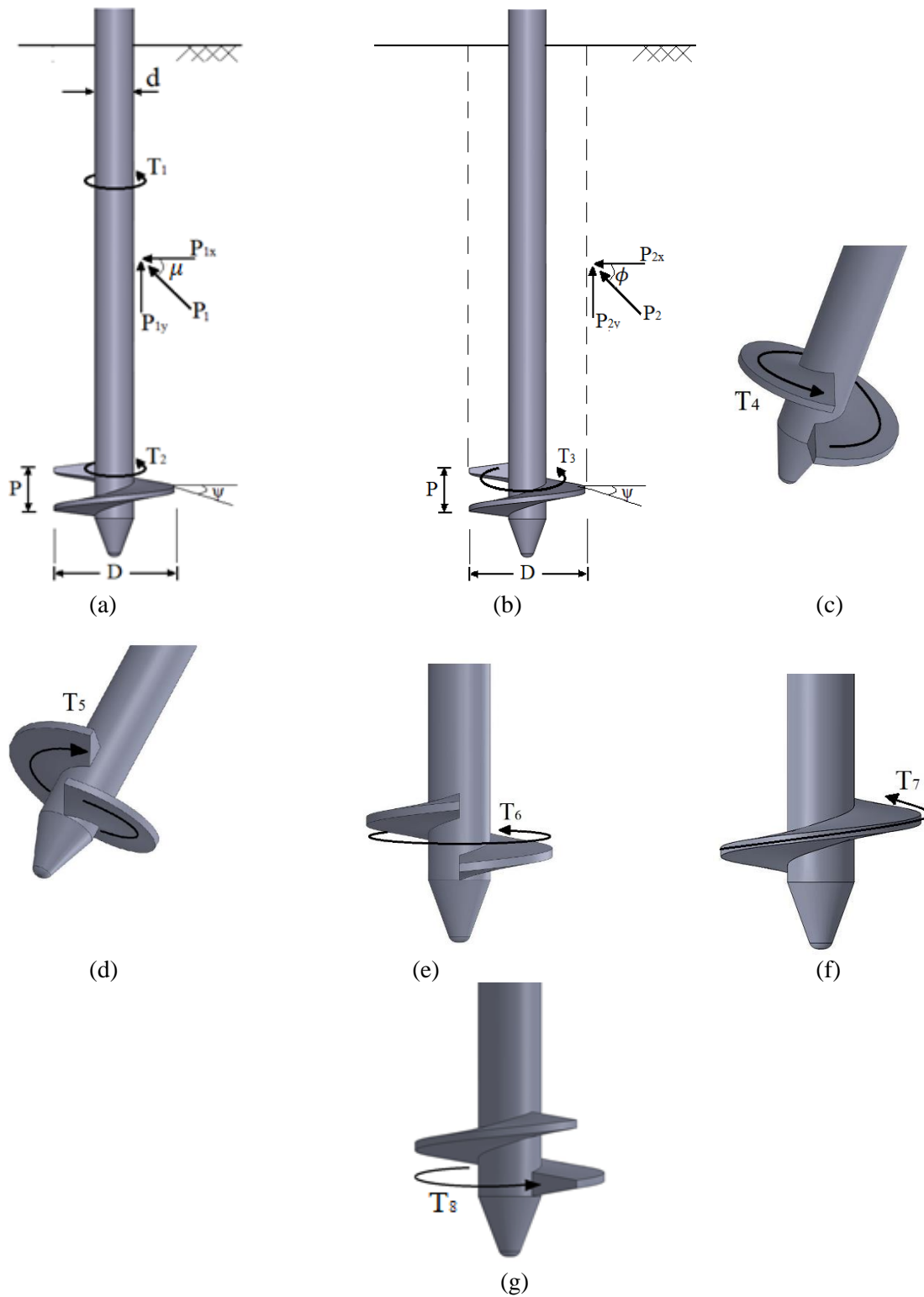


Figure 4.19: Diagrams showing locations where the various torque components act.

The torques resistances are given as follows:

- 1) Torque resistance due to passive lateral earth pressure exerted on the pile shaft over its length H_t (Figure 4.19a). This produces a moment acting on the shaft resisting its rotation T_1 (Eq. (4 – 8)) and a frictional moment acting on the n^{th} helix T_{2n} (Eq. (4 – 9)).

$$T_1 = 1/2 \gamma' H_t^2 \cdot \cos \mu \cdot K_p' \cdot K_f \cdot (\pi d) \cdot (d/2) \quad (4 - 8)$$

$$T_{2n} = 1/2 \gamma' (H_n^2 - H_{n-1}^2) \cdot \sin \delta \cdot K_p' \cdot \tan(\mu + \psi) \cdot (\pi d) \cdot (d/2) \quad (4 - 9)$$

Where K_p' = modified coefficient of passive earth pressure, with $K_p' = 0.3K_p$ as experimentally established by [42] & [47], K_p = coefficient of passive earth pressure, K_f = coefficient of friction between pile and surrounding soil ($K_f = \tan \delta$ for shaft friction and $\tan(\mu + \psi)$ for helix friction), H_n = depth of helix n (n = is the reference position starting from the top), and H_t = depth of top helix.

- 2) Torque resistance T_3 (Figure 4.19b) acting on helix due to the force of cylindrical column of sand overlaying the helix as a result of local compaction of sand layer caused by the helix during installation is shown in Eq. (4 – 10).

$$T_{3n} = 1/2 \gamma' (H_n^2 - H_{n-1}^2) \cdot \sin \phi \cdot K_p' \cdot \tan(\mu + \psi) \cdot (\pi D_n) \cdot (D_n/2) \quad (4 - 10)$$

Where D_n = Diameter of helix n

- 3) Active and passive earth pressure exerted on the upper (Figure 4.19c) and lower surface (Figure 4.19d) of helix, respectively, resulting from the downward advancement of the helix. This produces frictional resistances T_4 (Eq. (4 – 11)) and T_5 (Eq. (4 – 12)), respectively, acting against the installation torque.

For the topmost and bottommost helix Eqs. (4 – 11a) and (4 – 12a) will apply respectively, i.e. formula for single helix screw will apply.

$$T_{4n} = 1/4 \gamma' H_t \cdot K_a \cdot \pi (D_{t,h}^2 - d_t^2) \cdot \tan(\mu + \psi) \cdot (D^{n-r}/2) \quad (4 - 11a)$$

$$T_{5n} = 1/4 \gamma' H \cdot K_p \cdot \pi (D_{b,h}^2 - d_b^2) \cdot \tan(\mu + \psi) \cdot (D^{n-r}/2) \quad (4 - 12a)$$

Where $D_{b,h}$ = diameter of bottom helix and $D_{t,h}$ = diameter of top helix

For intermediary helices (i.e. excluding top and bottom helices), the torque acting on the upper and lower surface, respectively, is given by Eqs. (4 – 11b) and (4 – 12b).

$$T_{4n} = 1/4 \gamma' (H_n - H_{n-1}) \cdot K_a \cdot \pi (D_n^2 - d_n^2) \cdot \tan(\mu + \psi) \cdot (D^{n-r}/2) \quad (4 - 11b)$$

$$T_{5n} = 1/4 \gamma' (H_n - H_{n-1}) \cdot K_p \cdot \pi (D_n^2 - d_n^2) \cdot \tan(\mu + \psi) \cdot (D_{n-r}/2) \quad (4 - 12b)$$

Where K_a = coefficient of active earth pressure, K_p = coefficient of passive earth pressure, d_n = diameter of shaft at position n , and D_{n-r} is the diameter of the gyration of the helix n where concentrated forces act upon $D_{n-r} = \frac{\sqrt{D_n^2 + d_n^2}}{2}$, (i.e. radius of gyration of a ring = $\frac{\sqrt{D^2 + d^2}}{4}$)

- 4) Torque resistance T_6 (Eq. (4 – 13)), due to force resulting from the passive lateral earth pressure acting on the surface area of the screw pitch due to its inclination in the third dimension (Figure 4.19e).

$$T_{6n} = 1/2 \gamma' H_n \cdot p \cdot K_p \cdot \sqrt{(\pi D_n)^2 + p^2} \cdot (D_{n-r}/2) \quad (4 - 13)$$

- 5) Torque resistance T_7 (Eq. (4 – 14)) due to passive earth pressure exerted on the outer perimeter of the screw blade or helix (Figure 4.19f).

$$T_{7n} = \gamma' H_n \cdot t_{o,h} \cdot K_p \cdot \tan(\mu) \cdot (\pi D_n) \cdot (D_n/2) \quad (4 - 14)$$

Where $t_{o,h}$ = outer thickness of helix

- 6) Moment of resistance T_8 (Eq. (4 – 15)) due to cutting edge of helix penetrating into the soil (Figure 4.19g).

$$T_{8n} = \gamma' H \cdot N_q \cdot \left(\frac{D_{b,h}^2 - d_b^2}{2} \right) \cdot t_{h-ave} \quad (4 - 15)$$

Where $t_{h-ave} = 1/2 (t_{o,h} + t_{i,h})$ is the average cross sectional thickness of helix, $t_{i,h}$ = Inner thickness of helix and $N_q = e^{\pi \tan \phi} \tan^2 \left(45^\circ + \frac{\phi}{2} \right)$ [46] is the soil bearing capacity factor.

Therefore, the required installation torque value is given by the following expression shown in Eq. (4 – 16).

$$T = T_1 + \sum_{n=1}^i T_{2n} + T_{3n} + T_{4n} + T_{5n} + T_{6n} + T_{7n} + T_{8n} \quad (4 - 16)$$

Where i is the number of helices.

$$i = \frac{(H - H_t)}{p} + 1 \quad (\text{number of helices})$$

4.4.3 Axial Capacity

The cylindrical shear prediction models are based on the assumption that a cylindrical shear surface connecting the top and the bottom helices develops as shown in Figure 4.20. The total axial capacity in

compression and tension (or uplift) is assumed to be the contribution of the bearing resistance from the helices, the shear resistance along the cylindrical shear surface and the resistance due to friction between the shaft and the soil. In this study, the original models proposed by [45] will be used with slight modifications due the small geometrical differences between steel screw piles (based on which these models were developed) and the proposed E-UHPFRC screw piles. Figure 4.20 shows the resistance involved in the cylindrical shear approach for the partially threaded and fully-threaded E-UHPFRC models.

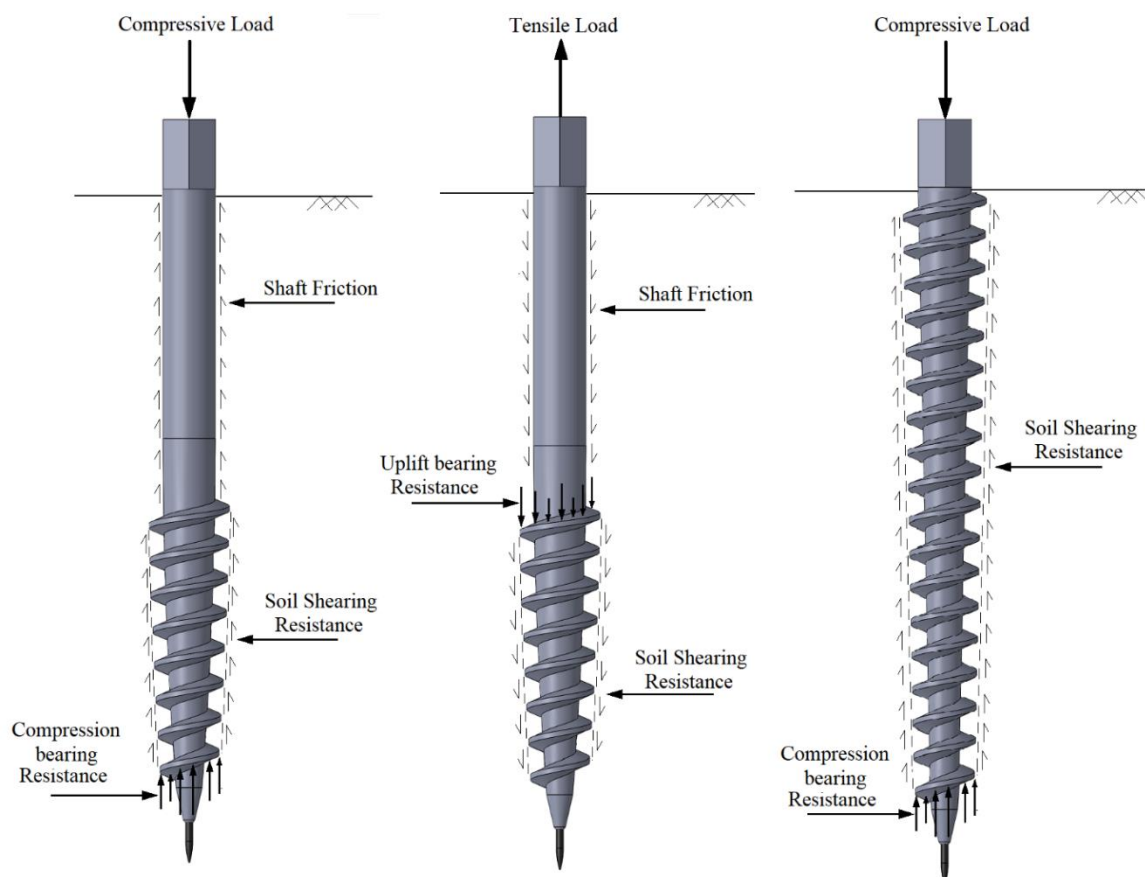


Figure 4.20: Cylindrical shear approach for determining axial capacity of screw piles

The axial capacity of a screw pile or threaded anchors in cohesionless soil is expressed by Eq. (4 – 17).

$$Q = Q_{helix} + Q_{bearing} + Q_{shaft} \quad (4 - 17)$$

Q_{helix} = Soil shearing resistance mobilised along the cylindrical failure surface

$Q_{bearing}$ = Bearing capacity of the bottom helix (in compression) or top helix (in uplift)

Q_{shaft} = Shaft resistance developed along the pile shaft

The axial capacity components for partially-threaded E-UHPFRC piles under compression (Figure 4.20a) can be expressed as shown in Eq. (4 – 18) to (4 – 20)

$$Q_{helix} = 1/2 \gamma' (H^2 - H_t^2) \cdot P_{cyl.} \cdot K_c \cdot \tan \phi \quad (4 - 18)$$

$$Q_{bearing} = \gamma' \sum_{n=1}^i H_n \cdot 1/4 \pi \{ (D^2 - d^2)_n - (D^2 - d^2)_{n+1} \} N_q \quad (4 - 19)$$

$$Q_{shaft} = 1/2 \gamma' H_t^2 \cdot P_s \cdot K'_p \cdot \tan \phi \quad (4 - 20)$$

Where γ' = effective unit weight of sand, $P_{cyl.} = \pi D_{cyl.}$ is the perimeter of soil cylinder envelope, $D_{cyl.} = 1/2 (D_{t,h} + D_{b,h})$ is the diameter soil cylinder envelope, $D_{b,h}$ = diameter of bottom helix, $D_{t,h}$ = diameter of bottom helix, $P_s = \pi d$ is the perimeter of the pile shaft, and N_q is the bearing capacity factor for cohesionless soil as given by [46] and as suggested by (Eq. (4 – 21))

$$N_q = e^{\pi \tan \phi} \tan \phi \left(45^\circ + \frac{\phi}{2} \right)^2 \quad (4 - 21)$$

Therefore, the axial capacity of partially-threaded E-UHPFRC piles in compression (Q_c) is given by Eq. (4 – 22)

$$\begin{aligned} Q_c = & 1/2 \gamma' (H^2 - H_t^2) \cdot \pi D_{cyl.} \cdot K'_p \cdot \tan \phi + 1/4 \gamma' \pi \sum_{n=1}^i H_n \{ (D^2 - d^2)_n - (D^2 - d^2)_{n+1} \} \\ & + 1/2 \gamma' H_t^2 \cdot \pi d \cdot K'_p \\ & \cdot \tan \phi \end{aligned} \quad (4 - 22)$$

For the initial sizing of screw piles, Eq. (4 – 23) can be used, but the actual compressive capacity should be re-calculate using Eq. (4 – 22).

$$\begin{aligned} Q_c = & 1/2 \gamma' (H^2 - H_t^2) \pi D_{cyl.} \cdot K'_p \cdot \tan \phi + 1/4 \gamma' H \cdot \pi (D_{b,h}^2) N_q + 1/2 \gamma' H_t^2 \cdot \pi d \cdot K'_p \\ & \cdot \tan \phi \end{aligned} \quad (4 - 23)$$

Similarly, the axial capacity of a partially-threaded E-UHPFRC piles under tension (uplift) is given by Eq. (4 – 24).

$$\begin{aligned} Q_u = & 1/2 \gamma' (H^2 - H_t^2) \pi D_{cyl.} \cdot K'_p \cdot \tan \phi + 1/4 \gamma' H \cdot \pi (D_{t,h}^2 - d^2) F_q + 1/2 \gamma' H_t^2 \cdot \pi d \\ & \cdot K'_p \tan \phi \end{aligned} \quad (4 - 24)$$

Where F_q is the breakout factor for cohesionless soils as shown in Figure 4.21 and as recommended by [45].

To calculate the diameters of intermediary helices (between top and bottom helix) and the shaft along the threaded portion (tapered portion), Eq. (4 – 25) and (4 – 26) can be used.

$$\theta = \tan^{-1} \left[\frac{\left(\frac{d_t - d_b}{2} \right)}{(H - H_t)} \right]$$

$$d_k = d_b + 2((k - 1)p \tan \theta) \quad (4 - 25)$$

$$D_{k,h} = d_k + 2w_h \quad (4 - 26)$$

Where θ = tapering angle and k = is the helix number counted from bottom, p = pitch of helix

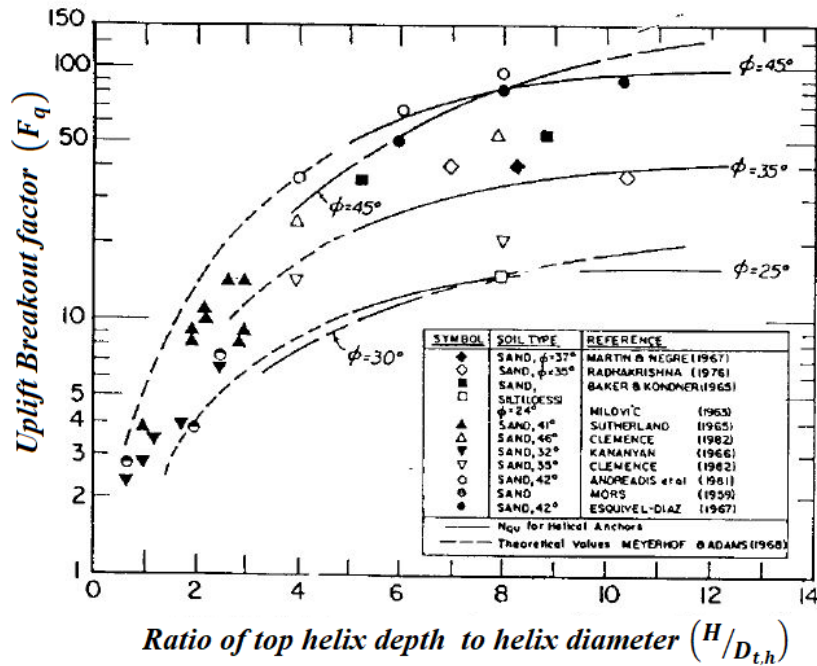


Figure 4.21: Variation of breakout factor with $H/D_{t,h}$ [45]

The fully-threaded screw pile is only suitable for resisting compression loading, as its capacity against uplift load is very low due to the tapered nature of the entire cross section and because its thread extends up to near the ground level, thus does not possess much uplift bearing resistance. Also the axial capacity in compression will have no contribution from shaft friction (i.e. $Q_{shaft} = 0$) as shown in Eq. (4 – 27).

$$Q_c = Q_{helix} + Q_{bearing}$$

$$Q_c = \frac{1}{2} \gamma' H^2 \cdot \pi D_{cyl} \cdot K_p' \cdot \tan \phi + \frac{1}{4} \gamma' H \cdot \pi D_{b,h} \cdot N_q \quad (4 - 27)$$

4.4.4 Design Assumptions

- (1) The minimum width of shaft at any point should be at least three times the fibre length of E-UHPFRC
- (2) The height of the threaded portion is $\geq 20\%$ of the pile height for partially threaded screw piles.
- (3) For geometrical computations, the helix can be assumed to be a plate.

4.4.5 Design Procedure

- (1) Calculate design axial load in compression ($Q_c = F.S. \times P_c$) and uplift ($Q_u = F.S. \times P_u$). Where F.S. = factor of safety, P_c = applied compressive load and P_u = applied uplift load
- (2) Select soil properties γ' and ϕ and calculate soil parameters μ , K_p , K'_p , K_a and N_q .
- (3) Select steel fibre length l_f (average fibre length to be used in the case of RTSF, or blend of different fibre lengths) and define the tapered profile of the threaded portion by calculating the diameter at shaft lower end d_b ($d_b \geq 3 \times l_f$) and diameter of upper end $d_t = 2 \times d_b$.
- (4) Calculate diameters for the top and bottom helices ($D_{b,h}$ and $D_{t,h}$ respectively); where $D_{b,h} = 2.5d_b$; $w_h = \frac{(D_{b,h} - d_b)}{2}$; $D_{t,h} = d_t + 2w_h$; w_h = is the helix flange width (Fig 4.18b).
- (5) Assume pitch of helix (p) and calculate helix inner and outer thickness ($t_{i,h}$ and $t_{o,h}$ respectively) using the criteria: $d_b \leq p \leq d_t$; $t_{i,h} = p/2$ and $t_{o,h} = t_{i,h}/4$
- (6) Estimate the installation depth H required to resist the design compressive force by assuming a single helix pile using Eq. (4 – 23) (an appropriate estimate is that which the calculated Q_c is about 75 – 85% of the actual Q_c (Eq. (4 – 22)).
- (7) Calculate $H_t = 0.8H$ and F_q from Figure 4.21 and check if these parameters are adequate to achieve the design uplift capacity Q_u using Eq. (4 – 24). If the calculated Q_u is less than the design Q_u increase H until the calculated Q_u is \geq design Q_u . Note that for piles resisting only compressive loads a fully threaded pile should be used ($H_t = 0$).

- (8) Calculate the number of helices required; $i = \left(\frac{H-H_t}{p} \right) + 1$. Calculate the actual compressive capacity of the pile including the contribution of all helices using Eq. (4 – 22). If the capacity does not satisfy the required design capacity, then go back to step (6) or go back to step (3).
- (9) Calculate the sum of torque resistance acting on the bottom helix $\sum T_{h,bot}$ and the total torque resistance acting on the entire pile T (due to contribution shaft and all helices).
- (10) Calculate shear stresses at top end of shaft τ_t (where machine grips the pile) and at lower end τ_b of shaft (around the bottom helix) due to T (total torque) and $\sum T_{h,bot}$ respectively; where $\tau_t = \frac{T r_t}{J_t}$ and $\tau_b = \frac{\sum T_{h,bot} r_b}{J_b}$. Where $J = \frac{\pi}{2} d^4$ is the polar moment of circular solid shaft. Check if τ_t & $\tau_b \leq \tau_{max}$; if YES go to step (12) and if NO go to step (3).
- (11) Calculate shear stress at bottom helix – shaft interface due to compressive load and top helix – shaft interface due to uplift load (assuming the helix is a plate); $\tau_{int.} = \frac{\sum Q_c}{(t_{i,h} \times \pi d_b)}$ and $\frac{\sum Q_u}{(t_{i,h} \times \pi d_t)}$. Check if $\tau_{int.} \leq \tau_{max}$; if YES end design and if NO go to step (5) and recalculate $t_{i,h}$ by changing p .

4.4.6 Design example:

Design an E-UHPFRC screw pile to resist a compressive and uplift loads of 50kN and 35kN respectively for installation in loose, dense and saturated dense sand with properties shown in Table 4.7. The E-UHPFRC used has a shear strength of 30MPa. A factor of safety F.S. = 2 is used for both load and torque resistance.

Table 4.7: Input design data

Soil Type	Soil Properties Input			Step (2): Calculated Soil Properties						
	Unit weight γ (kN/m ³)	Effective Unit weight; γ' (kN/m ³)	Angle of internal friction; ϕ (°)	μ	K_p	K'_p	K_a	N_q	K_f	F_q
Loose sand (L.S.)	17.75	17.75	31	0.36	3.12	1.56	0.32	20.63	0.38	20
Dense Saturated Sand (D.S.S.)	19.03	9.22	42	0.49	5.04	2.52	0.20	85.37	0.53	63
Dense Sand (D.S.)	19.03	19.03	42	0.49	5.04	2.52	0.20	85.37	0.53	27

Table 4.8: Pile design parameters Using f 3 – FFF mechanical properties

Soil Type	Step (3) – (4)					Step (5)			Step (7) – (9)					Step (10)		Step (11)		Step (12)
	l_f (mm)	d_b (mm)	d_t (mm)	$D_{b,h}$ (mm)	$D_{t,h}$ (mm)	p (mm)	$t_{i,h}$ (mm)	$t_{o,h}$ (mm)	Q_c (kN)	Q_u (kN)	H (mm)	H_t (mm)	i	T (kN m)	$T_{h,bot}$ (kN m)	τ_t (MPa)	τ_b (MPa)	$\tau_{int.}$ (MPa)
L.S.	11.6	75	150	187	262	100	50	12.5	103	98	3514	2812	8	7.18	0.81	21.69	19.60	8.76
D.S.S.	11.6	70	140	175	245	100	50	12.5	101	79	2489	1991	6	4.91	0.96	18.24	28.59	9.18
D.S.	11.6	90	180	225	315	100	50	12.5	151	70	1464	1171	4	6.95	2.00	12.13	27.93	10.63

To further understand the behaviour of E-UHPFRC screw piles, relationships between the various design parameters are explored as shown in Figure 4.22 and 4.23. These relationships are established based on similar soil data and geometrical details of E-UHPFRC pile designed for installation in DSS in the design example shown in Table 4.8 (*soil type = DSS, H = 2500mm, H_t = 2000mm, d = 140mm, i = 6, d_t = 140mm, d_t = 70mm, D_{t,h} = 245mm, D_{b,h} = 175mm, p = 100mm*).

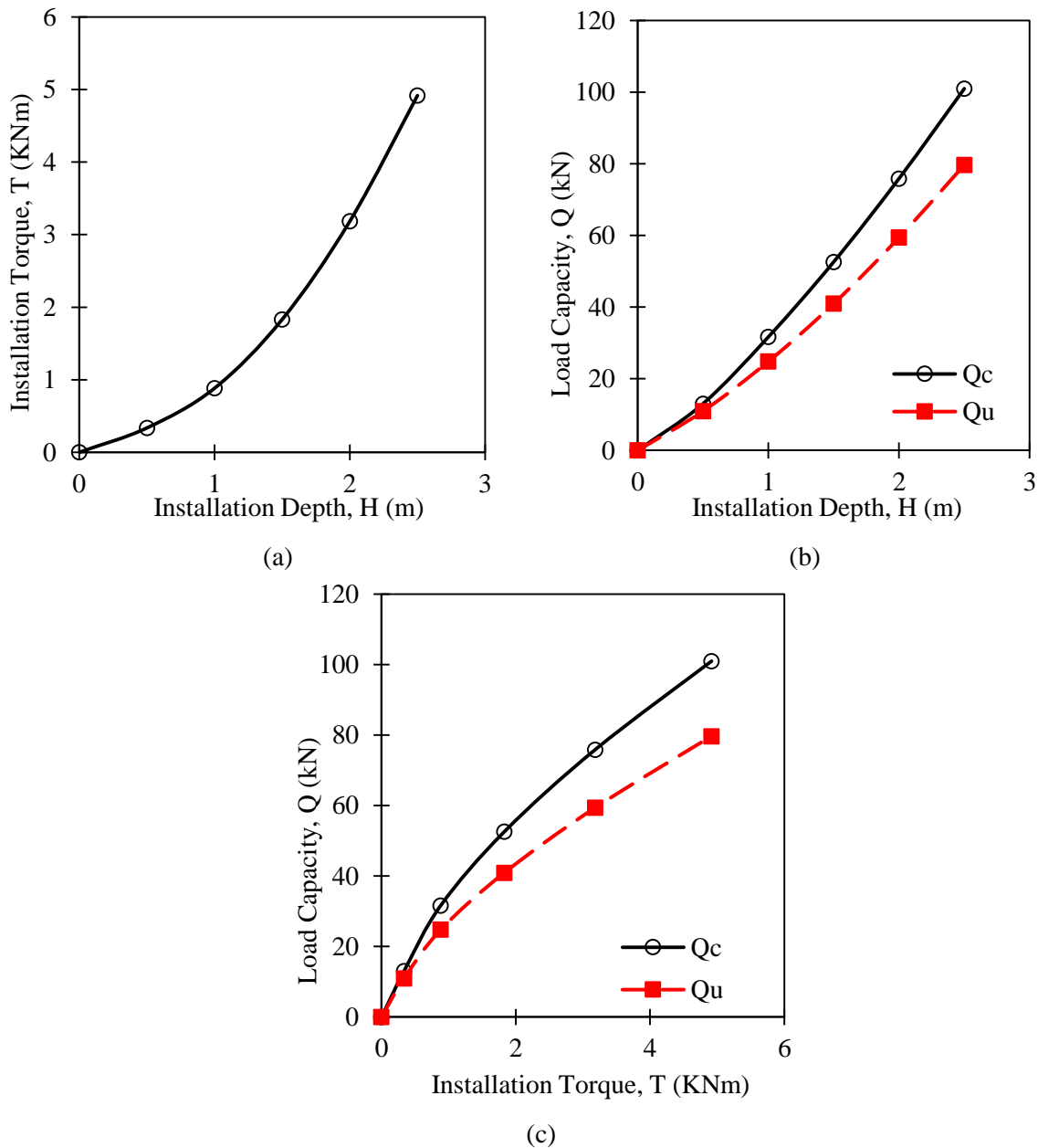


Figure 4.22: (a) Relationship between installation depth and installation torque; (b) installation depth and load capacity; (c) load capacity and installation torque.

Figure 22(a) shows the relationship between required installation torque (or total torque resistance) T and installation depth H . It can be seen that a rather exponential relationship exists between T and H ,

where T increases much faster than the increase in H . The relationship between load capacity (in compression (Q_c) and uplift (Q_u)) shown in Fig 4.22(b) indicates only a slightly nonlinear relationship between Q and H , where the first meter of installation depth offers less resistance than subsequent lengths. A nonlinear relationship is also observed between Q and T . As expected, the torque increases faster than the installed load capacity of the piles.

The effect of installation depth H on individual torque resistances and on individual helices are shown in Figure 4.23.

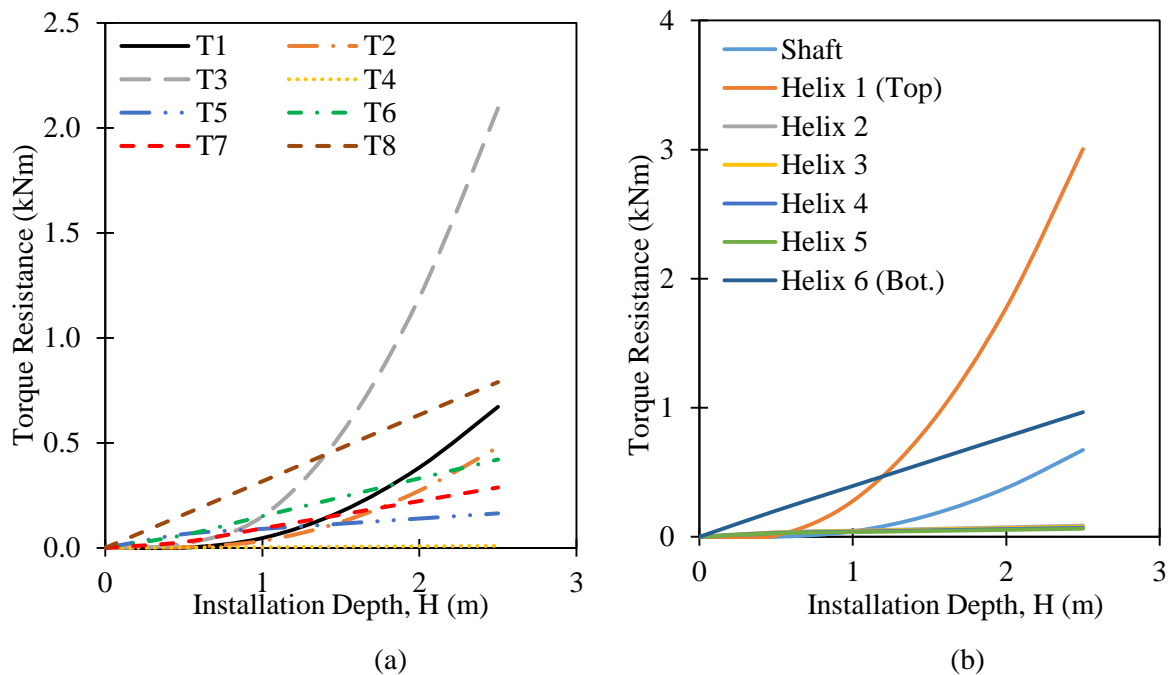


Figure 4.23: Effect of installation depth on (a) individual torque resistances and (b) on torque resistance of individual helices

It can be observed that H affects the individual torque resistances to various degrees (Fig 4.23(a)). Initially, T_8 (resistance due to cutting edge) shows the highest increase in Torque resistance (increase linearly) up to a depth of about 1.5m, and is then overtaken by T_3 (resistance due cylindrical column of the sand overlaying the helix). This resistance (T_3) then increases exponentially with an increase in H . Torque resistances acting on lower and upper surface of helices T_4 and T_5 , respectively, show the least increase with depth. The remaining torque resistances show intermediate levels of resistance. When there is a need to reduce the required installation torque, it is recommended to optimise the resistance of T_3 , T_8 and T_1 (shaft resistance). The effect of H on resistance of individual helices (Figure 4.23(b))

shows that the bottom helix attracts the highest initial torque resistance due to the fact that it houses the cutting edge of the screw pile that exerts a high torque resistance due to bearing on the soil (T_8). At about $H = 1.2m$ the top helix shows the highest torque resistance and that continues to increase exponentially with depth. This is due to the fact that the top helix (Helix 1) bears against a large cylindrical column of sand with height equivalent to H_t (height of shaft) and as such the resistance on helix 1 increases due to the large T_3 acting on it. The pile shaft shows a relatively high torque resistance, and this resistance increases exponentially with H . This is mainly due to the skin friction between the pile shaft and the surrounding soil. Such resistance from the shaft can be minimised by surface treating the shaft to reduce the coefficient of friction between E-UHPFRC and the soil. The remaining parts of the pile (mainly the intermediary helices; Helices 2,3,4 and 5) offer little resistance to the installation torque.

Figure 4.24 shows the effect of sand density on installation torque (or torque resistance) of E-UHPFRC screw piles having the same geometrical properties as the one discussed earlier. Comparisons between the torque resistances that develop during installation of such a screw pile in various soil types are given in (Figure 4.24).

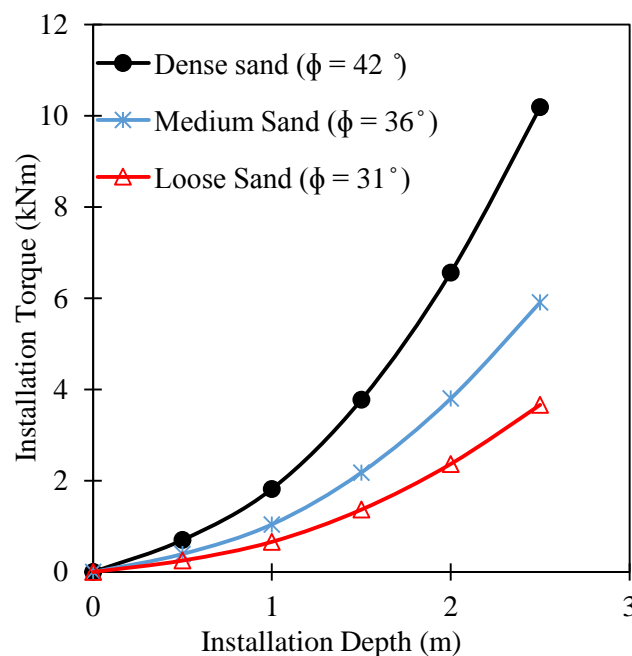


Figure 4.24: Effect of sand type on installation torque

As expected, the installation torque increases as the value of ϕ increases. For E-UHPFRC screw piles to be installed in dense sand even at shallow depths, the E-UHPFRC mix must be of very high shear strength (in this study 4 mixes in particular) to be able to resist the shear and tensile stresses that developed during installation. Average strength mixes (mixes containing FFF and mixes with lower dosage of CCC) can be used to design screw piles for installation in medium and loose sands.

4.5 Conclusions

This two-part study initially investigates experimentally the shear properties of E-UHPFRC mixes containing two types of recycled steel fibres (RTSC and RTSF) used separately and in hybrids solutions. Other mechanical properties including compressive strength, modulus of elasticity and flexural strength are also presented. The second part of the study presents the development of design guidelines for E-UHPFRC screw piles. Based on the experimental findings on E-UHPFRC mixes, and the theoretical modelling of E-UHPFRC screw piles the following conclusions can be drawn:

- The asymmetric four-point loading arrangement (modified Iosipescu test) can be used to determine the shear response of UHPFRC prism specimens.
- Mixes containing RTSC offer superb shear performance that is comparable to mixes containing manufactured steel fibres reported in the literature. For the same fibre dosage, mixes containing RTSF show lower shear strength (about 64 – 74% the strength of mixes containing RTSC)
- Nonetheless, mixes containing RTSF can be designed to achieve strengths comparable to mixes containing RTSC and manufactured fibres by using higher dosages of RTSF or by using hybrid mixes of RTSF and RTSC.
- RTSF and RTSC offer a sustainable alternative to manufactured steel fibres in UHPFRC, while achieving good shear performance.
- The post peak response of E-UHPFRC specimens under direct shear is very brittle, hence, only the pre-peak response is recommended for design purposes.
- Analytical modelling of the proposed E-UHPFRC screw piles carried out using existing verified models [42-53] confirms the viability of E-UHPFRC screw piles in cohesionless soils.

- The installation torque needed for E-UHPFRC screw piles depends the geometrical properties of the screw pile and the soil properties. The installation torque required to install a given screw pile increases with increase in installation depth and with density of sand.
- The dominant factors affecting the magnitude of the required installation depth are the frictional resistance exerted on the pile shaft, the locally compacted column of sand overlaying the top helix, and the bearing resistance exerted by the cutting edge (located on the bottom helix).

4.6 References

- 1 Federal Highway Administration, Ultra-High Performance Concrete: A State-of-the-Art Report for the Bridge Community, Mclean, VA, 2013.
- 2 C. Shi, Z. Wu, J. Xiao, D. Wang, Z. Huang, Z. Fang, A review on ultra-high performance concrete: Part I. Raw materials and mixture design, *Constr. Build. Mater.* 101 (2015) 741–751.
- 3 D. Wang, C. Shi, Z. Wu, J. Xiao, Z. Huang, Z. Fang, A review on ultra-high performance concrete: Part II. Hydration, microstructure and properties, *Constr. Build. Mater.* 96 (2015) 368–377.
- 4 Z. B. Haber, I. De la Varga, B.A. Graybeal, Nakashoji, B., & El-Helou, R. Properties and behavior of UHPC-class materials (No. FHWA-HRT-18-036). United States. Federal Highway Administration. Office of Infrastructure Research and Development 2018.
- 5 M.N. Isa, K. Pilakoutas, M. Guadagnini, H. Angelakopoulos, Mechanical performance of affordable and eco-efficient ultra-high performance concrete (UHPC) containing recycled tyre steel fibres, *Constr. Build. Mater.* 255 (2020) 119272.
- 6 R. Zhong, K. Wille, R. Viegas, Material efficiency in the design of UHPC paste from a life cycle point of view, *Constr. Build. Mater.* 160 (2018) 505–513.
- 7 K. Neocleous, H. Angelakopoulos, K. Pilakoutas, M. Guadagnini, Fibre-reinforced roller compacted concrete transport pavements, *Proc. Inst. Civ. Eng. Transp.* 164 (2011) 97–109.
- 8 Mirsayah, A. A., & Banthia, N. (2002). Shear strength of steel fiber-reinforced concrete. *ACI Materials Journal*, 99(5), 473–479
- 9 L. Ahmed, A. Ansell, Direct shear strength of high-strength fibre concrete, *Mag. Concr. Res.* 62 (2010) 379–390.
- 10 Wang, Z., Chen, L., Guadagnini, M., & Pilakoutas, K. (2019). Shear Behavior Model for FRP-Confined and Unconfined Rubberized Concrete. *Journal of Composites for Construction*, 23(5).
- 11 Xu, B., Bompa, D. V., Elghazouli, A. Y., Ruiz-Teran, A. M., & Stafford, P. J. (2018). Behaviour of rubberised concrete members in asymmetric shear tests. *Construction and Building Materials*, 159, 361–375.
- 12 Z.P. Baz̃ant, P.A. Pfeiffer, Shear fracture tests of concrete, *Mater. Struct.* 19 (2) (1986) 111–121.

- 13 Khanlou, A., Macrae, G. A., Scott, A. N., Hicks, S. J., & Clifton, G. C. (2012). Shear Performance of Steel Fibre-Reinforced Concrete. Australasian Structural Engineering Conference, Perth, Australia, July 11-13th 2012, 1(2006), 8
- 14 JSCE-SF6,, Method of Test for Shear Strength of Steel Fiber Reinforced Concrete (SFRC), Japan Society of Civil Engineers, Tokyo, 1990, pp. 67–69.
- 15 H.N. Tuan, H. Otsuka, Y. Ishikawa, E. Takeshita, Study on shear strength under direct shear of concrete test, Jpn. Concr. Inst. 28 (1) (2006) 1529–1534.
- 16 A.H. Mattock, N.M. Hawkins, Shear transfer in reinforced concrete—recent research, Pci J. 17 (2) (1972) 55–75.
- 17 J. Watkins, Fracture toughness test for soll-cement samples in mode II, Int. J. Fract. 23 (4) (1983) 135–138.
- 18 N. Iosipescu, A. Negoita, A new method for determining the pure shearing strength of concrete. Concrete (London), 1969, 3(1), 63.
- 19 Wu, P., Wu, C., Liu, Z., & Hao, H. (2019). Investigation of shear performance of UHPC by direct shear tests. Engineering Structures.
- 20 T.T. Ngo, J.K. Park, S. Pyo, D.J. Kim, Shear resistance of ultra-high-performance fiber-reinforced concrete, Constr. Build. Mater. 151 (2017) 246–257.
- 21 Arup Geotechnics, 2005. Design of Screw Piles: Assessment of Pile Design Methodology. Ove Arup & Partners Ltd, London.
- 22 G. C., Vernon-Inkpen, "Concrete pile." U.S. Patent 996,688, issued July 4, 1911.
- 23 Cummings, Robert A. "Corrugated concrete pile." U.S. Patent 1,041,035, issued October 15, 1912.
- 24 Vernon-Inkpen, George Charles. "Concrete screw-pile for foundations and similar purposes." U.S. Patent 1,070,862, issued August 19, 1913.
- 25 G., Grimaud. "Reinforced-concrete stake." U.S. Patent 1,563,024, issued November 24, 1925.
- 26 Gillen Jr, William F. "Precast concrete threaded pilings." U.S. Patent 4,239,419, issued December 16, 1980.

- 27 H. Hu, P. Papastergiou, H. Angelakopoulos, M. Guadagnini, K. Pilakoutas, Mechanical properties of SFRC using blended Recycled Tyre Steel Cords (RTSC) and Recycled Tyre Steel Fibres (RTSF), *Constr. Build. Mater.* 187 (2018) 553–564
- 28 BS EN 12390-2:2009: Testing hardened concrete. Making and curing specimens for strength tests, BSI 389 Chiswick High Road, London W4 4AL, UK. (2009).
- 29 BSI, EN 12390-3: Testing hardened concrete, Part 3: Compressive strength of test specimens, BSI 389 Chiswick High Road, London W4 4AL, UK. (2013).
- 30 BSI, EN 12390-13: Testing hardened concrete, Part 3: Determination of secant modulus of elasticity in compression, BSI 389 Chiswick High Road, London W4 4AL, UK. (2013).
- 31 BS EN 14651, Test method for metallic fibred concrete — Measuring the flexural tensile strength (limit of proportionality (LOP), residual), *Br. Stand. Inst.* 3 (2005) 1–17.
- 32 S. Abbas, A.M. Soliman, M.L. Nehdi, exploring mechanical and durability properties of ultra-high performance concrete incorporating various steel fibre lengths and dosages, *Constr. Build. Mater.* 75 (2015) 429–441.
- 33 M. Shafieifar, M. Farzad, A. Azizinamini, Experimental and numerical study on mechanical properties of Ultra High Performance Concrete (UHPC), *Constr. Build. Mater.* 156 (2017) 402–411.
- 34 H.S. El-Din, H. Mohamed, M.A.E.-H. Khater, S. Ahmed, Effect of Steel Fibers on Behavior of Ultra High Performance Concrete, in: *First Int. Interact. Symp. UHPC*, Des Moines, Iowa, 2016: pp. 1–10.
- 35 S. Abbas, M.L. Nehdi, M.A. Saleem, Ultra-High Performance Concrete: Mechanical Performance, Durability, Sustainability and Implementation Challenges, *Int. J. Concr. Struct. Mater.* 10 (2016) 271–295.
- 36 Federal Highway Administration, *Ultra-High Performance Concrete: A State-of-the-Art Report for the Bridge Community*, Mclean, VA, 2013.

- 37 A. Khanlou, G.A. Macrae, A.N. Scott, S.J. Hicks, G.C. Clifton, Shear Performance of Steel Fibre-Reinforced Concrete, Australasian Structural Engineering Conference, Perth, Aust. July 11-13th 2012. 1 (2012) 8.
- 38 A.A. Mirsayah, N. Banthia, Shear strength of steel fiber-reinforced concrete, *ACI Mater. J.* 99 (2002) 473–479.
- 39 B. Boulekbatche, M. Hamrat, M. Chemrouk, S. Amziane, Influence of yield stress and compressive strength on direct shear behaviour of steel fibre-reinforced concrete, *Constr. Build. Mater.* 27 (2012) 6–14.
- 40 Federal Highway Administration, Material Property Characterization of Ultra-High Performance Concrete, FHWA-HRT-06-103, Washington, DC, 2006.
- 41 ASTM C469, Standard Test Method for Static Modulus of Elasticity and Poisson's Ratio of Concrete in Compression, ASTM Int. (2014).
- 42 A. Ghaly, and A. Hanna. "Experimental and theoretical studies on installation torque of screw anchors." *Canadian geotechnical journal* 28, no. 3 (1991): 353-364.
- 43 Sakr, Mohammed. "Retracted: Relationship between Installation Torque and Axial Capacities of Helical Piles in Cohesionless Soils." *Journal of Performance of Constructed Facilities* 29, no. 6 (2015): 04014173.
- 44 H. Ding, L. Wang, P. Zhang, Y. Liang, Y. Tian, X. Qi, The recycling torque of a single-plate helical pile for offshore wind turbines in dense sand, *Appl. Sci.* 9 (2019).
- 45 Mitsch, M.P., Clemence, S.P., 1985. The uplift capacity of helix anchors in sand. In: *Uplift Behaviour of Anchor Foundations in Soil*. American Society of Civil Engineers, New York, pp.26–47.
- 46 Meyerhof, G.G., Adams, J.I., 1968. The ultimate uplift capacity of foundations. *Canadian Geotechnical Journal* 5(4), 225–244.
- 47 S. Clemence and F. Pepe, "Measurement of Lateral Stress Around Multi helix Anchors in Sand," *Geotechnical Testing Journal* 7, no. 3 (1984): 145-152

- 48 Zhang, D.J.Y., Chalaturnyk, R., Robertson, P.K., Segó, D.C., Cyre, G., 1998. Screw anchor test program (Part I & II): instrumentation, site characterisation and installation. In: Proceedings of the 51st Canadian Geotechnical Conference. Edmonton.
- 49 Livneh, B., Naggar, M.H.M., 2008. Axial testing and numerical modelling of square shaft helical piles under compressive and tensile loading. *Can. Geotech. J.*45(8),1142–1155.
- 50 Tappenden, K., Segó, D., Robertson, P., 2009. Load transfer behaviour of full- scale instrumented screw anchors. In: *Contemporary Topics in Deep Foundations*. American Society of Civil Engineers, USA, pp. 472–479.
- 51 Nasr, M.H., 2009. Performance-based design for helical piles. In: *Contemporary Topics in Deep Foundations*. American Society of Civil Engineers, USA, pp.496–503.
- 52 Nasr, M.H., 2004. Large capacity screw piles. In: *Proceedings of the International Conference: Future Vision and Challenges for Urban Development*. Cairo, Egypt, 20–22 December, pp.1–15.
- 53 Tappenden, K. M., Segó D. C. 2007. Predicting the axial capacity of screw piles installed in Canadian soils. In *The Canadian Geotechnical Society (CGS), OttawaGeo2007 Conference* (pp. 1608-1615).

Chapter 5: Conclusions and Recommendations for Future Work

This chapter presents the main conclusions of this thesis and recommendations for future work.

5.1 Conclusions

The aim of this research was to investigate the feasibility of developing an Eco-Efficient Ultra-High Performance Fibre Reinforced Concrete (E-UHPFRC) by utilising recycled steel fibres (RTSC and sorted RTSF) for use in screw piles and other structural applications. An extensive experimental work, complemented by numerical and analytical analyses, was carried out. The fresh and hardened properties of different E-UHPFRC mixes were examined, including their flexural and shear properties. Finally, the performance of screw piles made with the newly developed E-UHPFRC was examined in detail, and a design methodology was proposed. The main findings and conclusions drawn from this study are summarised below.

5.1.1 Mechanical performance of affordable and eco-efficient ultra-high performance fibre reinforced concrete (E-UHPFRC) containing recycled tyre steel fibres (Chapter 2)

- Mixes containing RTSC offer comparable performance to that of mixes containing manufactured steel fibres (MSF) reported in the literature [4] (for similar fibre dosages and curing regimes). This can be related to the fact that RTSC share similar properties with MSF in terms of cleanliness, geometry and mechanical strength.
- The performance of mixes containing RTSC is affected by fibre length. Owing to the better anchorage provided by longer fibres, mixes containing RTSC with length of 12 and 15mm show superior strength (11 and 19% more than mixes containing 9 and 6mm long RTSC, respectively) and post cracking stiffness.
- Sustainable UHPFRC mixes can be effectively developed with RTSF fibres, provided the fibres are clean, with little or no impurities. However:
 - a) Very short fibres can fail to develop high strength due to insufficient anchorage length, while longer fibres affect workability making the mix susceptible to balling.
 - b) Improved flexural performance can be achieved only when 50% or more of the fibres have lengths within the range of 9-15mm.
- For the same fibre dosage, the use of RTSF:

- a) Reduces the workability of mixes (10-13% decrease in flow diameter depending on fibre dosage)
 - b) Slightly reduces fresh density,
 - c) Reduces compressive strength and modulus of elasticity.
- For the same fibre dosage, the flexural strength of mixes containing only RTSF (FFF) is about 40% lower than that of mixes containing only RTSC (CCC). To achieve similar strength values, hybrid fibres or a higher dosage of RTSF need to be used.
 - The use of new design parameters (f_R -values) is proposed for the design of E-UHPFRC flexural members at serviceability and ultimate limit states, and analytical predictive models are proposed for these parameters.
 - The δ – CMOD models proposed by BS EN 14651 [[36]] and RILEM TC 162 – TDF [6] are not suitable for strain hardening materials like E-UHPFRC. A new model is proposed to predict the hinge length based on fibre types and dosage.
 - The use of RTSF in UHPFRC offers significant cost and environmental benefits. The total efficiency of mixing containing only RTSF (FFF) is always higher than that of mixes with RTSC/MSF and varies from 69 – 195%, depending on fibre dosage.

5.1.2 Determination of Tensile Characteristics and Design of Eco-Efficient UHPFRC (Chapter 3)

- Experimental results show that compared to RTSC (CCC) mixes, the inclusion of RTSF causes a reduction in flexural strength, energy absorption and fracture energy. Nevertheless, similar mechanical properties to RTSC only mixes can be achieved by using higher RTSF dosages or hybrid RTSC-RTSF mixes.
- Inverse analysis is shown to be an effective tool to estimate the tensile characteristics of UHPFRC. The mesh dependency of crack models encountered when modelling the softening part of UHPFRC is solved by adopting an adaptive fracture energy approach. The approach uses fracture energy, characteristic length and mesh size as input parameters.

- The determined tensile properties of RTSC mixes are similar, and in some cases higher, than those reported in literature for mixes containing MSF cured under the same conditions [7-65].
- The MC10 [39] model for strain hardening materials is shown to largely overestimate both the tensile strength and energy absorption of UHPFRC by up to 31 and 76%, respectively.
- A model for predicting the constitutive tensile $\sigma - \varepsilon$ law of E-UHPFRC based on simple mix parameters (compressive strength, flexural strength, fracture energy, fibre dosage and RTSF content) is developed. The proposed model predicts well the flexural capacities of E-UHPFRC at all performance levels and it is well suited for design.

5.1.3 Direct shear Behaviour of E-UHPFRC Containing Recycle Steel Fibres and E-UHPFRC Screw Piles (Chapter 4)

- RTSF and RTSC offer a sustainable alternative to manufactured steel fibres in UHPFRC, while achieving good shear performance.
- Mixes containing RTSC offer superb shear performance that is comparable to mixes containing manufactured steel fibres reported in the literature [12]. For the same fibre dosage, mixes containing RTSF show lower shear strength (about 64 – 74% the strength of mixes containing RTSC)
- Mixes containing RTSF can be designed to achieve shear strengths comparable to mixes containing RTSC and manufactured fibres by using higher dosages of RTSF or by using hybrid mixes of RTSF and RTSC.
- The post peak response of E-UHPFRC specimens under direct shear is very brittle, hence, the design of E-UHPFRC elements should be based only on the pre-peak shear response.
- Analytical modelling of the proposed E-UHPFRC screw piles carried out using existing verified models [13-21] confirms the viability of E-UHPFRC screw piles in cohesionless soils.
- The installation torque needed for E-UHPFRC screw piles depends on the geometrical properties of the screw pile and the soil properties. The installation torque required to install a given screw pile increases with increase in installation depth and with density of sand.

- The dominant factors affecting the magnitude of the required installation depth are the frictional resistance exerted on the pile shaft, the locally compacted column of sand overlaying the top helix, and the bearing resistance exerted by the cutting edge (located on the bottom helix).

5.1.4 Final Remarks

This work provides compelling evidence that an eco-efficient UHPFRC (E-UHPFRC) that is both cost effective and environmentally friendly can be achieved by utilising processed waste products such as GGBS, RTSF and RTSC, and that such material can meet the workability and strength requirements of conventional UHPFRC. The newly developed E-UHPFRC, along with the proposed design models and its proven efficiency in application such as screw piles, provides the construction industry with an all-round efficient material (both in terms of mechanical efficiency and sustainability) that can be used for novel applications.

5.2 Recommendations for Future Use

This research focused on developing and investigating the mechanical properties of E-UHPFRC, as well as proposing design models for E-UHPFRC screw piles and other structural applications. Due to time limitation (PhD funding duration) and the restrictions imposed at the onset of the COVID-19 pandemic, various other important aspects were not investigated, and are thus recommended for future studies as described below.

5.2.1 Improvement in Cleaning and Optimising the Length Distribution of RTSF

- The approach employed in this study to clean and sort RTSF involves the use of sieves and sieve shaker. However, this method is not very efficient (a lot of fibres of desired length are lost resulting in a low yield) and requires excessive manual labour. Also the approach does not guarantee that the desired fibre distribution can be achieved under a specified number of cleaning steps. Thus, there is a need to devise a standardized technique for sorting RTSF that can yield the desired fibre length distribution with little wastage, irrespective of the nature of the original RTSF. Moreover, an alternative and more efficient method should be developed, e.g. using robotic systems coupled with machine vision and artificial intelligence algorithms.

- RTSF was mainly characterised based on fibre length distribution, the filament diameters were not actually taken into account. Future research work should therefore consider the effect of aspect ratios (length to diameter ratio). This will help in accounting for the effect of embedment areas of filaments in analytical/mechanistic computations, which can lead to the development of more accurate design models.

5.2.2 Improvement in Evaluating the Market value and Actual Environmental Credentials of Cleaned and Sorted RTSF and of RTSC

The data used to carry out the mix efficiency study were gathered mostly from the literature, suppliers, and relevant databases of global warming potential – GWP. However, obtaining the market price and GWP of RTSF and RTSC was challenging because these materials have not been commercialised and are yet to be widely used in the construction industry (currently they are mostly supplied to laboratories for research studies). As such, data regarding these two materials used in the analysis are completely supplier dependant and will vary from supplier to supplier. Since research institutions use these materials in relatively small quantities, the price of RTSF and RTSC will be different if they are produced in large scale and are supplied for large construction project. Thus an in-depth investigation on fair market price and a more accurate estimate of the GWP of processing RTSF and RTSC, should be carried out.

5.2.3 Mix Design Optimisation

To allow for a broader optimisation on the efficiency of E-UHPFRC, there is also a need to optimise the mix proportion of the paste. The mix adopted in this study is based on the low cement mix design by [28]. However, the adopted mix can be further optimised to reduce its cost and environmental credentials, while maintaining appropriate mechanical and durability characteristics. Future studies should focus on optimising the paste component through adjusting: the water to cement ratio; type, grading and quantity of fine aggregate; quantity of cement; quantity of pozzolanic materials (Silica fume and GGBS) and the use of any required admixture.

5.2.4 Future Experimental Work

- **Microstructure study on E-UHPFRC mixes**

Although examining the UHPFRC microstructure was outside the scope of this research project, it is crucial that future work focuses on the microstructure properties of E-UHPFRC using modern techniques, such as X-ray computed tomography and CT-Scan, to obtain useful information about the distribution and orientation of RTSF in UHPC mortar, nature of bond between the fibre types and steel rebars and UHPC paste, as well porosity and internal structure of the designed E-UHPFRC mixes. Such information can help relate the observed variation between the mechanical properties of mixes containing RTSF and those containing RTSC/MSF.

- **Durability, shrinkage, fatigue and chemical resistance**

An in-depth understanding of the durability and long-term performance of the proposed E-UHPFRC is crucial to encourage the widespread use of this cost and environmentally efficient material. Future studies need to examine the performance of E-UHPFRC against shrinkage, creep, fatigue, high temperature and freeze-thaw cycles as well as resistance to chemical attacks such as carbonation, sulphate attack, alkali-silica reaction etc. The results from these studies can be utilised to carry out more detailed and accurate Life Cycle Cost Analyses (LCCA) and Performance Assessments of E-UHPFRC structures.

- **Torsion Test**

Due to time limitations and the delays arising from the lockdown due to the COVID-19 pandemic, torsion tests on E-UHPFRC specimens (which were part of the original work plan) could not be performed. The torsion tests would provide the information required to further strengthen the analysis and design of E-UHPFRC screw piles, as well as provide valuable data to support the use of E-UHPFRC in other structural applications, such as bridges.

- **E-UHPRC Screw piles testing**

The development of E-UHPFRC screw piles presented in this work is mainly based on analytical modelling. To further validate the suitability and effectiveness of this novel development, there is a

need to produce E-UHPFRC screw pile prototypes and carry out experimental and field testing. Results from the experimental testing can be used to optimise the design process as well as the development of more efficient installation techniques. Moreover, there is need to conduct comparative analysis in terms of cost, environmental credentials and durability performance between E-UHPFRC screw piles and conventional steel screw piles.

5.2.5 Life Cycle Cost analysis (LCCA) and Performance Assessment of E-UHPRC structures

A LCCA and performance assessment of E-UHPFRC elements could not be carried out without additional experimental data, particularly on long-term performance. It is recommended that when sufficient information is available, LCCA and performance assessments are carried out considering not only production, design, and construction of E-UHPFRC elements, but also operation, maintenance, as well as demolition and possible re-use. It is believed that such studies will confirm the unparalleled performance of E-UHPFRC and provide further evidence to encourage a more widespread use of this novel material.

5.2.6 Validation and Calibration of Design Models

The proposed prediction and design models in this study were developed from data generated strictly based on the studied mixes. The suitability and accuracy of these models for predicting mechanical properties of other UHPFRC mixes have not been studied. It is recommended that the suitability of these models be checked against various other UHPFRC mixes and where possible recalibrate the models to achieve wider coverage of application.

5.3 References

- 1 S. Abbas, A.M. Soliman, M.L. Nehdi, exploring mechanical and durability properties of ultra-high performance concrete incorporating various steel fibre lengths and dosages, *Constr. Build. Mater.* 641 75 (2015) 429–441.
- 2 M. Shafieifar, M. Farzad, A. Azizinamini, Experimental and numerical study on mechanical properties of Ultra High Performance Concrete (UHPC), *Constr. Build. Mater.* 156 (2017) 402–754 411. 755
- 3 H.S. El-Din, H. Mohamed, M.A.E.-H. Khater, S. Ahmed, Effect of Steel Fibres on Behaviour of 756 Ultra High Performance Concrete, in: *First Int. Interact. Symp. UHPC*, Des Moines, Iowa, 2016: 757 pp. 1–10. 758
- 4 S. Abbas, M.L. Nehdi, M.A. Saleem, Ultra-High Performance Concrete: Mechanical Performance, Durability, Sustainability and Implementation Challenges, *Int. J. Concr. Struct. Mater.* 10 (2016) 271–295. 759
- 5 BS EN 14651, Test method for metallic fibred concrete — Measuring the flexural tensile strength (limit of proportionality (LOP), residual), *Br. Stand. Inst.* 3 (2005) 1–17. 760
- 6 B.I.G. Barr, M.K. Lee, E.J. De Place Hansen, D. Dupont, E. Erdem, S. Schaeerlaekens, B. Schnütgen, H. Stang, L. Vandewalle, Round-robin analysis of the RILEM TC 162-TDF beam-bending test: Part 2 - Approximation of δ from the CMOD response, *Mater. Struct. Constr.* 36 (2003) 621–630. 761
- 7 A.M.T. Hassan, S.W. Jones, G.H. Mahmud, Experimental test methods to determine the uniaxial tensile and compressive behaviour of Ultra High Performance Fibre Reinforced Concrete(UHPFRC), *Constr. Build. Mater.* 37 (2012) 874–882. 762
- 8 V. Savino, L. Lanzoni, A.M. Tarantino, M. Viviani, Tensile constitutive behaviour of high and ultra-high performance fibre-reinforced-concretes, *Constr. Build. Mater.* 186 (2018) 525–536. 763
- 9 Y. Kusumawardaningsih, E. Fehling, M. Ismail, A.A.M. Aboubakr, Tensile strength behaviour of UHPC and UHPFRC, *Procedia Eng.* 125 (2015) 1081–1086. 764

- 10 S. Paschalis, A. Lampropoulos, Fibre content and curing time effect on the tensile characteristics of ultra-high performance fibre reinforced concrete, *Struct. Concr.* 18 (2017) 577–588.
- 11 The International Federation for Structural Concrete (fib). Model Code 2010. *Fib Model Code for Concrete Structures 2010*.
- 12 Wu, P., Wu, C., Liu, Z., & Hao, H. (2019). Investigation of shear performance of UHPC by direct shear tests. *Engineering Structures*.
- 13 Mitsch, M.P., Clemence, S.P., 1985. The uplift capacity of helix anchors in sand. In: *Uplift Behaviour of Anchor Foundations in Soil*. American Society of Civil Engineers, New York, pp.26–47.
- 14 Meyerhof, G.G., Adams, J.I., 1968. The ultimate uplift capacity of foundations. *Canadian Geotechnical Journal* 5(4), 225–244.
- 15 S. Clemence and F. Pepe, "Measurement of Lateral Stress Around Multi helix Anchors in Sand," *Geotechnical Testing Journal* 7, no. 3 (1984): 145-152
- 16 Zhang, D.J.Y., Chalaturnyk, R., Robertson, P.K., Sego, D.C., Cyre, G., 1998. Screw anchor test program (Part I & II): instrumentation, site characterisation and installation. In: *Proceedings of the 51st Canadian Geotechnical Conference*. Edmonton.
- 17 Livneh, B., Naggar, M.H.M., 2008. Axial testing and numerical modelling of square shaft helical piles under compressive and tensile loading. *Can. Geotech. J.* 45(8), 1142–1155.
- 18 Tappenden, K., Sego, D., Robertson, P., 2009. Load transfer behaviour of full-scale instrumented screw anchors. In: *Contemporary Topics in Deep Foundations*. American Society of Civil Engineers, USA, pp. 472–479.
- 19 Nasr, M.H., 2009. Performance-based design for helical piles. In: *Contemporary Topics in Deep Foundations*. American Society of Civil Engineers, USA, pp. 496–503.
- 20 Nasr, M.H., 2004. Large capacity screw piles. In: *Proceedings of the International Conference: Future Vision and Challenges for Urban Development*. Cairo, Egypt, 20–22 December, pp. 1–15.
- 21 Tappenden, K. M., Sego D. C. 2007. Predicting the axial capacity of screw piles installed in Canadian soils. In *The Canadian Geotechnical Society (CGS), OttawaGeo2007 Conference* (pp. 1608-1615).

- 22 Larsen, I. L., & Thorstensen, R. T. 2020. The influence of steel fibres on compressive and tensile strength of ultra-high performance concrete: A review. *Construction and Building Materials*, 256, 119459.
- 23 J. Lee and G. L. Fenves, 1998. Plastic-damage model for cyclic loading concrete structures. *Journal of Engineering Mechanics*, Vol. 124, No. 8, pp. 892-900.
- 24 W. S. A Nana, T. T. Bui, A. Limam, and S. Abouri, 2017. Experimental and numerical modeling of shear behavior of full-scale RC slabs under concentrated loads. *Structures*, Vol. 10, pp.96-116.
- 25 T. Jankowiak and T. Lodygowski, 2005. Identification of parameters of concrete damage plasticity constitutive model. *Foundation of civil and environmental engineering*, Vol. 6, pp. 53–69.
- 26 R. Malm, 2009. Predicting shear type crack initiation and growth in concrete with non-linear finite element method. TRITA-BKN, Bulletin 97, Royal Institute of Technology, Division of Structural Design and Bridges, Stockholm, Sweden.
- 27 R. Malm, 2006. Shear cracks in concrete structures subjected to in-plane stresses. TRITA-BKN, Bulletin 88, Royal Institute of Technology, Division of Structural Design and Bridges, Stockholm, Sweden
- 28 Le T. Ultra high performance fibre reinforced concrete paving flags. Liverpool, UK: University of Liverpool; 2008.

Appendix A: Data and Experimental Results for Chapter 2

Mechanical performance of affordable and eco-efficient ultra-high performance fibre reinforced concrete (UHPFRC) containing recycled tyre steel fibres

This appendix presents additional information, details and photos on the fresh and mechanical performance of the E-UHPFRC described in Chapter 2.

A.1 Additional Information

A.1.1 Mix Design.

The choice of fibre dosages was made based on recommendations from literature and preliminary test results. Two percent (2%) minimum dosage was based on recommendations by researchers [22] that fibre dosage $\geq 1.5\%$ is mostly required (depending on curing method) to achieve a post crack tensile strength of 5MPa (which is a requirement for been defined as UHPFRC). While the choice of maximum fibre dosage of 4% was made because preliminary study shows that mixes containing 4% fibre dosage RTSF tend to ball (fibres lump together), thus adversely affecting the workability and uniformity of the mix.

Similarly, selection of RTSC minimum fibre length of 9mm and maximum length of 15mm was based on scientific and practical reasons. The preliminary test results shows that the flexural performance of mixes containing 9mm fibres was lower compared to mixes containing fibre of length 12mm and 15mm. Meanwhile, for mixes made with fibres of more than 15 mm length (18mm and 20mm) the workability of such mixes was found to be adversely affected particularly for 4% fibre dosage, the fibres shows signs of balling (lumping), as such fibre lengths were not considered in the studies.

A.1.2 Limitations of Proposed Prediction Models

The following limitations applies to the prediction models proposed in this this study:

- The models were calibrated to predict tensile characteristics of mixes containing fibre dosages of 2 – 3% only. Their suitability when applied to mixes containing fibre dosages outside this range have not be ascertained.
- The models were developed based on flexural response of E-UHPFRC containing recycled tyre steel fibres. Its accuracy when applied on mixes containing other types of steel fibres have not been studied.

A.2 E-UHPFRC Mix Constituent Characteristics

A.2.1 Fine Aggregate Properties Summary Data Sheet (CH30)



PO Box 282, Nantwich,
Cheshire, CW5 9DH

Email: enquiries@mineralsmarketing.com
Phone: +44 (0) 1270 625 573
Fax: +44 (0) 8709 127 479

Minerals Marketing CHSP30 Product Information

Source Lower Withington, Cheshire
Geology Glacial Deposit of the Pleistocene Period
Description Washed and Graded High Silica Sand

Chemical Analysis:

	Typical %	Limit %
SiO ₂	98.49	97.5 Min
Fe ₂ O ₃	0.09	0.14 Max
Al ₂ O ₃	0.70	
K ₂ O	0.34	
LOI	0.22	0.40 Max

Physical Analysis:

Microns	Typical % Retained Each Sieve	Limit %	Typical % Cumulative Retained	Limit %	Typical % Cumulative Passing	Limit %
1180	0.1	0.3 Max	0.1		99.9	
1000	0.1		0.2		99.8	99.0 Min
710	0.8		1.0	8.0 Max	99.0	95.0 Min
600	2.1		3.1		96.9	
500	22.0		25.1		74.9	
425	37.7		62.8		37.2	
355	26.6		89.4		10.6	
300	7.9		97.3		2.7	
250	1.6		98.9	90.0 Min	1.1	
180	0.7		99.6		0.4	
125	0.4		100.0		0.0	
-125	0.0					

	Typical	Range / Limit
Hydraulic Conductivity	2196 mm/hour	
Average Grain Size	458 Microns	
Grain Shape	Rounded	
Loose Bulk Density kg/m ³	1550	
Clay Content %	0.1	0.3 Max

The information contained in this sheet does not constitute a specification, but is issued in good faith.
A specification can be issued if required.



PO Box 282, Nantwich,
Cheshire, CW5 9DH

Email: enquiries@mineralsmarketing.com
Phone: +44 (0) 1270 625 573
Fax: +44 (0) 8709 127 479

Minerals Marketing CNHST95 Product Information

Source Congleton, Cheshire
Geology Glacial Deposit of the Pleistocene Period
Description Washed, Surface Treated, and Graded Silica Sand

Chemical Analysis:

	Typical %	Limit %
SiO ₂	94.68	93.00 Min
Fe ₂ O ₃	0.28	0.35 Max
Al ₂ O ₃	2.52	
K ₂ O	1.47	
LOI	0.34	0.55 Max

Physical Analysis:

Microns	Typical % Retained Each Sieve	Limit %	Typical % Cumulative Retained	Limit %	Typical % Cumulative Passing	Limit %
1000	0.0		0.0		100.0	
710	0.0		0.0		100.0	
500	0.0		0.0	0.4 Max	100.0	99.6 Min
355	0.1		0.1		99.9	
250	0.6		0.7		99.3	
212	1.9		2.6		97.4	
180	13.4		16.0		84.0	
150	23.2		39.2		60.8	
125	25.4		64.6		35.4	
90	32.3		96.9		3.1	
63	3.0		99.9	99.5 Min	0.1	0.5 Max
-63	0.2	0.5 Max				

	Typical	Range / Limit
AFS Number	94	90 - 103
Acid Demand (No. of mis N/10 HCl to pH3)	3.4	7.0 Max
Average Grain Size	148 Microns	
Grain Shape	Sub Rounded	
Loose Bulk Density kg/m3	1420	

The information contained in this sheet does not constitute a specification, but is issued in good faith.
A specification can be issued if required.

A.2.2 Cement Properties Summary Data Sheet (HST95)

Hanson Packed Cement

High Strength 52,5N

Technical Data Sheet



Hanson High Strength 52,5N (HS52), is a quality assured Portland cement is manufactured to comply with the requirements of EN 197-1 CEM I strength class 52,5N. Hanson HS52 is produced using carefully selected raw materials and strict quality control throughout each stage of the manufacturing process to ensure a consistent final product is achieved.

APPLICATIONS

Hanson HS52 is a commonly used cement for a wide range of applications. These applications cover but are not limited to, general Ready-Mixed concrete, High Strength Pre-Cast and Pre- Stressed Concretes, Sprayed Concrete, Concrete Block Paving (CBP), Grout, Mortar, Render and Screeds.

QUALITY

Hanson HS52 is CE Marked in accordance with Constructions Products Regulation 305/2011/EU. In addition to applying a system of factory production control, based on ISO 9001 and defined in BS EN 197-2, independent sampling and testing of the Hanson HS52, known as Assessment and Verification of Constancy of Performance (AVCP) System 1+, also confirms conformity with all the requirements of BS EN 197-1. A Declaration of Performance (DoP) and CE mark are available online at www.hanson.co.uk.

COMPATIBILITY

Hanson HS52 is suitable for use with a wide range of additives and admixtures to extend the properties and uses of concretes, mortars, renders and screeds. It is recommended that trial mixes are carried out to determine optimum proportions.

DATA AND CERTIFICATION

Hanson Technical provides current data and routine certification of tests for all essential characteristics including compressive strengths of mortar prisms, fineness, setting times, soundness and chemical composition including alkali levels. These are available on a weekly basis and can be accessed from www.hanson.co.uk.

MIX DESIGN

Concrete mix designs need to be adapted to suit individual circumstances. It is strongly recommended that trial mixes are carried out prior to commencement of work to ensure that the mix design and material combinations meet the requirements of the specification and method of use.

HEXAVALENT CHROMIUM (VI)

In accordance with the Regulation EC 1907/2006 (REACH), the soluble chromium (VI) content is limited to a maximum of 2ppm. The chromium (VI) content is determined in accordance with EN 196-10. The maximum shelf life of packed cement is stated on the bag.



Hanson Portland Cement CEM I 52,5N – Technical Data Sheet

AVAILABILITY

Hanson HS52 cement is supplied in 25 kg bags throughout the UK.

PRODUCT DECLARATION

Parameter	Units	Max Limit
Declared Mean Alkali (Na ₂ Oeq) ¹	%	≥0.75
Chloride ²	%	≥0.07
Sulfate	%	≥4.00

¹ Declared Mean Alkali (DMA) = Certified Average Alkali (Mean of last 25 results) + (1xSD)

² Mean of last 25 results.

MANAGEMENT SYSTEMS

Hanson Cement are approved to the following management systems;

ISO 9001 – Quality management

ISO 14001 – Environmental management

OHSAS 18001 – Occupational Health and Safety Management

BES 6001 – Responsible Sourcing of Construction Products

ISO 50001 – Energy Management

STORAGE

Bags should be stored unopened clear of the ground in cool dry conditions and protected from excessive draft and all sources of moisture. The maximum shelf life of packed cement is stated on the bag.

CONDITIONS OF USE

- Methods to prevent loss of moisture from exposed surfaces of concrete, known as curing, should be employed for at least the first 7 days after casting
- As a general rule, concrete should be placed within the range of 10°C to 30°C.
- In cold weather, freshly poured concrete should be protected from low temperatures to avoid frost damage.
- In hot weather and mass concrete pours, there is increased risk of loss of water by evaporation and cracking caused by thermal stresses which could reduce ultimate strength.
- Hanson Cement cannot be held responsible for poor workmanship.
- Due to the nature of raw materials used in the production of HS52, slight variations in colour may occur.
- Hanson HS52 produced at different manufacturing works may also have variation in colour.

TECHNICAL SUPPORT

For further advice please contact Hanson Cement's Technical Helpline on 0330 123 2441.

HEALTH AND SAFETY

Please refer to Material Safety Data Sheet for full information.

For further information contact:

Hanson Cement
Ketton
Stamford
Lincolnshire
PE9 3SX

Hanson.co.uk

Customer Services:

Tel: 0330 123 4525
Fax: 01780 727 008
Email: cement@hanson.com



A.2.3 Ground Granulated Blast Furnace Slag Summary Data Sheet (GGBS)

Updated January 2019

Hanson Purfleet REGEN GGBS

Technical Data Sheet

**1. STANDARDS AND CERTIFICATES**

Description	Certificate	Standard	Certificate Number
Ground Granulated Blastfurnace Slag	CE	BS EN 15167-1	1333-CPR-00133

Certificate issued by CPC, 1 Mount Mews, High Street, Hampton, Middlesex, TW12 2SH

2. DECLARED COMPOSITION

	Units	Average Values	Requirement	
			Minimum	Maximum
Granulated Blastfurnace Slag (GBS) ^a	%	100	-	-

^a Granulated blastfurnace slag is sourced/imported from various locations and blended to create a consistent feed.

3. CHEMICAL CHARACTERISTICS

The chemical characteristics are determined in accordance with BS EN 196-2

	Units	Average Values	Requirement	
			Minimum	Maximum
MgO	%	8	-	18
S ₂ -	%	0.8	-	2.0
SO ₃	%	0.3	-	2.5
LOI	%	0.9	-	3.0
Cl-	%	0.02	-	0.10
Moisture ^b	%	≤0.1	-	1.0

^b Moisture content is determined in accordance with Annex A of BS EN 15167-1.

Purfleet REGEN GGBS – Technical Data Sheet

4. PHYSICAL CHARACTERISTICS

	Test Method	Units	Average Values	Requirement	
				Minimum	Maximum
Specific Surface Area	BS EN 196-6	m ² /kg	470	275	-
Initial Setting Time	BS EN 196-3	Minutes	200 ^c	-	290 ^d
7 Day Activity Index ^e	BS EN 196-1	%	65 ^c	45	-
28 Day Activity Index ^e	BS EN 196-1	%	88 ^c	70	-

^c Data generated on a blend of 50:50% GGBS:Test Cement (Test cement meets the requirements specified in BS EN 15167-1).

^d Setting time maximum requirement is two times the setting time of the test cement without the addition of GGBS.

^e The activity index is expressed as the ratio (in %) of the compressive strength of the combination 50:50% GGBS:Test Cement, to the compressive strength of the test cement without the addition of GGBS.

5. MECHANICAL CHARACTERISTICS

The mechanical characteristics^c are determined in accordance with BS EN 196-1.

Compressive Strength	Units	Average Values	Requirement	
			Minimum	Maximum
7 Day	MPa	32.0	-	-
28 Day	MPa	53.5	-	-

6. PRODUCTION AND DELIVERY

The GGBS is produced at Hanson Cement's Purfleet works and is produced utilising the vertical mill and/or ball mills on site. The GGBS is stored in 8 silos on site. The GGBS is despatched by road to customers local to the GGBS works.

7. MANAGEMENT SYSTEMS

The plants management system is certified to ISO 9001.

8. DECLARATION OF PERFORMANCE

In compliance with Regulation 305/2011/EU of the European Parliament and of the Council of 9th March 2011 (the Construction Products Regulation or CPR), a declaration of performance can be accessed from www.hanson.co.uk.

The average values given above represent the previous 12 months production, and are provided as guidelines only. The minimum and maximum requirements are guaranteed limits.

For further information contact:

Hanson Cement
Ketton
Stamford
Lincolnshire
PE9 3SX

Hanson.co.uk

Customer Services:

Tel: 0330 123 4525
Fax: 01780 727 008
Email: cement@hanson.com



A.2.4 Microsilica Summary Data Sheet

Elkem Silicon Materials,
PO Box 8126, Vaagsbygd,
NO-4675 Kristiansand, NORWAY



Elkem Microsilica® 940

Fibre cement applications – Product data sheet

1. Description

Elkem Microsilica® Grade 940 is a dry silica fume available in two forms: Undensified and Densified. In use, it acts physically as a filler and chemically as a highly reactive pozzolan.

A key ingredient in many construction materials, Elkem Microsilica® is used in fibre cement products as a process aid, to improve ingredient dispersion and to improve hardened properties and overall durability.

2. Chemical properties

Property	Unit	Typical value
SiO ₂	%	> 90.0
H ₂ O	%*	< 1.0

Test methods available on request. Typical values for guidance only. *When packed.

3. Physical properties

Property	Unit	Typical value
Retention on 45µm sieve	%	< 1.5
Bulk density U	kg/m ³ *	200 - 350
Bulk density D	kg/m ³ *	500 - 700

Test methods available on request. Typical values for guidance only. *When packed.

4. Packing

The product is available in 25 kg bags, various other size bags and bulk road tanker. Please contact our representative for more details.

5. Storage & handling

Elkem Microsilica® Grade 940 should be kept in dry storage. Products that have been subjected to moisture and allowed to dry again may result in inferior performance.

6. Quality assurance

Elkem Silicon Materials is certified to ISO 9001. The chemical and physical properties of Elkem Microsilica® are regularly tested.

7. Health, safety & environment

Refer to Product Safety Information (PSI) document on Elkem website: elkem.com

8. Additional information

See additional Elkem data sheets and technical papers on our website: elkem.com

All data listed are reference values subject to production related tolerances. Although reasonable care has been taken in the preparation of the information contained herein, it still remains the duty of the user to prove the suitability of this material for their application.


This data sheet is property of Elkem ASA and may not be used without written permission, copied or made available to others. The receiver is responsible for every misuse.

elkem.com

Elkem Microsilica® is a registered trademark. Copyright Elkem ASA

Revised April 2020

A.2.5 High-range Water Reducing Admixture – Sika ViscoCrete Summary Data Sheet

Construction	Product Data Sheet Edition 12/07/2016 Identification no: 02 13 01 01 100 0 000409 Sika® ViscoCrete® 30HE (UK)		CE
	Sika® ViscoCrete® 30HE (UK)		
	Accelerating High Range Water Reducing/Superplasticising Concrete Admixture		
	Product Description	Sika® ViscoCrete® 30HE (UK) is a liquid admixture for concrete which is used as an accelerating high range water reducer or superplasticiser. It meets the requirements of BS EN 934-2.	
	Uses	Sika® ViscoCrete® 30HE (UK) has been specifically formulated for the production of concrete mixes which require high early strength development, powerful water reduction and excellent flowability.	
		<ul style="list-style-type: none"> ■ Precast concrete ■ Fast track concrete ■ Self compacting concrete 	
	Characteristics / Advantages	<ul style="list-style-type: none"> ■ Significantly increased early age strength ■ Excellent water reduction ■ Excellent flowability ■ Reduced drying shrinkage ■ Improved surface finish 	
	Tests		
	Approvals / Standards	Conforms to the requirements of BS EN 934-2 Tables 3.1 & 3.2 DoP 02 13 01 01 100 0 000422 1088, certified by Factory Production Control Body 0086, Certificate 541325, and provided with the CE mark	
	Product Data		
Form			
Appearance / Colour	Light Brown Liquid		
Packaging	25 litre drum and 1000 litre IBC		
Storage			
Storage Conditions / Shelf-Life	12 months from date of production if stored in unopened and undamaged original sealed containers protected from moisture at temperatures between +5°C and +25°C.		
			

Technical Data	
Chemical Base	Modified Polycarboxylate
Density	1.06 kg/litre
pH Value	4.4 ± 1.0
Water Soluble Chloride Content	<0.1% w/w (chloride free)
Alkali Content	< 0.40%
System Information	
Application Details	
Consumption / Dosage	<ul style="list-style-type: none"> ■ 0.2 - 0.8% by weight of cement (medium workability) ■ 1.0 – 2.0% by weight of cement (high workability/SCC)
Dispensing	<ul style="list-style-type: none"> ■ Sika®ViscoCrete® 30HE (UK) should be dispensed through suitable calibrated equipment
Application Conditions / Limitations	<ul style="list-style-type: none"> ■ Sika®ViscoCrete® 30HE (UK) should not be added to dry cement ■ Sika®ViscoCrete® 30HE (UK) should be added with the mixing water
Compatibility	<p>Sika®Admixtures:</p> <ul style="list-style-type: none"> ■ Compatibility information available on request <p>Cements:</p> <ul style="list-style-type: none"> ■ All cement combinations
Notes on Application / Limitations	Support from our Technical Service Department is recommended.
Value Base	All technical data stated in this Product Data Sheet are based on laboratory tests. Actual measured data may vary due to circumstances beyond our control.
Local Restrictions	Please note that as a result of specific local regulations the performance of this product may vary from country to country. Please consult the local Product Data Sheet for the exact description of the application fields.
Health and Safety Information	For information and advice on the safe handling, storage and disposal of chemical products, users shall refer to the most recent Material Safety Data Sheet containing physical, ecological, toxicological and other safety-related data.
Legal Notes	The information, and, in particular, the recommendations relating to the application and end-use of Sika products, are given in good faith based on Sika's current knowledge and experience of the products when properly stored, handled and applied under normal conditions in accordance with Sika's recommendations. In practice, the differences in materials, substrates and actual site conditions are such that no warranty in respect of merchantability or of fitness for a particular purpose, nor any liability arising out of any legal relationship whatsoever, can be inferred either from this information, or from any written recommendations, or from any other advice offered. The user of the product must test the product's suitability for the intended application and purpose. Sika reserves the right to change the properties of its products. The proprietary rights of third parties must be observed. All orders are accepted subject to our current terms of sale and delivery. Users must always refer to the most recent issue of the local Product Data Sheet for the product concerned, copies of which will be supplied on request.

A.3 E-UHPFRC Mix Design

Table A.1 E-UHPFRC mix proportion

Mix ID	Constituent Materials (Kg/m ³)							
	Cement	GGBS	Silica Fume	Silica Sand	Plasticizer	Water	RTSC	RTSF
Plain	657	418	119	1051	59	185	0.0	0.0
f 2 - CCC	657	418	119	1051	59	185	157.0	0.0
f 2 - CCF	657	418	119	1051	59	185	104.7	52.3
f 2 - CFF	657	418	119	1051	59	185	52.3	104.7
f 2 - FFF	657	418	119	1051	59	185	0.0	157.0
f 3 - CCC	657	418	119	1051	59	185	235.5	0.0
f 3 - CCF	657	418	119	1051	59	185	157.0	78.5
f 3 - CFF	657	418	119	1051	59	185	78.5	157.0
f 3 - FFF	657	418	119	1051	59	185	0.0	235.5
f 4 - CCC	657	418	119	1051	59	185	314.0	0.0
f 4 - CCF	657	418	119	1051	59	185	209.3	104.7
f 4 - CFF	657	418	119	1051	59	185	104.7	209.3
f 4 - FFF	657	418	119	1051	59	185	0.0	314.0

A.4 Photos of Experimental Activities

A.4.1 E-UHPFRC production





Figure A.1: UHPFRC production

A.4.3 Specimens Preparation



Figure A.2: Specimens Preparation

A.4.4 Test Set-ups

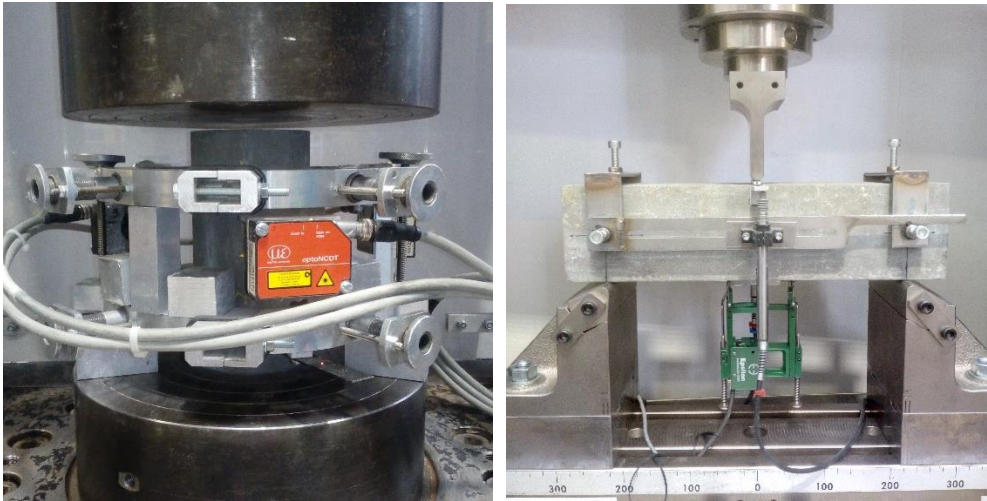


Figure A. 3: Test setup (a) Modulus of Elasticity (b) Three-point flexural test

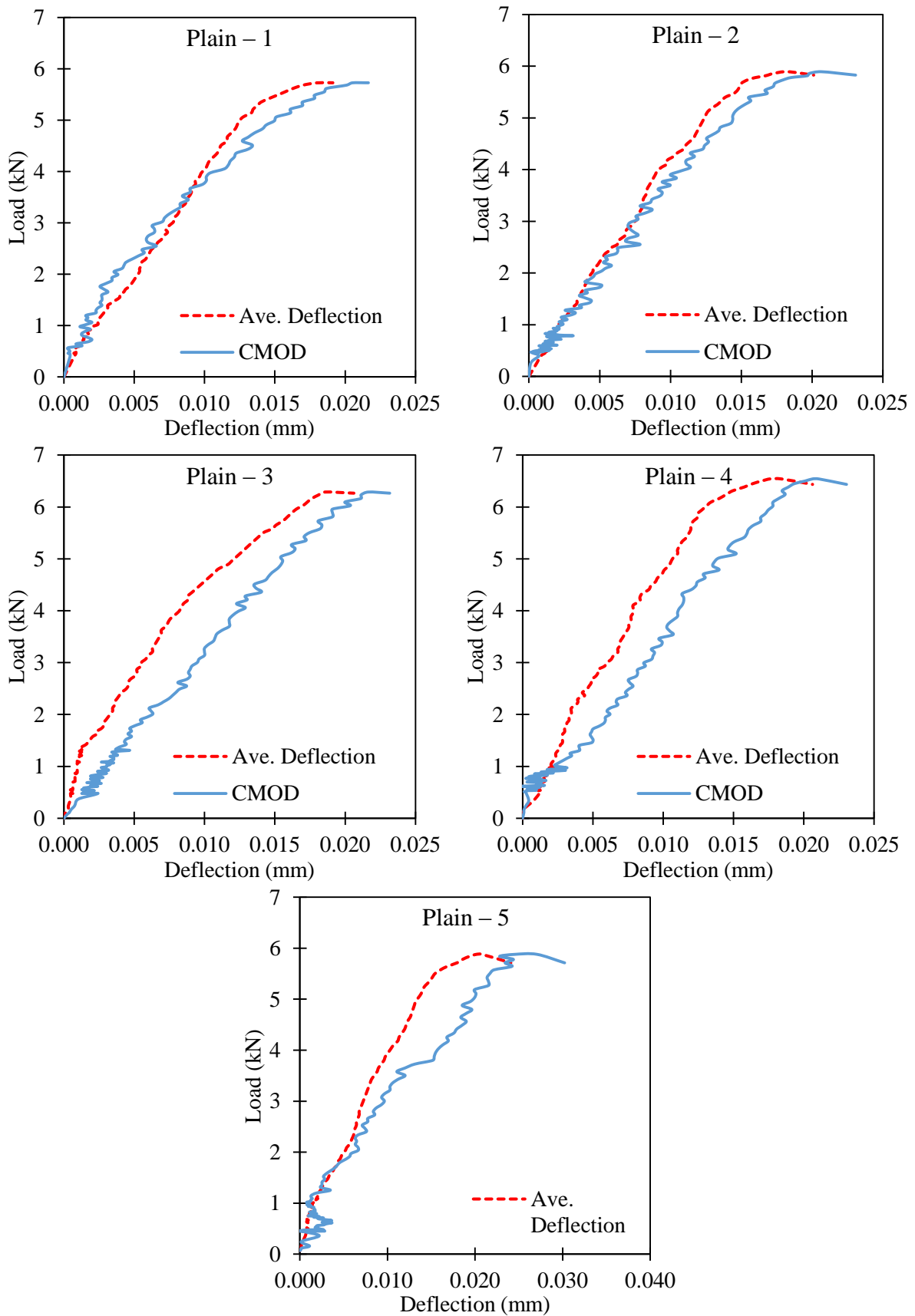
A.5 Results**A.5.1 Modulus of Elasticity**

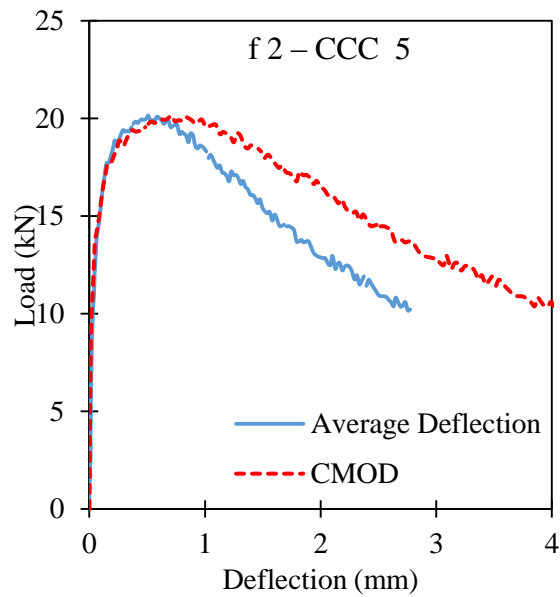
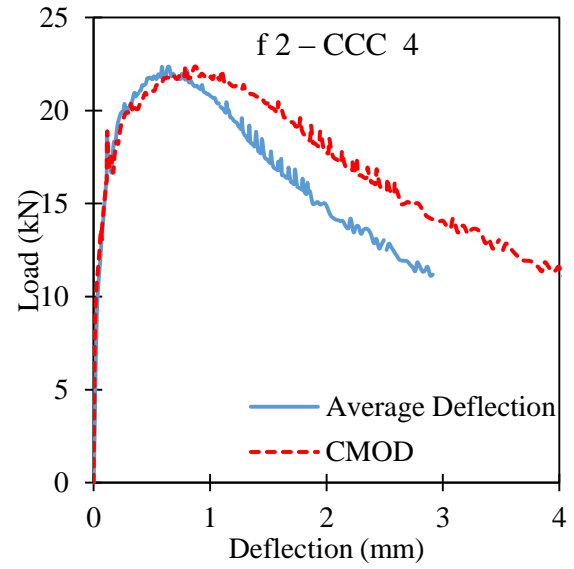
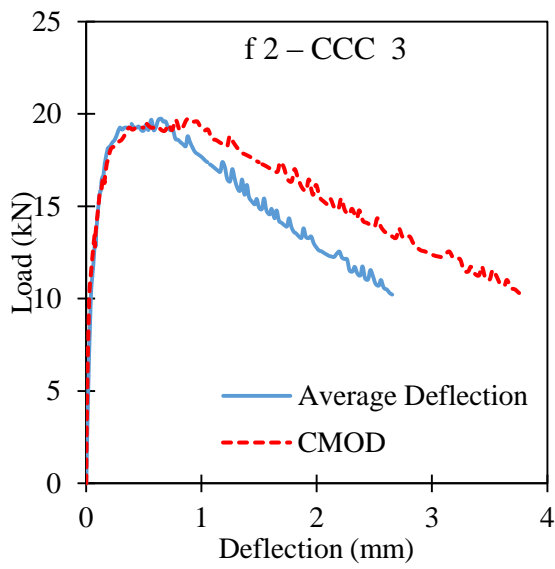
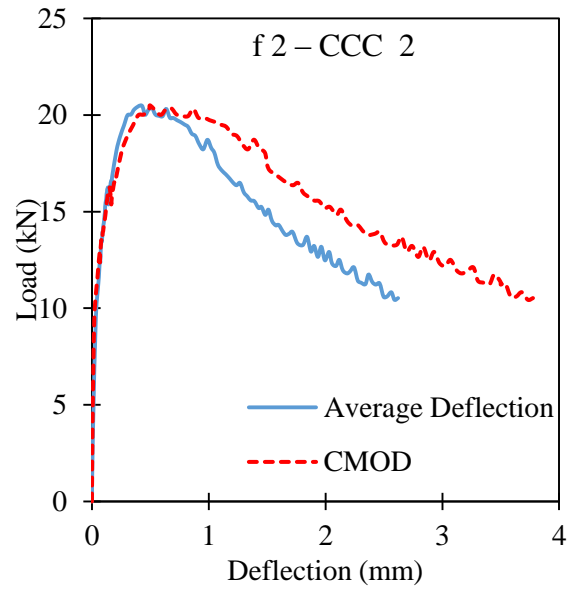
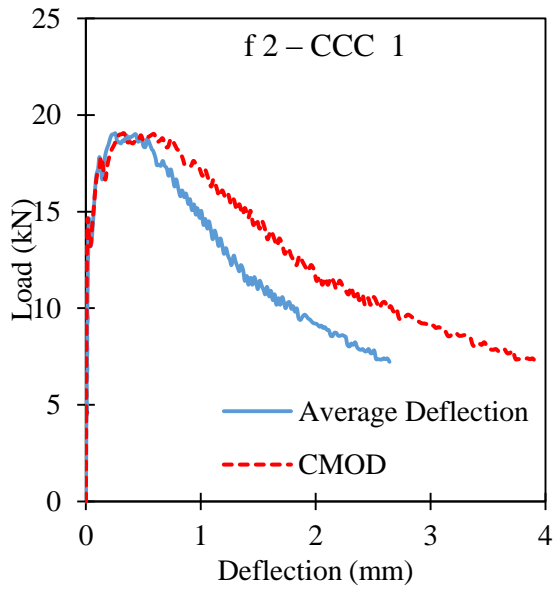
	Mix ID	Casting Date	Specimen		Average	Std. Dev	Coe. of Var.
	Plain	25/01/2019	1	50.3	49.6	0.65	0.01
			2	49.1			
			3	49.4			
2%	f 2 – CCC	28/01/2019	1	51.2	51.4	0.56	0.01
			2	52.0			
			3	51.0			
	f 2 – CCR	29/01/2019	1	51.9	51.5	0.47	0.01
			2	51.0			
			3	51.6			
	f 2 – CRR	30/01/2019	1	50.9	50.7	0.51	0.01
			2	51.1			
			3	50.1			
	f 2 – RRR	31/01/2019	1	50.1	50.5	0.31	0.01
			2	50.7			
			3	50.5			
3%	f 3 – CCC	04/02/2019	1	51.4	52.5	1.05	0.02
			2	52.6			
			3	53.5			
	f 3 – CCR	05/02/2019	1	52.7	52.1	0.53	0.01
			2	52.1			
			3	51.7			
	f 3 – CRR	06/02/2019	1	51.2	51.8	0.65	0.01
			2	52.5			
			3	51.7			
	f 3 – RRR	07/02/2019	1	50.9	51.0	0.32	0.01
			2	50.7			
			3	51.4			
4%	f 4 – CCC	11/02/2019	1	53.1	53.6	0.59	0.01
			2	53.4			
			3	54.2			
	f 4 – CCR	12/02/2019	1	53.9	53.2	0.64	0.01
			2	52.7			
			3	53.0			
	f 4 – CRR	13/02/2019	1	53.0	53.4	1.07	0.02
			2	52.5			
			3	54.6			
	f 4 – RRR	14/02/2019	1	53.0	52.6	0.49	0.01
			2	52.8			
			3	52.1			

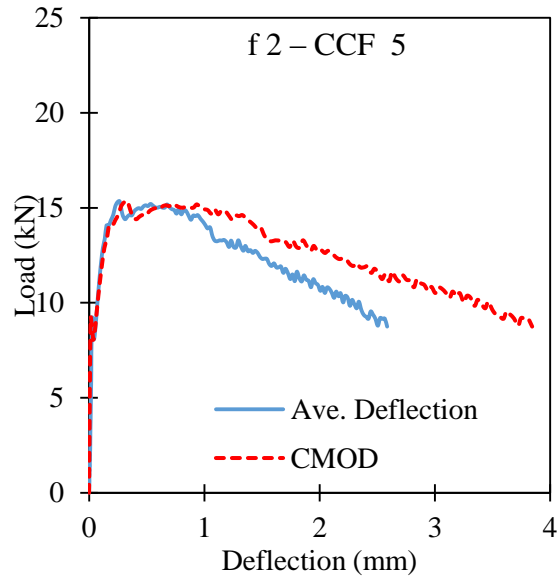
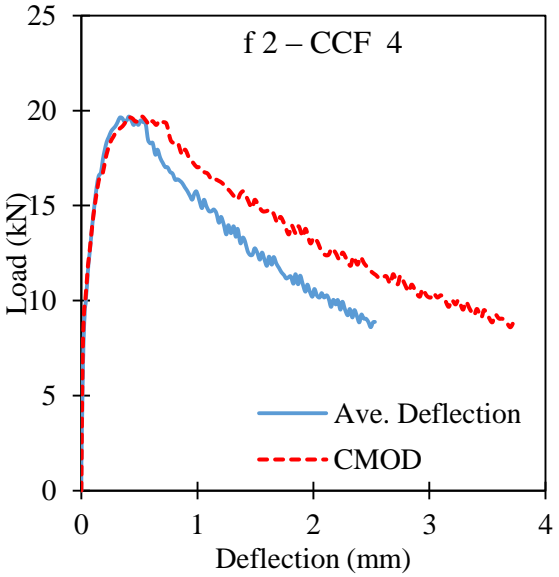
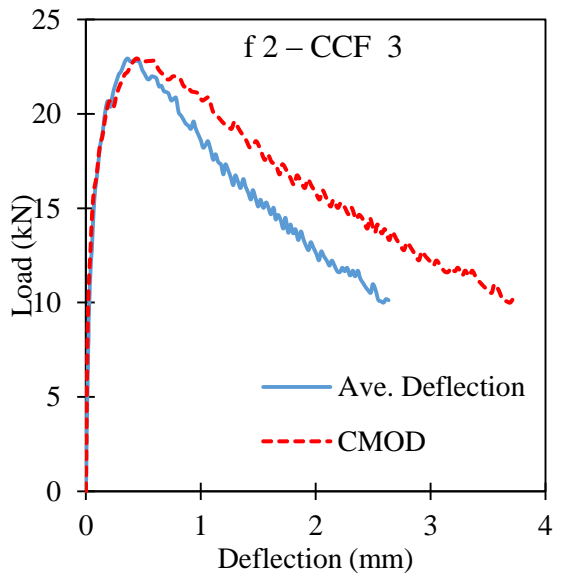
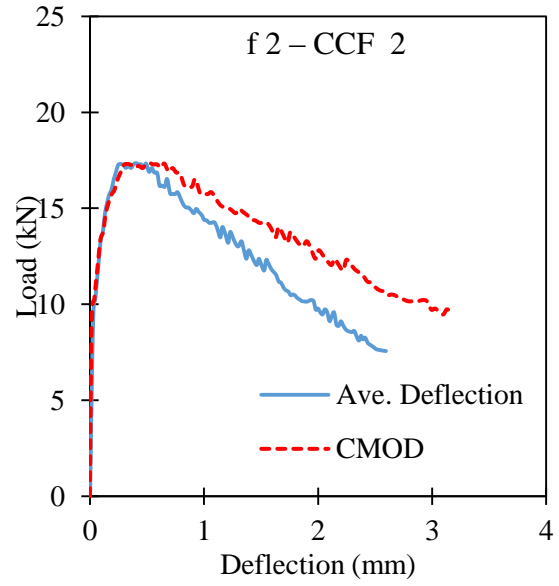
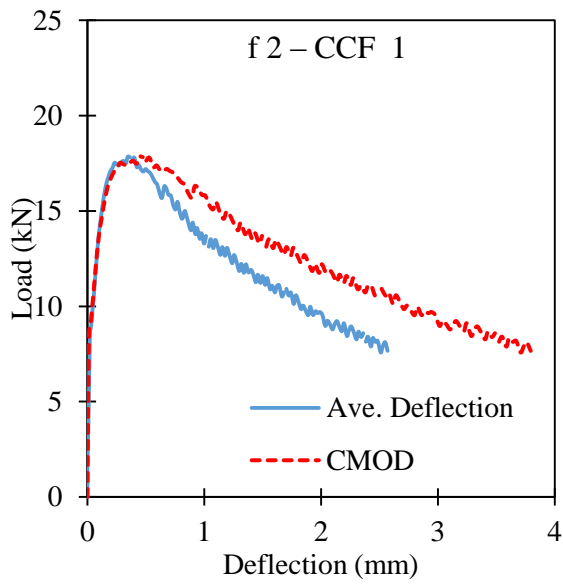
A.5.2 Compressive Strength

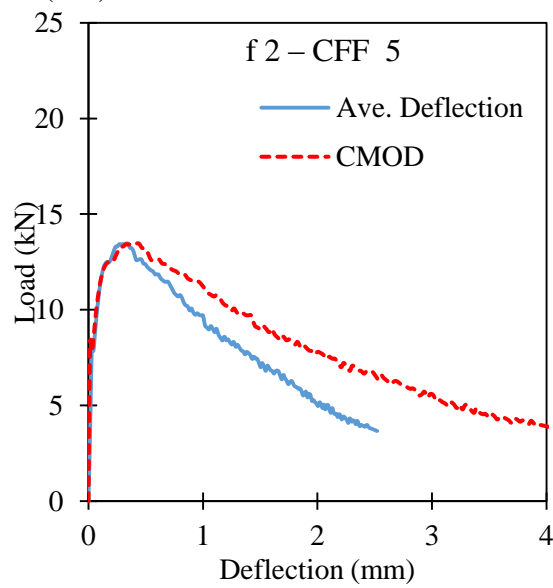
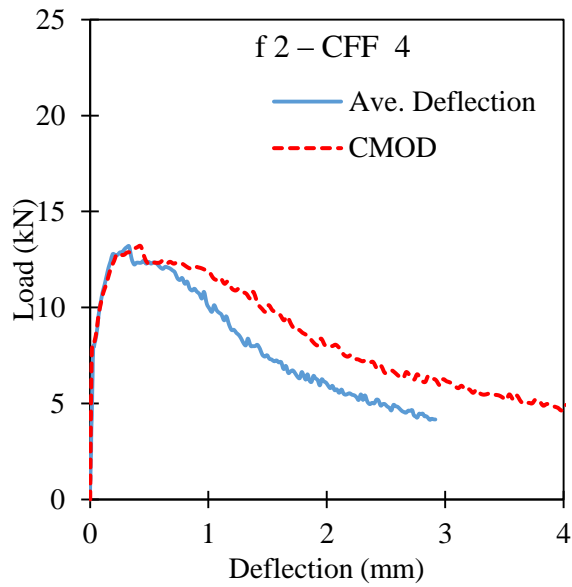
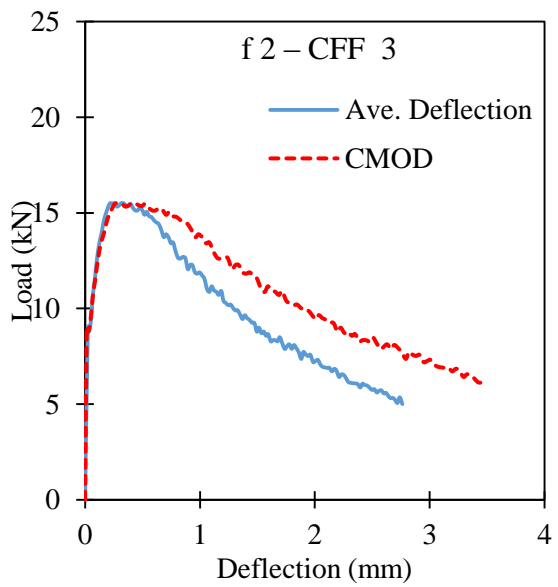
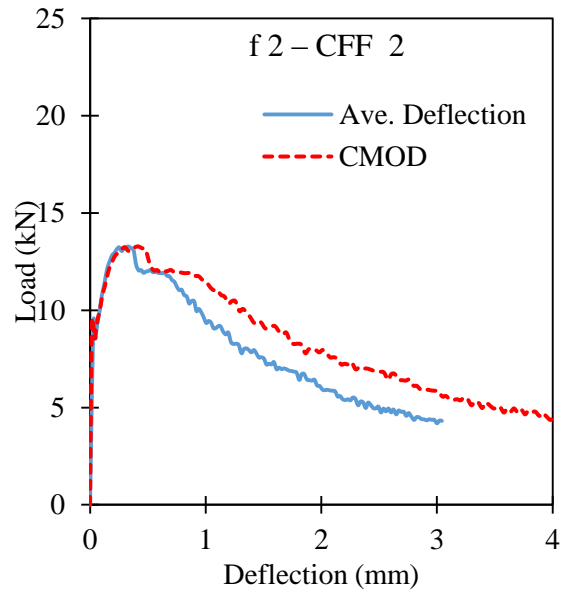
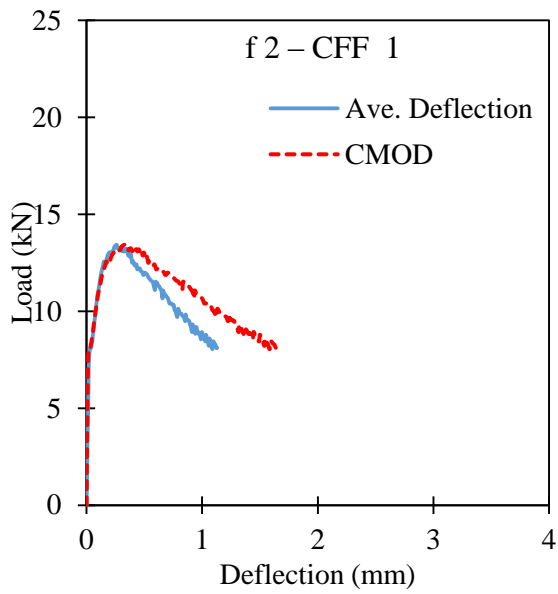
Fibre Dosage	Mix ID	Casting Date	Specimen		Average	Std. Dev	Coe. of Var.
	Plain	25/01/2019	1	157.4	158	1.63	0.01
			2	160.0			
			3	157.0			
2%	f 2 – CCC	28/01/2019	1	179.7	173	6.08	0.04
			2	167.8			
			3	171.7			
	f 2 – CCR	29/01/2019	1	177.5	171	5.55	0.03
			2	167.1			
			3	168.8			
	f 2 – CRR	30/01/2019	1	157.6	159	11.30	0.07
			2	148.5			
			3	171.0			
	f 2 – RRR	31/01/2019	1	158.5	158	5.41	0.03
			2	152.4			
			3	163.2			
3%	f 3 – CCC	04/02/2019	1	175.0	173	8.85	0.05
			2	163.6			
			3	181.0			
	f 3 – CCR	05/02/2019	1	164.3	169	4.89	0.03
			2	174.0			
			3	168.1			
	f 3 – CRR	06/02/2019	1	173.3	167	8.41	0.05
			2	170.7			
			3	157.6			
	f 3 – RRR	07/02/2019	1	151.3	160	10.46	0.07
			2	155.9			
			3	171.3			
4%	f 4 – CCC	11/02/2019	1	172.8	172	5.90	0.03
			2	165.6			
			3	177.3			
	f 4 – CCR	12/02/2019	1	171.7	169	3.31	0.02
			2	165.2			
			3	169.8			
	f 4 – CRR	13/02/2019	1	169.9	170	3.72	0.02
			2	174.0			
			3	166.5			
	f 4 – RRR	14/02/2019	1	165.3	165	9.18	0.06
			2	174.7			
			3	156.4			

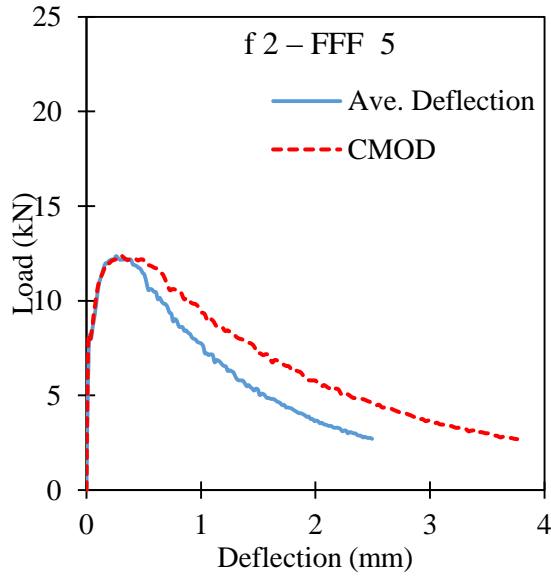
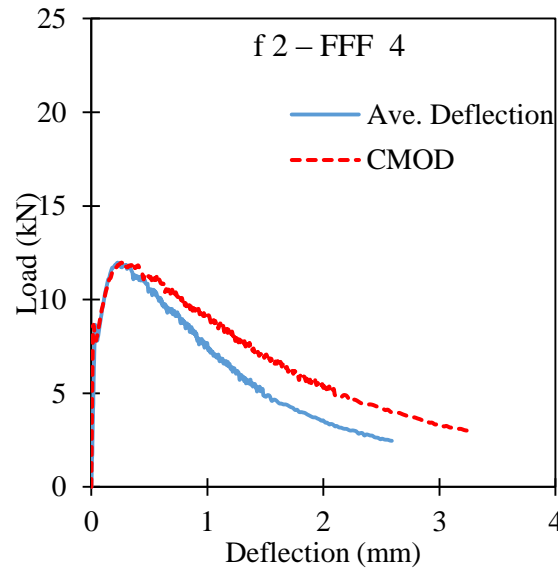
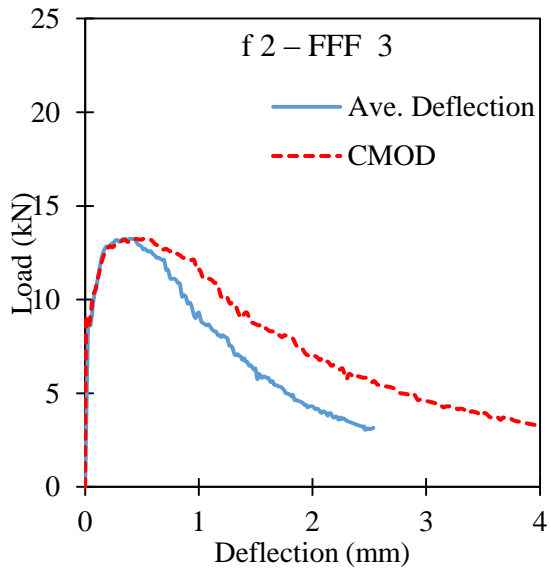
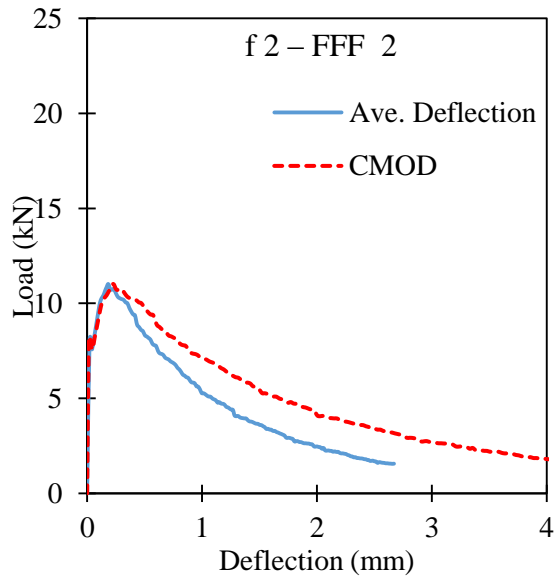
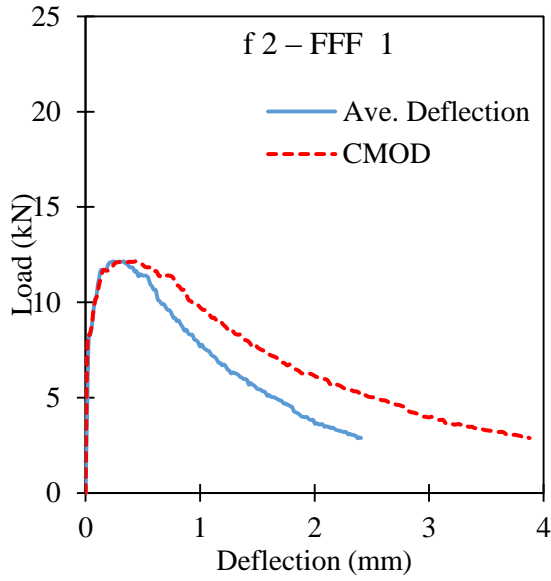
A.5.3 Flexural Strength Test

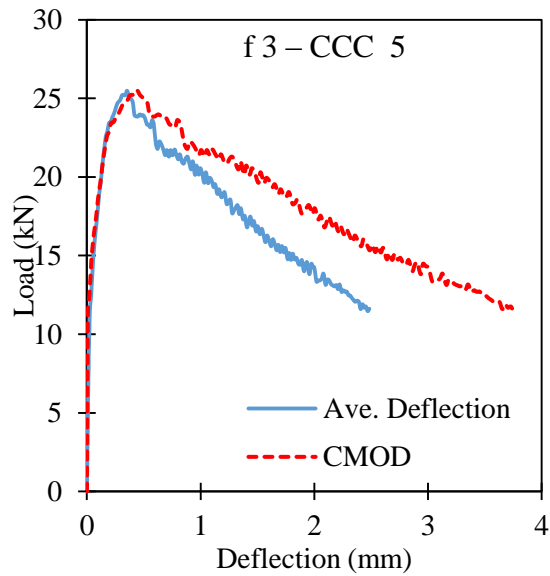
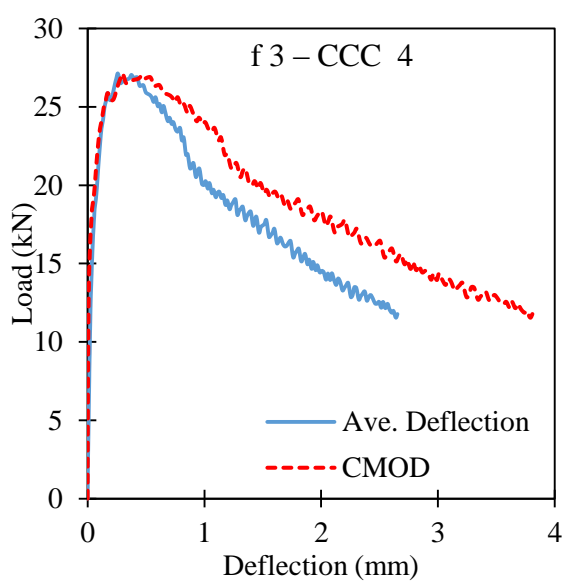
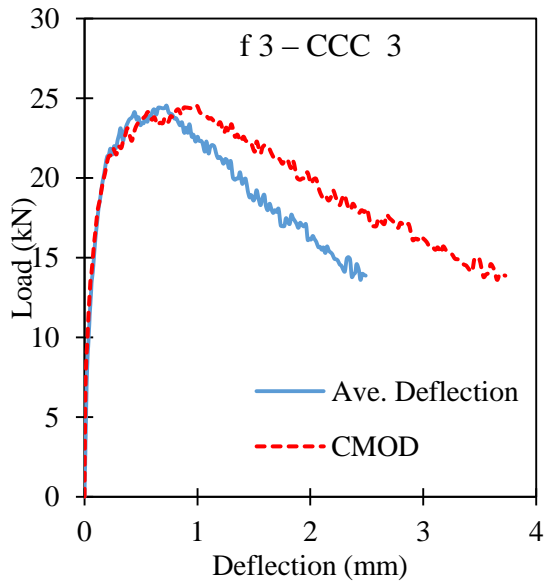
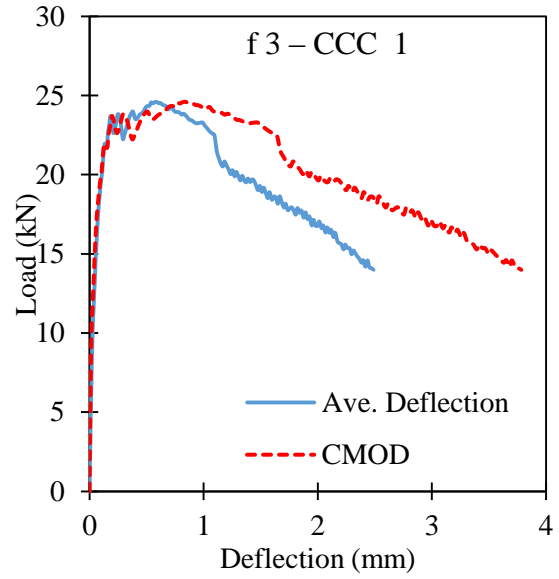
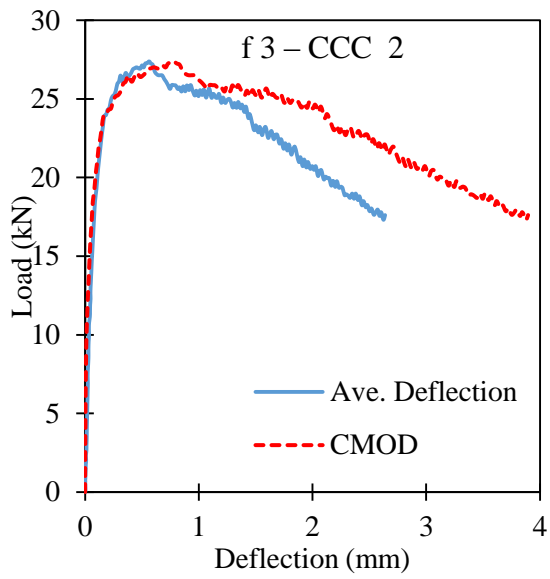


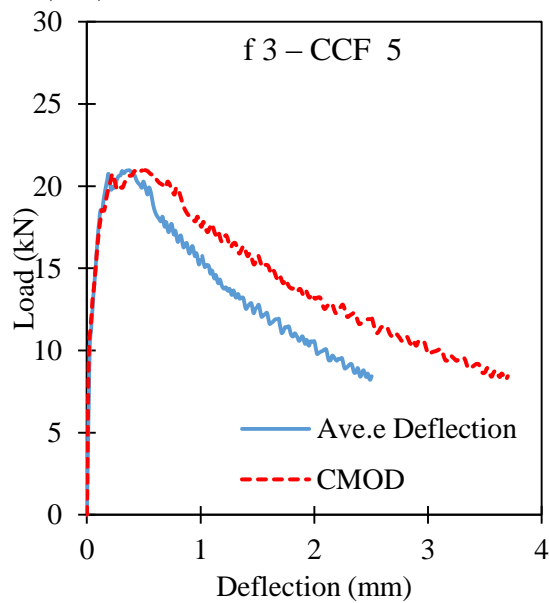
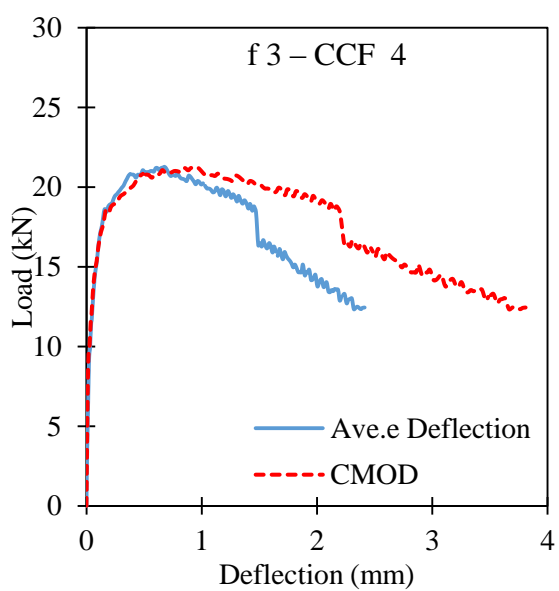
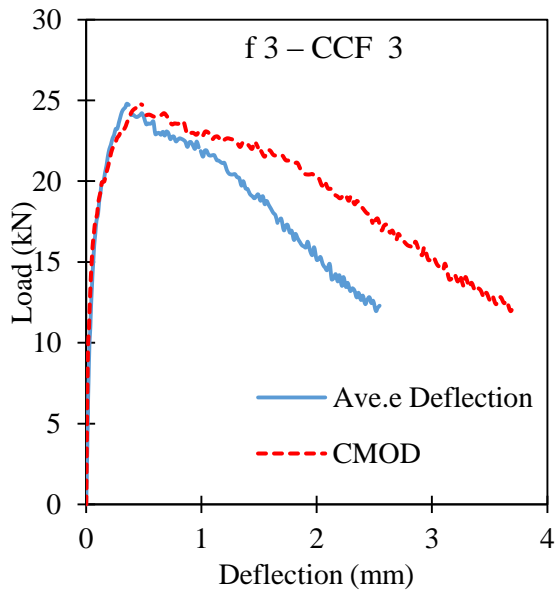
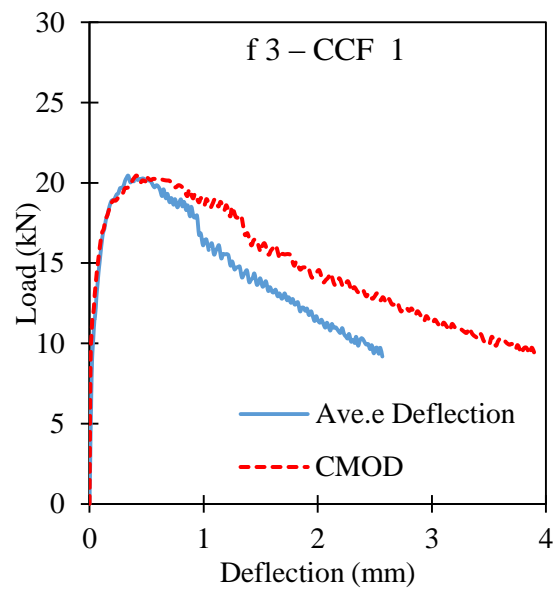
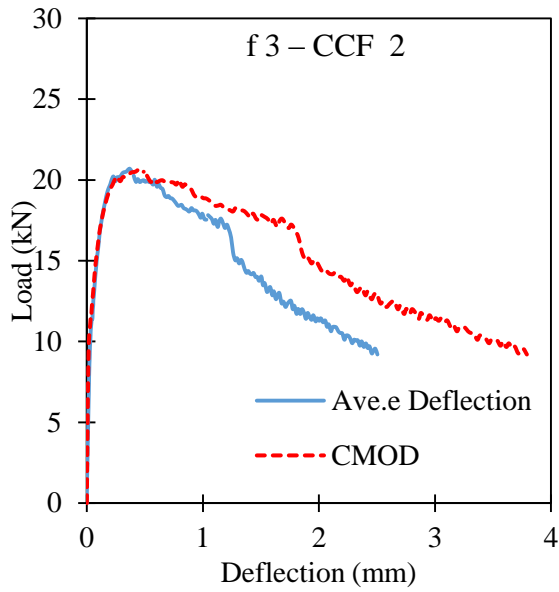


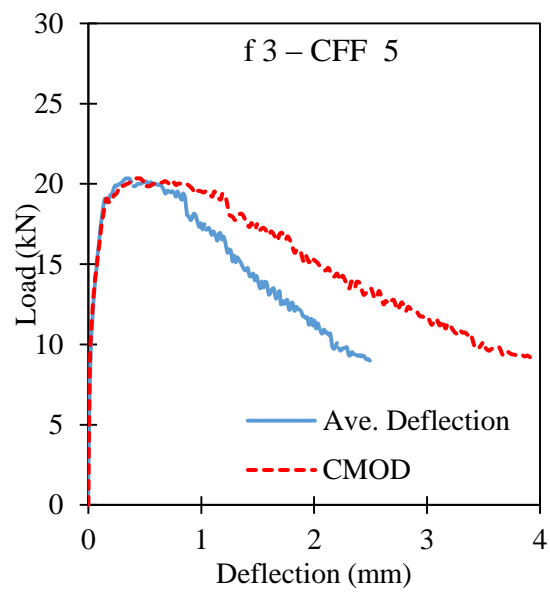
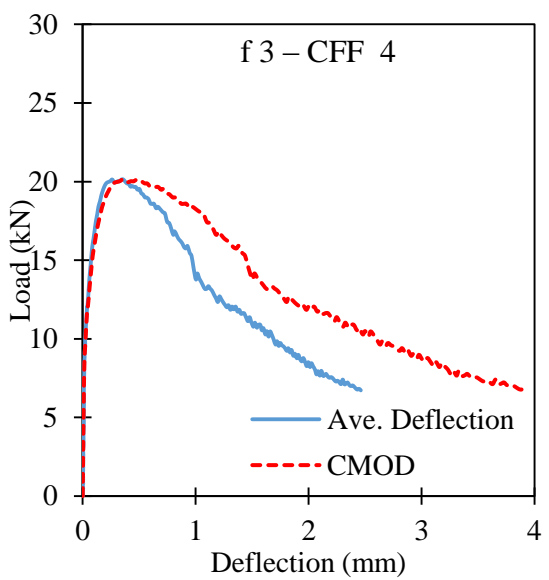
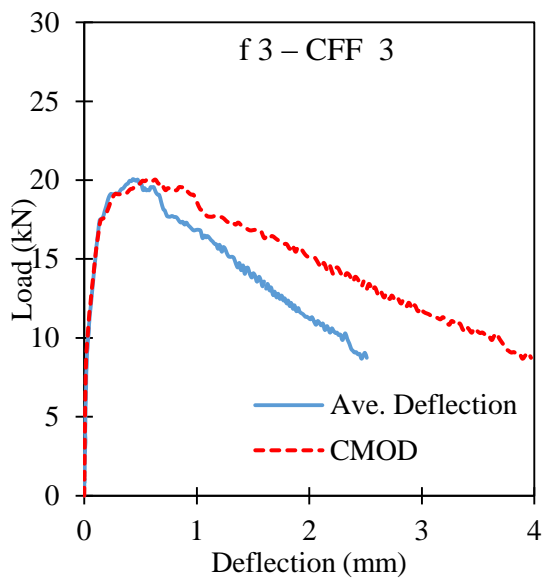
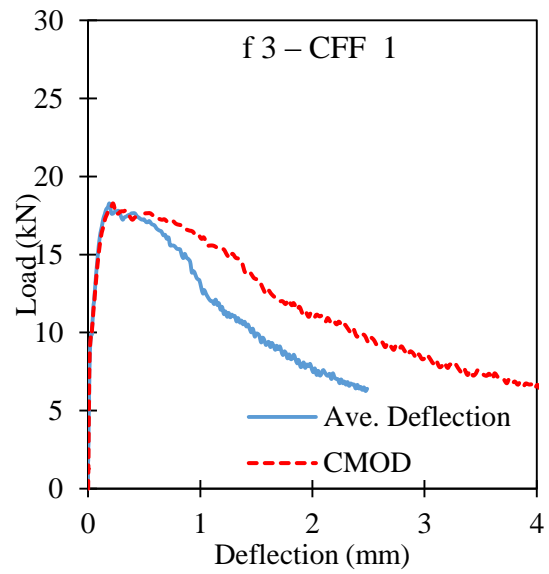
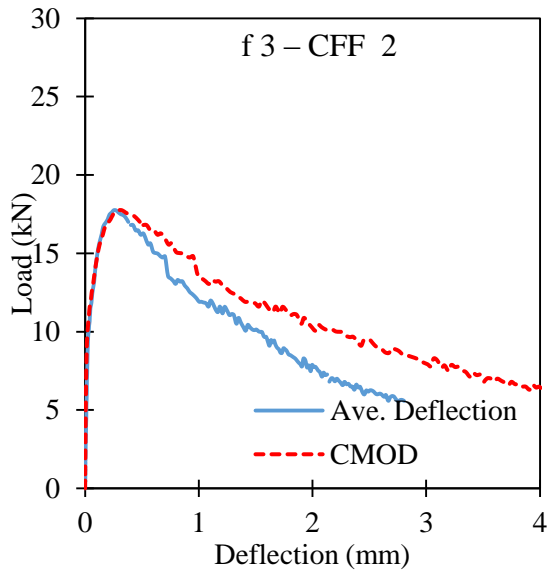


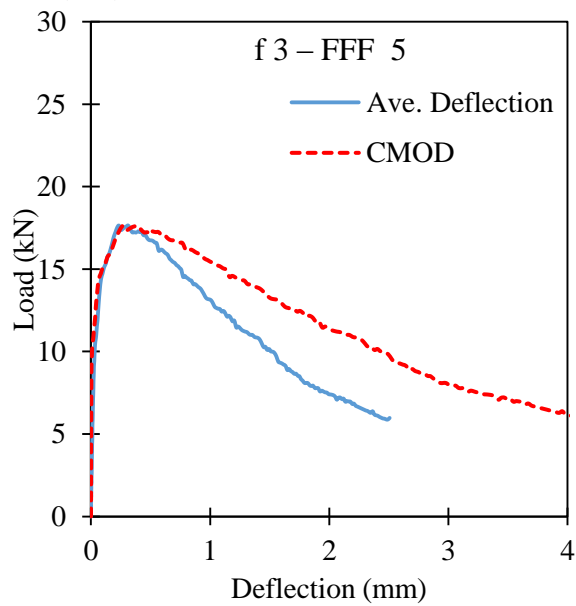
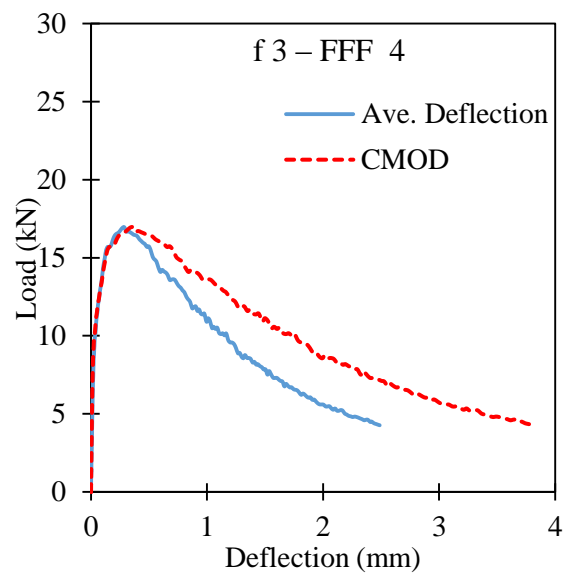
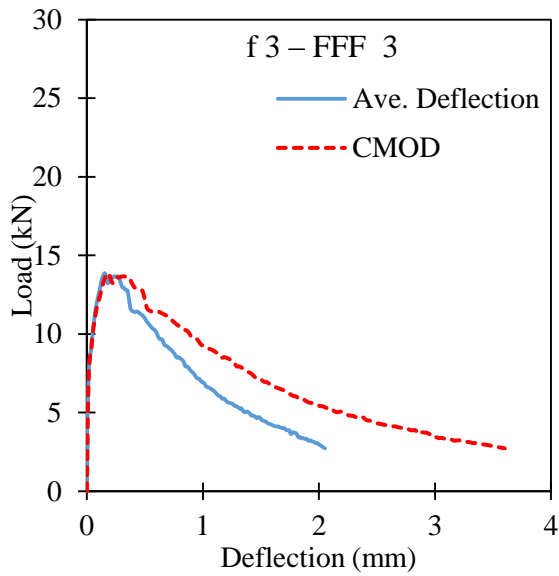
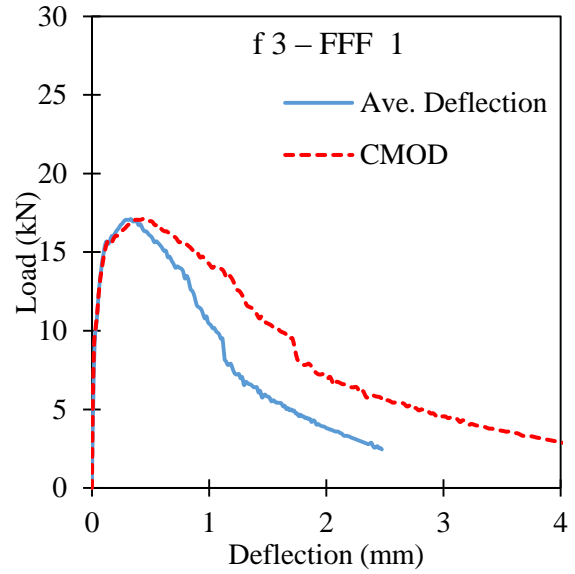
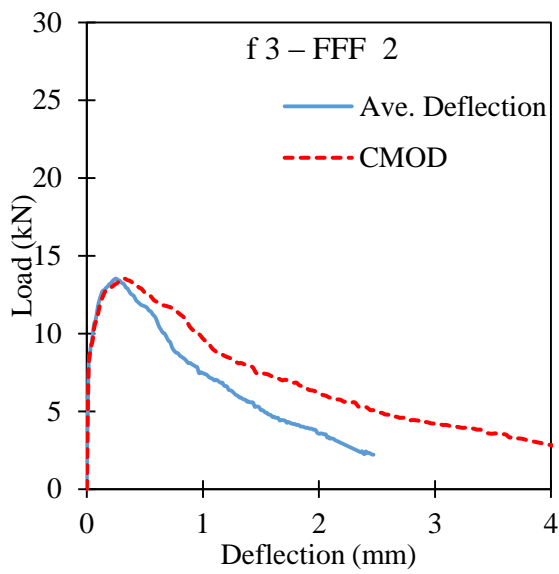


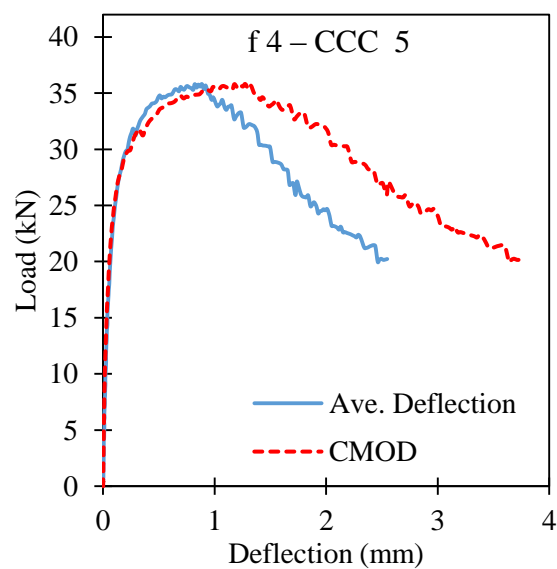
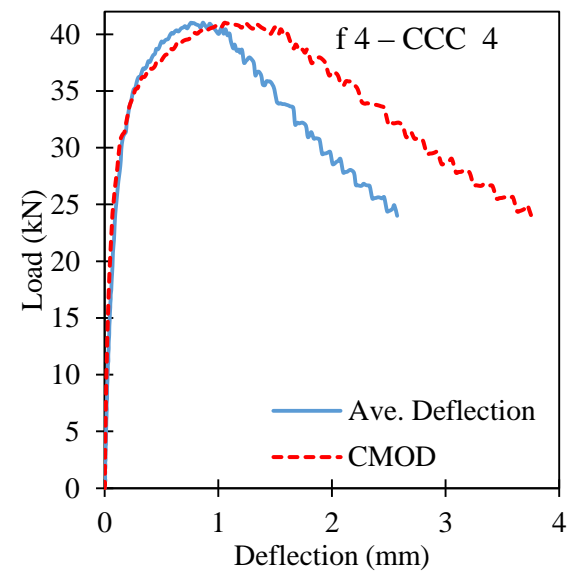
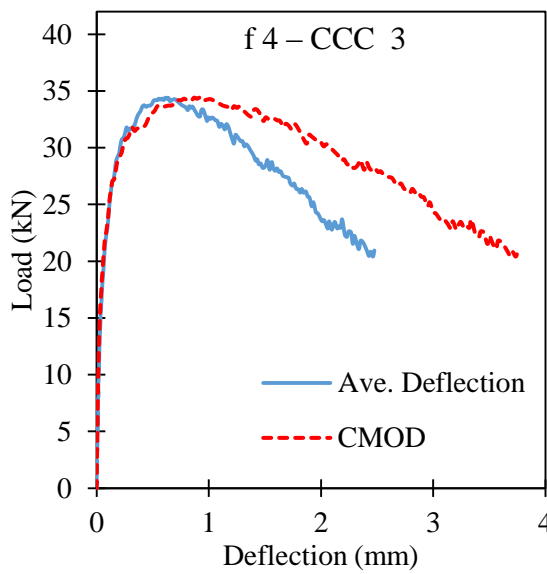
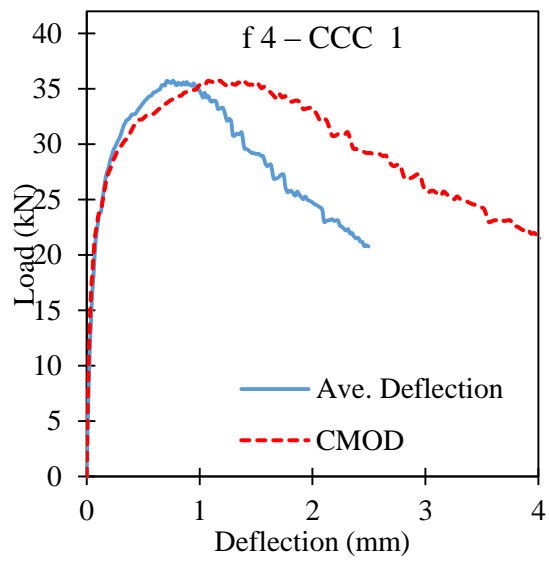
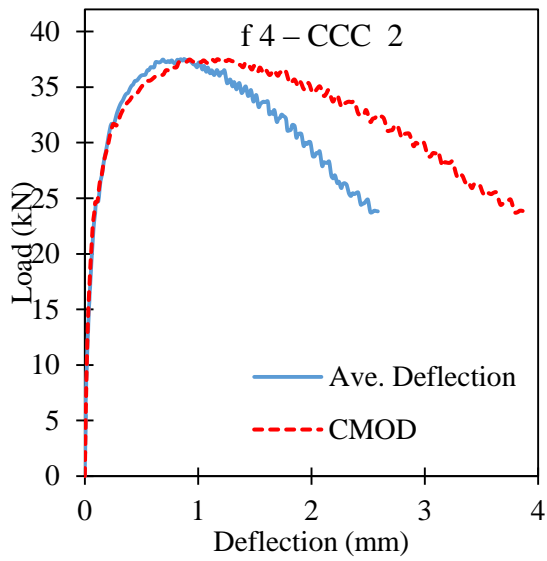


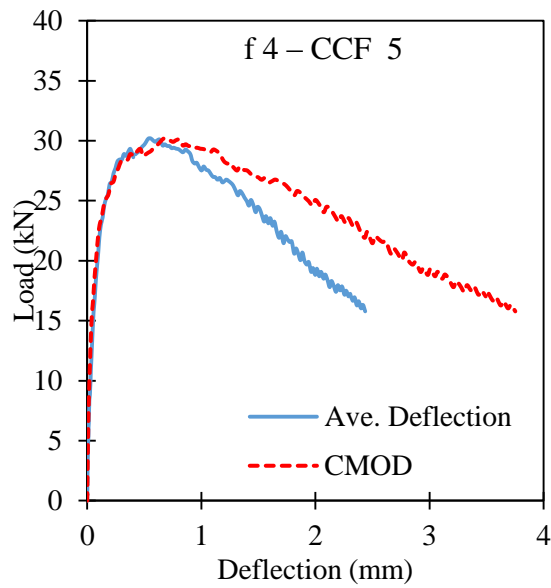
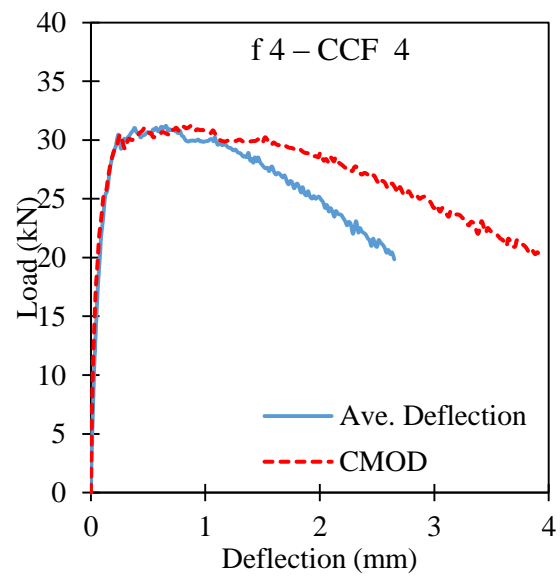
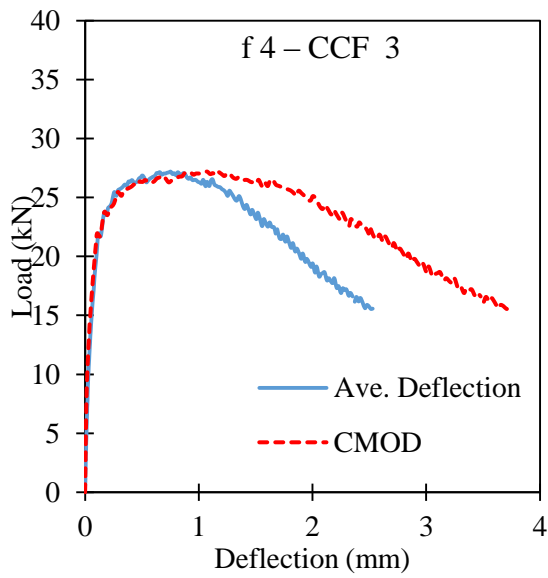
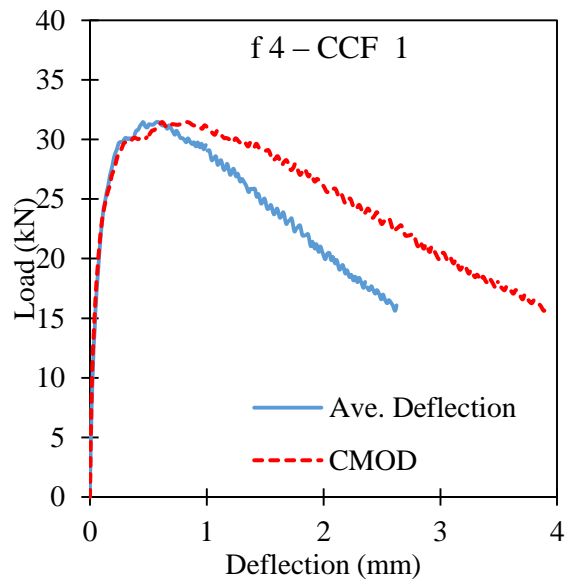
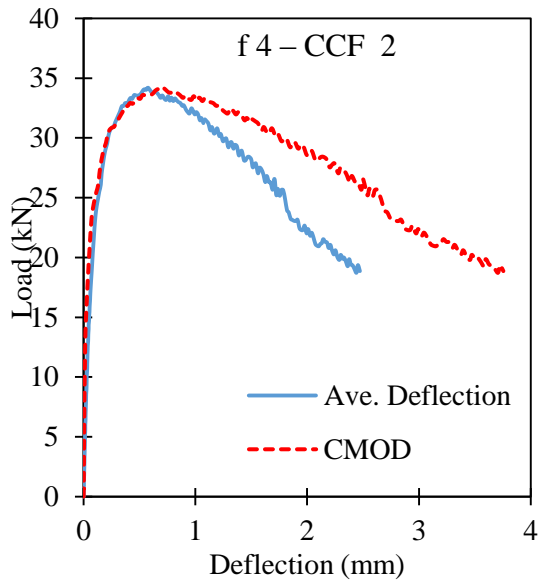


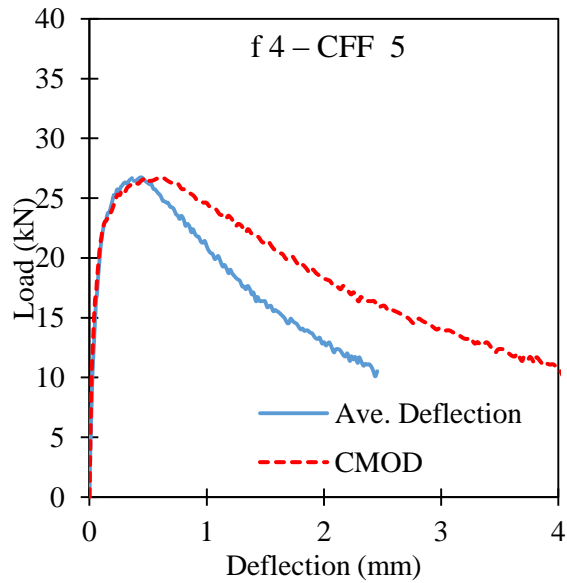
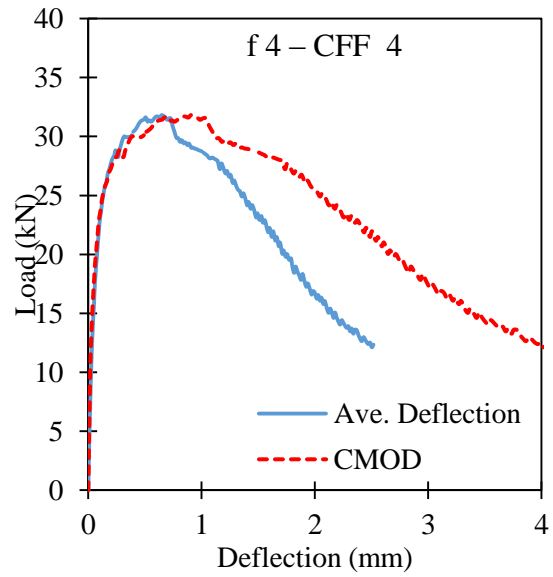
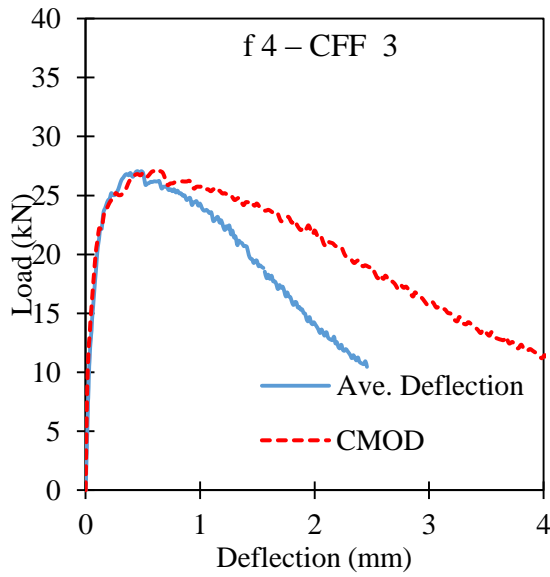
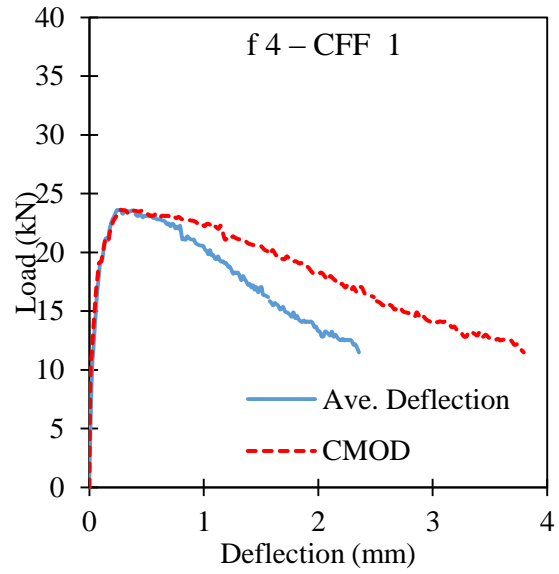
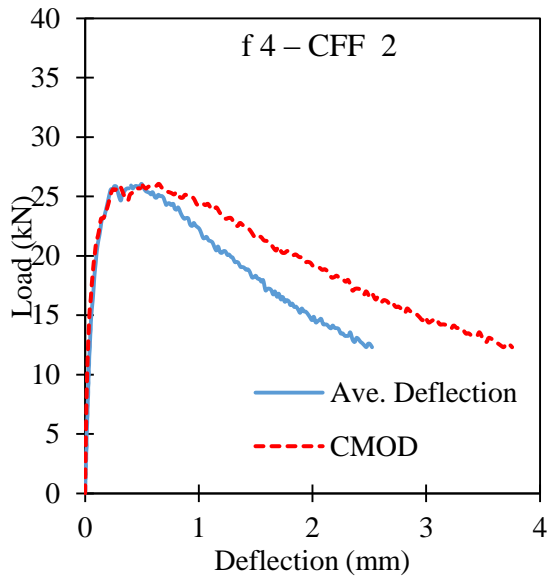


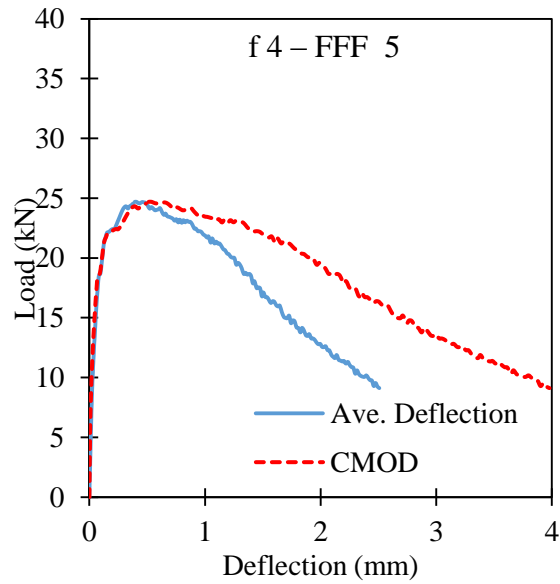
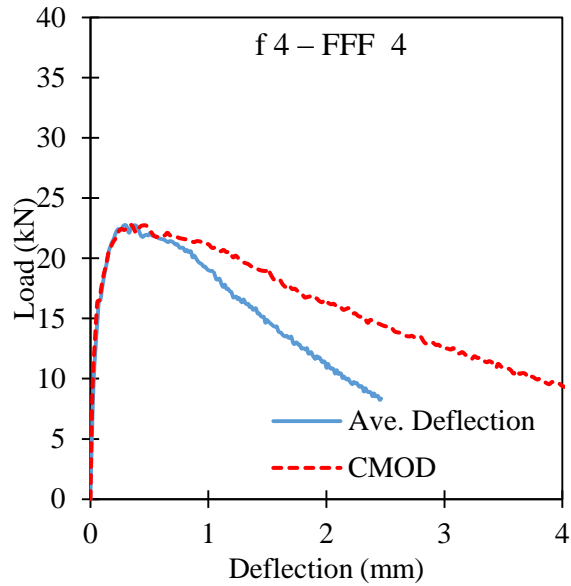
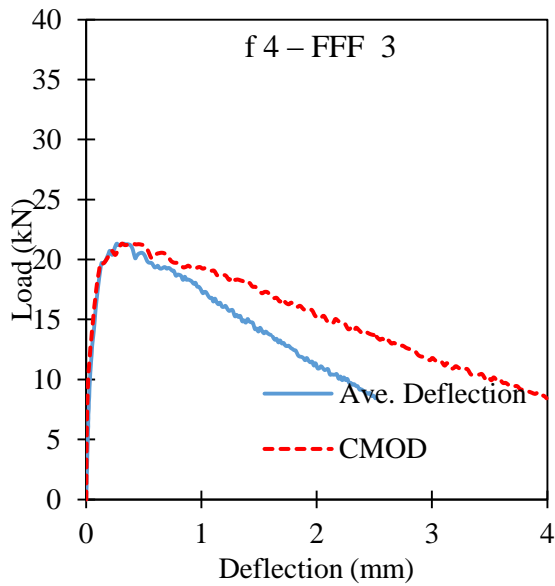
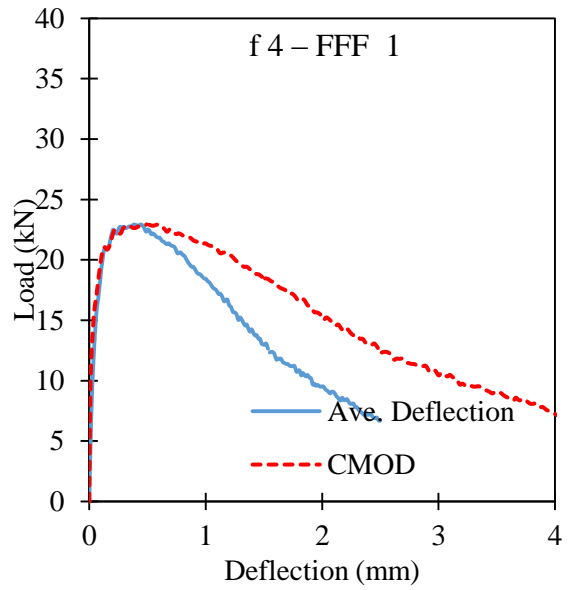
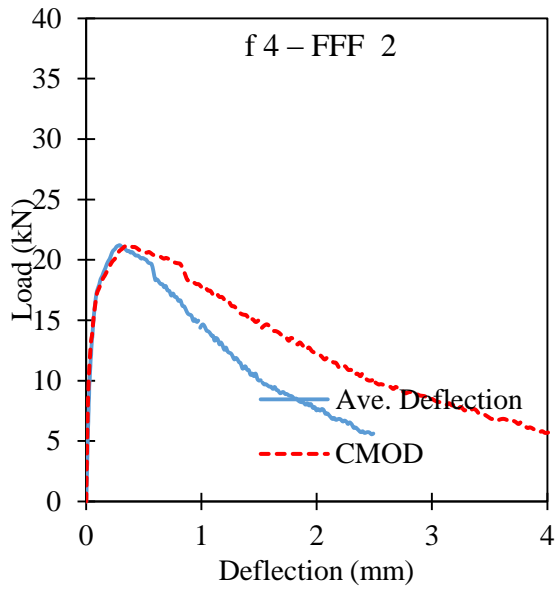












Appendix B: Finite Element Inverse Analysis Chapter 3

This appendix presents additional information regarding Finite Element Inverse Analysis presented in Chapter 3.

B.1 Additional Information

B.1.1 Relationship between Flexural and Tensile Strength in Bending

When a material is tested in flexure, i.e. under bending; tensile stresses are produced at the bottom layers; zero stress at neutral axis and compressive stresses in layers above the neutral axis. For material such as UHPFRC where the compressive strength is significantly higher than the tensile strength, the tensile properties controls the flexural behaviour of the material. The initiation of crack motion is in the tensile portion of the specimen and the, post crack flexural behaviour of the material will be determined by the propagation of the crack in the tensile portion of the specimen. Thus the flexural response of such materials can only be precisely predicted by accurately predicting its tensile characteristics.

B.1.2 Additional Information on effect of mesh size

The effect of finite element size on energy dissipation of a flexural prism (tensile properties same as for plate test) was investigated using four different mesh sizes (see Figure 5.1). Corresponding flexural responses are shown in Figure 5.2.

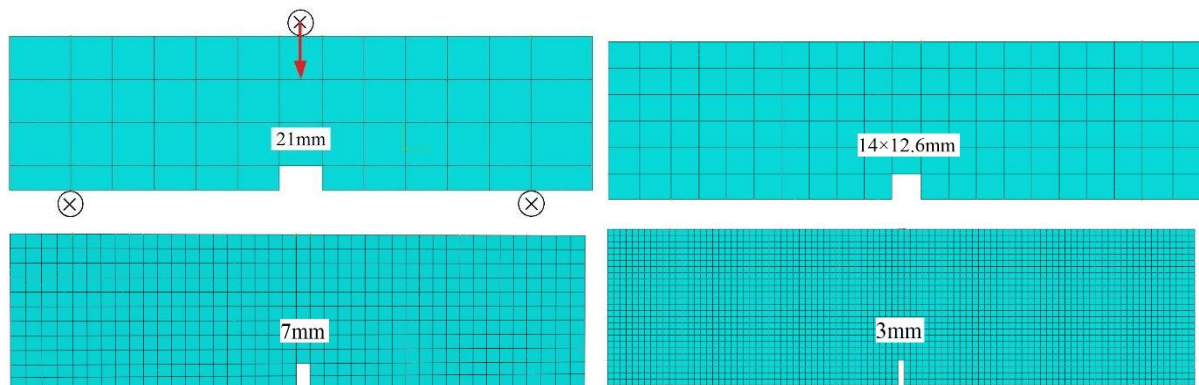


Figure 5.1: Mesh sizes for numerical analysis Figure 5.2:

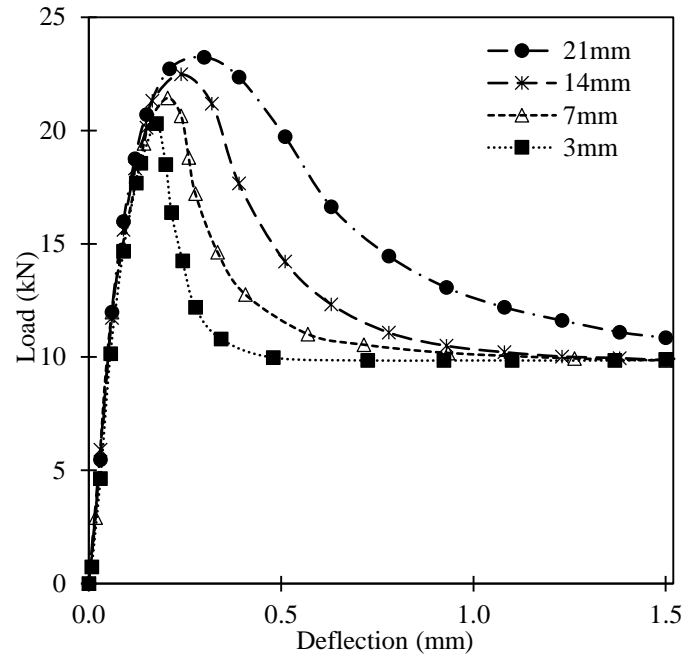


Figure 5.2: Effect of Mesh sizes on energy dissipation of prism

It can be seen that the amount of energy dissipation decreases as the finite element sizes decreases. Also all mesh sizes (both coarse and fine element) dissipate less energy compared to the true energy dissipation capacity of the material. To avoid the problem of mesh sensitivity in the prism test inverse analysis, a mesh independent solution needs to be developed. This can be achieved by adopting a similar approach to the plate test using the characteristic length scaling parameter (Eq. (3 – 10) and Eq. (3 – 11)).

B.1.3 Additional Information Regarding Concrete Damage Plasticity Parameters

The default values of the concrete damage plasticity parameters were used, except for the viscosity parameter (ν), where $\nu = 2 \times 10^{-6}$ was used to avoid convergence problems. Based on preliminary analysis conducted on selected mixes, it was found that the eccentricity (ϵ), the ratio of the second stress invariant on the tensile meridian to that on the compressive meridian (K_c) and the ratio of initial biaxial compressive yield stress to initial uniaxial compressive yield stress (f_{bo}/f_{co}) did not affect the flexural response of the modelled E-UHPFRC prisms. Thus, values for these parameters were kept at default values. However, the dilation angle (ψ) was found to affect the post crack flexural ductility of E-UHPFRC prisms. The larger the dilation angle, the more ductile the material behave. Referring to literature, Lee and Fenves [23] specified $\psi=31^\circ$ for normal concrete; [24] suggested $\psi=37^\circ$ based on

validation with shear test results; [25] calibrated it to $\psi=38^\circ$; and [26] showed that a ψ between 30° and 40° for normal strength concrete can have the best agreement with the experimental response. Malm [27] reported that ψ may be limited to 56.3° , but this cap value corresponds to a very high compressive strength (greater than 140 MPa) which may not be justified due to scarcity of the experimental results at this high strength. The suggestions from the literature shows that ψ greatly varies between 30° to 56.3° and might be higher for high strength concrete. Due to this ambiguity, and the observation that the default value (i.e. $\psi=45^\circ$) is about the average of the reported values, this study adopts the use of default value of ψ . However, it is recommended under “Recommendations for Future Study” that future studies investigate and find a suitable values of ψ for UHPFRC and other high performance concretes.

B.1.4 Limitations of Proposed Uniaxial Tensile Models

The following limitations applies to the inverse analysis approach presented in this research:

- The models were calibrated to predict tensile characteristics of mixes containing fibre dosages of 2 – 3% only. Their suitability when applied to mixes containing fibre dosages outside this range have not be ascertained.
- The models were developed based on flexural response of E-UHPFRC containing recycled tyre steel fibres. Its accuracy when applied on mixes containing other types of steel fibres have not been studied.
- The models can only predict the tensile characteristics approximately to the breaking point of E-UHPFRC. Thus the model cannot predict the entire tensile response of E-UHPFRC in the softening phase

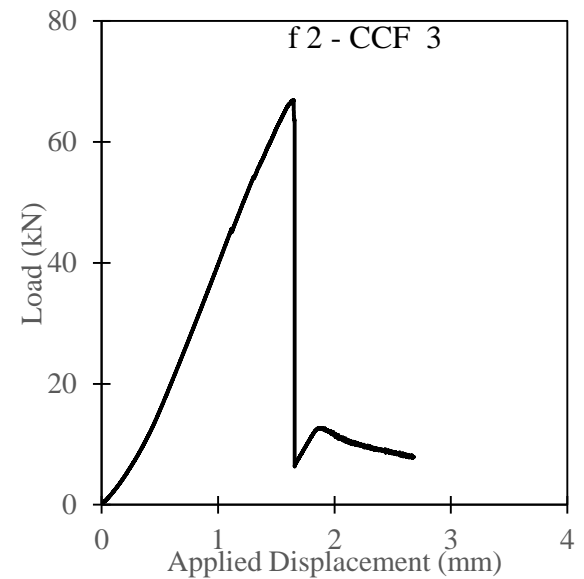
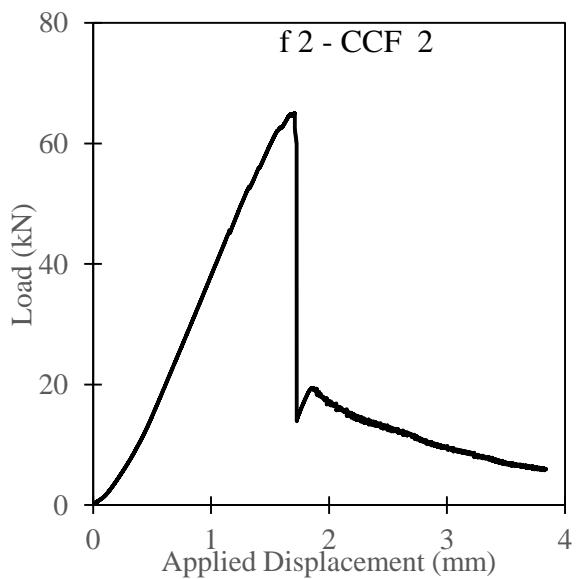
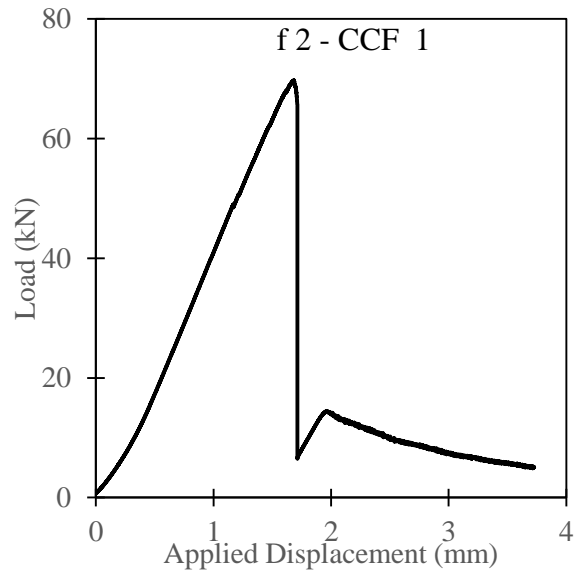
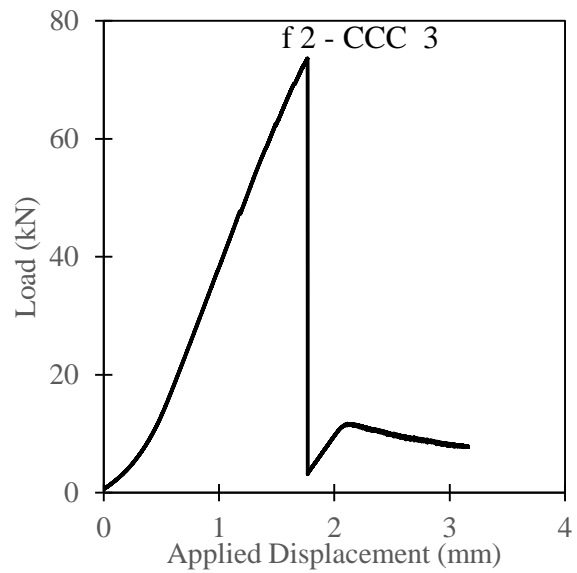
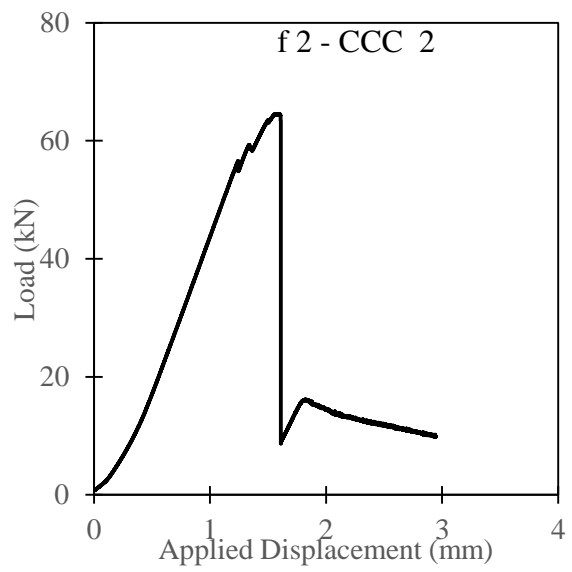
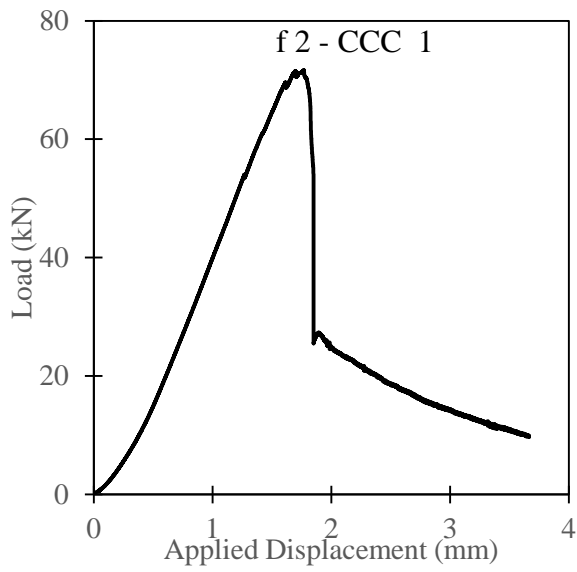
Appendix C: Experimental Results for Chapter 4

Shear Behaviour of E-UHPC Containing Recycle Steel Fibres

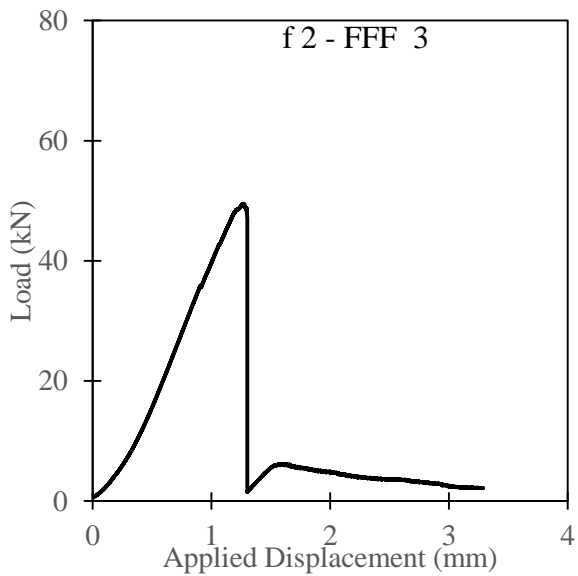
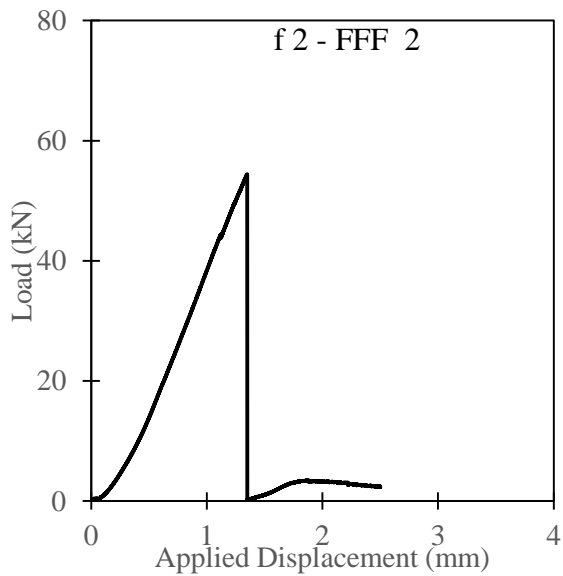
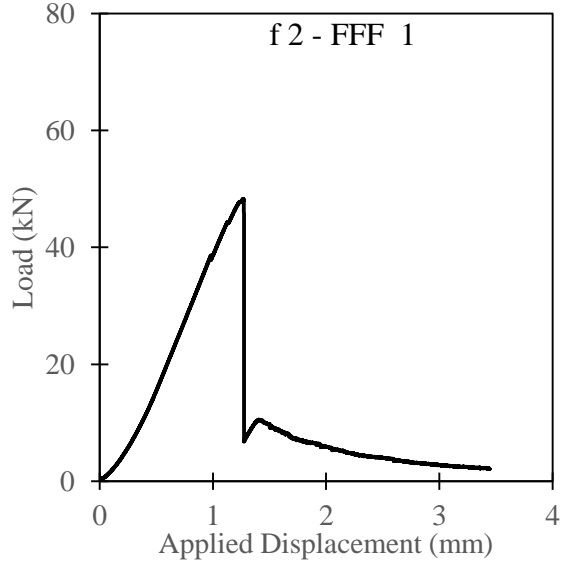
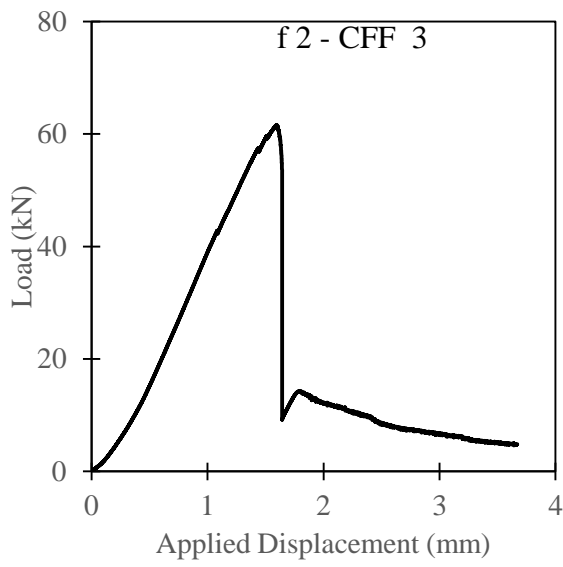
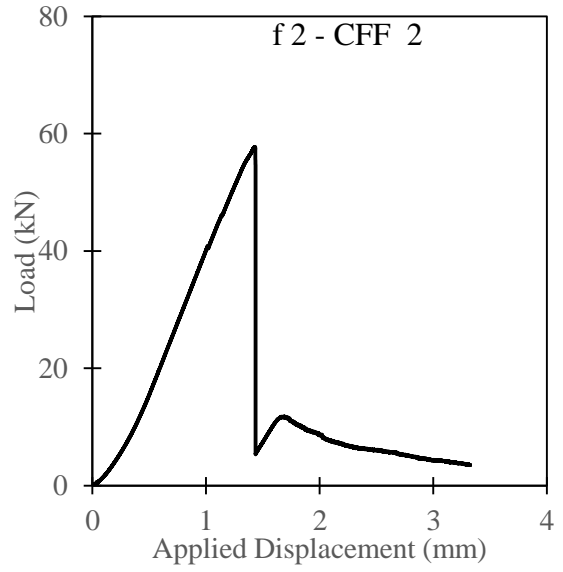
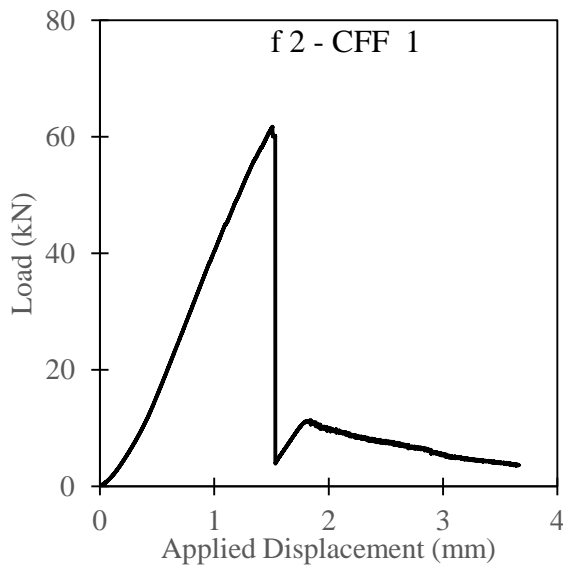
This appendix presents additional Experimental results on the shear behaviour of E-UHPFRC described in Chapter 4.

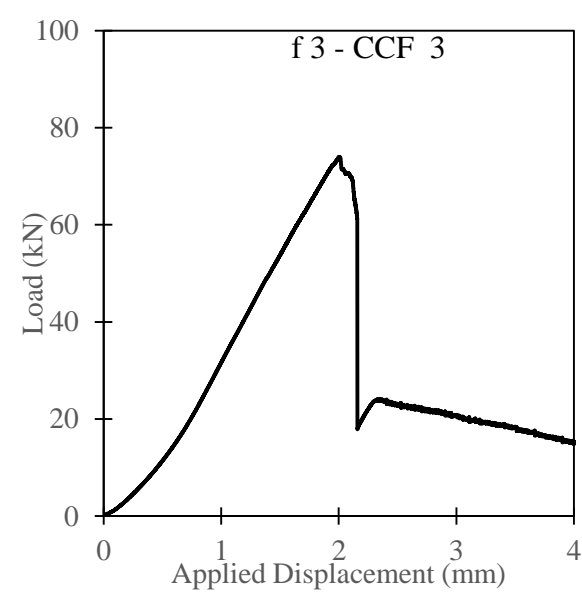
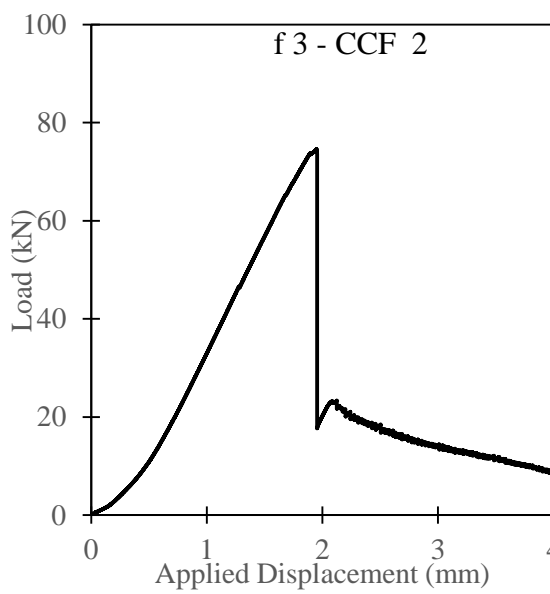
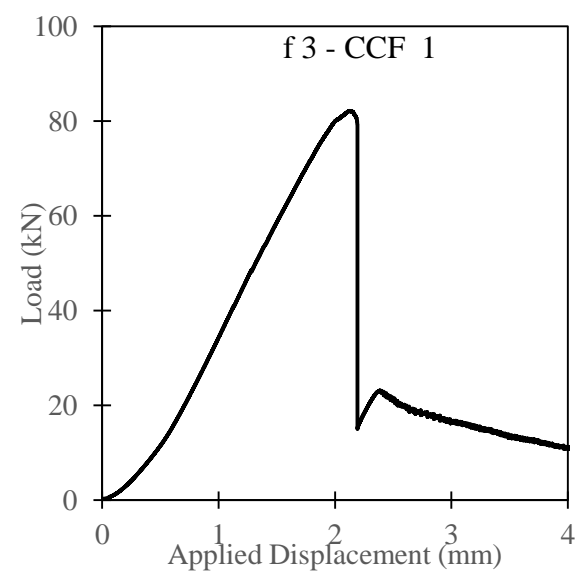
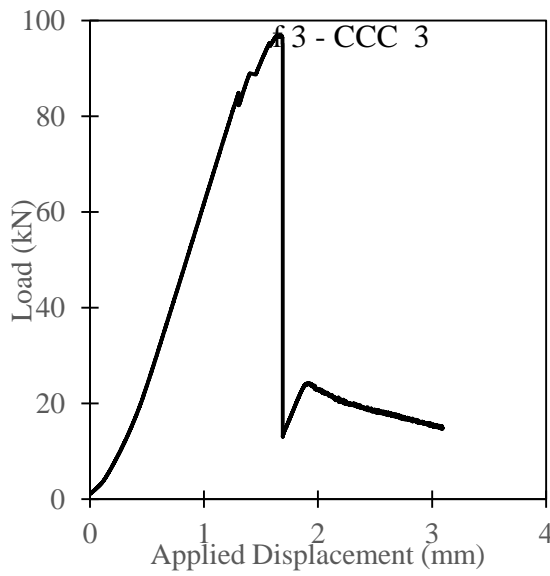
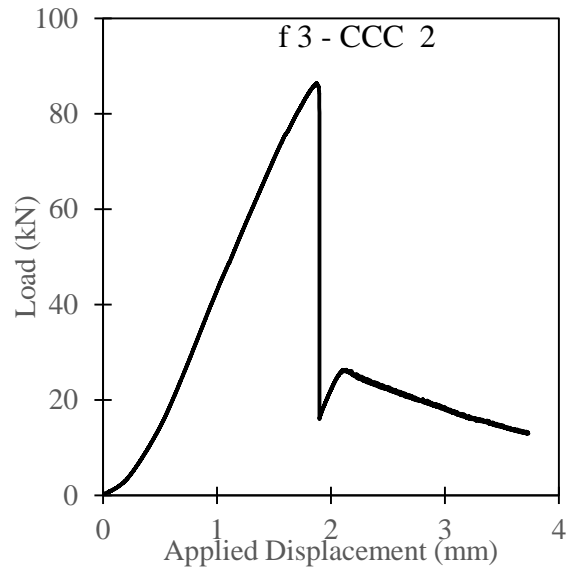
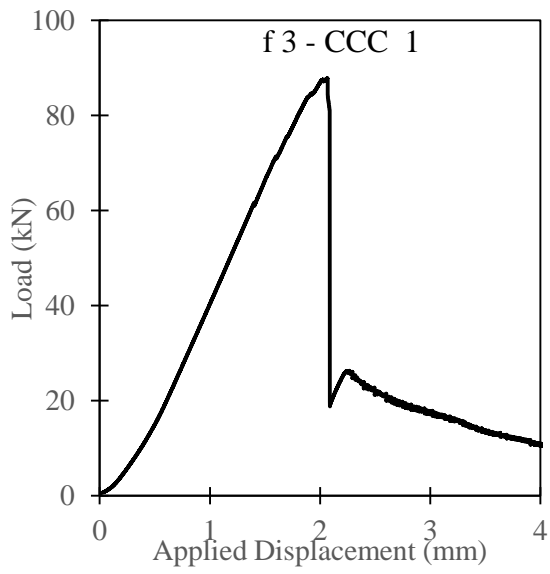
C1: Chapter 4: Additional Information

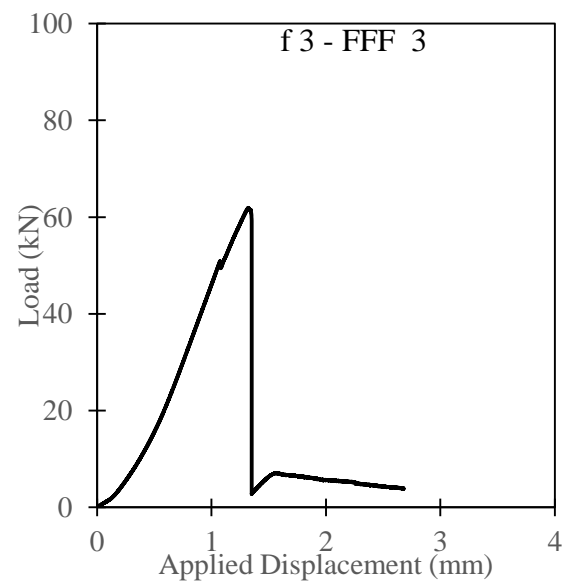
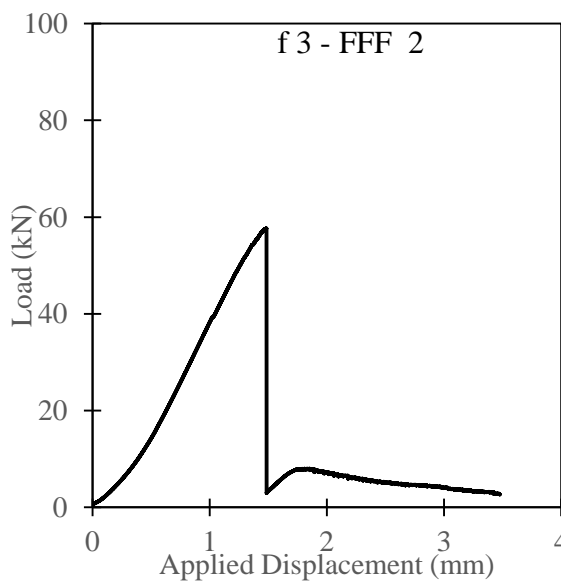
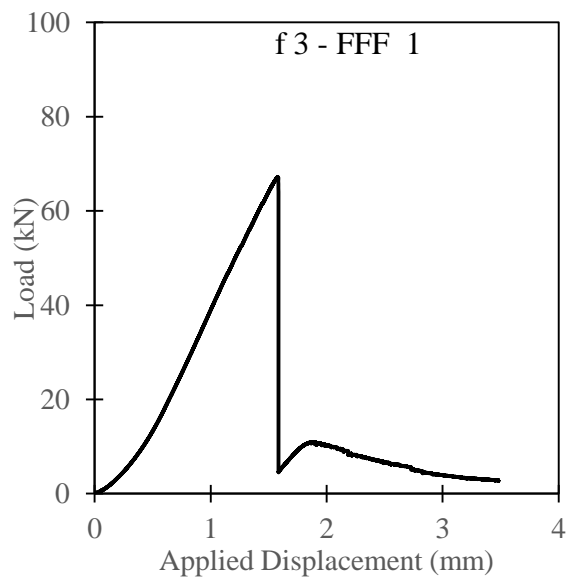
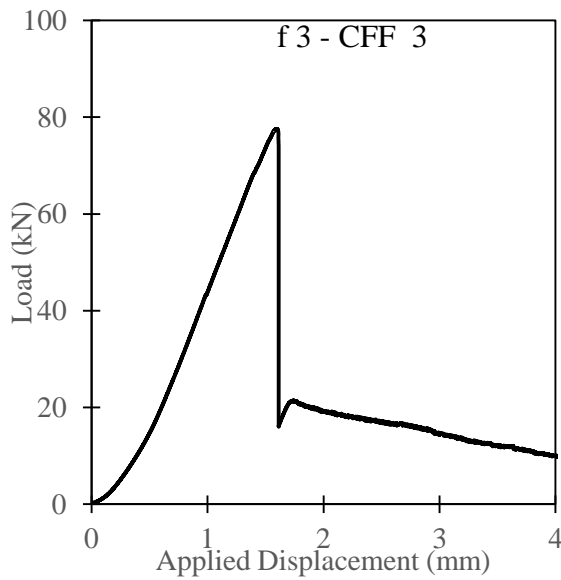
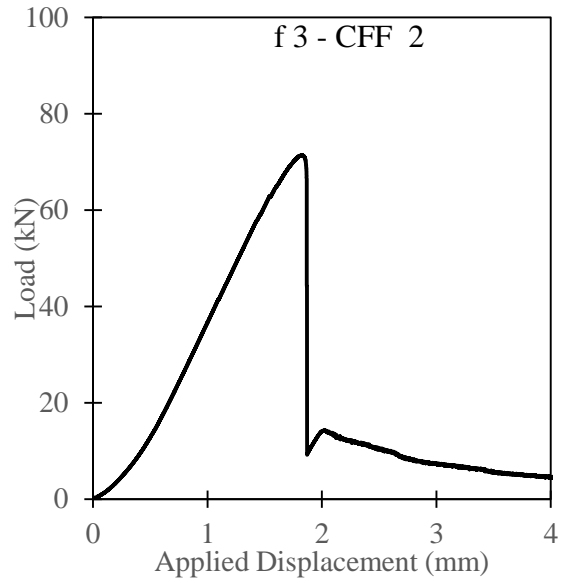
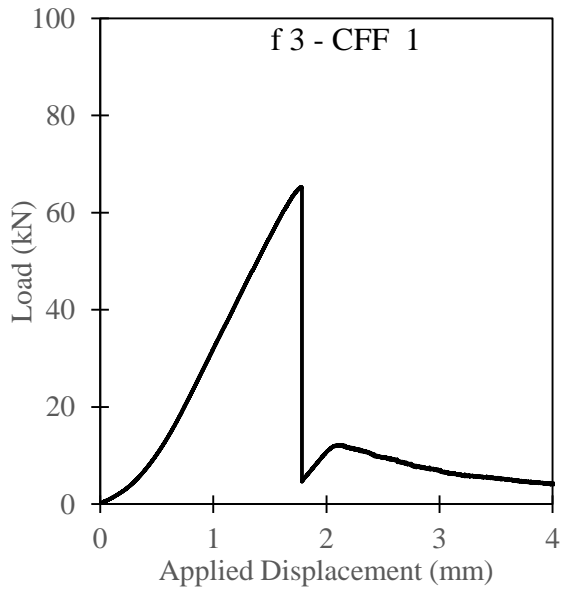
C.1 Shear Behaviour: Load – Applied Displacement relationship



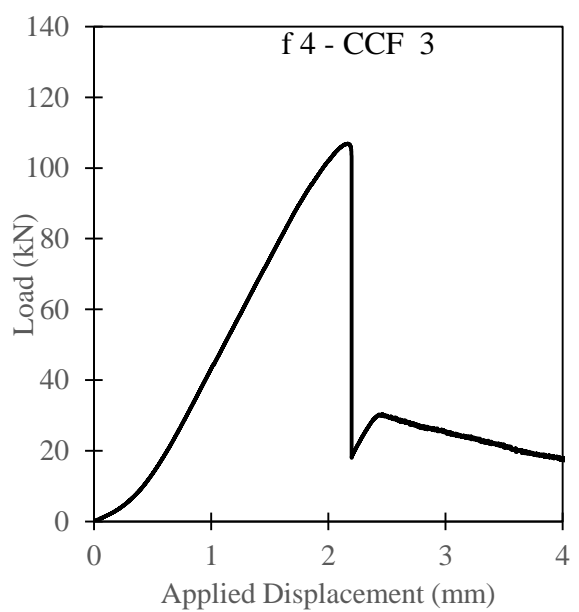
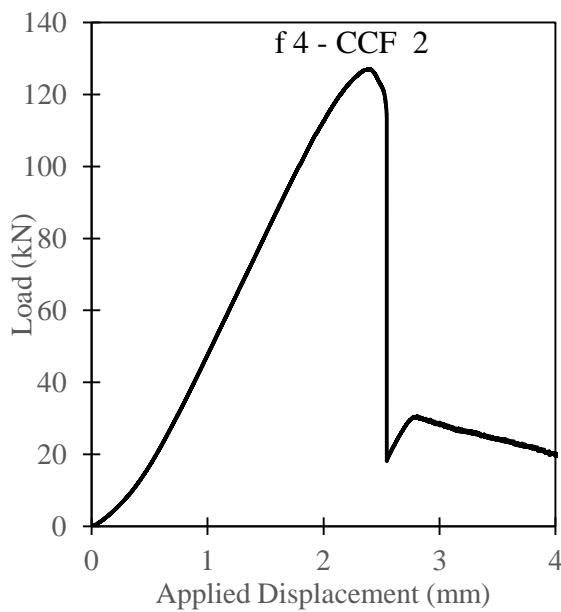
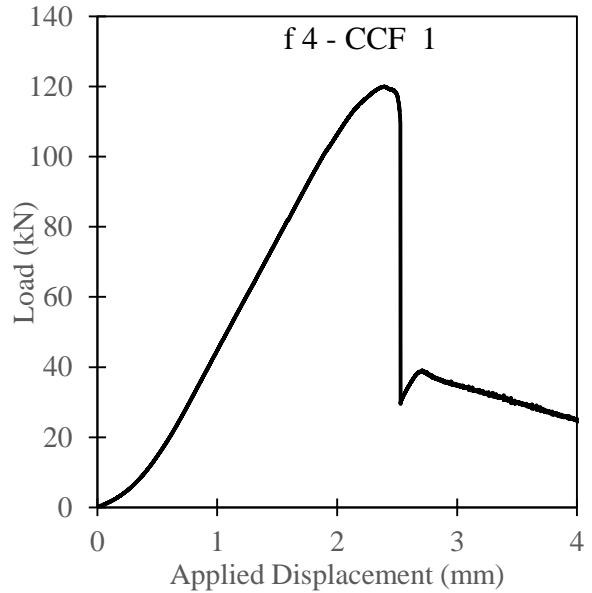
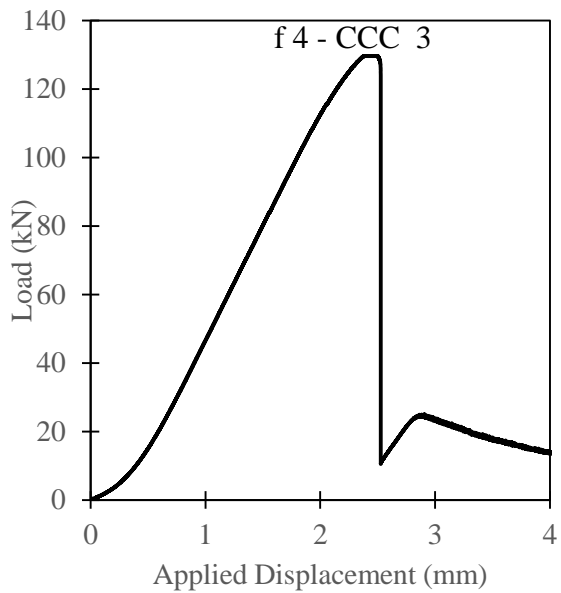
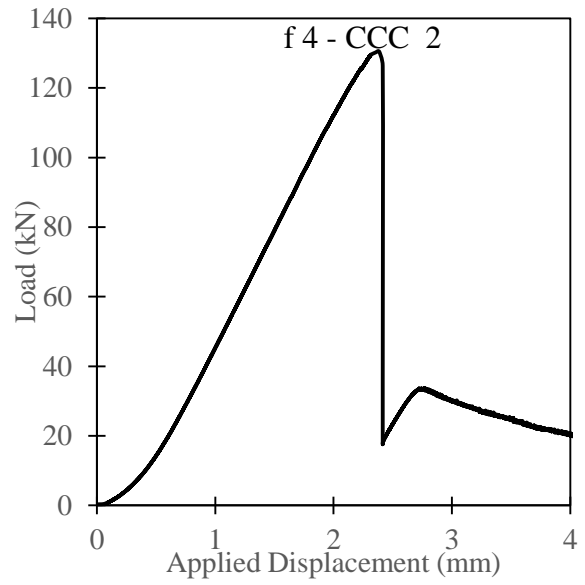
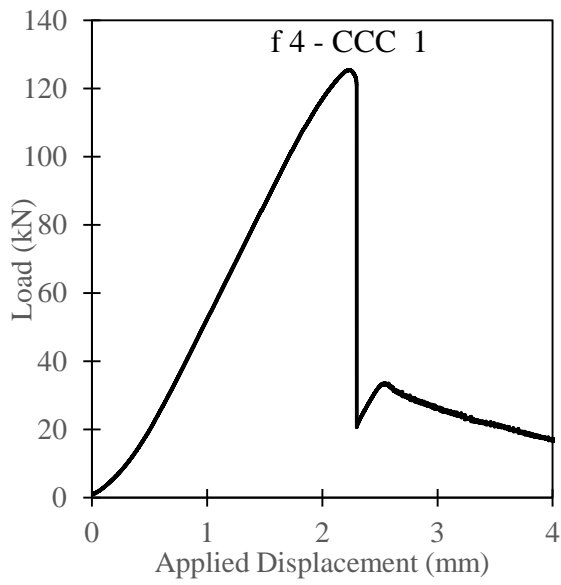
Appendix B

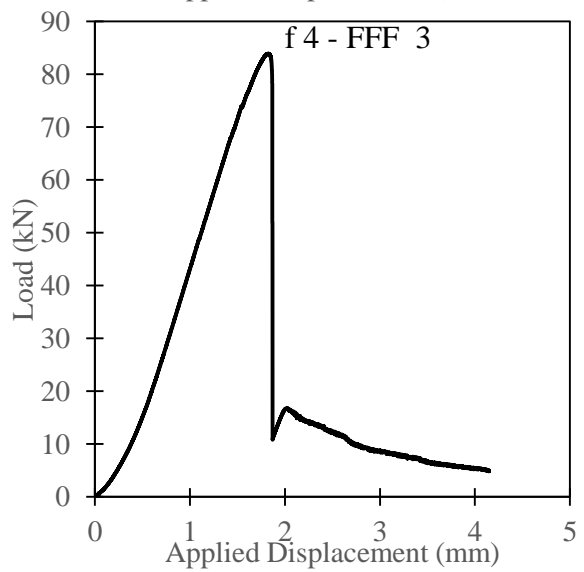
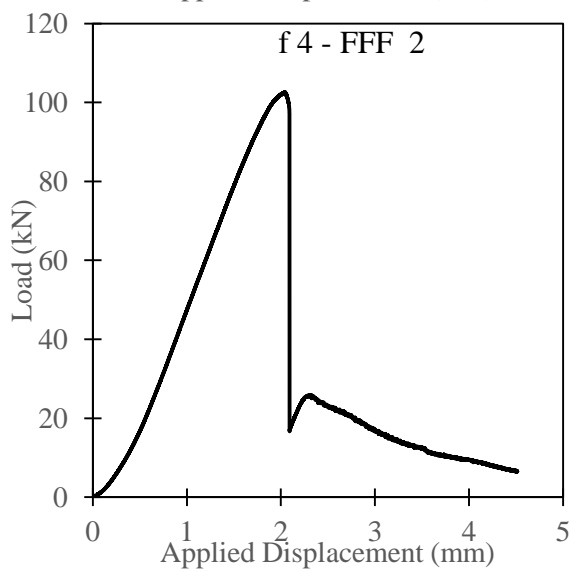
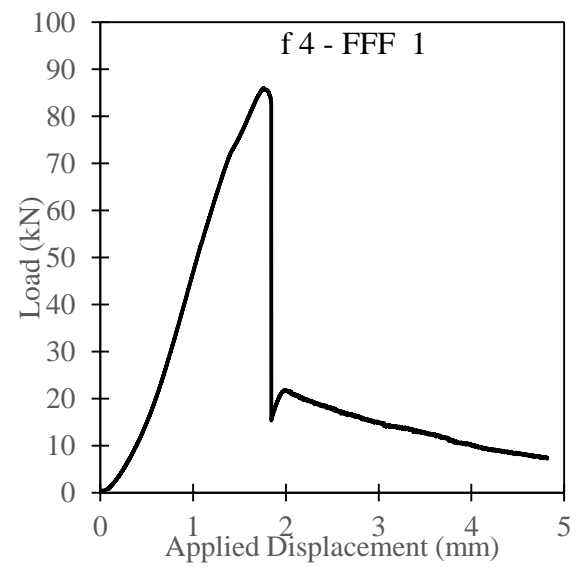
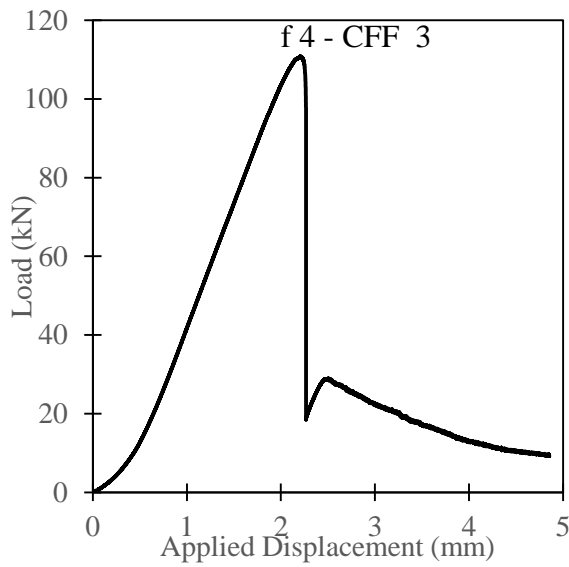
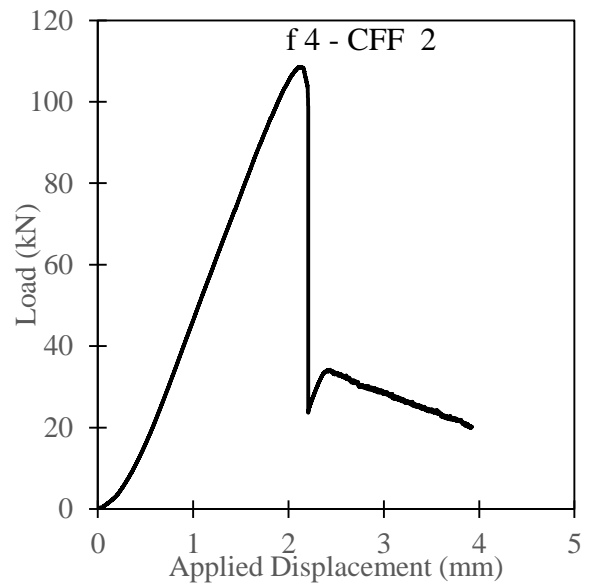
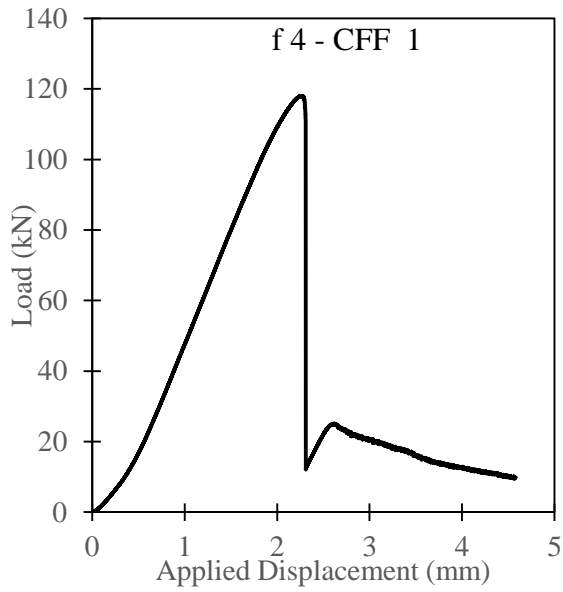




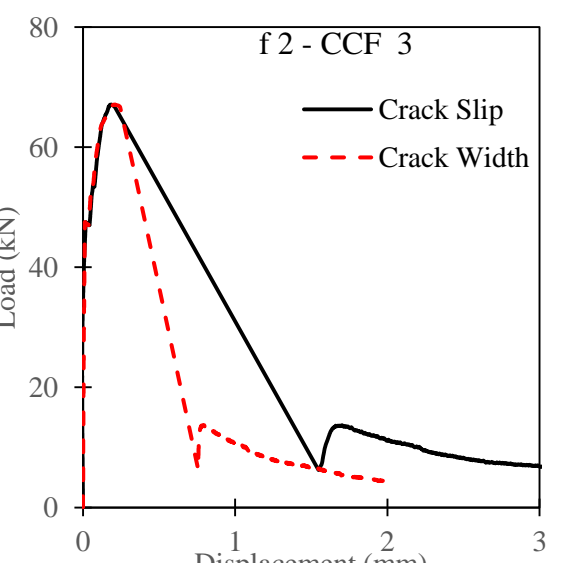
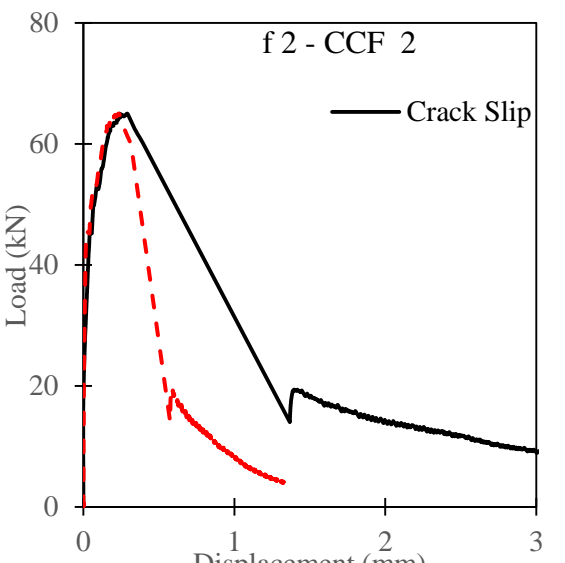
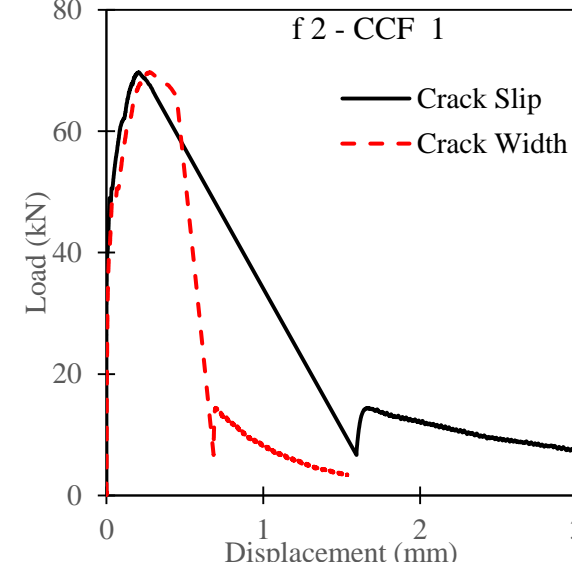
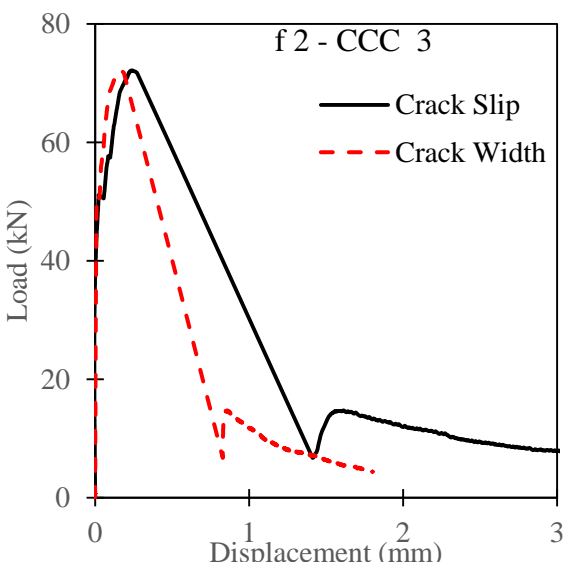
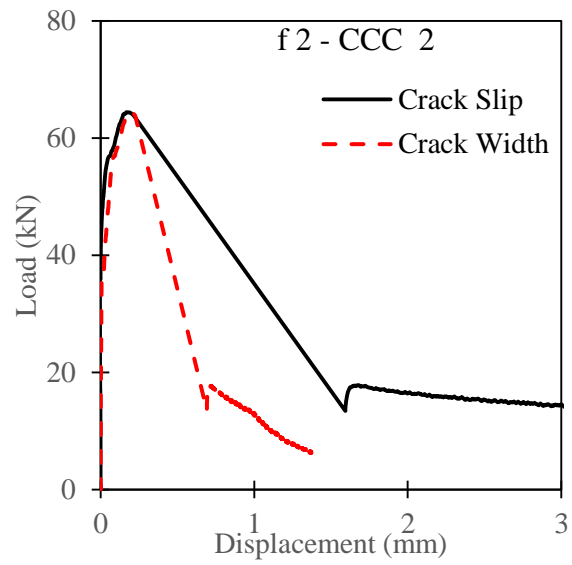
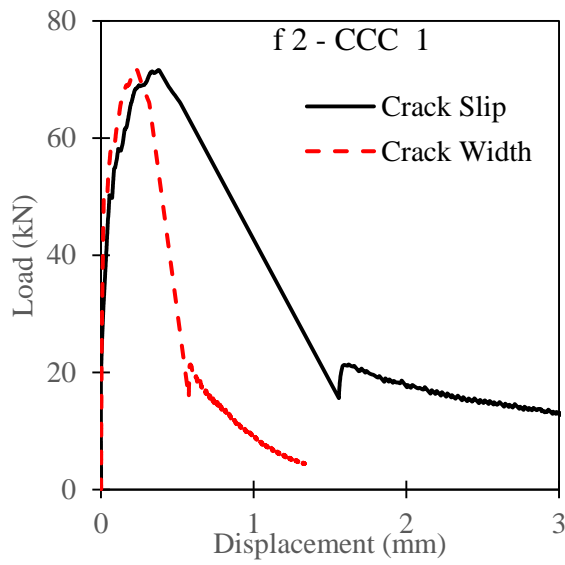


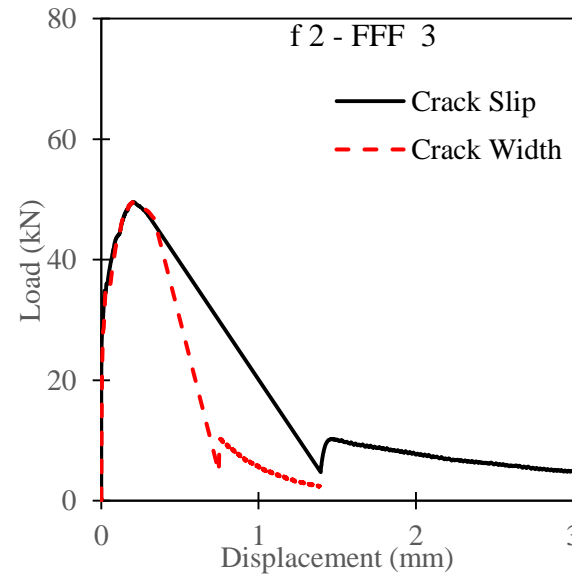
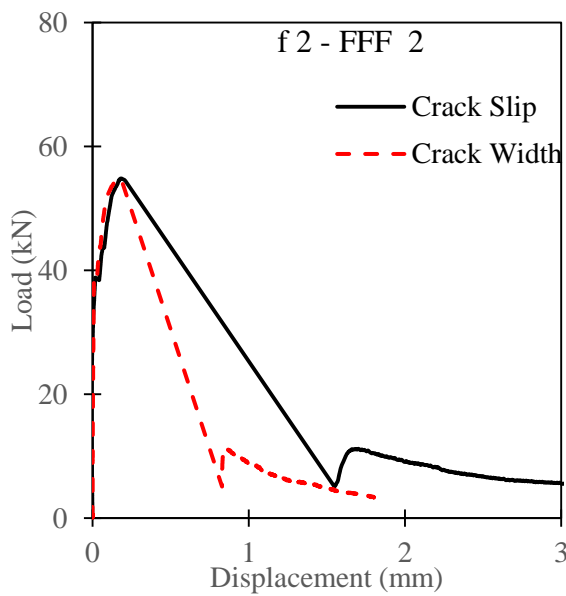
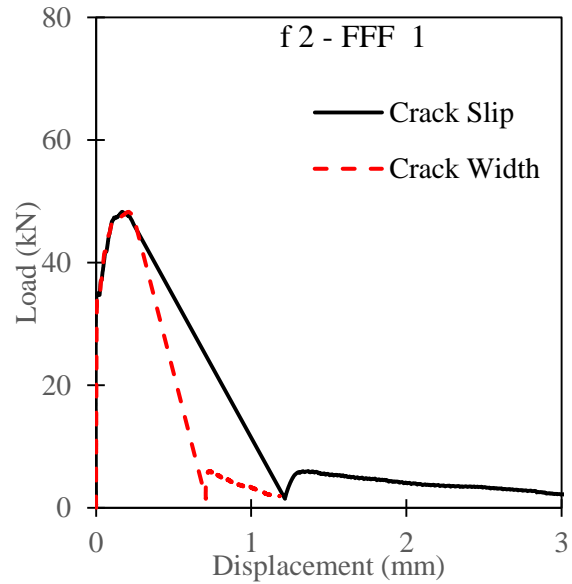
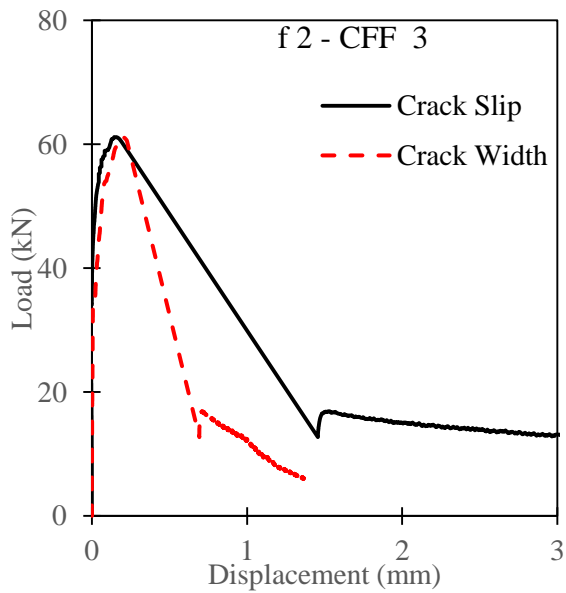
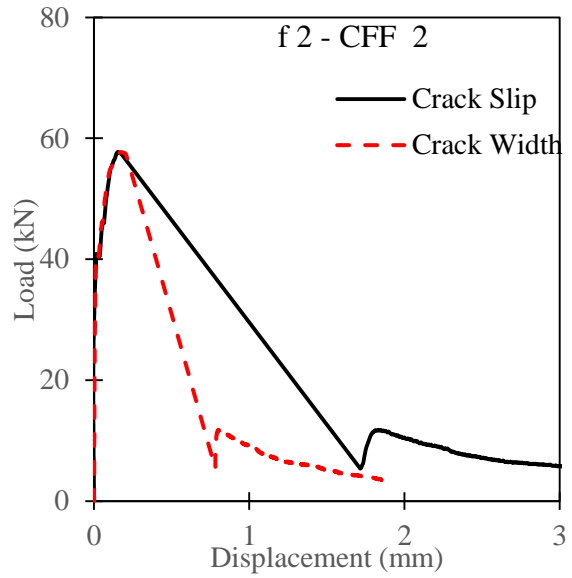
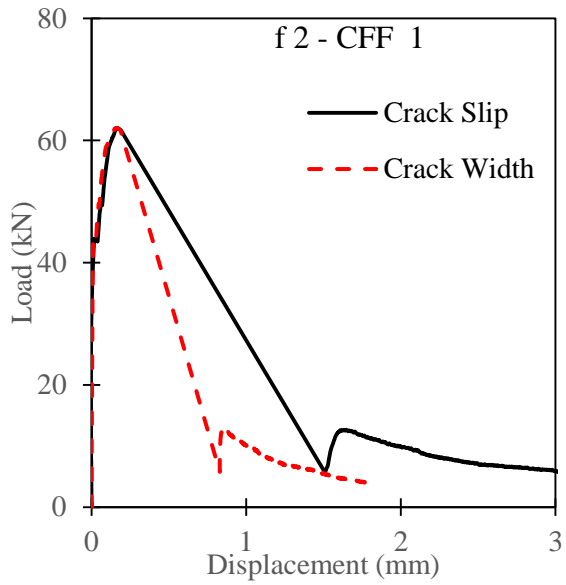
Appendix B

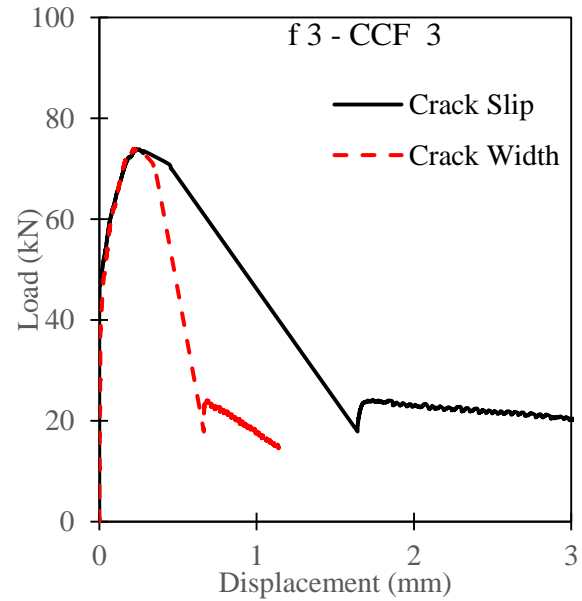
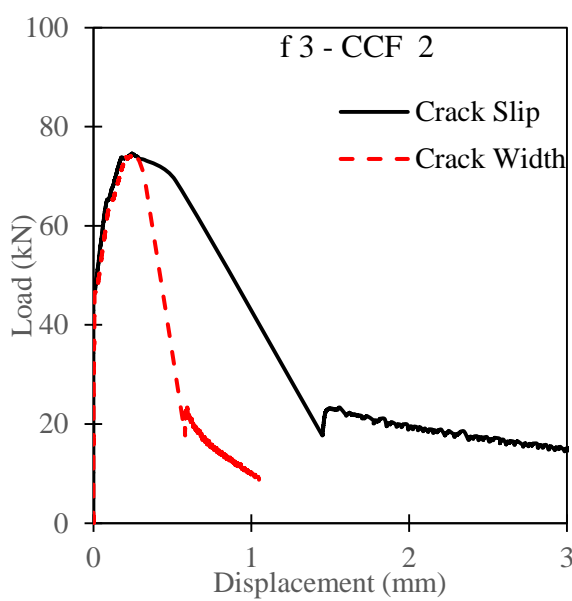
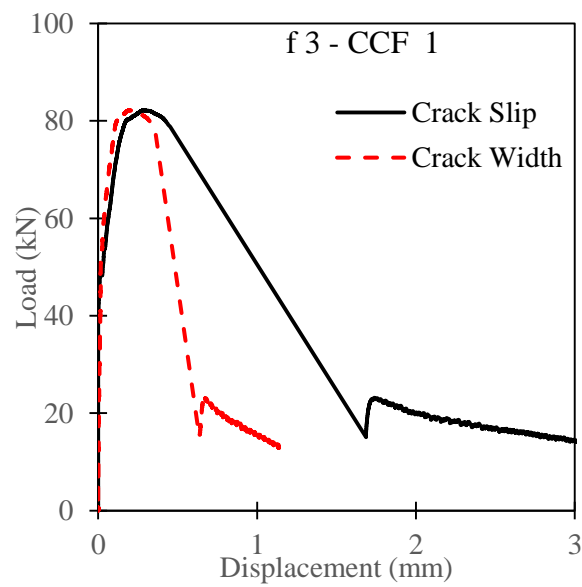
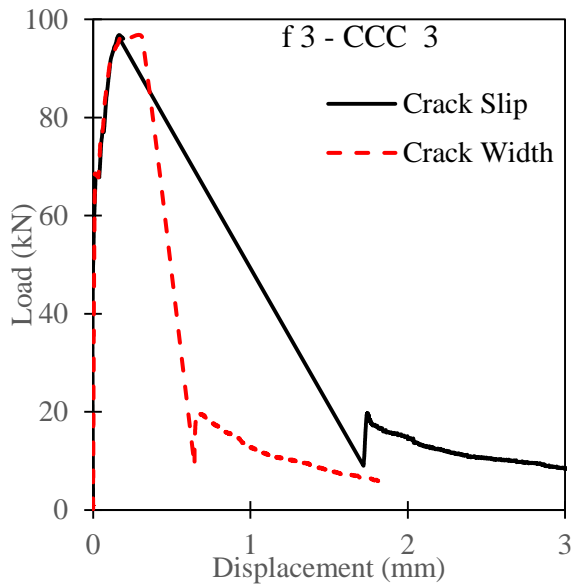
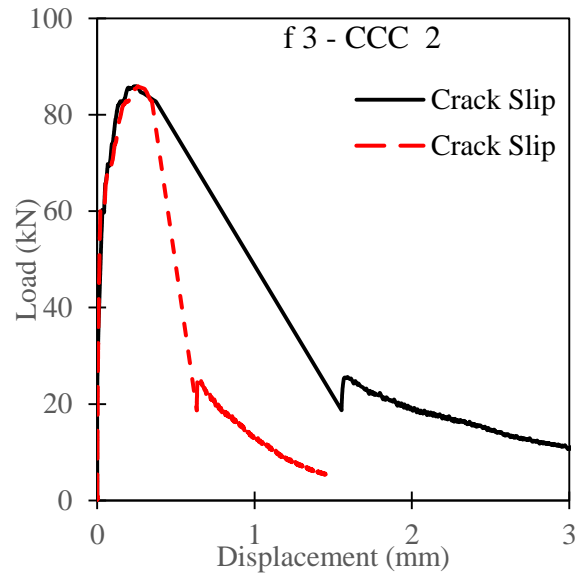
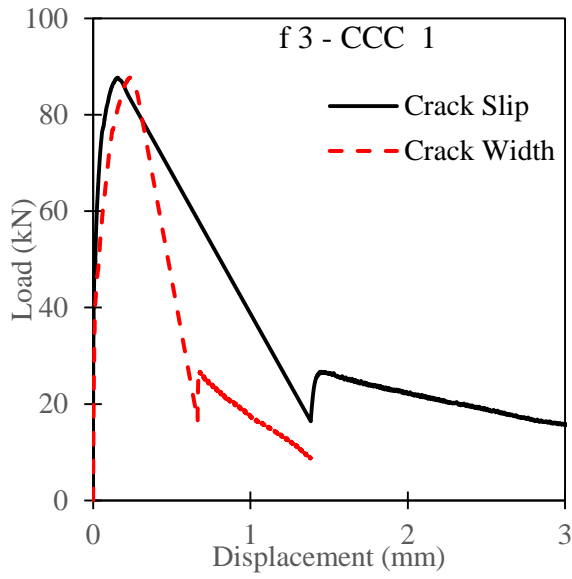


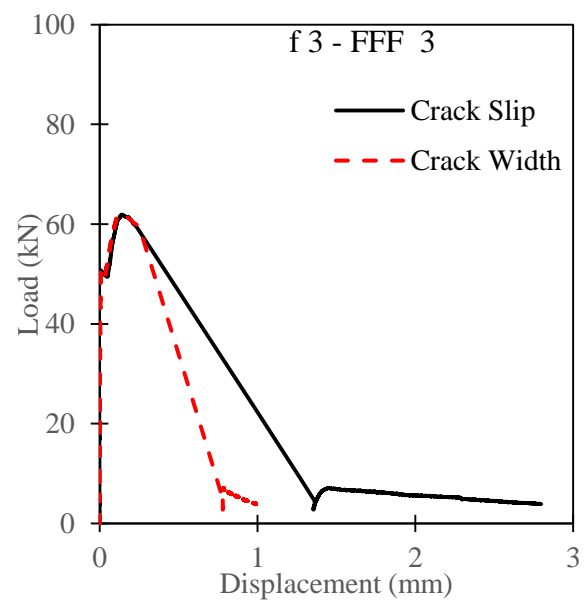
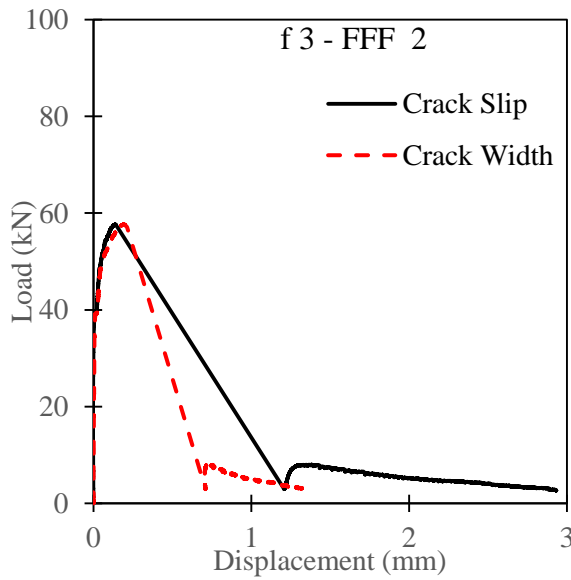
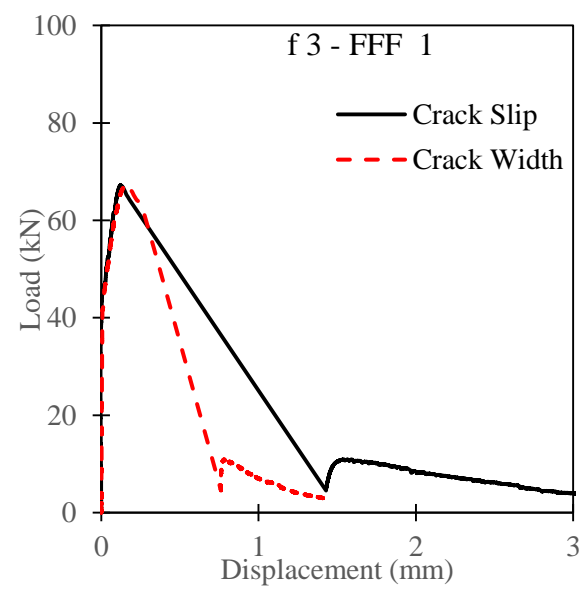
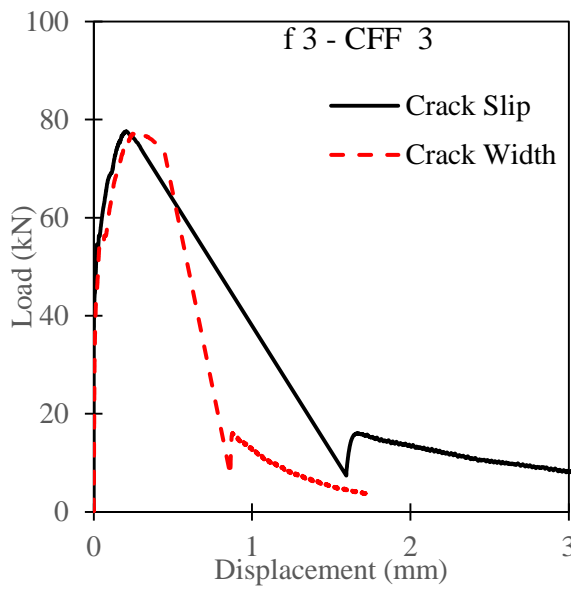
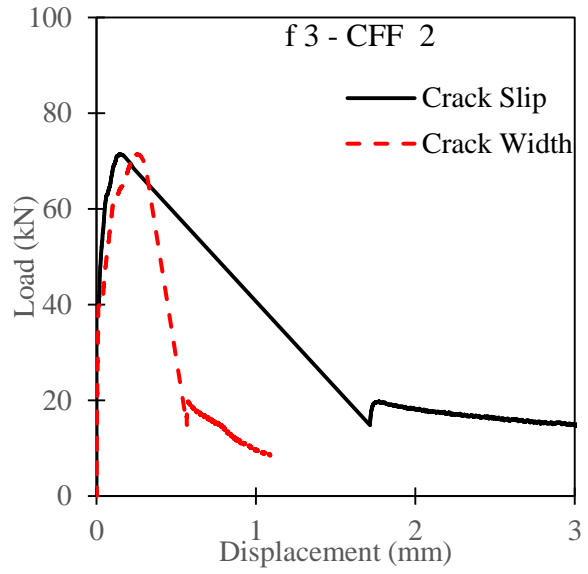
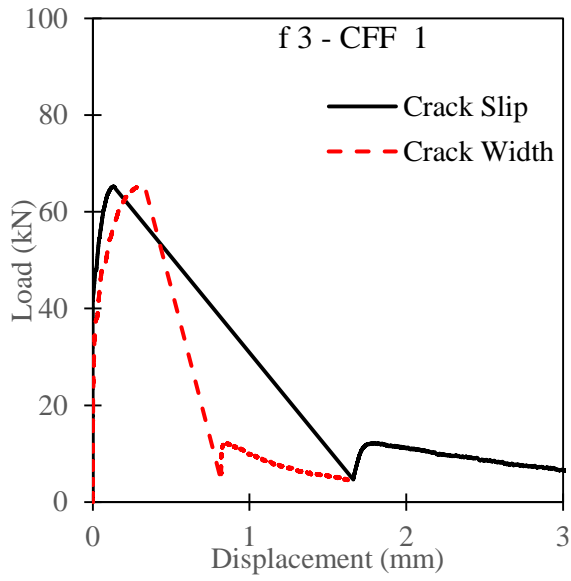


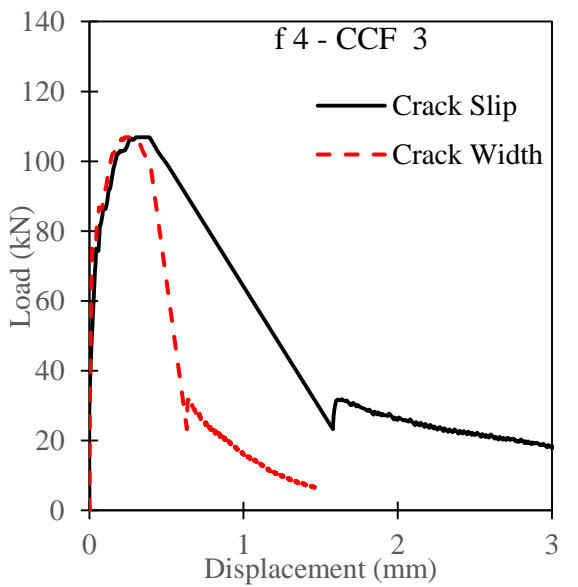
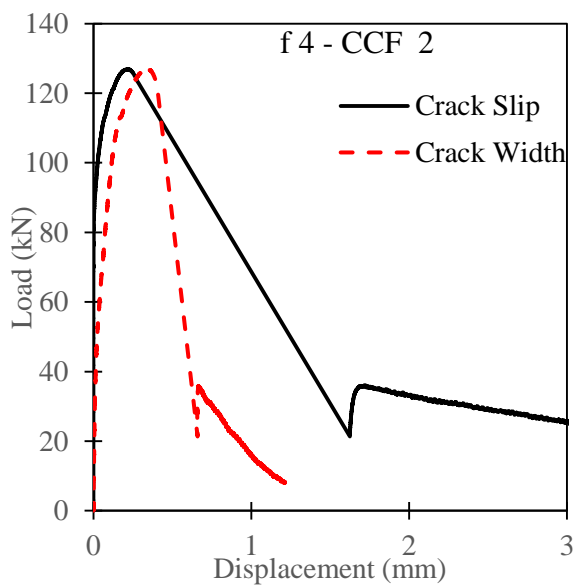
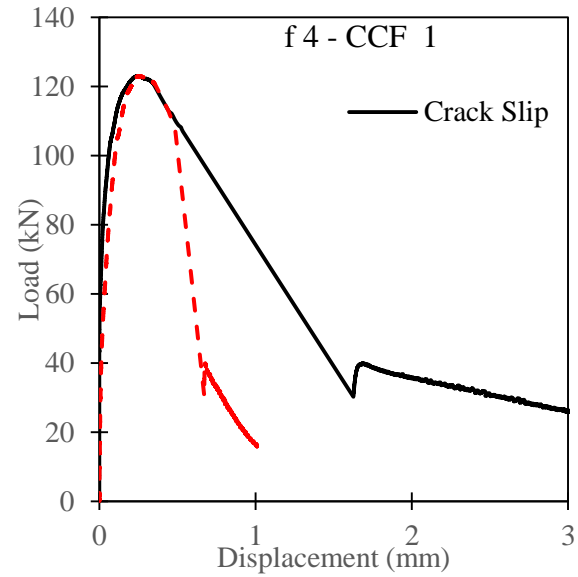
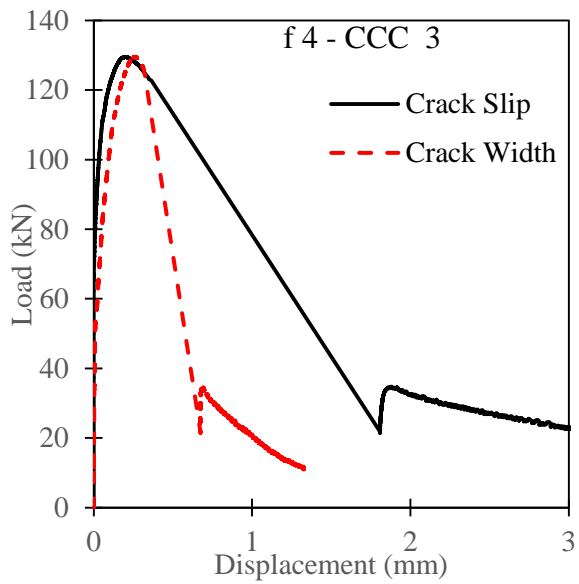
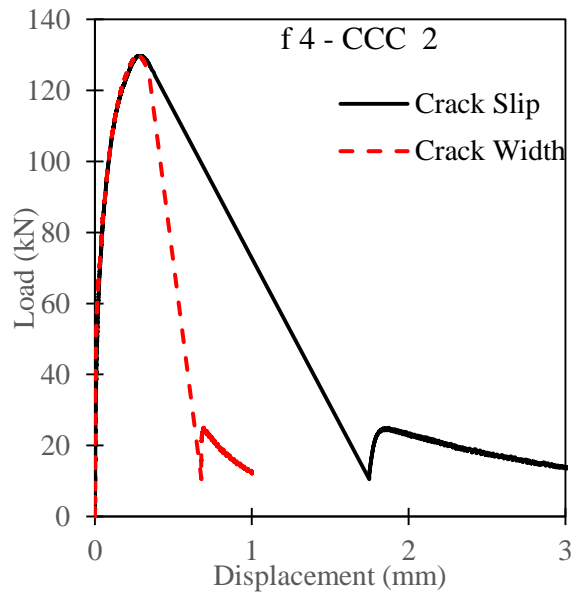
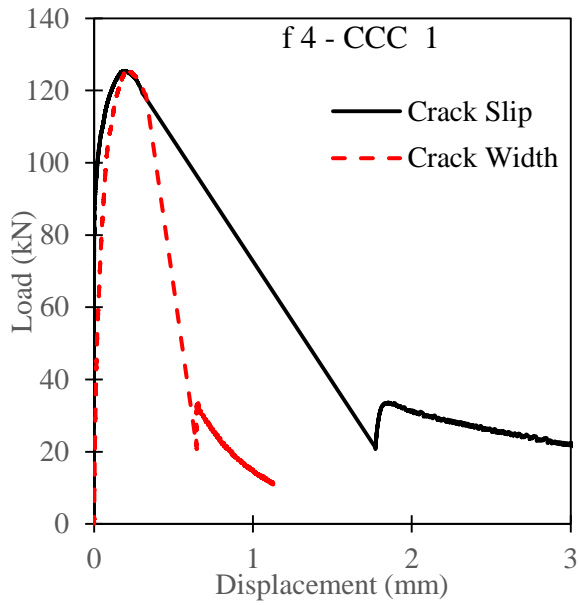
B.2 Shear Behaviour: Load – Crack Slip/Width Displacement relationship

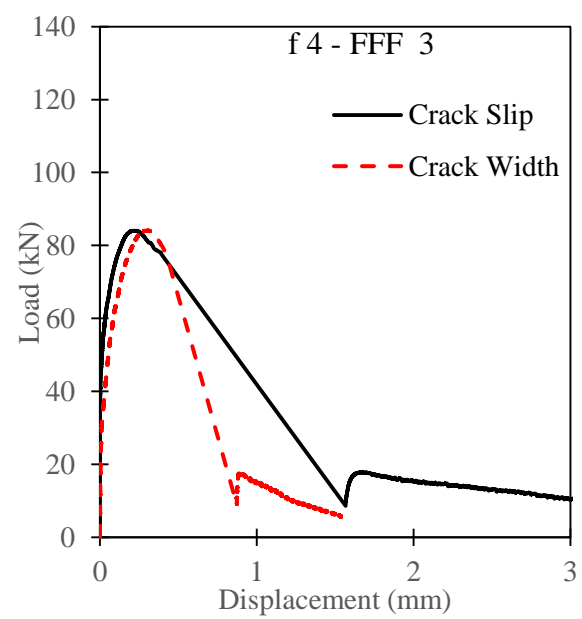
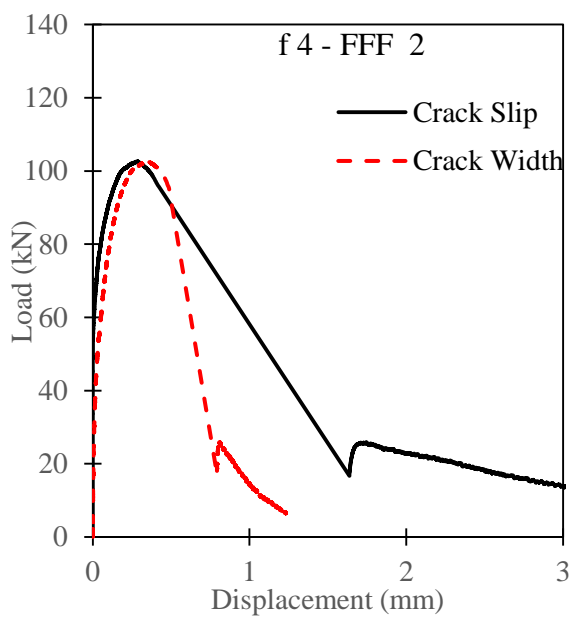
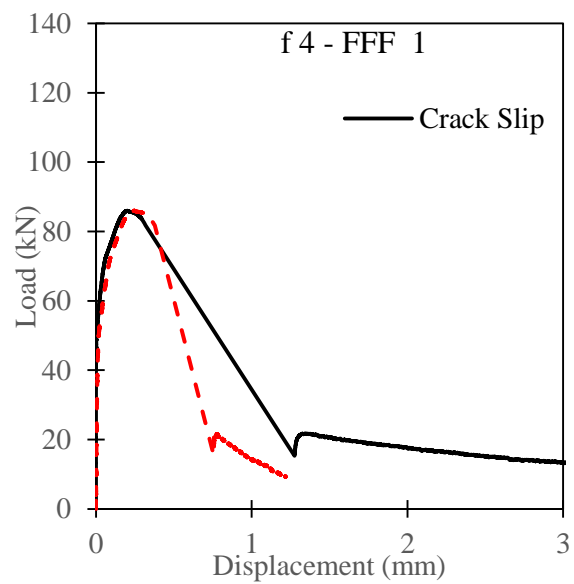
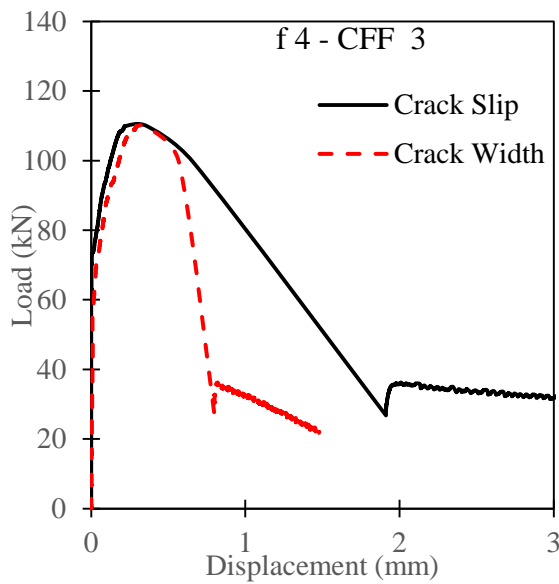
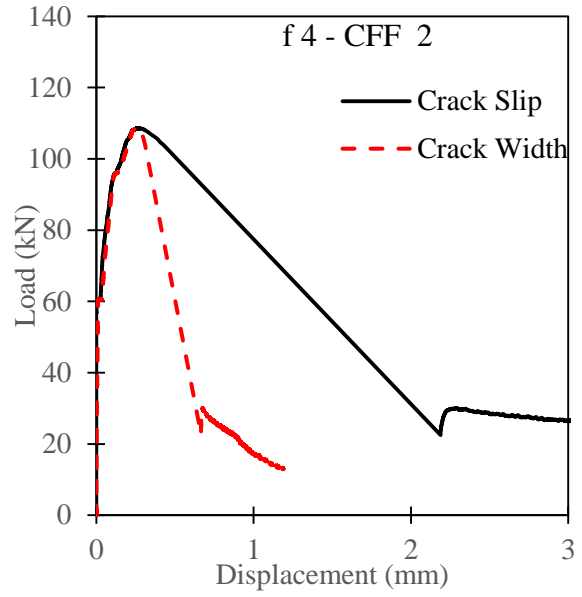
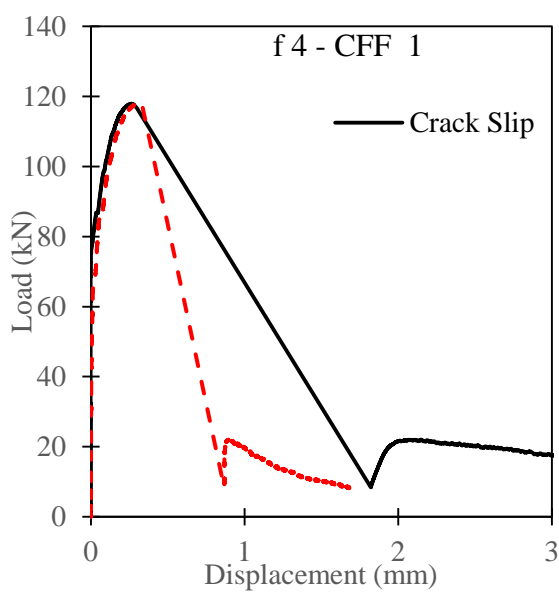












Appendix D: Torque Resistance derivations for Chapter4

This appendix presents additional information on derivation of torques resistances presented in Chapter 4.

D.1 Torque Resistance Derivations

D.1.1 Resistance due to Lateral earth Pressure P_1

P_1 have two components P_{1x} produces moment acting on the shaft resisting its rotation (T_1) and P_{1y} produces frictional moment acting on the helix (T_2) as shown in Eq. (D1) and (D2). Figure A1 shows the distribution of lateral earth pressure along the pile depth.

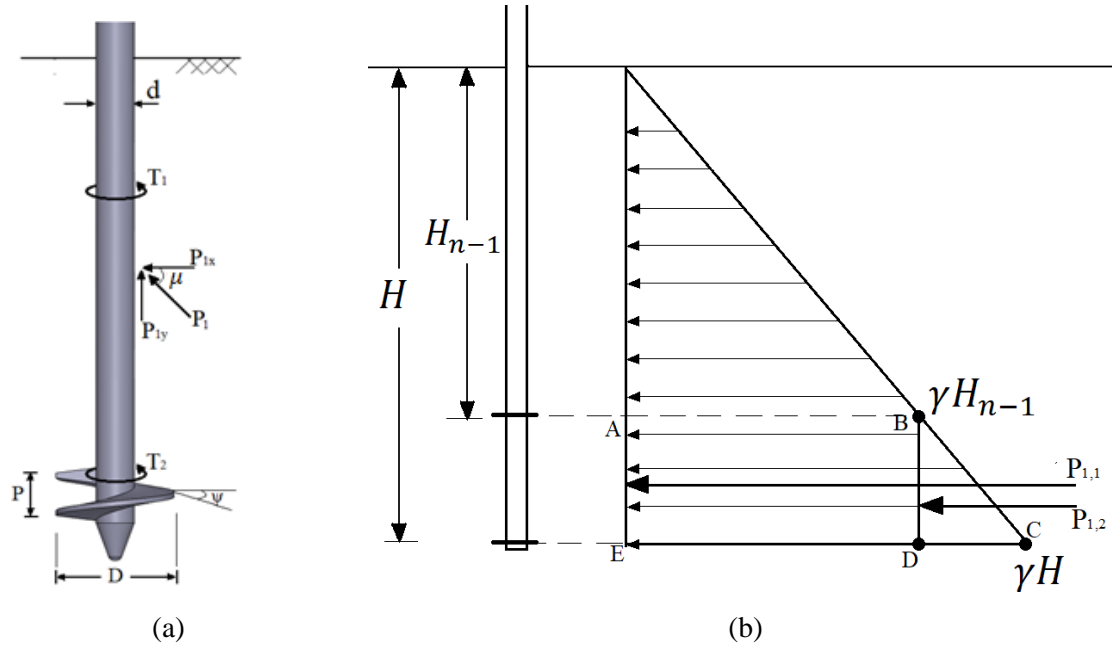


Figure D1: (a) Forces due to P_1 (b) Lateral earth pressure distribution along the pile depth

For a multi helix or threaded screw (Fig D1(b)), the resultant force for a helix located at depth H is given by the area of the stress diagram (ABCDE) below the helix above it. Thus the resultant force due to the lateral earth pressure at this region can be calculated as;

$$\begin{aligned}
 P_1 &= P_{1,1} + P_{1,2} \\
 P_{1,1} &= (\gamma' H_{n-1}) \times (H_n - H_{n-1}) \\
 P_{1,2} &= \frac{1}{2} \times (\gamma' H_n - \gamma' H_{n-1}) \times (H_n - H_{n-1}) = \frac{1}{2} \gamma' (H_n - H_{n-1})^2 \\
 \therefore P_1 &= \gamma' H_{n-1} (H_n - H_{n-1}) + \frac{1}{2} \gamma' (H_n - H_{n-1})^2 \quad (D1) \\
 &= \gamma' [(H_{n-1} (H_n - H_{n-1}) + \frac{1}{2} (H_n - H_{n-1})^2)] \\
 &= \gamma' [(H_n H_{n-1} - H_{n-1}^2) + \frac{1}{2} (H_n^2 - H_n H_{n-1} - H_n H_{n-1} + H_{n-1}^2)] \\
 &= \gamma' [(H_n H_{n-1} - H_{n-1}^2) + (\frac{1}{2} H_n^2 - H_n H_{n-1} + \frac{1}{2} H_{n-1}^2)] \\
 &= \gamma' (-H_{n-1}^2 + \frac{1}{2} H_n^2 + \frac{1}{2} H_{n-1}^2) \\
 P_1 &= \frac{1}{2} \gamma' (H_n^2 - H_{n-1}^2)
 \end{aligned}$$

The torque resistance is then calculated using the relationship in Eq. (D2 – D3)

$$T_1 = P_{1x} \times P_s \times d/2 \times K'_p \times K_f \quad (D2)$$

$$T_2 = P_{1y} \times P_h \times D/2 \times K'_p \times K_f \quad (D3)$$

Where $P_s = \pi d$ is the perimeter of pile shaft, $P_h = \pi D$ is the perimeter of pile shaft, d and D represents the diameter of shaft and helix respectively, and $d/2$ represents the lever arm of the moment. $K'_p =$ Modified coefficient of passive earth pressure ($K'_p = 0.2K_p$ to $0.5K_p$; K_p is the full passive pressure = $\frac{(1+\sin\phi)}{(1-\sin\phi)}$). The use of $K'_p = 0.3K_p$ based on experimental test measurements using transducers located around the installation path of screw anchors as found by [Ghaly] will be adopted in this study as similar experimental results were found by [Clemence and Pepe 1984], $K_f =$ coefficient of friction between pile and surrounding soil ($K_f = \tan\mu$ and $\tan(\mu + \psi)$ for shaft and helix friction respectively),

$$P_{1x} = P_1 \cos\mu$$

$$P_{1y} = P_1 \sin\mu$$

Therefore the torque due to $P_{1,x}$ will be given by

$$T_1 = 1/2 \gamma' (H_n^2 - H_{n-1}^2) \cdot \cos\mu \cdot K'_p \cdot K_f \cdot (\pi d) \cdot (d/2) \quad (D5)$$

The torque due to $P_{1,y}$ acting on the helix will be given by

$$T_2 = 1/2 \gamma' (H_n^2 - H_{n-1}^2) \cdot \sin\mu \cdot K'_p \cdot \tan(\delta + \psi) \cdot (\pi d) \cdot (d/2) \quad (D6)$$

Where $H_n =$ depth to n^{th} helix

Note: For the topmost helix in a partially threaded pile, the same principle and formulas (both T_1 and T_2) for a single helix pile applies to it (the topmost helix only). i.e. $H_{n-1} = 0$

$$T_1 = 1/2 \gamma' H^2 \cdot \cos\mu \cdot K'_p \cdot K_f \cdot (\pi d) \cdot (d/2) \text{ and } T_2 = 1/2 \gamma' H^2 \cdot \sin\mu \cdot K'_p \cdot \tan(\delta + \psi) \cdot (\pi d) \cdot (d/2)$$

D.1.2 The torque due to $P_{2,y}$ acting on the cylindrical column of the sand overlaying the helix

This is due to Torque resistance T_3 acting on helix due to the force of cylindrical column of sand overlaying the helix as a result of local compaction of sand layer caused by the helix during installation is shown in as shown in Figure D2.

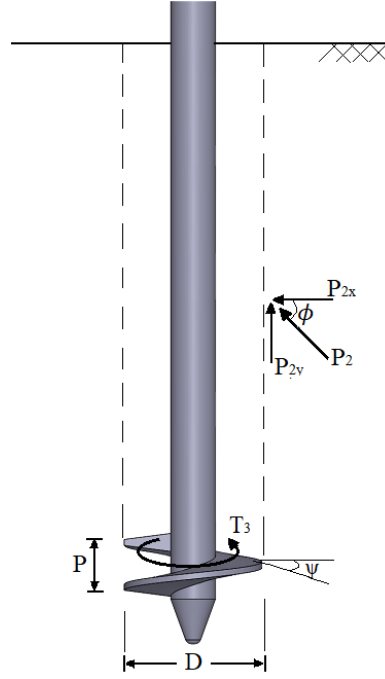


Figure D2: Forces due to P_2

$$P_{2,y} = P_2 \times \sin \phi$$

$$P_2 = \gamma' H_{n-1} (H_n - H_{n-1}) + \frac{1}{2} \gamma' (H_n - H_{n-1})^2 = \frac{1}{2} \gamma' (H_n^2 - H_{n-1}^2)$$

$$T_3 = P_2 \times \sin \phi \times P_{cyl.} \times \frac{D_{cyl.}}{2} \times K'_p \times K_f$$

$$T_3 = \frac{1}{2} \gamma' (H_n^2 - H_{n-1}^2) \cdot \sin \phi \cdot K'_p \cdot \tan(\mu + \psi) \cdot (\pi D_n) \cdot \left(\frac{D_n}{2}\right) \quad (D7)$$

Also, For the topmost helix in a partially threaded pile, the same principle and formulas for a single helix pile applies to it (the topmost helix only). i.e. $H_{n-1} = 0$, therefore;

$$T_3 = \frac{1}{2} \gamma' H_n^2 \cdot \sin \phi \cdot K'_p \cdot \tan(\mu + \psi) \cdot (\pi D) \cdot \left(\frac{D}{2}\right) \quad (D8)$$

D.1.3 Active and passive earth pressure exerted on helix surface

Active and passive earth pressure exerted on the upper and lower surface of helix respectively resulting from the downward advancement of the helix. This produces frictional resistances T_4 and T_5 acting on the upper and lower surface of helix respectively acting against the installation torque.

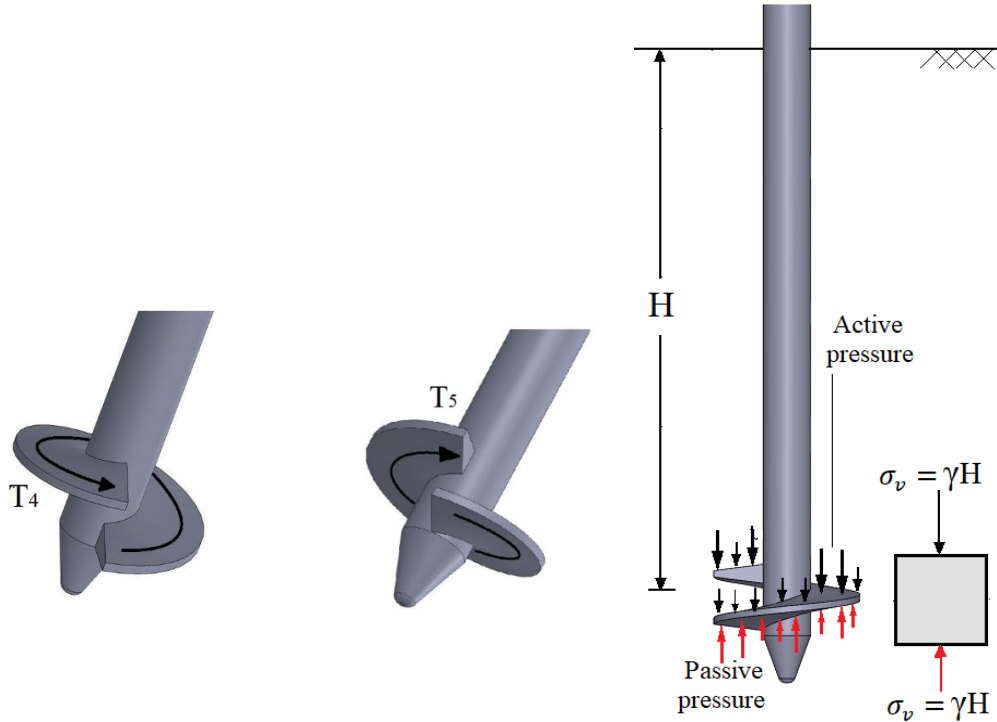


Figure D3: (a) Resisting moment acting on upper surface of helix due to active earth pressure (b) Resisting moment acting on lower surface of helix due to passive earth pressure (c) Vertical and lateral effective stresses

$$T = \sigma_v \times K_{a/p} \times \text{Area of helix} \times K_f \times \left(\frac{D_{n-r}}{2} \right)$$

Where σ_v = the average effective vertical pressure (weight of sand column), K_a = active earth pressure coefficient, A_t = area of helix top surface, A_b = area of helix bottom surface ($A_t = A_b = \frac{\pi}{4}(D_n^2 - d_n^2)$), D_{n-r} is the diameter of the gyration of the helix where concentrated forces act upon

$D_{n-r} = \frac{\sqrt{D_n^2 + d_n^2}}{2}$, (i.e. radius of gyration of a ring = $\frac{\sqrt{D^2 + d^2}}{4}$). Therefore

$$T_{4n} = \frac{1}{4} \gamma' (H_n - H_{n-1}) \cdot K_a \cdot \pi (D_n^2 - d_n^2) \cdot \tan(\mu + \psi) \cdot \left(\frac{D_{n-r}}{2} \right) \quad (D9)$$

$$T_{5n} = \frac{1}{4} \gamma' (H_n - H_{n-1}) \cdot K_p \cdot \pi (D_n^2 - d_n^2) \cdot \tan(\mu + \psi) \cdot \left(\frac{D_{n-r}}{2} \right) \quad (D10)$$

For the topmost and bottommost helix Eqs. (D11) and (D12) will apply respectively, i.e. formula for single helix screw will apply.

$$T_{4n} = \frac{1}{4} \gamma' H_t \cdot K_a \cdot \pi (D_{t,h}^2 - d^2) \cdot \tan(\mu + \psi) \cdot \left(\frac{D_{n-r}}{2} \right) \quad (D11)$$

$$T_{5n} = \frac{1}{4} \gamma' H \cdot K_p \cdot \pi (D_{b,h}^2 - d^2) \cdot \tan(\mu + \psi) \cdot \left(\frac{D_{n-r}}{2} \right) \quad (D12)$$

D.1.4 Torque resistance T_6

This is due to force resulting from the passive lateral earth pressure acting on the surface area of the screw pitch due to its inclination in the third dimension.

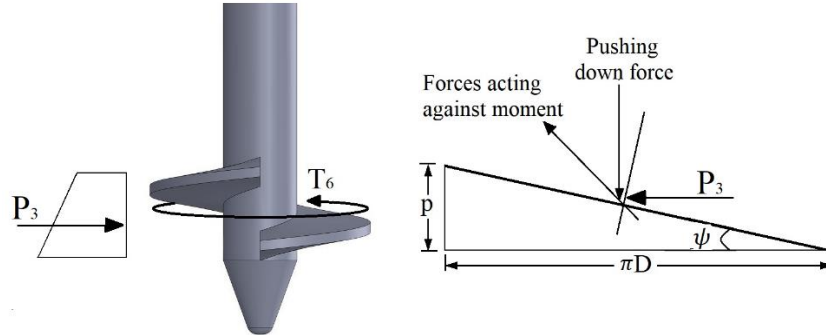


Fig D4: Forces due to inclination of helix in third dimension

$$T_{6n} = 1/2 \gamma' H_n \cdot p \cdot K_p \cdot \sqrt{(\pi D_n)^2 + p^2} \cdot (D_n - r/2) \quad (D13)$$

Where p = pitch of helix

D.1.5 Force due to passive earth pressure exerted on the outer perimeter of the screw blade or helix.

The resulting frictional resistance due to this force produce resisting moment T_7 against the installation torque. As shown in Fig D5 and Eq. (D14).

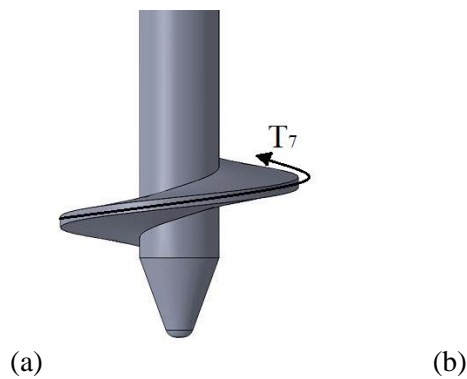


Figure D5: Torque resistance acting along helix perimeter

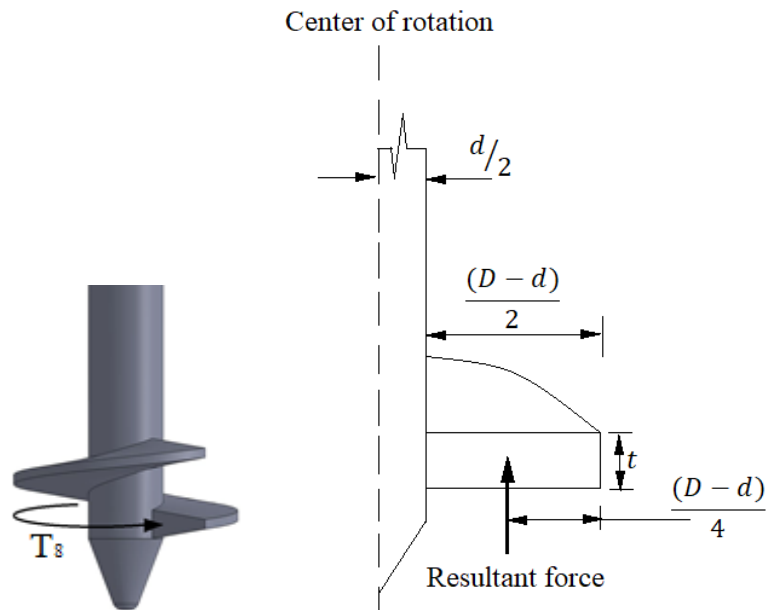
$$T_7 = \sigma_v \times t_{o,h} \times P_h \times K_p \times K_f \times (D_n/2)$$

$$T_{7n} = \gamma' H_n \cdot t_{o,h} \cdot K_p \cdot \tan(\mu) \cdot (\pi D_n) \cdot (D_n/2) \quad (D14)$$

Where $t_{o,h}$ = outer thickness of helix

D.1.6 Moment of resistance T_8 (Eq. (D15)) due to cutting edge of helix penetrating into the soil.

$$T_8 = \gamma' H \times \text{Area of the cutting edge} \times \text{bearing resistance} \times \left(\frac{D_n - d_n}{4} + \frac{d_n}{2} \right)$$



$$T_8 = \text{Resultant force} \times (\text{lever arm})$$

$$T_8 = (\gamma' H \times \text{Area of the cutting edge} \times \text{bearing resistance}) \times \left(\frac{D_n - d_n}{4} + \frac{d_n}{2} \right)$$

$$T_8 = \gamma' H \times \left(\frac{D_n - d_n}{2} \times t \right) \times N_c \times \left(\frac{D_n - d_n}{4} + \frac{d_n}{2} \right)$$

$$T_8 = \gamma' H \cdot N_c \cdot \left(\frac{D_n^2 - d_n^2}{2} \right) \cdot t \tag{D15}$$

If the cutting edge is inclined or tapered the resultant force should be resolved accordingly.